Fabrication of nano-structured duplex and ferritic stainless steel by planetary milling followed by consolidation

A Thesis submitted in partial fulfilment of the
Requirements for the degree of

Doctor of Philosophy
In
Metallurgical and Materials Engineering

By

Shashanka R
(Roll Number-511MM607)

Under the supervision of

Dr. Debasis Chaira

Department of Metallurgical and Materials Engineering

National Institute of Technology Rourkela

Rourkela-769008

INDIA

July- 2016

Fabrication of nano-structured duplex and ferritic stainless steel by planetary milling followed by consolidation

July, 2016 **Shashanka R**

“Dedicated to my beloved Parents”

Declaration

Date:

I hereby declare that the work presented in the thesis entitled "**Fabrication of nano-structured duplex and ferritic stainless steel by planetary milling followed by consolidation**" submitted for Ph.D. Degree to the National Institute of Technology, Rourkela has been carried out by me at Department of Metallurgical and Materials Engineering, National Institute of Technology, Rourkela under the supervision of Dr. Debasis Chaira. I hereby declare that the work is original and has not been submitted in part or full by me for any degree or diploma to this or any other University/Institute.

Shashanka R
Department of Metallurgical and
Materials Engineering
National Institute of Technology
Rourkela-769008
Odisha, India

Contents **Page No.**

CHAPTER 4 Synthesis of nano-structured duplex and ferritic stainless steel powder by DDPM and consolidation by conventional sintering and spark plasma sintering **58-118**

CHAPTER 5 Non-lubricated sliding wear behaviour of nano-yittria dispersed and yittria free duplex and ferritic stainless steel **119-143**

CHAPTER 6 Corrosion study of spark plasma sintered duplex and ferritic stainless steel by linear sweep voltammetric method **144-162**

Department of Metallurgical and Materials Engineering
National Institute of Technology Rourkela
Rourkela-769008

CERTIFICATE

This is to certify that the thesis entitled "**Fabrication of nano-structured duplex and ferritic stainless steel by planetary milling followed by consolidation**" being submitted by **Mr**. **Shashanka R** to the National Institute of Technology Rourkela, for the award of the degree of **Doctor of Philosophy** is a record of bonafide research work carried out under my supervision and guidance. The results presented in this thesis have not been submitted elsewhere for the award of any other degree or diploma. This work in my opinion has reached the standard of fulfilling the requirements for the award of the degree of **Doctor of Philosophy** in accordance with the regulations of institute.

Date:

Dr. Debasis Chaira

(Supervisor)

Acknowledgement

At final steps towards my PhD programme I would like to acknowledge my institute and many people who have made this wonderful PhD journey possible. First of all, it is my immense privilege to express my profound gratitude and indebtedness to my supervisor Dr. Debasis Chaira, Department of Metallurgical & Materials Engineering, National Institute of Technology Rourkela. He has been an inextinguishable fire of inspiration and a wonderful mentor for me. Without his great efforts and effective guidance this work could not have been possible. He has guided me at all stages during this research work. I take the liberty to dedicate this section of thesis to him and thank him from the bottom of my heart for all that he has given me. I will cherish all the moments of enlightenment he has shared with me. He has been a real idol for me and I will always remember him for his attitude of pushing all limits for his dear students.

I would like to convey my sincere gratitude to Prof. S. C. Mishra, Head of the Department, Department of Metallurgical and Materials Engineering, National Institute of Technology Rourkela, for constant guidance and encouragement. I would take pleasure of thanking all doctoral scrutiny committee members for fulfilling their duties of assessing my PhD work without fail.

I am grateful to our honorable director Prof. Sunil Kumar Sarangi for his continuous encouragement and motivational speeches. He has been a core academician with magnanimous personality who inspired many research students like me in a great way.

This is my complete privilege to thank CSIR for awarding senior research fellowship from 2011 to 2014. I thank Dr. Kumara Swamy, Kuvempu University, Karnataka for allowing me to carry out electrochemical measurements in his lab. He has been a great inspiration for me right from my masters. I take this opportunity to thank Dr. Anindya Basu, Department of Metallurgical and Materials Engineering, National Institute of Technology, Rourkela for allowing me to conduct wear measurements. I thank Powder Metallurgy Association of India (PMAI) for sponsoring me for the overseas conference POWDERMET-2015, San Diego, USA. I am grateful to Dr. D. Chakravarty, Scientist D, ARCI, Hyderabad for conducting spark plasma sintering of stainless steel samples. I thank Dr. B. Mishra, Deputy Director, DISIR, Rajgangpur, Odisha for allowing me to use tubular furnace for sintering. I am also

grateful to Dr. S.K. Karak, Dr. K. Dutta, Dr. S. N. Alam of Metallurgical and Materials Engineering department, NIT Rourkela for their valuable input and advice during the research work.

Further my appreciation goes to the entire Metallurgical and Materials Engineering faculty and staff of NIT Rourkela for all their help along the way. I would like to thank Dr. S. Bal, Scientific officer, Department of Metallurgical and Materials Engineering, National Institute of Technology Rourkela and our laboratory members U.K. Sahu, S. Pradhan, S. Hembram, A. Acharya, A. Pal, R. Pattanaik for constant practical assistance and help whenever required. I would like to thank the National Institute of Technology Rourkela for allowing me to come and pursue my PhD degree.

I would like to acknowledge my beloved friends P. Sahani, R.K. Behera, Ram Kumar, Mohan, Vinay Kumar for their unconditional help and support during my research work. I also thank my dearest friends Sharath, Mithun, Krishnamurthy for their help and motivation all the time.

I would like to especially acknowledge my aunty Vasantha Kumari for teaching me and look after me during my childhood days. Without her effort it could not have been possible to pursue my higher education. I am very grateful to my sweet brother Pratheek, sister in law Asha, my uncle Raghu Prasad, aunties Ambika, Savitha and my sister Roopashree for their love, affection and understanding me along the way. I love to dedicate my sincere appreciation for my grandparents Bhadrachari, Sharadamma, Mayachari and Sharada for their perpetual love.

Finally my special thanks to my parents Rajendrachari and Shakunthala for their unconditional love, motivation and assisting me throughout my life. Without their help and encouragement it would not have been possible for me to undertake this work. Thank you all.

All errors and limitations remaining in this thesis are solely by me.

Shashanka R
Date:

Abstract

The use of stainless steel has been increased extensively in various fields from past few decades. Now a day stainless steels are in great demand due to good corrosion resistance, high toughness, low thermal expansion, high energy absorption, good weldability, high strength, high thermal conductivity, creep resistance, wear resistance, higher yield strength and excellent high temperature oxidation resistance properties. The stainless steels are mainly used in refrigeration cabinets, bench work, cold water tanks, chemical and food processing, water treatment plant, street furniture, electrical cabinets, chemical, oil, petrochemical, marine, nuclear power, paper and pulp industries. Properties of the materials improve tremendously when bring down their size to nano level. Hence, we synthesized nano structured duplex and ferritic stainless steel by high energy planetary milling.

Nano-structured duplex and ferritic stainless steel powders were prepared by milling of elemental Fe, Cr and Ni powder in pulverisette planetary mill for 40 hours and then consolidated by conventional pressureless sintering. Activation energy for formation of duplex and ferritic stainless steel were calculated by Kissinger method using differential scanning calorimetry and was found to be 159.24 and 90.17 KJ/mol respectively. Both duplex and ferritic stainless steel powders were consolidated at 1000, 1200 and 1400°C in argon atmosphere to study microstructure, density and hardness. In duplex stainless steel, 90% of maximum sintered density and 550HV of Vickers microhardness were achieved at 1400°C sintered temperature. Similarly, 92% sintered density and 263HV microhardness were achieved for ferritic stainless steel sintered at 1400°C.

The nano-structured duplex and ferritic stainless steel powders were also prepared by milling elemental powders in a specially designed dual-drive planetary mill (DDPM) for 10 hours. The progress of milling and phase transition of stainless steel have been studied by means of x-ray diffraction. The crystallite size and the lattice strain of the duplex stainless steel after 10 hours milling are 9nm and 5.59×10^{-3} respectively. Similarly, the crystallite size and the lattice strain of the ferritic stainless steel after 10 hours milling are 8nm and 9.05×10^{-3} respectively. Annealing of milled powder at 750°C promotes ferritic to austenitic transformation in both argon and nitrogen atmosphere as limited transformation takes place after milling. However, nitrogen favours the transformation to a greater extent than argon. Lattice parameters

calculated from both high resolution transmission electron micrographs (HRTEM) and Nelson-Riley method match with duplex and ferritic stainless steel. It has been found that initially particles are flattened and finally become almost spherical of size around 10-15 micrometer in both cases.

The effect of process controlling agent (PCA) such as stearic acid (SA), effect of ball to powder weight ratio (BPR 6:1and 12:1), milling speed (64 and 75% critical speed) and dry and wet milling were studied during planetary milling of elemental Fe–18Cr–13Ni (duplex) and Fe–17Cr–1Ni (ferritic) powders for 10h in a dual drive planetary mill (DDPM). We have found that all these mill parameters have great influence in tuning the final particle morphology, size and phase evolution during milling. It was found that addition of PCA, a BPR of 12:1, dry milling and 75% critical speed is more effective in reducing particle size and formation of duplex and ferritic stainless steel after 10h milling of elemental powder compositions than their counterparts.

Yittria free and yittria dispersed duplex and ferritic stainless steels were fabricated by both conventional sintering and spark plasma sintering (SPS) methods. The effect of sintering temperature, sintering atmosphere and addition of Y_2O_3 nanoparticles on phase transformation, microstructure, mechanical properties were evaluated during conventional sintering. Non-lubricated sliding wear properties of conventional and spark plasma sintered stainless steel samples against a diamond indenter were compared successfully at 10 and 20N wear loads. Spark plasma sintered stainless steel samples show maximum wear resistance compared to conventionally sintered stainless steel. The present study also involves the comparison of wear behaviour of yittria dispersed and yittria free stainless steel sintered conventionally at 1000°C in argon and nitrogen atmospheres. The wear mechanism of all the stainless steel samples were studied by scanning electron microscopy (SEM), energy dispersive spectroscopy (EDS) and found to be abrasive and oxidation wear. Qualitative analysis of wear track and wear debris confirm the presence of oxygen during wear. Wear debris of less harder ferritic stainless steel samples are found to be flakes and harder duplex is spherical.

The microstructure and corrosion properties of spark plasma sintered yittria dispersed and yittria free duplex and ferritic stainless samples were studied. Spark plasma sintering (SPS) was carried out at 1000°C by applying 50MPa pressure with holding time of 5minutes. The

SPS duplex, ferritic and yittria dispersed duplex and ferritic stainless steel samples were characterized by field emission scanning electron microscopy (FESEM) and XRD. Linear sweep voltammetry (LSV) tests were employed to evaluate corrosion resistance of the samples. Corrosion studies were carried out in 0.5, 1 and 2M concentration of NaCl and H_2SO_4 solutions at different quiet time of 2, 4, 6, 8 and 10 seconds. Yittria dispersed stainless steel samples show more resistance to corrosion than yittria free stainless steel samples. It was observed that as concentration of NaCl and H_2SO_4 increases from 0.5M to 2M the corrosion resistance decreases due to the availability of more Cl^{-} and SO_4^{-} ions at higher concentration. Maximum pitting potential (E_P) at 0.5M NaCl (almost equal to NaCl present in sea water) of yittria dispersed duplex and ferritic stainless steel samples are 1.45V and 0.64V respectively. Similarly, yittria free duplex and ferritic stainless steel samples show 0.63V and 0.57V respectively. E_P value of yittria dispersed duplex and ferritic stainless steel samples at 0.5M H_2SO_4 are 0.30V and 0.23V respectively. Similarly, yittria free duplex and ferritic stainless steel samples show E_P value of 0.18V and 0.14V respectively at 0.5M H_2SO_4. Corroded samples were then characterized by FESEM and optical microscopy to confirm the presence of corrosion region.

Carbon paste electrode was modified with yittria free and yittria dispersed duplex stainless steel respectively to study their electrocatalytic behaviour in detecting folic acid. We determined optimum concentration of both the modifiers which show maximum anodic peak current in determining the folic acid. Electro catalytic properties of analyte were investigated at 2, 4, 6, 8, 10 and 12mg concentrations of modifier. Among all, 8mg yittria dispersed duplex stainless steel modified carbon paste electrode showed maximum current sensitivity than 4mg yittria free duplex stainless steel modified carbon paste electrode in 2mM folic acid concentration and 0.2M phosphate buffer solution of pH 7.2 at scan rate of 100mVs-1. We reported the effect of scan rate, concentration of folic acid and pH effect on oxidation peak of folic acid in both the modified carbon electrodes. Plot of all the above effects shows linear relationship and their electrode reactions were adsorption controlled. We successfully fabricated reliable, stable and fast response electrochemical sensor to detect folic acid.

Keywords: Stainless steel; Planetary milling; Powder metallurgy; Phase transformation; Nanostructured materials; Process control agent; Milling parameters; Yittria; Spark plasma sintering; Conventional sintering; Wear properties; Mechanical properties; Cyclic voltammetry; Electrochemical sensor; Folic acid; Pitting corrosion; Linear sweep voltammetry

LIST OF FIGURES

Chapter 4 Synthesis of nano-structured duplex and ferritic stainless steel powder by DDPM and consolidation by conventional sintering and SPS

Chapter 4.1 Synthesis of nano-structured duplex and ferritic stainless steel powders by dual-drive planetary milling (DDPM)

Chapter 5 Non-lubricated sliding wear behaviour of nano-yittria dispersed and yittria free duplex and ferritic stainless steel fabricated by powder metallurgy

Chapter 6 Corrosion study of spark plasma sintered duplex and ferritic stainless steel samples by linear sweep voltammetric method

Chapter 7 Electrochemical investigations of duplex and yittria dispersed duplex stainless steel at carbon paste electrode in detecting folic acid: A cyclic voltammetry study

LIST OF TABLES

Nomenclature

γ	Specific surface energy
ΔS	Change in surface area
wt.%	Weight percentage
MPa	Mega pascal
°C	Degree in Celsius
°F	Degree in Fahrenheit
ϖ	Rotation
K_c	Critical speed constant
P	Equilibrium pressure
P_0	Saturated vapour pressure of nitrogen
V	Amount of gas forming a monolayer
C	Constant of heat of adsorption in the first layer
gf	Gram force
N	Newton
nm	Nano meter
µm	Micro meter
T_p	Crystallization peak temperature
R	Gas constant
E_C	Activation energy
α-Fe	Ferrite
γ-Fe	Austenite

Q	Total volume of wear debris
Å	Angstrom
β	Full width half maxima (FWHM)
η	Lattice strain
λ	Wavelength of the Cu target
I_P	Pitting current
E_P	Pitting potential
V	Voltage
J	Current density
M	Molar
A	Ampere
i_p	Peak current
n	Stoichiometric number of electrons involved in the electrode reaction
A	Area of electrode
D	Diffusion coefficient
C_o	Concentration
υ	Scan rate

Abbreviations

PM	Powder metallurgy
DDPM	Dual drive planetary mill
SPS	Spark plasma sintering
BPR	Ball to powder weight ratio
PCA	Process controlling agents
MA	Mechanical alloying
P5 mill	Fritsch Pulverisette-5 mill
rpm	Rotations per minute
DSC	Differential scanning calorimeter
LSV	Linear sweep voltammetry
%CS	Critical speed in percentage
SA	Stearic acid
XRD	X-ray diffraction
SEM	Scanning electron microscopy
EDS	Energy dispersive spectroscopy
FESEM	Field emission scanning electron microscopy
BET	Brunauer, Emmett, and Teller
HRTEM	High resolution transmission electron microscopy
SAED	Selected area electron diffraction
HV	Vickers hardness

DMCPE	Duplex modified carbon paste electrode
YDMCPE	Yittria dispersed duplex modified carbon paste electrode
CPE	Carbon paste electrode
FA	Folic acid
N-R plot	Nelson-Riley plot
ISE	Indentation size effect
JCPDS	Joint committee on powder diffraction standards
(h k l)	Miller indices
BSE	Back scattered electrons
PBS	Phosphate buffer solution

CHAPTER 1

Introduction and Literature review

1.1 Introduction

Stainless steel is an alloy of Fe with minimum 11% Cr and 0.08 to 0.2% of carbon, the percentage of Cr can be tuned according to the required applications. Chromium improves the corrosion resistance properties to stainless steel by forming strong oxide layer; higher the amount of Cr stronger is the oxide layer. Stainless steel is used worldwide in industries, business, home, hospitals, construction and almost everywhere. Due to the wide applications of stainless steel, researchers developed plenty of standardized stainless steel grades with hundreds of different chemical compositions. Depending upon the properties, structures and compositions, stainless steels are mainly divided in to four categories:

1) Austenitic stainless steel
2) Ferritic stainless steel
3) Duplex stainless steel
4) Martensitic stainless steel

Among all the stainless steels, duplex and ferritic stainless steels are the two important types having a wide range of applications.

Duplex stainless steel contains almost equal proportions of ferrite and austenite phases. Ferrite phase imparts more strength while austenite phase assures the toughness and better corrosion resistance. It has the combining features of two major classes of stainless steel, austenite and ferrite and thus made it very attractive for numerous applications. This kind of stainless steels are having very good toughness, high corrosion resistance, low thermal expansion, high energy absorption, weldability and high strength compared to single phase austenitic and ferritic stainless steel; hence used in chemical, oil, petrochemical, marine, nuclear power, paper and pulp industries.

On the other hand, ferritic stainless steel exhibits body centred cubic structure with less than 0.08% of carbon, 10.5 to 28% of chromium and very low percentage of expensive nickel. Generally, ferritic stainless steel has poor corrosion resistance due to low chromium and nickel content. Additional elements such as molybdenum, copper and aluminium can be added to ferritic stainless steel to improve their properties and structures. This steel is magnetic in nature, hence used as sticking memos on the fridge, storing knives and other metallic implements. It is also used as pans in induction cooker which involves the generation of heat by transfer of magnetic energy. Some of the properties such as low thermal expansion, excellent oxidation resistance at high temperature, high thermal conductivity, creep resistance, high yield strength and less stress corrosion properties make ferritic stainless steel an important type of stainless steel. Similarly, addition of nano Y_2O_3 particles in to ferritic stainless steel improves their properties tremendously. Hence, yittria dispersed stainless steel is used as blankets for nuclear reactors and as oxidation resistant at high temperature operations.

In the present study, duplex and ferritic stainless steels have been synthesized by high energy planetary milling of elemental Fe, Cr and Ni powders. The compositions of duplex and ferritic stainless steel were selected from Schaeffler diagram as shown in the Figure 1.1. Schaeffler diagram is one of the original methods of predicting balancing phases in stainless steels.

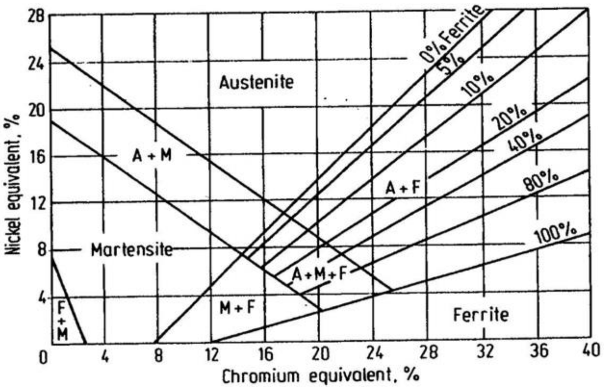

Figure 1.1 Schaeffler diagram

From the diagram, chromium equivalent can be calculated for ferrite stabilizing elements and nickel equivalent for austenite stabilizing elements. Both the equivalents are used as axes in a diagram which depicts the compositional equivalent areas of austenite, ferrite and martensite phases. The formula for Cr_{eq} and Ni_{eq} are as follows:

$$Cr_{eq} = \%\ Cr + 1.4\ (\%\ Mo) + 0.5\ (\%\ Nb) + 1.5\ (\%\ Si) + 2\ (\%\ Ti) \qquad \textbf{(1)}$$

$$Ni_{eq} = \%\ Ni + 30\ (\%\ C) + 0.5\ (\%\ Mn) + 30\ (\%\ N) \qquad \textbf{(2)}$$

Preparation of stainless steel is a time consuming method, which involves series of processes like melting, casting, forming, heat treatment, de-scaling, cutting and finishing etc.

Powder metallurgy (PM) involves mass production of small objects with complex shape at low cost. It is not possible to produce combination of metal and non-metal, metal-metal compositions by other methods but can be achieved by PM routes. PM involves the formation of near net shaped, homogeneous and less scrap materials and requires very less or no finishing operations to fabricate final product. PM parts can be manufactured with controlled porosity and can be infiltrate the pores by adding other low melting materials or lubricants.

Therefore, PM proved to be one of the best solid state powder processing methods to prepare alloy of elemental powder. Many synthesis routes like equal channel angular processing, hydrostatic extrusion, high pressure torsion, ultrasonic shot peening, hydraulic pressings are used to refine the structure of metals and alloys by plastic deformation and solid solution mechanism. But planetary milling is one of the most simple and widely used plastic deformation methods to achieve extreme refinement, metastable crystalline and quasi-crystalline phases, nano-structured and amorphous phases.

Dual drive planetary mill (DDPM) is a high energy planetary ball mill specially designed to prepare nano-structured stainless steel powder alloy by milling elemental composition of Fe, Cr and Ni. This method of stainless steel powder preparation is cost effective and highly feasible. Commercially available low/high energy planetary mills do not generate enough energy during milling. Therefore, milled powders are subjected to post heat treatment after milling. But DDPM milled powders do not require any post heat treatment as it can produce more than 50g acceleration field and it is limited to 10g acceleration field in commercially available planetary mills. In the present study, our target is not to provide the heat from external sources to obtain a stabilized final desired product. Stabilized product should form without external heat being supplied. DDPM can produce high temperature and easily induce chemical reactions between powders by increasing the diffusion kinetics of solid-state chemical reactions. But this kind solid state of chemical reaction is not possible in other commercially available planetary mills.

One of our targets is to prepare stainless powder in bulk amount in lesser milling time. Another advantage of DDPM is the capable of synthesizing extremely fine, homogeneous and spherical nano crystalline powders that can be easily fabricated and consolidated using conventional and spark plasma sintering methods. Nano-structured stainless steel attracted much attention due to the extreme improvement in physical, chemical and mechanical properties. Consolidation of nano-structured materials and retention of nano-grain size is really a great challenge. Conventional sintering cannot eliminate all the pores but it can reduce up to certain level and there is a rapid grain growth. Spark plasma sintering (SPS) can reduce porosity even better than conventional sintering and at the same time it can retain nano-size even after consolidation. Due to diffusion of atoms, the powder surfaces get eliminated at different stages during sintering, starting from neck formation to final elimination of pores at the end of process. The power source for solid state processes is from the change in free energy between the neck and the surface of particle and this energy promotes transfer of materials in a faster way. The transfer takes place through grain boundary and results in particle reduction and disappearance of pores. SPS is an advanced sintering technique which involves fabrication of poorly sinterable materials by applying load and heat simultaneously and has many advantages over conventional sintering method. It involves discharging of spark plasma at gaps of the particles with an on-off electrical current and induces neck formation, thermal diffusion process on the particles. This results in hindered grain growth, efficient shrinkage in less time and cleaner grain boundaries for effective interface formation.

In this thesis, a successful attempt has been made to prepare nano-structured ferritic and duplex stainless steel powders in bulk amount by high energy dual drive planetary milling of elemental Fe, Cr and Ni powders followed by their characterization and consolidation. We have studied the effect of milling parameters such as types of mill, ball to powder weight ratios (BPR), process controlling agents (PCA), mill speed, milling time and milling atmosphere on the morphology, phase transformation and particle size of stainless steel powders. The oxygen active compound like Y_2O_3 nanoparticles were dispersed in to stainless steel and its effect was studied successfully. Nano yittria dispersed and yittria free stainless steel powders were consolidated by both conventional and spark plasma sintering (SPS) methods. The effect of sintering temperatures and atmospheres to investigate the hardness, density, microstructures, phase transformation and wear resistance properties were also evaluated. Further study of innovative applications such as corrosion studies by linear sweep voltammetric method and potent applications of stainless steel powders as electrochemical sensor was also conducted. The electro catalytic properties of yittria dispersed and yittria free stainless steel powders towards biologically active compounds were studied.

1.2 Literature Review

This section has been divided into four sub-sections. The first sub-section describes a review of the nanostructured materials and their methods of synthesis; the second one explains the details of planetary milling; the third one gives a detailed description of synthesis of different types of stainless steels by planetary milling; and final sub-section describes the electrochemical studies such as corrosion properties of stainless steels.

1.2.1 Nano-structured materials

Nano-structured materials are single phase or multi phase materials having crystallite size in the order of 1-100 nano meters with either one or two or three dimensions. Due to the nano crystallite size, a large fraction of the atoms are located in the grain boundaries. The grain boundaries between the two grains decelerate or sometime arrest the propagation of defects during stress operations. This enhances the strength of materials due to the availability of larger interface area. Further grain refinement increases the volume fraction of interfaces and where the density of grain boundaries reaches 10^{19}cm^{-3}. Hence, nano-structured materials exhibit higher strength, hardness and high diffusion rates due to the shorter diffusion paths and consequently reduced sintering time for compacting powders. Therefore, nano-structured materials exhibit improved physical, mechanical, electrical and magnetic properties compared to micron size conventional materials. Some of the commonly used methods for preparing nano-structured materials are as follows:

- Electric arc discharge method [1]
- Inert gas condensation [2]
- Electrodeposition [3]
- Rapid solidification [4]
- Sol-gel processing [5]
- Chemical vapour deposition [6]
- Planetary ball milling [7]

Planetary ball milling method used to prepare nano-structured materials in large quantity at a shorter span of time. Planetary ball milling can produce nano-crystalline materials in its solid state at room temperature and can be easily scaled to industrial levels. Thompson and Politis (1987) [9] reported the formation of nano-structured materials by mechanical alloying for the first time. Later, Shingu et al. (1988) [10] specifically mentioned the formation of “nano meter order crystalline structures produced by mechanical alloying”. Further, Koch (1993) [11] has successfully concise the results on the synthesis and structure of nano-crystalline materials produced by mechanical attrition method and has recently given an updated description on the methods for nano-crystalline synthesis (Koch 1997) [12]. It is possible to bring down the grain size to nano level irrespective of pure metals, inter-metallics and alloys by mechanical alloying (MA) method. Therefore MA method appears to be ubiquitous in nature. The mechanism of nano-structured materials by MA has been described by Hellstern et al. (1989) [18].

One of the disadvantages of mechanical alloying is contamination of powder materials, mainly comes from grinding medium and the jar surface. Myers and Barnett (1953) [13], Thompson and Bankston (1970) [14], Ando (1986) [15], Hickson and Juras (1986) [16], Iwansson and Landström (2000) [17] reported the influence of contamination from grinding medium during milling. All of these studies emphasize the importance of an appropriate choice of grinding medium for the elements of interest. Contamination can be reduced by repeated pulverizing and washing the powder samples several times before its analysis [8]. Contamination can also be minimized by using a proper canister inside the jar surface and selection of same material compositions of grinding medium, jar and material to be synthesised.

1.2.2 Planetary milling

Planetary ball mills owe their name due to the planetary movement of its vials. Schaffer and McCormick (1989) [19, 20] first reported the induced wide variety of solid–solid and liquid-solid chemical reactions during milling. In early 1894, Carry M. reported that conversion of mechanical energy to chemical energy leads to chemical reactions. He observed such chemical reactions in high-energy mills and he referred that process as high energy milling or mechanochemical synthesis. McCormick [22], Takacs [23], and Matteazzi [24] reported the detailed description about the induced chemical reactions in high-energy milling. They reported that most of the high energy milling reaction follows displacement reactions as follows:

$$M_xO + yR \rightarrow xM + R_yO$$

Metal oxide (M_xO) is reduced to high reactive metal (M)

Tschakarov et al. (1982) [25] became the first to report reaction milling in high-energy mills and they used high-energy mill to produce different metal chalcogenides followed by the reactions as follows:

$$xM + yN \rightarrow M_xN_y$$

Where, M = Ag, Cu, Cd, Zn, In, Ti, Ge, Sn, Pb, As, Bi and N = S, Se, Te.

Usually solid-state reactions involve the formation of product phases at the grain boundaries of the reactants. Further mature of product phase involves diffusion of reactant phase atoms through product phase. This results in the formation of barrier layer and prevents further solid-solid reactions because these types of reactions require elevated temperatures to promote diffusion at sensible rates. Therefore, high energy planetary mills are suitable for chemical reactions as they produce high temperature during milling. Almost all the chemical reactions involved in a high-energy milling are thermodynamically feasible at room temperature.

Mechanochemical process can be applied in many important fields to produce ultrafine powders, nano-structured materials, processing of mineral and wastes, combustion reactions, refining the metals, production of a very fine dispersion of secondary phase particles like Y_2O_3 nanoparticles, refining the microstructure of matrix, extending the solubility limits, formation of amorphous phases etc.

Microstructural refinement during high energy milling process results in welding, fracture and particle deformation due to the continuous collision of ball-powder-jar. The creation of high density dislocations at grain boundaries in powders can promote the solute micro segregation at dislocations and lead to the extended solid solutions. During milling, the chemical energy transmitted to crystalline powders and results in deformed random nano-crystalline materials at higher milling time. It is possible to synthesize materials that exhibit nano meter grain size but the particle size typically decreases to only micrometer level during milling. Figure 1.2 represents the mechanism of ball-powder-ball collision during milling process.

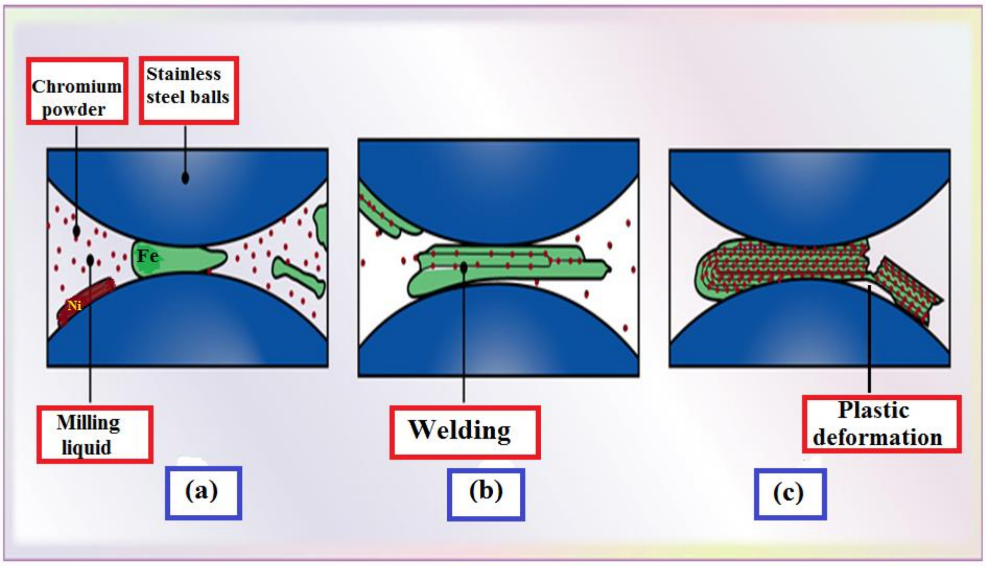

Figure 1.2 The mechanism of ball-powder-ball collision during milling process

During high energy milling the powder particles undergo series of mechanisms due to the high impact energy exerted by ball and jars. Powder particles repeatedly undergo flattening, cold welding, work hardening, fragmentation and re-welding. In case of ductile-ductile and ductile-brittle material combinations, soft particles becomes flat and weld together to form a single large lamellar structure. Sometimes the size of the lamella even exceeds the size of the parent elements before milling. At this stage, the formed lamellar structures contain characteristic layers of various starting constituents. Further milling results in work hardening and fracture by fatigue failure mechanism. This microstructure refinement continues further due to the absence of strong agglomeration forces and due to the domination of fragmentation over cold welding. At this stage, particle structure gets refined steadily due to high impact energy of grinding balls on walls of jar, but the particle size continues to be same. Further increase in milling time causes steady-state equilibrium balance between the rate of welding and this tends to increase the particle size. Smaller fragmented particles withstand deformation without further fracture and tend to re-weld in to large particles [26].

The reduction of grain size to a nano meter scale leads to increase in the volume fraction of grain boundaries which include many point and linear defects, especially dislocations vacancies, stacking faults and consequently leads to the shorter diffusion path and more defect storage sites. Therefore, the rate of diffusion is more for mechanically alloyed materials and the rate increases further with temperature.

1.2.2.1 Process variables

Mechanical alloying is one of the complex processes and involves optimization of various milling parameters to achieve desired materials. All of the milling process variables are not completely independent. Some of the important parameters that have an ability to alter the properties of final constituents of powders are

1. Type of mill
2. Milling container
3. Milling speed
4. Milling time
5. Grinding medium
6. Ball-to-powder weight ratio
7. Extent of filling the vial
8. Milling atmosphere

9. Process control agent
10. Temperature of milling

The morphology, phase transformation and particle size of materials can be altered by optimizing the milling parameters.

1. Type of mill

There are number of different types of ball mills are available in the market and are differ in their capacity, operation speed and their ability to control the process by varying the temperature of milling and the extent of minimizing the contamination of the powders. Therefore, it is very important to choose a suitable mill based upon the type, final composition and quantity of the powders used for mechanical alloying. Some of the commonly used mills are SPEX shaker mills, Fritsch Pulverisette planetary ball mills, attritor mills and specially designed mills. All these mills are differing in capacity, energy and used for specific applications.

2. Milling container

Milling container comprises of grinding vessel, jars, balls etc. During milling, the impact of grinding medium on the walls of the container takes place. This results in the material dislodgment from the container and incorporated in to powders. This can contaminate and alter the chemical composition of the powders. If the material of grinding medium and the milling powder is same, then contamination can be minimized as there is very less variation of chemical composition of powders. Therefore, selection of milling container plays a very important role during milling process. Shape and the internal design of milling container can also play an important role during milling process. Alloying at the flat ended vials occurs significantly at higher rates than in the round ended containers [27]. Some of the common types of materials used for grinding vessels are hardened steel, tool steel, hardened chromium steel, tempered steel, stainless steel, bearing steel and tungsten carbide [28].

3. Milling speed

It is easy to understand that energy input of the mill increases with increase in mill speed and this depends upon the mill design. But in conventional ball mills, at higher mill speed balls gets pinned to the inner walls of the container and do not fall down to exert any impact force and milling does not occurs. The speed of the mill at this stage is called as ‘critical mill speed’. Hence maximum mill speed should maintain just below the critical speed so that balls can fall down from the maximum height to produce high impact milling. Maximum impact energy due to high mill speed increases the temperature of the container. This is advantageous for those materials where diffusion is required to promote alloying of the powders. But in some cases it is disadvantageous where higher temperature can promote material transformation and results in decompositions of supersaturated solid solutions or meta-stable phases during milling [29].

4. Milling time

Milling time is a very important milling parameter; the chosen time should be such that a steady state between fracturing and cold welding of powder particle must achieve. Milling time usually depends upon the type of the mill used, intensity of milling, ball-to-powder weight ratio and temperature of the milling. Based upon these milling parameters milling time should be fixed, but it should be realized that prolonged milling time can cause the level of contamination and some undesirable phases [30]. Therefore, it is suitable that the powder is milled just for the required duration and not any longer.

5. Grinding medium

Generally high density materials are used as grinding medium because they can create high impact energy on the powder particles and promotes solid solution formation. Some of the commonly used high density materials used as grinding medium are tool steel, hardened steel, tempered steel, chromium steel, stainless steel etc. It is desirable to have the grinding vessel and grinding medium made from same materials to avoid cross contamination. Milling efficiency can also depend upon the size of the grinding medium. A high density and large grinding medium is appreciable when the large high density balls transfer maximum impact energy to the powder particles. The final constitution of the powder particles also depends upon the size of the grinding medium used [31]. Therefore, it is possible to control the shape, size and phases of final composition by varying the size of the grinding medium. Several researchers reported that smaller balls can produce intense frictional force, which can promote amorphous phase transformation [32, 33]. Atzmon (1990) [34] reported that use of different diameter balls can enhance the collision energy to the greater extent than the same diameter balls. Another advantage of using different diameter balls that it can minimize the amount of cold welding and the amount of powder coated onto the surface of the balls [35]. Same diameter grinding balls forms tracks inside the container and consequently balls roll along the well defined trajectory instead of colliding the end surfaces. This reduces the efficiency of the mill. Therefore, it is very important to use the combination of smaller and larger balls to randomize their motion [36].

6. Ball-to-powder weight ratio

Ball to powder weight ratio (BPR) is one of the important milling parameter can be varied from as low as 1:1 [37] to as high as 220:1 [38] to obtain desired constitution of powders. Commonly used ball to powder ratio in most of the mills is 10:1. Higher the BPR, shorter is the milling time required. Therefore, BPR plays a very significant role in deciding the time required for mechanical alloying. Due to the higher BPR there is an increase in weight proportion and the number of collisions per unit time; consequently more impact energy is transferred to the powder and thus alloying takes place in a very short time. Due to high impact energy exerted by grinding balls on the inner walls of the container, more heat will generate and this could alter the constitution of the powders. Mechanical alloying (MA) with low BPR values will produce metastable phases, whereas a high BPR value produces equilibrium phases [39].

7. Extent of filling the vial

There should be an enough space for the grinding balls and the powder particles to move around freely and collide in the container; otherwise alloying do not takes place properly. If the amount of grinding balls and powder is very less, then rate of alloy formation is more due to the high impact energy exerted by balls on the powders. If the quantity of balls and powders is more, then there is no enough space for the balls to move freely inside the container. This results in less impact energy exerted by balls on powder and therefore rate of alloy formation becomes slow. About 50% of the vial should leave as empty to increase the efficiency of the mill.

8. Milling atmosphere

Milling atmosphere plays a major role in the contamination of powder during MA. Therefore, milling is carried out either in evacuated or inert gas such as argon or helium atmospheres. High purity argon is used as one of the common ambient to prevent oxidation or contamination of powders during milling. The loading and unloading of the powders should be performed in an atmosphere controlled glove box. Different type of atmospheres is used to prepare specific materials. Miki et al. (1992) [40] and Calka et al. (1992) [41] reported the use of nitrogen atmosphere to prepare nitrides. Chen et al. (1996) [42] used hydrogen atmosphere during milling to prepare hydrides. If the powder is highly reactive, then there is a chance of forming oxides and nitrides using air in the vial. Therefore, it is very important to maintain inert atmosphere during milling. Many researchers reported that the type of atmosphere can also affect the final phase of the powders [43]. Lee et al. (1987) [44] reported that some of the gases such as oxygen enhances the kinetics of amorphization.

9. Process control agent (PCA)

True alloying occurs among the powder particles only when an equilibrium balance is maintained between cold welding and fracturing of particles. The ductile powder particles get cold weld together due to the heavy plastic deformation. Therefore, PCA is added to the powder mixtures to minimize the effect of cold welding during MA. PCA acts as surface active agent; they may be solids, liquids or gases. Most of the PCA are organic compounds and they adsorb on the surface of powder particles and reduce the cold welding of powder particles. Adsorbed surface active agents reduce the surface tension of the materials and thus inhibit the agglomeration. Energy (E) required for the size reduction of powders during milling is given as follows:

$$E = \gamma \Delta S \qquad \textbf{(3)}$$

Where, γ is the specific surface energy and ΔS is the increase of surface area.

Decrease in surface energy leads to the shorter milling times and very fine powder particles. Some of the important PCA are stearic acid, hexane, methanol, ethanol etc, and their quantity should lie between 1-5 wt.% of total powder charge. During milling, most of these compounds decompose, interact and get incorporated as dispersoids or as inclusions in to the powder particles. But these compounds are not necessarily harmful to alloy system and increase the strength of the materials by dispersion strengthening mechanism [45]. Gaffet et al. (1993) [46] reported that PCA can alter the solid solubility levels and affect the final phase formation. The shape, size and purity of the final powder particles depend upon the nature and quantity of PCA used during milling. Lai and Lu (1998) [31] reported that use of large amount of PCA can reduce the particle size exponentially for a given milling duration. Niu (1991) [47] reported that the use of liquid PCA (ethyl acetate) leads to the homogeneous distribution of particle size. The quantity of PCA used during milling determines the final yield of the powder. The quantification of PCA depends upon the cold welding of the powder particles, chemical and thermal stability of the PCA and on BPR.

10. Temperature of milling

Milling temperature has a significant effect in promoting diffusion processes irrespective of solid solution formation, intermetallics, nano-crystalline or amorphous phase. Therefore, temperature of milling is a very important milling parameter which decides the constitution of final powder. Very few studies are reported where the temperature of milling has been varied intentionally to investigate the solid solubility levels, type of phases formed etc. Qin (1997) [48] reported that the extent of solid solubility decreases at higher milling temperatures. Fu and Johnson (1993) [49] and Mishurda (1993) [50] reported equilibration effects and maximum diffusivity at higher milling temperatures. Lee et al. (1990) [51] observed the increase in amorphization kinetics at higher milling temperatures.

1.2.2.2 Types of planetary ball mills used

Generally, high energy planetary mills are differ in their capacity, efficiency of milling and specially designed arrangements for heating, cooling etc. Based upon these factors different types of high energy mills are available to prepare mechanically alloyed powders. Detail description of different mills used for MA was reported by Suryanarayana (1998) [52]. Brief descriptions of different types of planetary ball mills are given below.

Figure 1.3 Fritsch Pulverisette (P-5) two station planetary mill

One of the very popular and commonly used planetary mills to perform MA experiments is Pulverisette planetary mill, where a few grams of the powder can be milled at a time. Therefore, theses kind of planetary mills are more suitable for research purposes. These type of planetary mills are available in the market and are manufactured by Fritsch GmbH in Germany and marketed by Gilson Co., in the US and Canada. Due to the planet like movement of the vials, these types of mills owed the name planetary mills. These mills are assembled on a rotating support disk; a special drive mechanism induces to rotate about its own axes. During milling centrifugal force is produced due to the rotation of vials around their own axes and due to the rotation of supporting disk. Both grinding vials and rotating disk rotates in opposite directions.

The produced centrifugal force directly acts on the grinding medium and causes grinding balls to run down inside the vial (Friction effect). On the other hand grinding balls lift the powder to be grinded and moves freely inside the vials. Then grinding balls along with the powder collide against the opposite side of the vial (Impact effect). In earlier versions of planetary mills, the disk and vial rotation speed controlling arrangements were missing. But now a day planetary mills with speed regulatory system are available. Figure 1.3 shows Fritsch Pulverisette (P-5) two station planetary mill. Rajamani et al. (2000) [53] and Chaira et al. (2007) [54] designed a new type of planetary mills consists of a gyratory shaft and two cylindrical steel jars. Both jars and gyratory shaft will rotate simultaneously and separately at higher speeds. The high speed rotation of the mill tends grinding balls to move strongly and violently inside the vial, leading to large impact energy that improves the MA performance. The detailed description of mill fabrication and design are provided in the next chapter (see section 2.1).

1.2.2.3 Wet milling versus dry milling

Another important milling parameter that has a significant effect on powder morphology is the type of milling media either dry or wet milling. During dry milling the parameters such as milling energy, mill speed, milling time, BPR plays an important role in tuning the particle morphology. Similarly, during wet milling the properties like viscosity, pH and density of milling media plays an important role. If the viscosity of milling media is more then there is a slight hindrance of movement of grinding balls. This slightly decreases the effective rate of collision and impact energy on powders. But effective rate of collision of balls with powder particles during dry milling is more. The impact energy generated during dry milling is more; the balls can move freely inside the jars as there is no liquid media to hinder the ball and particle movement, leading to effective MA. During wet milling, liquid gets coated over the elemental particles and thus reduces the contact of the particles and the grinding balls. This separation of particles and balls is due to the damping force exerted by liquid media. This reduces the effective collision between balls-powder-jar and hence larger particles [55]. Some of the disadvantages of dry milling over wet milling are particle agglomeration due to sudden decrease in the particle size, high degree of contamination due to the high impact energy, generation of more heat due to the strong collisions of grinding balls and container. Therefore, wet milling is proved to be the better method to carryout milling operations.

1.2.3 Synthesis of stainless steel powders by planetary milling

1.2.3.1 Synthesis of duplex stainless steel

Several researchers have prepared duplex stainless steel powder by planetary milling of elemental Fe, Cr and Ni powders. Enayati and Bafandeh (2008) [56] studied the phase transition of stainless steel powders prepared in a planetary ball mill under argon atmosphere after 60h milling and pointed out the presence of dual structure. Similarly, Haghir et al. (2009) [57] synthesized high-nitrogen Fe–18Cr–11Mn stainless steel powder in a high energy planetary ball mill (Retsch, PM100) after 120h of milling and studied phase transformation of α to γ. Shashanka and Chaira (2014) [58] prepared ferritic and duplex stainless steel powders by elemental milling of Fe, Cr and Ni powders in a dual drive planetary mill for 10h as compared to 40h in pulverisette mill. They studied the phase transformation of duplex and ferritic stainless steel powders both in argon and nitrogen atmospheres and concluded that nitrogen acts as austenitic stabilizer. Dobrzanski et al. (2007) [59] synthesized duplex stainless steel by mixing powder composition of Fe–17Cr–13Ni–2.2Mo along with elemental powders such as Si, Mn and Cu in a turbula mixer followed by planetary milling. They consolidate the powder sample at 800 MPa load and at 2300°F sintering temperature in argon atmosphere for 1h. Brytan et al. (2009) [60] prepared duplex stainless steel by mixing ferritic stainless steel powder (16.86%Cr, 1.15%Si, 0.18%Mn, 0.02%C) with controlled addition of elemental alloying powders and sintered at 1250°C in a vacuum furnace with argon atmosphere for different time periods. Kazior et al. (2004) [61] reported the synthesis of boron alloyed duplex stainless steels by sintering the mixture of austenitic and ferritic stainless steels powders and investigated their mechanical properties. Prieto et al. (1994) [62] and Rosso and Grande (2000) [63] prepared duplex stainless steels by powder metallurgy route using pre alloyed powders by mixing a ferritic stainless steel powder with an austenite stabilising element powder. They observed that the austenite stabilising element will diffuse in to ferritic phase during sintering and caused the destabilisation and produce the bi-phased duplex microstructure. Kazior et al. (1999) [64] prepared duplex stainless steel by mixing commercially available austenitic and ferritic stainless steels powders. Kazior et al. (2000) [65] and Marcu-Puscas et al. (2001) [66] reported the preparation of duplex microstructure by inter diffusing the alloying elements during sintering. They investigated the phase transformation of mixtures of both austenitic and ferritic stainless steels powders during sintering, mechanical properties and corrosion resistance of sintered duplex stainless steels. Dobrzanski et al. (2007) [67] prepared duplex stainless steel by mixing austenitic and martensitic base powders by controlled addition of Cr, Ni, Mo and Cu alloying elements. Powder mixtures were compacted at 800MPa load and sintered in a vacuum furnace with argon atmosphere at temperatures from 1200°C to 1285°C for 0.5, 1 and 2 h. They studied the effect of sintering parameters like sintering time, temperature, atmosphere and gas pressure on the mechanical properties of duplex stainless steels. Martin et al. (2011) [68] consolidated duplex stainless steel at 650 and 700MPa in nitrogen and hydrogen atmospheres and different cooling rates (furnace, gas and water) to study the microstructure and mechanical properties. They reported that water cooling can increase the hardness of duplex stainless steel. Vijayalakshmi et al. (2011) [69] investigated the microstructural evolution, mechanical properties of duplex stainless steel at 1100, 1200, 1300 and 1350°C sintering temperatures. They correlated micro structural changes at different temperatures and concluded that the surface hardness mainly depends upon the phases present in the materials.

1.2.3.2 Synthesis of ferritic stainless steel

Pandey et al. (2014) [70] prepared ferritic stainless steel by DDPM with different BPR (10:1, 15:1 and 20:1) and milling speeds (250, 300 and 350 rpm). They reported that crystallite size and particle size of ferritic stainless steel decreases with increase in BPR and milling speed. Similarly, BET surface area and strain also increases with BPR and milling speed. Rahmanifard et al. (2010) [71] studied the effect of BPR (10:1 and 15:1) and milling speed (300 and 420rpm) during milling of ODS ferritic stainless steel. They observed that crystallite size and particle size of ferritic stainless steel powder reduces whereas lattice parameter increases with increase in BPR and milling speeds. They concluded that milling by using 8mm diameter ball, 420rpm milling speed and ball-to-powder weight ratio of 10:1 can reduce the milling time to 30h. Karak et al. (2010) [72] reported the effect of sintering temperature and addition of nano-yittria dispersoids on the wear resistance of ferritic stainless steel. They consolidated stainless steel by hot iso static pressing at 600, 800 and 1000°C under 1.2GPa uniaxial pressure. They found that wear mechanism was fretting wear and concluded that wear resistance increases with increase in sintering temperature. Shashanka and Chaira (2015) [73] prepared ferritic stainless steel powder by milling elemental Fe, Cr and Ni in a specially designed dual drive planetary mill for 10h followed by conventional pressureless sintering. Consolidation of ferritic stainless steel was performed at 1000, 1200 and 1400°C to study the mechanical properties, phase transformation and activation energy. Hong-wei et al. (2008) [74] prepared nano-crystalline 430L stainless steel by high-energy ball milling and spark plasma sintering techniques. They reported that the hardness can be improved with an increase in sintering temperature and holding time. Karak et al. (2011) [75] reported the preparation of yittria dispersed ferritic stainless steel by mechanical alloying followed by hot isostatic pressing at 600, 800 and 1000°C temperatures. They observed tremendous improvement in the mechanical properties of yittria dispersed ferritic stainless steel compared with yittria free ferritic stainless steel.

1.2.4 Electrochemical corrosion studies of stainless steel

Shankar et al. (2004) [76] studied pitting corrosion resistance of yittria dispersed stainless steel by cyclic polarization experiments in 3.56 wt. % NaCl solution. They concluded that the addition of Y_2O_3 did not affect the pitting corrosion resistance. The corrosion resistance values obtained for Y_2O_3 dispersed stainless steels are comparable with the wrought stainless steel samples. The pitting resistance of the samples sintered at 1250°C is superior to the samples sintered at 1400°C. Lal and Upadhyaya (1987) [77] studied the effect of Y_2O_3 addition on sintering behaviour of austenitic stainless steel. They reported that 4wt. % addition of yittria increases both sintered density and corrosion resistance, which was attributed to the interaction of Cr_2O_3 with dispersoids. Ningshen et al. (2014) [78] reported the corrosion resistance of 12% and 15% Cr oxide dispersion strengthened (ODS) steels in 3M and 9M HNO_3 respectively. They observed that 12% chromium ODS steel exhibits high corrosion rate than 15% chromium ODS steel at both 3M and 9M HNO_3 concentrations. The pitting corrosion potential value of both types of ODS steels shift close to the trans-passive region due to the increase in HNO_3 concentration. Balaji et al. (2007) [79] studied the corrosion resistance of yittria aluminium garnet (YAG) dispersed austenitic stainless steel sintered at 1200 and 1400°C respectively. Different concentrations (1, 2.5 and 7.5 wt.%) of the second phase YAG was added to austenitic stainless steel. The corrosion studies were carried out in 0.1N H_2SO_4 using potentiodynamic polarization. They reported that addition of YAG does not increase corrosion rate appreciably but super-solidus sintering show higher corrosion resistance than solid-state sintering. Bettini et al. (2013) [80] investigated the effect of nano sized chromium nitrides and exposure time on the corrosion behaviour of a 22% Cr duplex stainless steel. They concluded that the exposure temperature has a strong effect on the corrosion behaviour of duplex stainless steel than finely dispersed chromium nitrides. Fajardo et al. (2014) [81] reported the electrochemical corrosion of a new low-nickel stainless steel in carbonated alkaline solution in the presence of chlorides. They observed that low-nickel stainless steel also exhibits similar corrosion behaviour like conventional AISI 304 stainless steel. The corrosion potential and polarization resistance of both the stainless steel are of same order. Wang et al. (2011) [82] investigated the localized corrosion of 304 stainless steel in presence of droplets of 1M NaCl solution by using wire beam electrode method. They found that, heterogeneous current distributions along with isolated anodic peak current likely to be located near the edge of the droplet. Therefore, stainless steel experienced more severe localized corrosion with increase of the droplet size.

1.2.5 Objectives

- Fabrication of a high-energy planetary mill (dual-drive planetary) which can produce more than 50g acceleration field as compared to 10g acceleration field as in commercially available planetary mills.
- In the present study, our target is not to provide the heat from external sources to obtain a stabilized final desired product. Stabilized product should form without external heat being supplied.
- We also target to prepare stainless powder in bulk amount in lesser milling time.
- Optimization of milling parameters for the synthesis of nano-structured duplex and ferritic stainless steel.
- The nano-size stainless steel powder will be sintered by spark plasma sintering to retain nano-structure even after sintering.

- The different mechanical properties of the sintered products will be investigated for various applications of stainless steel products.
- The effect of yittria on the pitting corrosion of duplex and ferritic stainless steel samples sintered by SPS is to be studied.
- To investigate the electro catalytic applications of duplex and yittria dispersed duplex stainless steel powders in detecting bio-active compounds.

1.2.6 Scope of the thesis

Chapter 1 discusses about introduction and literature review. A detailed study of experimental work and different experimental techniques are provided in chapter 2. This chapter also explains the mill fabrication, mill mechanics and synthesis of duplex and ferritic stainless steel and different characterization techniques. Chapter 3 contains the synthesis of nano-structured duplex and ferritic stainless steel by conventional pulverisette planetary mill and consolidation by pressureless sintering. It includes the detail study of activation energy, enthalpy calculation and Curie temperature using differential scanning calorimeter (DSC) data. The effect of sintering temperature on hardness, density and microstructure of the stainless steels are also studied. Chapter 4 comprises of synthesis of nano-structured duplex and ferritic stainless steel by specially designed DDPM and consolidation by conventional and spark plasma sintering techniques. This chapter involves the investigation of phase transformation and microstructure study of nano-structured duplex and ferritic stainless steel powder prepared by DDPM and the detail study of optimization of milling parameters such as process controlling agents, ball to powder weight ratio, milling speed and milling atmospheres on particle size, phases and morphology of stainless steel powders. This chapter also includes the fabrication of yittria dispersed and yittria free duplex and ferritic stainless steel by conventional and SPS methods and the detail study of effect of yittria addition, sintering temperature, sintering atmosphere and sintering methods on the morphology, phase transformation, density and hardness of duplex and ferritic stainless steel.

Chapter 5 explains the non-lubricated sliding wear behaviour of nano-yittria dispersed and yittria free duplex and ferritic stainless steel fabricated by conventional and SPS techniques against a diamond indenter. This chapter contains the detail investigation of wear mechanisms, wear depth and the effect of applied load, yittria addition on the wear behaviour of duplex and ferritic stainless steel. Chapter 6 consists of the corrosion studies of SPS consolidated yittria dispersed and yittria free duplex and ferritic stainless steel by linear sweep voltammetry. This chapter involves the investigation of effect of different electrolytes at different concentrations, effect of yittria addition and the effect of quiet time on the pitting potential of stainless steel. This chapter also includes the brief explanation of corrosion studies performed by a new technique ‘linear sweep voltammetry’ (LSV). In chapter 7, we discussed the electrochemical sensitivity applications of duplex and yittria dispersed duplex stainless steel powders in detecting biologically active compounds like folic acid. This chapter includes the optimization of electrochemical properties such as concentration of analyte, pH, scan rate and concentration of modifiers to study the electrocatalytic properties of duplex and yittria dispersed duplex stainless steel. A summary and conclusions with main findings are presented in chapter 8. Finally, a comparative study on synthesis of both the stainless steels by pulverisette planetary mill and DDPM has been presented in Appendix. Comparison of present results with existing literatures is also briefly shown here.

References

1) Andrea Szabo, Caterina Perri, Anita Csato, Girolamo Giordano, Danilo Vuono, Janos B. Nagy, Synthesis Methods of Carbon Nanotubes and Related Materials, *Materials.* 3 **(2010)** 3092-3140.

2) C.N.R. Rao, P. John Thomas, G.U. Kulkarni, Nanocrystals:: Synthesis, Properties and Applications, Springer Science & Business Media, **2007**.

3) Injeti Gurrappa, Leo Binder, Electrodeposition of nanostructured coatings and their characterization—a review, *Sci. Technol. Adv. Mater.* 9 **(2008)** 043001.

4) Robert Kelsall, Ian W. Hamley, Mark Geoghegan, Nanoscale Science and Technology, John Wiley & Sons, **2005**.

5) J.D. Mackenzie, E.P. Bescher, Chemical Routes in the Synthesis of Nanomaterials Using the Sol–Gel Process, *Acc. Chem. Res.* 40 **(2007)** 810–818.

6) C.R. Bhattacharjee, Abhijit Nath, Chemical Vapour Deposition (CVD) Technique and the Synthesis of Carbon Nanomaterials (CNMs), *Journal of Chemical and Pharmaceutical Research*. 4(1) **(2012)** 706-713.

7) C. Suryanarayana, Mechanical alloying and milling, *Pro. Mater. Sci.* 46 **(2001)** 1–184.

8) A. Takamasa, S. Nakai, Contamination introduced during rock sample powdering: Effects from different mill materials on trace element contamination, *Geochemical Journal*. 43 **(2009)** 389-394.

9) J.R. Thompson, C. Politis, Formation of Amorphous Ti-Pd Alloys by Mechanical Alloying Methods, *Europhys Lett.* 3 **(1987)** 199–205.

10) P.H. Shingu, B. Huang, S.R. Nishitani, S. Nasu, *Suppl Trans Japan Inst Metals*. 29 **(1998)** 3–10.

11) C.C. Koch, The synthesis and structure of nano-crystalline materials produced by mechanical attrition, *Nanostructured Mater*. 2 **(1993)** 109–129.

12) C.C. Koch, Synthesis of nanostructured materials by mechanical alloying: Problems and Opportunities, *Nanostructured Mater*. 9 **(1997)** 13–22.

13) A.T. Myers, P.R. Barnett, Contamination of rock samples during grinding as determined spectrographically, *Amer. Jour. Sci*. 251 **(1953)** 814–830.

14) G. Thompson, D.C. Bankston, Sample contamination from grinding and sieving determined by emission spectrometry, *Appl. Spectrosc*. 24 **(1970)** 210–219.

15) A. Ando, Preparation method of rock samples, *Bulletin of the Geological Survey of Japan.* 37 (1986) 347–348 (in Japanese).

16) C.J. Hickson, S.J. Juras, Sample contamination by grinding, *Canad. Mineral.* 24 **(1986)** 585–589.

17) J.K. Iwansson, O. Landström, Contamination of rock samples by laboratory grinding mills, *Jour. Radioanal. Nucl. Chem.* 244 **(2000)** 609–614.

18) E. Hellstern, H.J. Fecht, C. Garland, W.L. Johnson. In: L.E. McCandlish, D.E. Polk, R.W. Siegel, B.H. Kear, editors. Multicomponent ultrafine microstructures, Pittsburgh, PA: *Mater. Res. Soc.* 132 **(1989)** 137–42.

19) G.B. Schaffer, P.G. McCormick, Reduction of metal oxides by mechanical alloying, *Appl Phys Lett.* 55 **(1989)** 45–46.

20) P.G. McCormick, V.N. Wharton, G.B. Schaffer. In: W.M. Small, editor. Physical chemistry of powder metals production and processing. Warrendale, PA: TMS, **(1989)** 19–34.

21) M. Carry, Transformations of Mechanical into Chemical Energy. (Third Paper.) Action of Shearing-Stress (Continued), *Phil Mag.* 34 **(1894)** 470–475.

22) P.G. McCormick, *Mater Trans Japan Inst Metals.* 36 **(1995)** 161–169.

23) L. Takacs, In: C. Suryanarayana at al., editors. Processing and properties of nano-crystalline materials, Warrendale, PA: TMS, **(1996)** 453–464.

24) P. Matteazzi, G. Le Caer, Mechanically activated room temperature reduction of sulphides, *Mater Sci. Eng. A.* 156 **(1992)** 229–37.

25) C.G. Tschakarov, G.G. Gospodinov, Z. Bontschev, Uber den mechanismus der mechanochemischen synthese anorganischer verbindungen, *Journal of solid state chemistry.* 41 **(1982)** 244–252.

26) F.H. Froes, C. Suryanarayana, K. Russell, C-G Li, Synthesis of intermetallics by mechanical alloying, *Mater. Sci. Eng. A.* 192/193 **(1995)** 612–623.

27) J.L.Harringa, B.A. Cook, B.J. Beaudry, Effects of vial shape on the rate of mechanical alloying, *J. Mater. Sci.* 27 **(1992)** 801–804.

28) L.M. Di, H. Bakker, Phase transformation of the compound V_3Ga induced by mechanical grinding, *J. Phys. C: Condens. Matter.* 3 **(1991)** 3427–3432.

29) S.D. Kaloshkin, I.A. Tomlin, G.A. Andrianov, U.V. Baldokhin, E.V. Shelekhov, Phase transformations and hyperfine interactions in mechanically alloyed Fe-Cu solid solutions, *Mater. Sci. Forum.* 235–238 **(1997)** 565–570.

30) C. Suryanarayana, Does a disordered y-TiAl phase exist in mechanically alloyed Ti-Al powders, *Intermetallics.* 3 **(1995)** 153–160.

31) M.O. Lai, L. Lu, Mechanical alloying, Boston, MA: Kluwer Academic Publishers, 1998.

32) C. Suryanarayana, E. Ivanov, R. Noufi , M.A. Contreras, J.J. Moore, Phase selection in a mechanically alloyed Cu-In-Ga-Se powder mixture, *J. Mater. Res.* 14 **(1999)** 377–383.

33) L. Liu, S. Casadio, M. Magini, C.A. Nannetti, Y. Qin, K. Zheng, *Mater. Sci. Forum.* 235-238 **(1997)** 163–168.

34) M. Atzmon, In situ thermal observation of explosive compound-formation reaction during mechanical alloying, *Phys. Rev. Lett.* 64 **(1990)** 487–490.

35) L. Takacs, M. Pardavi-Horvath, Nanocomposite formation in the Fe_3O_4-Zn system by reaction milling, *J. Appl. Phys.* 75 **(1994)** 5864–5866.

36) M.S. El-Eskandarany, K. Aoki, H. Itoh, K. Suzuki, Effect of ball-to-powder weight ratio on the amorphization reaction of $Al_{50}Ta_{50}$ by ball milling, *Journal of the Less-Common Metals.* 169 **(1991)** 235–244.

37) Z-H. Chin, T-P. Perng, Amorphization of Ni-Si-C Powder by Mechanical Milling with SiC, *Mater. Sci. Forum.* 235-238 **(1997)** 121–126.

38) K. Varga, D.L. Beke, Phase transitions in Cu-Sb systems induced by ball milling, *Mater. Sci. Forum.* 225–227 **(1996)** 465–470.

39) K.B. Gerasimov, A.A. Gusev, E.Y. Ivanov, V.V. Boldyrev, Tribochemical equilibrium in mechanical alloying of metals, *J. Mater. Sci.* 26 **(1991)** 2495–2500.

40) M. Miki, T. Yamasaki, Y. Ogino, *Mater. Trans. Japan. Inst. Metals.* 33 **(1992)** 839–844.

41) A. Calka, J.S. Williams, Synthesis of Nitrides by Mechanical Alloying, *Mater. Sci. Forum.* 88-90 **(1992)** 787–794.

42) Y. Chen, J.S. Williams, Hydriding reactions induced by ball milling, *Mater. Sci. Forum.* 225-227 **(1996)** 881–888.

43) Y. Ogino, T. Yamasaki, S. Maruyama, R. Sakai, Non-equilibrium phases formed by mechanical alloying of Cr-Cu alloys, *J. Non-Cryst. Solids.* 117/118 **(1990)** 737–740.

44) P.Y. Lee, C.C. Koch, The formation and thermal stability of amorphous Ni-Nb alloy powder synthesized by mechanical alloying, *J. Non-Cryst. Solids.* 94 **(1987)** 88–100.

45) W.E. Frazier, M.J. Koczak, Mechanical and thermal stability of powder metallurgy aluminum-titanium alloys, *Scripta. Metall.* 21 **(1987)** 129–134.

46) E. Gaffet, M. Harmelin, F. Faudot, Far-from-equilibrium phase transition induced by mechanical alloying in the Cu-Fe system, *J. Alloy. Compd.* 194 **(1993)** 23–30.

47) X.P. Niu, PhD Thesis, Katholieke University, Leuven, Belgium, **1991**.

48) Y. Qin, L. Chen, H. Shen, In-situ X-ray diffraction examination of nano-crystalline $Ag_{37}Cu_{63}$ powders synthesized by mechanical alloying, *J. Alloy. Compd.* 256 **(1997)** 230–233.

49) Z. Fu, W.L. Johnson, Nanophase Zr-Al solid solutions by mechanical alloying at elevated temperatures, *Nanostruct. Mater.* 3 **(1993)** 175–180.

50) J.C. Mishurda, University of Idaho, Moscow, ID, unpublished results, **1993**.

51) C.H. Lee, M. Mori, T. Fukunaga, U. Mizutani, Effect of ambient temperature on the MA and MG processes in Ni-Zr alloy system, *Japan. J. Appl. Phys.* 29 **(1990)** 540–544.

52) C. Suryanarayana, In: Powder metal technologies and applications. ASM Handbook, Materials Park, OH: ASM International, 7 **(1998)** 80–90.

53) R.K. Rajamani, L. Milin, G. Howell, Dual drive planetary mill, United States Patent no. 6,086,242. **(2000).**

54) D. Chaira, B.K. Mishra, S. Sangal, Synthesis and characterization of silicon carbide by reaction milling in a Dual-drive planetary mill, *Mater. Sci. Eng. A.* 460-461 (2007) 111–120.

55) T. Sundararajan, S.B. Prabu, S.M. Vidyavathy, Combined effects of milling and calcination methods on the characteristics of nano-crystalline barium titanate, *Mater. Res. Bul.* 47 **(2012)** 1448–1454.

56) M.H. Enayati, M.R. Bafandeh, Phase transitions in nanostructured Fe–Cr–Ni alloys prepared by mechanical alloying, *J. Alloys Compd.* 454 **(2008)** 228–232.

57) T. Haghir, M.H. Abbasi, M.A. Golozar, M. Panjepour, Investigation of α to γ transformation in the production of a nanostructured high-nitrogen austenitic stainless steel powder via mechanical alloying, *Mater. Sci. Eng. A.* 507 **(2009)** 144–148.

58) R. Shashanka, D. Chaira, Phase transformation and microstructure study of nanostructured austenitic and ferritic stainless steel powder prepared by planetary milling, *Powder. Technol.* 259 **(2014)** 125–136.

59) L.A. Dobrzanski, Z. Brytan, M.A. Grande, M. Rosso, Properties of duplex stainless steels made by powder metallurgy, *Arch. Mater. Sci. Eng.* 28 **(2007)** 217–223.

60) Z. Brytan, L.A. Dobrzanski, M.A. Grande, M. Rosso, The influence of sintering time on the properties of PM duplex stainless steel, *J. Achiev. Mater. Manuf. Eng.* 37/2 **(2009)** 387–396.

61) J. Kazior, M. Nykiel, T. Pieczonka, T. Marcu Puscas, A. Molinari, Activated sintering of P/M duplex stainless steel powders, *J. Mater. Process. Tech.* 157–158 **(2004)** 712–717.

62) J.M. Ruiz-Prieto, W.M. Moriera, J.M. Torralba, L.E.G. Cambronero, Powder metallurgical duplex austenitic-ferritic stainless steel from prealloyed and mixed powders, *Powder. Metall.* 37 **(1994)** 57.

63) M. Rosso, M.A. Grande, Proceedings of the 2000 Powder Metallurgy World Congress, Kyoto, *Japan Society of Powder and Powder Metallurgy*. 2 **(2000)** 1017.

64) J. Kazior, T. Pieczonka, A. Molinari, *Proc. of 8 th Int. Scient. Conf. AMME,* Gliwice–Poland, **(1999)** 289.

65) J. Kazior, T.M. Puscas, T. Pieczonka, L. Fedrizzi, M. Nykiel, A. Molinari, *Proceedings of the 2000 International Conference on Powder Metallurgy & Particulate Materials,* New York, 7 **(2000)** 46.

66) T.M. Puscas, A. Molinari, J. Kazior, T. Pieczonka, M. Nykiel, Sintering transformation in mixtures of austenitic and ferritic stainless powders, *Powder. Metall.* 44 **(2001)** 48.

67) L.A. Dobrzanski, Z. Brytan, M. Actis Grande, M. Rosso, Influence of sintering parameters on the properties of duplex stainless steel, *J. Achiev. Mater. Manuf. Eng.* 20 **(2007)** 231-234.

68) F. Martin, C. Garcia, Y. Blanco, Effect of chemical composition and sintering conditions on the mechanical properties of sintered duplex stainless steels, *Mater. Sci. Eng. A.* 528 **(2011)** 8500–8511.

69) K. Vijayalakshmi, V. Muthupandi, R. Jayachitra, Influence of heat treatment on the microstructure, ultrasonic attenuation and hardness of SAF 2205 duplex stainless steel, *Mater. Sci. Eng. A.* 529 **(2011)** 447–451.

70) A. Pandey, K. Jayasankar, P. Parida, M. Debata, B.K. Mishra, S. Saroja, Optimization of milling parameters, processing and characterization of nano-crystalline oxide dispersion strengthened ferritic steel, *Powder. Technol.* 262 **(2014)** 162–169.

71) R. Rahmanifard, H. Farhangi, A.J. Novinrooz, Optimization of mechanical alloying parameters in 12YWT ferritic steel Nanocomposite, *Mater. Sci. Eng. A.* 527 **(2010)** 6853–6857.

72) S.K. Karak, C.S. Vishnu, Z. Witczak, W. Lojkowski, J.D. Majumdar, I. Manna, Studies on wear behavior of nano-Y2O3 dispersed ferritic steel developed by mechanical alloying and hot isostatic pressing, *Wear.* 270 **(2010)** 5–11.

73) R. Shashanka, D. Chaira, Development of nano-structured duplex and ferritic stainless steels by pulverisette planetary milling followed by pressureless sintering, *Mater. Charact.* 99 **(2015)** 220–229.

74) N. Hong-wei, H. Hang, L. Guang-qiang , L. Jing, Preparation of Nano-crystalline 430L Stainless Steel by HEBM and SPS, *Journal of Iron and Steel Research International.* 15 **(2008)** 73-76.

75) S.K. Karak, T. Chudoba, Z. Witczak, W. Lojkowski, I. Manna, Development of ultra high strength nano-Y2O3 dispersed ferritic steel by mechanical alloying and hot isostatic pressing, *Mater. Sci. Eng. A.* 528 **(2011)** 7475–7483.

76) J. Shankar, A. Upadhyaya, R. Balasubramaniam, Electrochemical behavior of sintered oxide dispersion strengthened stainless steels, *Corros. Sci.* 46 **(2004)** 487–498.

77) S. Lal, G.S. Upadhyaya, Effect of Y_2O_3 addition and sintering period on the properties of P/M 316L austenitic stainless steel, *J. Mater. Sci. Lett.* 6 **(1987)** 761–764.

78) S. Ningshen, M. Sakairi, K. Suzuki, S. Ukai, The corrosion resistance and passive film compositions of 12% Cr and 15% Cr oxide dispersion strengthened steels in nitric acid media, *Corros. Sci.* 78 **(2014)** 322–334.

79) S. Balaji, A. Upadhyaya, Electrochemical behavior of sintered YAG dispersed 316L stainless steel composites, *Mater. Chem. Phys.* 101 **(2007)** 310–316.

80) E. Bettini, U. Kivisakk, C. Leygraf, J. Pan, Study of corrosion behavior of a 22% Cr duplex stainless steel: Influence of nano-sized chromium nitrides and exposure temperature, *Electrochim. Acta.* 113 **(2013)** 280–289.

81) S. Fajardo, D.M. Bastidas, M. Criado, J.M. Bastidas, Electrochemical study on the corrosion behaviour of a new low-nickel stainless steel in carbonated alkaline solution in the presence of chlorides, *Electrochim. Acta.* 129 **(2014)** 160–170.

82) Y. Wang, W. Wang, Y. Liu, L. Zhong, J. Wang, Study of localized corrosion of 304 stainless steel under chloride solution droplets using the wire beam electrode, *Corros. Sci.* 53 **(2011)** 2963–2968.

CHAPTER 2

Experimental Details

2.1 Mill design

A high energy DDPM was developed particularly to synthesize bulk nano-structured stainless steel powder. The specially designed DDPM has a main shaft of 640 mm (L) in length and two steel jars of 100 mm (2R) diameter (volume—1000 ml each) which rotates about their own axes around the common axis of the main shaft. The planetary mill was attached with two 5HP motors to drive the main rotating shaft and the vials. The rotating speeds of both motors can be varied independently by two different frequency controllers. Figure 2.1 shows the photograph of the dual-drive planetary mill that was fabricated to synthesize nano-structured stainless steel powder.

Figure 2.1 Dual drive planetary mill

2.2 Mill mechanics

Before starting the milling experiments it is important to know the forces acting on grinding balls inside the jars. Figure 2.2 shows a schematic diagram of configuration of one half of the planetary mill where a jar rotates about its own primary axis ‘O’. The radius of rotation of the axis of the jar is ‘L/2’ and radius of the jar is ‘R’. Once these parameters are fixed, then it is very simple to characterize the planetary mill by the ratio of radius of rotation of the mill axis ‘*L/2’* to the radius of the mill ‘*R’*. Here ‘ϖ_1’ is the rotation of the gyratory arm and ‘ϖ_2’ is the mill speed. Mainly four different kinds of forces act on a ball inside any one of the jars during milling as shown in Figure 2.2. They are, (i) Centrifugal force about the fixed gyrating axes, (ii) Centrifugal force about the mill axis, (iii) Coriolis force due to the planetary motion (rotating coordinate system) (iv) Gravitational force.

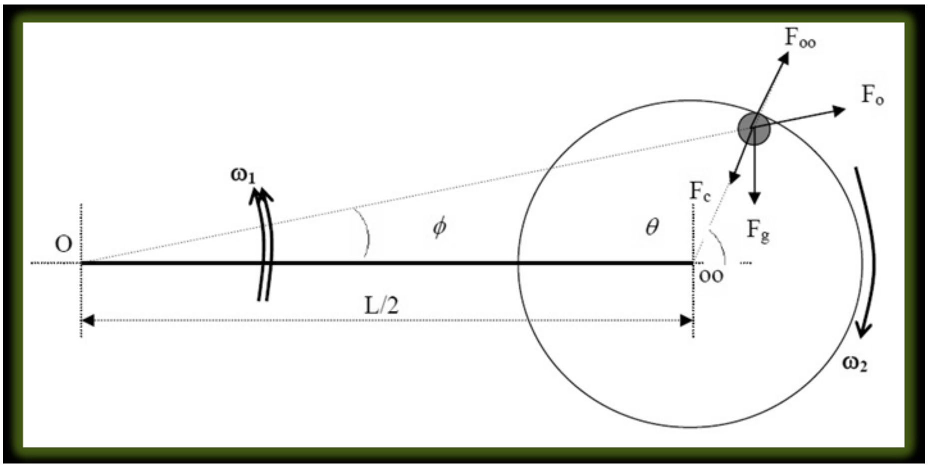

Figure 2.2 Schematic of the acceleration field in a planetary mill

These forces develop a special kind of acceleration field inside the mill, which is difficult to visualize.

$$F = F_c + F_o + F_{oo} + F_g \quad \textbf{(1)}$$

Gravitational force is very small when compared to centrifugal force, hence it is neglected. Therefore, ‘F’ is given by,

$$F = F_c + F_o + F_{oo} \quad \textbf{(2)}$$

Corresponding accelerations for these forces is gives as follows

$$a = a_c + a_o + a_{oo} \quad \textbf{(3)}$$

If ‘a_o’ is the centrifugal acceleration field around its fixed axis with the direction is outward from ‘O’

Solving the above equation gives the critical speed constant

$$K_c = \frac{\varpi_2}{\varpi_1} = -1 \pm \sqrt{\frac{L}{2R}} \quad \textbf{(4)}$$

Where, ‘K_c’ is the critical speed constant. The percentage of critical speed can be calculated as follows,

$$\%CS = \frac{n_2}{K_c \times n_1} \times 100 \quad \textbf{(5)}$$

Where n_1 is the gyrating (main shaft) speed and n_2 is the jar speed. In this work the mill was operated at 64% critical speed in all the cases.

$$K_c = -1 \pm \sqrt{\frac{640}{100}} = -1 \pm 2.52$$

Taking negative sign, as main shaft and jars are rotating in opposite direction.

$K_c = -1 - 2.52 = 3.52$

The percentage critical speed is calculated by considering the shaft speed (ϖ_1) and jar speed (ϖ_2) as 275 and 620rpm, respectively. Therefore

$$\%CS = \frac{620}{3.52 \times 275} \times 100 = 64$$

All the milling experiments are performed at 64% critical speed, but while investigating the effect of mill speed we fixed the mill speed at 75% critical speed.

For 75% critical speed, the shaft speed (ϖ_1) and jar speed (ϖ_2) were maintained at 275 and 726rpm, respectively.

$$\%CS = \frac{726}{3.52 \times 275} \times 100 = 75$$

2.3 Synthesis of duplex and ferritic stainless steel powder and consolidation

2.3.1 Pulverisette planetary milling

Elemental powder mixture of Fe (99.5% pure), Cr (99.8% pure) and Ni (99.5% pure) were used as starting materials. Elemental compositions of Fe–18Cr–13Ni (Duplex) and Fe–17Cr–1Ni (Ferrite) were selected from Schaeffler diagram to obtain duplex and ferritic stainless steel alloys during milling. Milling of the above compositions was carried out in Fritsch planetary mill (P5 mill) for 40h under toluene atmosphere to prevent oxidation. Mill speed of 300rpm and ball to powder weight ratio of 6:1 was maintained. The milling media consist of 500ml milling jar and 300 g of chrome steel balls of 10mm diameter each and it was filled around 40% by volume.

Milled powder samples of both duplex and ferritic stainless steel powders were compacted using hydraulic pressing machine with a load of 700MPa using polyvinyl alcohol as binder. Both the stainless steel samples show a wide range of sizes from micron- to nano level and hence it is difficult to compact samples without binder. The compacted pellets were sintered at 1000, 1200 and 1400°C in argon atmosphere with holding time of 1h each and samples were furnace cooled.

2.3.2 Dual drive planetary milling

Elemental powder mixture of Fe (99.5% pure), Cr (99.8% pure) and Ni (99.5% pure) powders were used as starting materials. An elemental composition of Fe–18Cr–13Ni (duplex) and Fe-17Cr-1Ni were selected from Schaeffler diagram. Milling of the above compositions was carried out in a specially designed DDPM mill for 10h under toluene atmosphere to prevent oxidation. The milling media of the DDPM consist of 1kg stainless steel balls of 8mm diameter. The milling was conducted at room temperature and 6:1 ball-to-powder weight ratio. The angular velocity of the vials and the supporting main shaft were 620 and 275rpm respectively. The effect of different milling parameters like PCA, mill speed, milling atmosphere, milling time and BPR were studied. In all the cases powders were milled in DDPM for 10h under toluene atmosphere (wet milling) to prevent oxidation. It was ensured that all the balls and powders were immersed in toluene. A volume of 30% jar was filled with balls and powders.

➢ *Effect of stearic acid (SA)*

Duplex and ferritic stainless steel powder samples were prepared by milling the elemental compositions of Fe, Cr and Ni powders in DDPM at a mill speed of 64% critical speed (CS) with 6:1 BPR for 10h in presence of SA and in the absence of SA under toluene atmosphere (wet milling). Before starting milling operation, 1wt. % of SA was added to Fe–18Cr–13Ni and Fe–17Cr–1Ni powder composition separately in two different jars of DDPM.

➢ *Effect of milling speed*

Another important milling parameter that has a significant effect on powder morphology is the milling speed. Both duplex and ferritic stainless steel powder samples were prepared by milling in DDPM at different percentage of critical speeds (% CS) in presence of toluene and at 6:1 BPR. The main shaft speed was kept constant at 275 rpm, whereas jar speed was varied. The jar speeds were kept at 620 and 726 rpm for 64% and 75% CS respectively. This increases the acceleration of the mill from 73g to 86g in case of 64% CS and 75% CS mill speed respectively.

➢ *Effect of milling atmosphere*

Milling was carried out in both wet and dry conditions. During dry milling argon gas was used as the milling atmosphere to prevent oxidation of both the stainless steels. Milling parameters were maintained at 64% CS, 6:1 BPR, 1wt. % SA and 10h milling time.

- *Effect of ball to powder weight ratio*

The wet milling was carried out at BPR of 6:1 and 12:1 using 1wt. % SA as PCA in both ferritic and duplex steel. Here, mill was run at 64% of CS.

Prepared stainless steel powders are mixed separately with 1wt.% Y_2O_3 nanoparticles by turbula shaker mixture (TURBULA® T2F, Willy A. Bachofen AG Maschinenfabrik, Switzerland) for 3 hours. Yittria dispersed and yittria free duplex and ferritic stainless steel powder samples were consolidated by conventional and Spark plasma sintering (SPS) methods. Yittria dispersed and yittria free stainless steel samples were compacted using hydraulic pressing at 700MPa load and poly vinyl alcohol as binder. Compacted stainless steel samples are conventionally sintered at 1000, 1200 and 1400°C respectively in a tubular furnace with holding time of 1h each at argon atmosphere. SPS was carried out at a pressure of 50MPa and at 1000°C temperature for 5 minutes in a 20mm diameter graphite die.

2.4 Characterization techniques used

2.4.1 Stainless steel powders

2.4.1.1 X-Ray diffraction

X-ray diffraction of the elemental compositions, milled powder and annealed powder samples were performed using Philips PANalytical diffractometer using filtered Cu Kα-radiation (λ = 0.1542 nm). X-ray diffraction was carried out at a scan rate of 2°/minute.

2.4.1.2 Scanning electron microscopy

Powder morphology of as received, milled, annealed and sintered stainless steel samples were investigated by scanning electron microscopy (SEM) using JEOL JSM-6480LV. Most of the images were taken in secondary electron and back scattered electron mode according to the requirement. Qualitative, quantitative analysis and elemental mapping were carried out for stainless steel powders as well as sintered pellets using INCA software, which has been attached to SEM. Elemental mapping was carried out to study the elemental distribution.

2.4.1.3 Particle size analysis

Particle size analysis was carried out in a laser particle size analyser (Malvern, Mastersizer 2000, UK). The powder particles were made suspended by dispersing them in a solution of dispersant like sodium hexa metaphosphate. Then He or Ne laser beam scatters the suspended powder particles with different scattering angles. Based upon the angle of scattering; particle size will be measured. The scattering phenomenon depends upon the wavelength of the light and the particle size, shape and refractive index of particles under study.

2.4.1.4 Field emission scanning electron microscopy (FESEM)

The morphology of stainless steel powder particles and sintered samples were investigated by using FESEM of model FEI NANO NOVA 450. The morphology of corroded stainless steel samples were studied by FESEM.

2.4.1.5 BET surface area analysis

Surface area of the milled stainless steel powders were measured by BET surface area analyzer (Quantachrome/AUTOSORB-1 model). Usually nano particles have large specific surface area due to the very fine size. The specific surface area is measured using the nitrogen gas adsorption technique developed by Brunauer, Emmett, and Teller, commonly known as the BET method. BET surface area measurement mainly based upon simplified adsorption gas model, solid surface and on pore structure. Nitrogen gas adsorb on particles in the form of multi layers, in which volume adsorbed is a summation of the adsorbed volumes of each layer.

BET surface area can also be calculated by using following equation

$$\frac{P/P_0}{S(1-P/P_0)} = \frac{1}{V_m C} + \frac{C-1}{V_m C}\frac{P}{P_0} \qquad \textbf{(6)}$$

Where, P is the equilibrium pressure, P_0 is the saturated vapour pressure of nitrogen, V is the amount of gas forming a monolayer on the solid surface (monolayer capacity) and C is a constant related to the heat of adsorption in the first layer. A plot of $(P/P_0) / S(1-P/P_0)$ versus P/P_0 gives a straight line from which the monolayer capacity V_m can be evaluated. From the obtained V_m value, the BET specific surface area can be calculated by using the cross-sectional area.

2.4.1.6 Differential scanning calorimetry (DSC) analysis

Thermal analysis of stainless steel powders samples were carried out in DSC (Netzsch, Germany). Powder samples were heat treated from room temperature to 1200°C at a heating rate of 10°C/minute in presence of inert argon atmosphere. Some of the DSC measurements were carried out at different heating rates like 6, 8 and 10°C/minutes to calculate activation energy by using Kissinger plot and also study the enthalpy change, curie temperature and crystallization temperature.

2.4.1.7 High resolution transmission electron microscopy (HRTEM)

HRTEM studies of the milled and annealed stainless steel powders were carried out using JEOL JEM-2100 to study the microstructure, lattice spacing and selected area electron diffraction (SAED) patterns. Samples have been prepared by dispersing the stainless steel powders in ethanol and sonicated for 30 minutes. One or two drops of the suspension were placed on a carbon coated Cu grid; then grid was dried for 30 minutes before mounting the grid onto the HRTEM sample holder.

2.4.2 Consolidation of stainless steel powders

2.4.2.1 Blending

Duplex and ferritic stainless steel powders were mixed separately with 1wt.% nano-Y_2O_3 (< 100nm) powder particles in a turbula shaker mixer (TURBULA® T2F, Willy A. Bachofen AG Maschinenfabrik, Switzerland) for 3h. The blended yittria dispersed stainless steel powders were consolidated by conventional and spark plasma sintering methods.

2.4.2.2 Compaction

Milled powder samples of stainless steel powders were compacted using hydraulic pressing machine (SoilLab) with a load of 700MPa using polyvinyl alcohol as binder. Both the stainless steel samples are having a wide range of sizes from micron- to nano level and hence it is difficult to compact samples without binder. Diameter of the die is 10mm and added zinc stearate powder was added as die wall lubricant for the easy operation.

2.4.2.3 Conventional sintering

Compacted pellets were sintered in a super kanthal heated tubular furnace (Naskar, India) at 1000, 1200 and 1400°C temperatures for 1h. Argon and nitrogen sintering atmospheres were maintained to study the effect of sintering atmosphere on the phase change, microstructure and mechanical properties of stainless steel. All the stainless steel samples were furnace cooled with heating rate of 5°C/minute. We also studied the effect of sintering temperature on the hardness, density, wear and microstructure of stainless steel.

2.4.2.4 Spark plasma sintering (SPS)

SPS is an advanced sintering technique that has attracted substantial interest for fabrication of poorly sinterable materials. The SPS process involves simultaneous application of load as well as heat on the materials to be sintered. SPS is a new method meant for consolidation of nano structured materials with hindered grain growth, efficient shrinkage in less time and cleaner grain boundaries for effective interface formation. This technique utilizes high temperature spark plasma generated by discharging exactly at the gaps of powder particles with an on-off electrical current. At the initial stage of SPS process, the generated spark plasma induces neck formation and thermal diffusion process on the particles to be sintered. Electric field formed by DC current can also facilitates thermal diffusion process. Therefore, SPS process involves densification of poorly sinterable materials at a very short interval of time and at low temperature when compared with conventional sintering process. Spark plasma sintering was carried out at a pressure of 50MPa and 1000°C temperature for 5 minutes in a 20mm diameter graphite die **(**SCM 1050, Sumitomo Coal Mining Co. Ltd., Japan**)**.

2.4.3 Characterization of consolidated stainless steel

2.4.3.1 Density and microhardness measurements

The density, microhardness values were measured by Archimedes method and Vickers microhardness methods respectively. Density of conventionally sintered and SPS samples were measured by density measurement kit (Contech model no: CB-300) by measuring the suspended weight and soaked weight of the specimens. Microhardness studies were carried out using LECO-LM248AT Vickers hardness tester fitted with a Vickers pyramidal diamond indenter. Hardness measurements were performed at 10, 25 and 50gf loads with a dwell time of 10 seconds. A minimum of 5 readings were taken for each sample.

2.4.3.2 Optical microscopy

Microstructure study of conventionally sintered and corroded SPS samples were performed in Carl Zeiss optical microscopy. The volume phase fractions of stainless steels were calculated by using an inbuilt Axio Vision Release 4.8.2 SP3 (08-2013) software.

2.5 Non-lubricated sliding wear study

The wear studies were carried out in ball-on-plate wear tester (Ducom, TR-208 M1) where Rockwell diamond indenter rotates at 20rpm with a speed of 0.0041m/s for 15 minutes on stainless steel samples at room temperature and a relative humidity of 70%. All the wear studies were performed at applied loads of 10 and 20N and track radius of 2mm was selected. Before and after wear tests, the diamond indenter was cleaned ultrasonically and dried. All the wear tests were performed 3-4 times to get the concordant values. The schematic diagram of wear test experimental setup is shown in Figure 2.3.

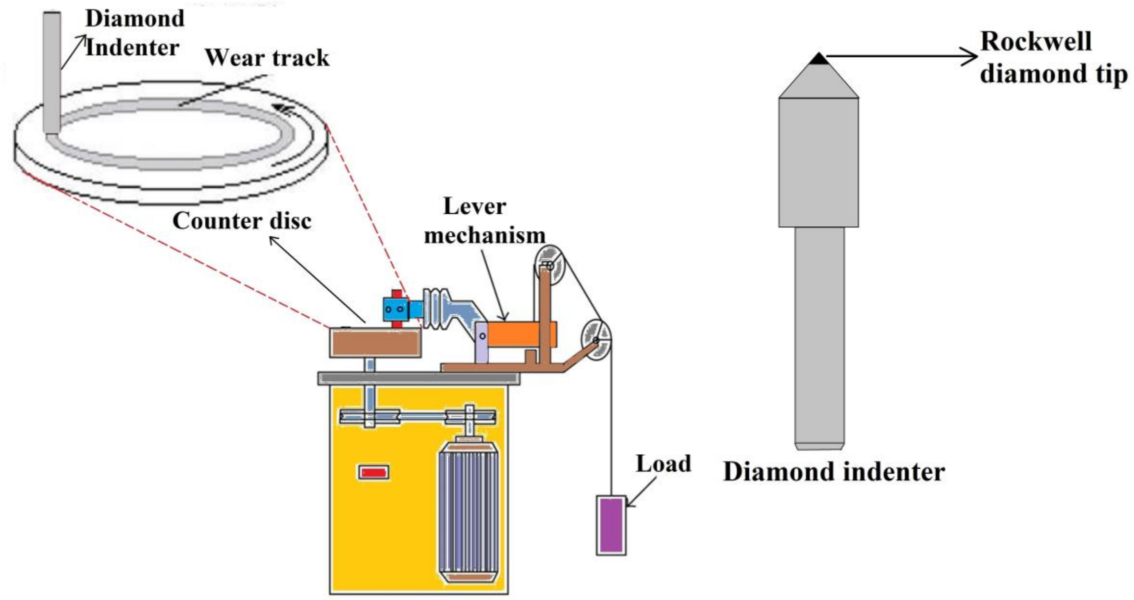

Figure 2.3 Schematic diagram of wear test experimental setup

The fundamental study of non-lubricated sliding wear of yittria free and yittria dispersed duplex and ferritic stainless steel samples were consolidated at different sintering temperatures (1000, 1200 and 1400°C) in argon and nitrogen (1000°C) atmospheres and SPS (1000°C) methods respectively. The wear track depth studies were carried out in Veeco Dektak 150 surface profilometer. Wear mechanism was studied by investigating the wear track and wear debris morphology by using JEOL JSM-6084LV scanning electron microscopy.

2.6 Corrosion study

The corrosion studies were carried out in a well established three electrode electrochemical cell using electrochemical work station CHI-660c model by Linear sweep voltammetry

(LSV) method. Potential scans were collected in a freely aerated NaCl and H_2SO_4 solutions at room temperature. The experiments were carried out in an electrochemical cell containing Ag/AgCl saturated KCl as reference electrode, stainless steel samples as working electrode (20mm diameter) and platinum counter electrode. Corrosion studies were carried out in 0.5, 1 and 2M concentration of NaCl and H_2SO_4 solutions at different quiet time of 2, 4, 6, 8 and 10 seconds by Linear sweep voltammetry (LSV) method. LSV is an important electrochemical technique involves solid electrode, fixed potential and fast scan rate. The slope of the ramp has units of volts per unit time and is generally called as scan rate of the experiment. The microstructure of consolidated stainless steel samples were investigated by Carl Zeiss optical microscope and phase fraction of corroded duplex and ferritic stainless steels were calculated by using Axio Vision Release 4.8.2 SP3 (08-2013) software.

2.7 Electro-catalytic study by cyclic voltammetry

The electrochemical experiments were carried out using electrochemical work station CHI-660c model. All the experiments were performed in a conventional three electrode system composed of working electrode (carbon paste electrode of 3mm diameter), a platinum wire as counter electrode and Ag/AgCl saturated KCl electrode as reference electrode as shown in the Figure 2.4.

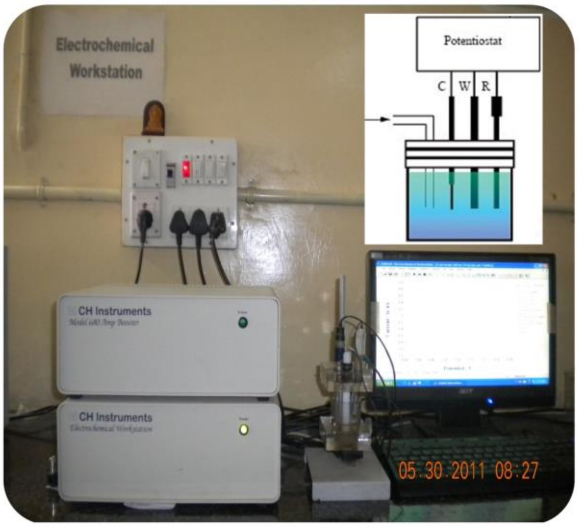

Figure 2.4 Cyclic voltammetry experimental setup

- *Fabrication of stainless steel electrodes*

The carbon paste electrode (CPE) was prepared by hand-mixing of graphite powder and silicon oil at a ratio 70:30 by wt. in an agate mortar. The homogeneous carbon paste electrode was packed into a cavity of a homemade carbon paste electrode (3.0 mm in diameter). The duplex modified carbon paste electrode (DMCPE) was prepared by mixing 2, 4, 6 and 8 mg yittria dispersed and yittria free duplex stainless steel powder individually with graphite powder and silicon oil. Surface was smoothed by rubbing slowly on a piece of weighing paper. The electrical contact was provided by copper wire connected to the paste at tube end. The bare CPE was prepared by without adding modifier. The electro-catalytic properties of yittria dispersed and yittria free duplex stainless steel powders towards folic acid (FA) detection was studied.

CHAPTER 3

Synthesis of nano-structured duplex and ferritic stainless steel powder by pulverisette planetary milling and consolidation by conventional sintering

3.1 Objectives and scope of the work

Nano-structured duplex and ferritic stainless steel powders were prepared by planetary milling of elemental Fe, Cr and Ni powder for 40h and then consolidated by conventional pressureless sintering. The progress of milling and the continuous refinement of stainless steel powders have been confirmed by means of x-ray diffraction and scanning electron microscopy. Activation energy for formation of duplex and ferritic stainless steel is calculated by Kissinger method using differential scanning calorimetry. Both duplex and ferritic stainless steel powders are consolidated at 1000, 1200 and 1400°C in argon atmosphere to study microstructure, density and hardness.

3.2 Fabrication of stainless steel

3.2.1 Synthesis of nano-structured stainless steel powder

Elemental powder mixture of Fe (99.5% pure), Cr (99.8% pure) and Ni (99.5% pure) were used as starting materials. Elemental compositions of Fe–18Cr–13Ni (Duplex) and Fe–17Cr–1Ni (Ferrite) were selected from Schaeffler diagram to obtain duplex and ferritic stainless steel alloy during milling. Milling of the above compositions was carried out in Fritsch pulverisette planetary mill (P5 mill) for 40h under toluene atmosphere to prevent oxidation. Mill speed of 300rpm and ball to powder weight ratio of 6:1 was maintained. The milling media consist of 500ml milling jar and 300g of chrome steel balls of 10mm diameter each and it was filled around 40% by volume.

3.2.2 Consolidation of nano-structured stainless steel powder by pressureless sintering

Milled powder samples of both duplex and ferritic stainless steel were compacted in hydraulic pressing machine with a load of 700MPa using poly vinyl alcohol as binder. Both the stainless steel samples were having wide range of sizes from micron to nano level and hence it is difficult to compact samples without binder. The compacted pellets were sintered at 1000, 1200 and 1400°C in argon atmosphere with holding time of 1h each and samples were furnace cooled.

3.3 Synthesis of nano-structured stainless steel powder

3.3.1 X-Ray Diffraction study

3.3.1.1 Milling of Fe-18Cr-13Ni and Fe-17Cr-1Ni composition

The XRD spectra of Fe-18Cr-13Ni (duplex composition) and Fe-17Cr-1Ni (ferrite composition) powders milled at 0, 2, 5, 10, 20 and 40h are shown in Figure 3.1 (a) & 3.1 (b) respectively. The sharp crystalline diffraction peaks of elemental powders start to broaden continuously with milling time. As milling proceeds, the elemental Cr and Ni begin to move inside Fe lattice and get vanished with further milling. This phenomenon is dominant at 20h as shown in the Figure 3.1 (a). The final milled powder samples are associated with refined grain size, defects and maximum internal strain. Duplex stainless steel powder composition exhibits ferrite phase till 20h of milling and slowly undergo phase transformation from ferrite to austenite with further milling. This was evidenced by the lattice parameter calculation by Nelson-Riley method. Average lattice parameter value of Fe-18Cr-13Ni after 20h of milling is 3.05X10^{-10}m near to ferrite but with further milling the same goes on increasing and becomes 3.50X10^{-10}m after 40h and is close to austenite lattice parameter. As milling proceeds further, the Fe (110) peak starts to displace towards lower angle side indicating the formation of dual phase steel consisting of both austenite and ferrite phases. This is due to the substitutional diffusion of Cr and Ni atoms in to Fe lattice and result in the broadening of peaks progressively with milling time.

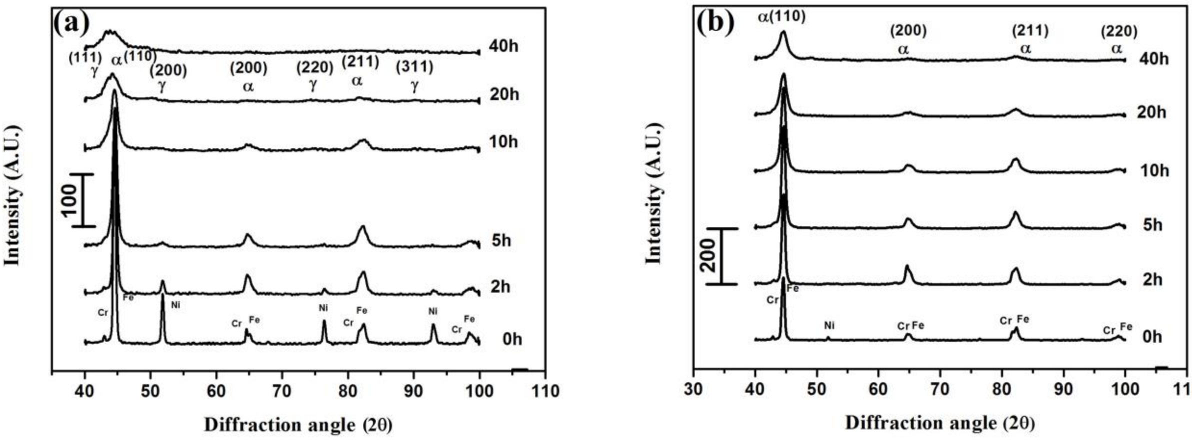

Figure 3.1 XRD spectra of (a) Duplex stainless steel (b) Ferritic stainless steel powder samples milled for 40h

3.3.1.2 Lattice parameter calculation

The lattice parameter is calculated using Nelson-Riley (N-R) extrapolation method by considering the three strong XRD peaks of duplex and ferritic stainless steel powders.

A graph of lattice parameter of both duplex and ferritic stainless steels calculated from N-R method versus milling time is shown in Figure 3.2. The lattice spacing value of austenite present in duplex and pure ferritic stainless steel powder is 3.53X10^{-10}m and 2.88X10^{-10}m respectively and these values are in good agreement with the standard lattice parameter of

FCC iron ($3.515 X 10^{-10}$m) and BCC iron ($2.866 X 10^{-10}$m). Increase in milling time increases the lattice spacing due to the presence of large amount of defects during milling.

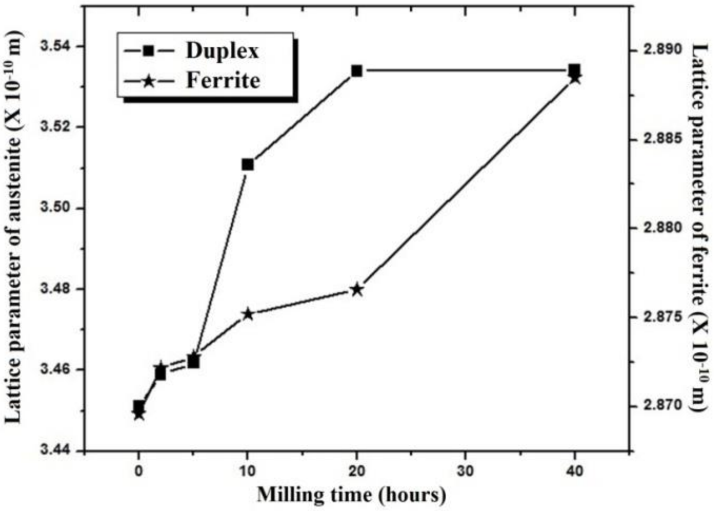

Figure 3.2 Variation of lattice parameter (calculated by Nelson-Riley extrapolation method) with milling time

3.3.1.3 Crystallite size and lattice strain calculation

We determined crystallite size and lattice strain using Williamson-Hall equation from XRD peaks. The crystallite size and strain of duplex and ferritic stainless steels were calculated from Williamson-Hall method and are represented graphically in Figure 3.3 (a) and 3.3 (b) respectively.

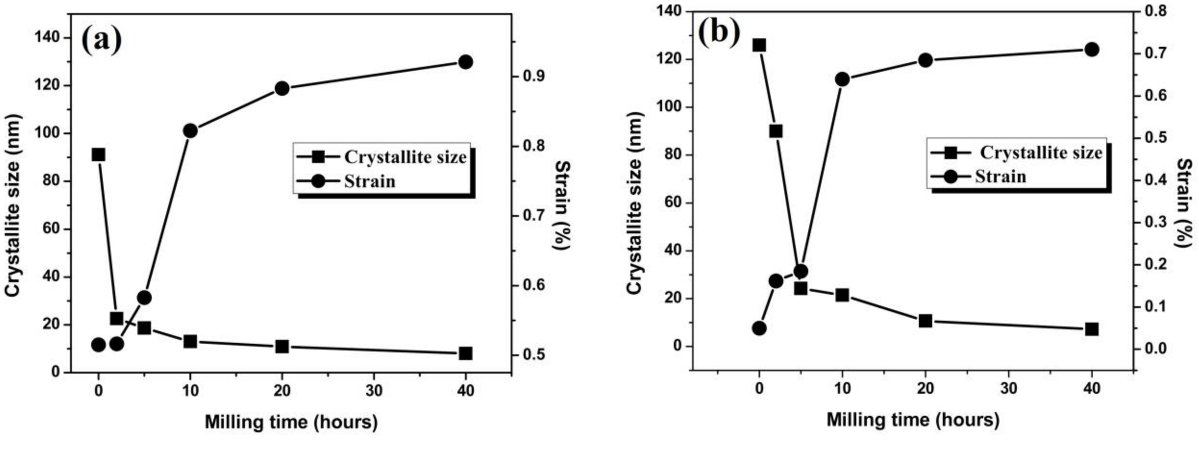

Figure 3.3 Graphical representation of variation of strain and crystallite size (Calculated by Williamson-Hall method) with 0, 2, 5, 10, 20 and 40h milling time of (a) Duplex stainless steel (b) Ferritic stainless steel powder samples

From the graph it is confirmed that as milling time increases, the crystallite size decreases and it attains a saturation level after 40h, where further refinement of crystallite size is quite difficult. But lattice strain goes on increasing with increase in milling time due to continuous contact of powder-ball, powder-powder and powder-jar surface. The strong collision between ball-powder-jar reduces the crystallite size from 94nm to 8nm in case of duplex and from 126nm to 7nm in case of ferrite after 40h of milling. Similarly, lattice strain goes on increasing from 0.50 to 0.92% and from 0.04 to 0.71% respectively for duplex and ferritic stainless steel.

3.3.2 Microstructure study

3.3.2.1 Scanning electron microscopy (SEM)

SEM micrographs of duplex and ferritic stainless steel powders milled at different time intervals are represented in Figure 3.4 and Figure 3.5 respectively.

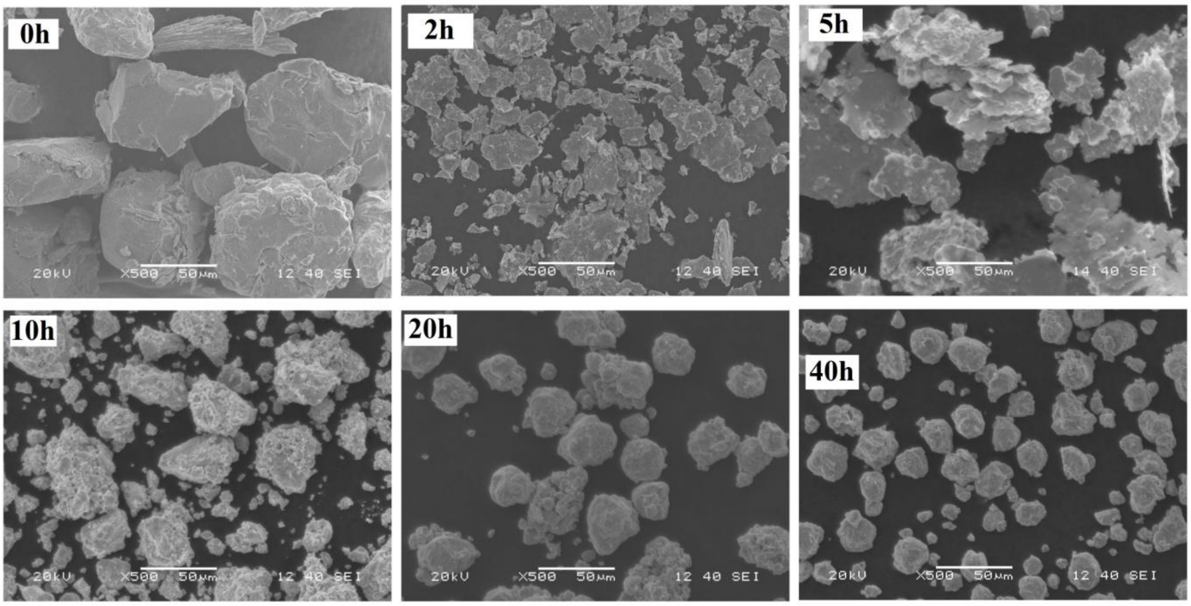

Figure 3.4 SEM micrographs of duplex stainless steel milled for different times in high energy planetary mill

It is found that before milling the powder particles are large and irregular in shape. As milling proceeds the particles begin to agglomerate and become flat after 2h of milling due to the ductile nature of Fe. After 5h of milling, two or more flat lamellae weld together to form a single large lamella. But as milling continues further up to 10h and 20h, the ductile powder particles get work hardened; Ni and Cr get entrapped into Fe lattice and powder particles start to refine.

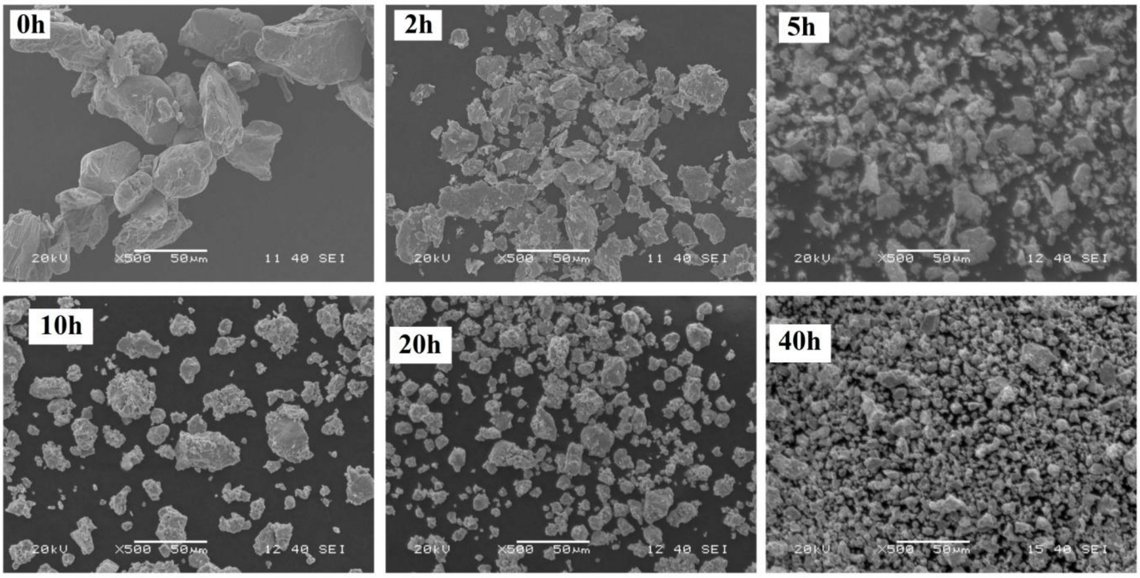

Figure 3.5 SEM micrographs of ferritic stainless steel samples milled for different times in high energy planetary mill

The particle size reduces again and further refining in the size of the particles become difficult beyond 40h of milling. Ni and Cr get uniformly distributed in Fe to form an alloy. It has been found that 40h of milling leads to the formation of fine and spherical shaped stainless steel powder particles. From the micrographs it is found that particle size of 40h milled duplex stainless steel powder is around 10-15µm and of ferritic stainless steel is around 5-10µm. SEM micrographs depicts the regular refinement of stainless steel powder particles at different intervals of milling time.

3.3.3 Particle size analysis

Figure 3.6 (a) and 3.6 (b) indicate the particle size distribution of duplex and ferritic stainless steel powders milled at time intervals of 0, 2, 5, 10, 20 and 40h respectively measured by Malvern Mastersizer. In both cases, particle size decreases with increase in milling time and thus cumulative size distribution curves shift towards left side indicating refinement and size reduction of powder particles. During milling, the rate of particle size refinement depends upon different milling parameters like milling speed, milling time, size of the balls used for milling, ball to powder weight ratio etc. Figure 3.6 (c) shows the fluctuation of median particle size with milling time in case of duplex and ferritic stainless steel powders. The median particle size decreases from 77 to 15µm during milling from 0 to 40h in case of duplex stainless steel powder. Similarly, median size reduces from 50 to 18µm in case of ferritic stainless steel powder. The values of crystallite size, lattice strain, lattice parameters and particle size of duplex and ferritic stainless steel after 40h of milling are tabulated in Table 3.1.

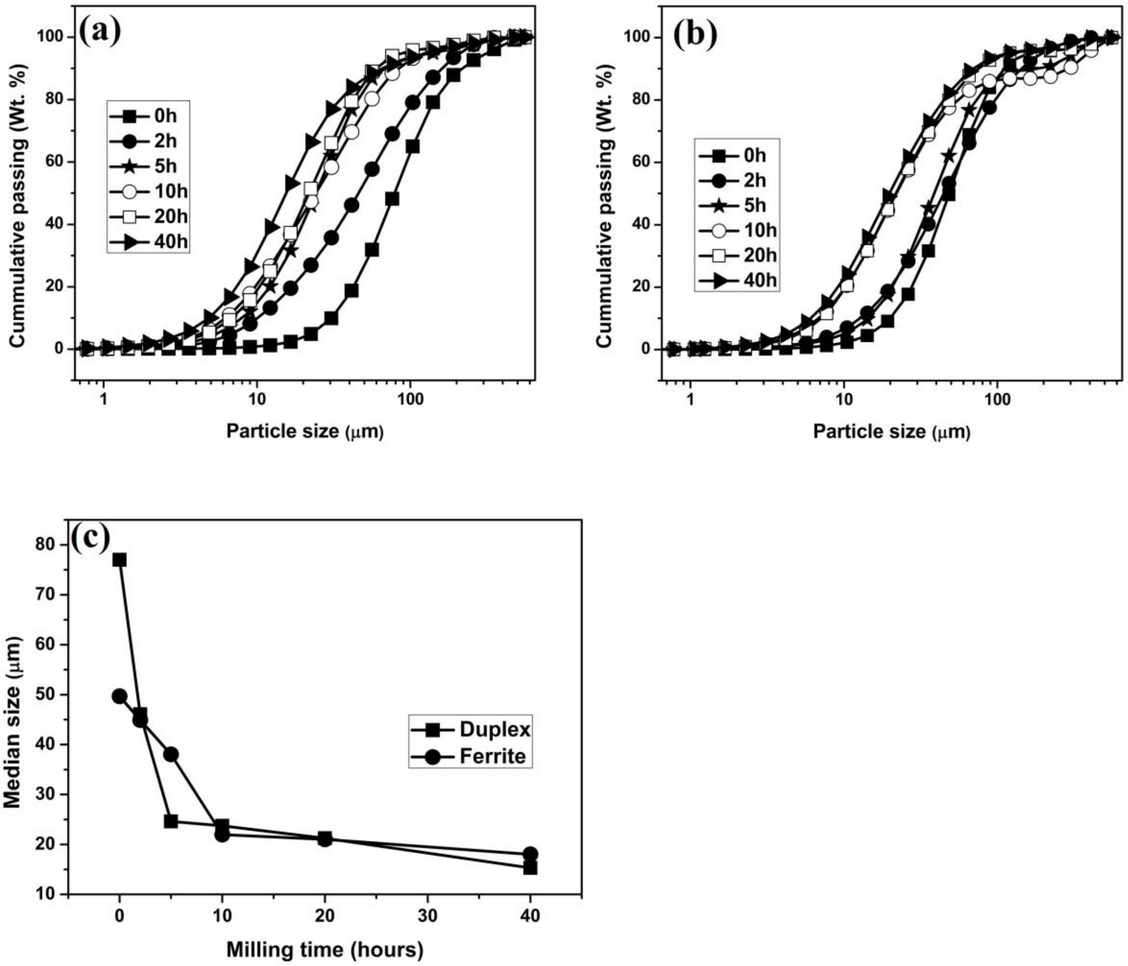

Figure 3.6 Particle size distribution of (a) Duplex stainless steel (b) Ferritic stainless steel samples milled at different time intervals (c) Variation of median size with milling time

Table 3.1 Crystallite size, lattice strain, lattice parameters and particle size of duplex and ferritic stainless steel after 40h of milling

Condition	Type of stainless steel	Crystallite size (nm)	Lattice strain (%)	Lattice parameter (Å)	Mean particle size (μm)
Milled in P5 planetary mill for 40h	Duplex stainless steel	8	0.92	3.53	15
	Ferritic stainless steel	7	0.71	2.88	18

3.3.4 Thermal analysis

Figure 3.7 (a) and 3.7 (b) show the DSC graphs of duplex and ferritic stainless steel powders at different heating rates respectively. The stainless steel powder samples prepared in the present work is partially amorphous in nature and hence broad exothermic peak is found. During milling stainless steel powders undergo series of collision, flattening, cold welding, work hardening and fragmentation hence powder sample attains meta stable non-equilibrium state. Eskandarany et al. [1] prepared amorphous austenitic stainless steel alloy by dry milling of elemental powders and studied their thermal properties. They observed single exothermic peak due to the amorphous austenitic stainless steel powder. During DSC run the non-equilibrium stainless steel alloy powder undergoes recovery, grain growth, relaxation processes and involves energy release during heating and hence exothermic peak [2]. Figure 3.7 (a) and 3.7 (b) depicts the broad exothermic peak which starts at 350K and ends at1325K in both types of stainless steel samples. Change in enthalpy of reaction, Curie, crystallization temperature of both duplex and ferritic stainless steel powders at different heating rates were measured and results are tabulated in Table 3.2.

Table 3.2 Changes in enthalpy of reaction, Curie, nucleation, crystallization temperature of both duplex and ferritic stainless steel powder at different heating rates

Type of stainless steel	**Heating rate (K/min)**	**Crystallization temperature (K)**	**Curie temperature (K)**	**Enthalpy change (KJ/mol)**
Duplex stainless steel	6	824	-	85.94
	8	833	-	96.60
	10	841	-	62.35
Ferritic stainless steel	6	796	1031	86.58
	8	805	1027	44.27
	10	822	1024	65.00

The tabulated results are complementary to the work published by Eskandarany et al. [1] and Raju et al. [3]. From the figure it is clear that the crystallization temperature of partial amorphous powder increases from 824 to 841K in case of duplex stainless steel powder and from 796 to 822K in case of ferritic stainless steel powder due to different heating rates of 6, 8 and 10K/min. This is due to the heat transfer lag and non-uniform heating at higher heating rates. In case of ferritic stainless steel, Curie temperature starts decreasing from 1031 to

1024K with increasing heating rate. A peak at around 475K is due to the transition of powders from a rigid to a flexible structure to relieve the stress.

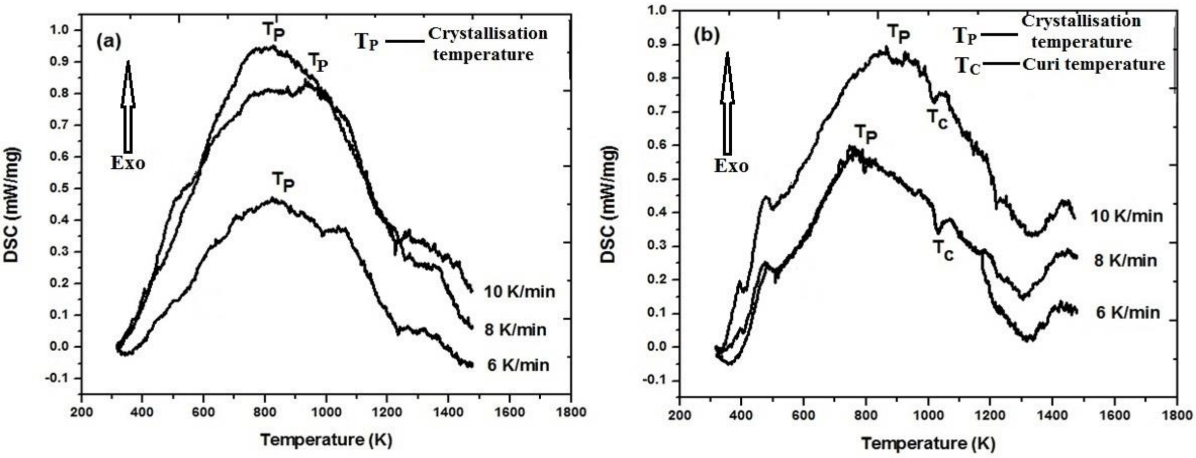

Figure 3.7 DSC graphs of (a) Duplex stainless steel (b) Ferritic stainless steel powder with 6, 8 and 10 K/min heating rates

Activation energy for the formation of duplex and ferritic stainless steel powders were calculated using Kissinger method [4, 5].

$$\ln \frac{\alpha}{T_P^2} = \frac{-E_C}{RT_P} + \text{Constant} \qquad \textbf{(1)}$$

Where T_p is crystallization peak temperature, α is the heating rate and R is the gas constant. A linear relationship between ln ($\alpha / T_p{}^2$) and 1000x1/ T_p for the crystallization temperatures is obtained using Eq. (1) and then the activation energy for formation of both duplex and ferritic steels are evaluated.

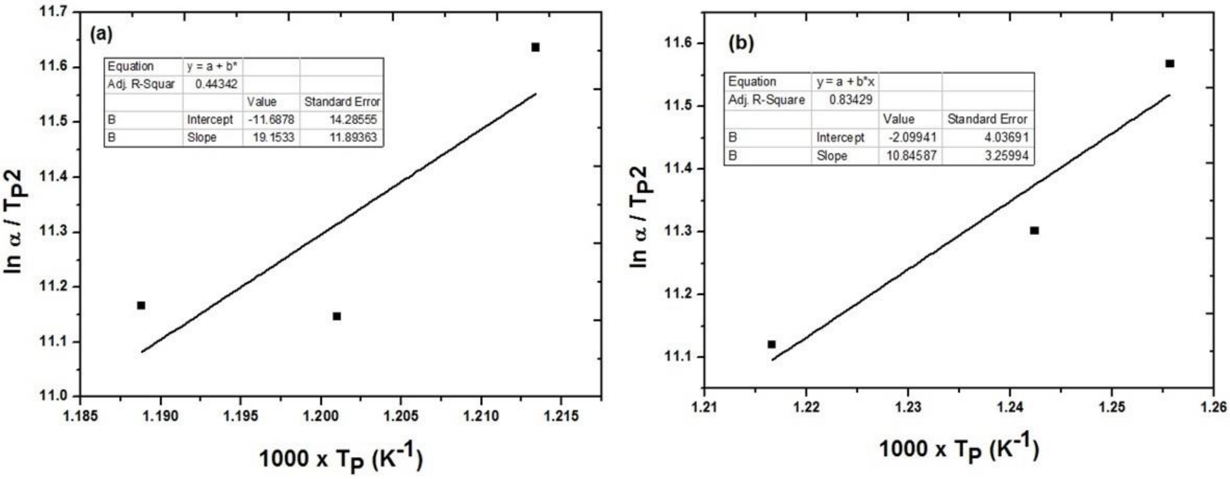

(a)

Equation	y = a + b*		
Adj. R-Squar	0.44342		
		Value	Standard Error
B	Intercept	-11.6878	14.28555
B	Slope	19.1533	11.89363

(b)

Equation	y = a + b*x		
Adj. R-Square	0.83429		
		Value	Standard Error
B	Intercept	-2.09941	4.03691
B	Slope	10.84587	3.25994

Figure 3.8 Kissinger plot to calculate activation energy of crystallization of (a) Duplex stainless steel (b) Ferritic stainless steel powder heated at different heating rates

Figure 3.8 (a) and 3.8 (b) show Kissinger plot of activation energy for formation of duplex and ferritic stainless steel powders and the values are summarized in Table 3.3. Curie temperature, activation energy and crystallization peak temperature of duplex and ferritic stainless steel are studied successfully using DSC.

Table 3.3 Activation energy values of duplex and ferritic stainless steel powders

Type of stainless steel	**Heating rate α (K/min)**	**Peak temperature T_P (K)**	$\frac{\alpha}{T_P^2}$ **(X 10^{-5})**	$\ln \frac{\alpha}{T_P^2}$	$1000 \times \frac{1}{T_P}$	**Activation energy E_a (KJ/mol)**
Duplex stainless steel	6	824	0.88	-11.63	1.213	159.24
	8	833	1.44	-11.14	1.201	
	10	841	1.41	-11.17	1.188	
Ferritic stainless steel	6	796	0.94	-11.56	1.255	90.17
	8	805	1.23	-11.30	1.242	
	10	822	1.48	-11.12	1.216	

3.4 Consolidation of stainless steel powder

3.4.1 *XRD of duplex and ferritic stainless steel samples*

Figure 3.9 (a) and 3.9 (b) show X-ray diffraction patterns of 40h milled powder and consolidated samples of both duplex and ferritic stainless steels respectively. XRD spectra of milled duplex stainless steel powder shows broadened strong diffraction peaks of ferrite and weak peaks of austenite.

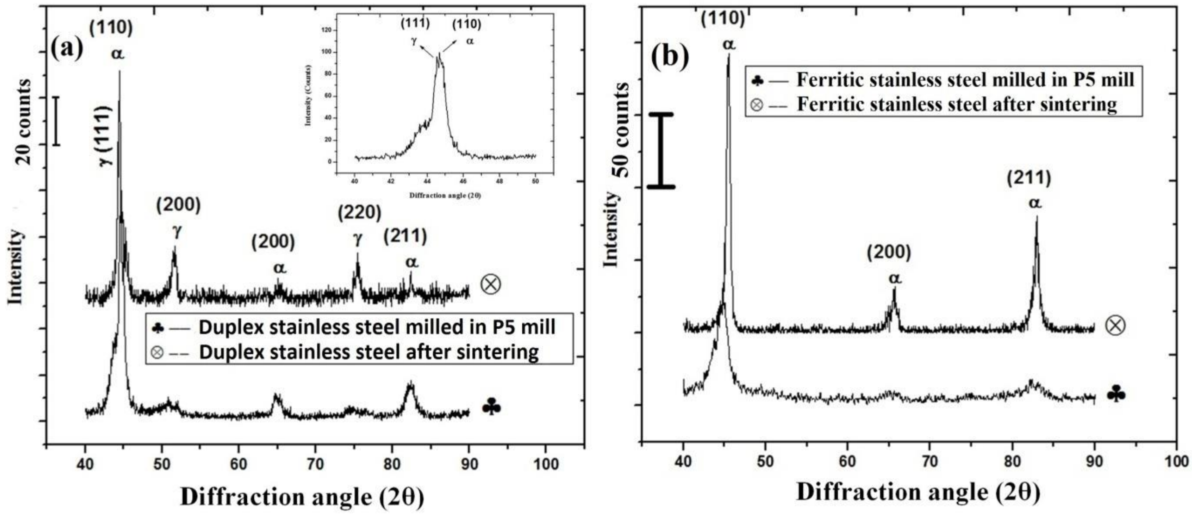

Figure 3.9 XRD spectra of 40 hours milled powder and consolidated (a) Duplex stainless steel (b) Ferritic stainless steel samples sintered at 1400°C for 1 hour

After 40 hours of milling, limited transformation from ferrite to austenite takes place but after consolidation duplex stainless steel show sharp diffraction peaks of ferrite and austenite phases. Figure 3.9 (a) shows the magnified view (scan range 40-50°) of the first peak in inset. It shows the presence of both ferritic and austenitic peaks. It must be mentioned here that consolidation of duplex steel by conventional sintering promotes ferritic to austenitic transformation as evident from strong austenite peaks along with ferrite peaks. During consolidation Cr and Ni move into the interstitial site of Fe lattice due to diffusion. Hence after consolidation strong peaks of ferrite and austenite are visible. However, same is not true just after milling due to limited diffusion of Cr and Ni into Fe lattice. No diffraction peaks of secondary phases like sigma phase; carbides or nitrides precipitations in both powders as well as consolidated duplex stainless steel samples are observed. During milling, different processes such as structural defect, amorphization and reduction in grain size occur and this results in the broadening of diffraction peaks. The XRD spectra of both milled and consolidated ferritic stainless steel samples show single phase of only ferrite. Both the sintered stainless steel samples show sharp, crystalline diffraction peaks due to the diffusion and rearrangement of atoms in a regular manner.

3.4.2 Microstructure analysis

Figure 3.10 shows optical micrographs of duplex and ferritic stainless steel samples consolidated at 1000, 1200 and 1400°C respectively. As sintering temperature increases from 1000 to 1400°C, number of pores decreases and density increases. Volume fractions of austenite and ferrite phases in duplex stainless steel at different sintering temperature were studied. The volume fractions of ferrite and austenite phases were determined by Axio Vision Release software. The amount of austenite phase increases with increase in temperature due to the phase transformation of ferrite to austenite at higher temperature in case of duplex steel. At higher temperature austenite phase become more stable. The pores (black), austenite (white) and ferrite (grey) regions are labelled in optical micrographs of duplex stainless steel. Similarly, ferritic stainless steel show pores (black) and ferrite (white) regions. At higher temperature austenite phase becomes more stable with significant increase in the rate of diffusion and atomic rearrangement.

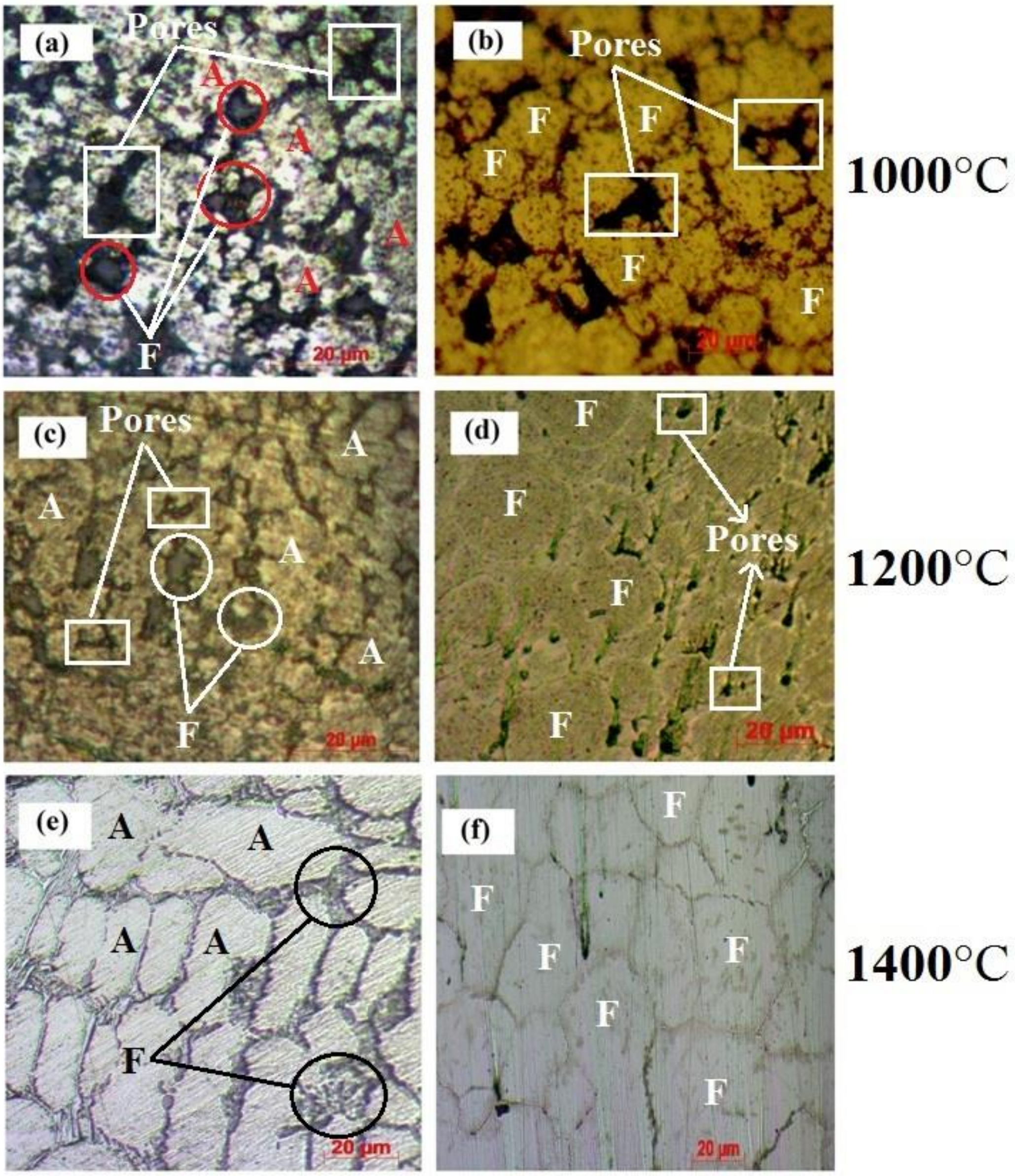

Figure 3.10 Optical microstructure of (a) (c) (e) Duplex stainless steel and (b) (d) (f) Ferritic stainless steel samples sintered respectively at 1000, 1200 and 1400°C for 1 hour

3.4.3 Density and hardness study

Figure 3.11 (a) shows the effect of temperature on the densities of duplex and ferritic stainless samples. Density of both the stainless steel samples increases with increase in sintering temperature. A maximum density of 90 % was achieved for both the types of stainless steel samples sintered at 1400°C. The hardness measurements were carried out at three different loads of 10, 25 and 50gf and for each sample, five trials of indentation were made with different load and the average values of the diagonal lengths of indentation marks were measured.

Table 3.4 Density, hardness and volume fractions of austenite and ferrite phases in duplex and ferritic stainless steel at different sintering temperature

Type of stainless steel	**Sintering temperature (°C)**	**Volume fraction (%)**		**Sintered density (%)**	**Vickers microhardness (HV)**		
		Austenite	**Ferrite**		**10gf**	**25gf**	**50gf**
Duplex stainless steel	1000	44	52	66	261	253	254
	1200	57	40	80	363	337	325
	1400	60	38	90	512	550	521
Ferritic stainless steel	1000	-	96	69	178	171	155
	1200	-	97	85	230	217	210
	1400	-	97	92	263	251	229

The Vickers microhardness value at each load was calculated using the relation [6].

$$HV = 1.8544\frac{P}{d^2} \tag{2}$$

Where, P is the applied load and d is the diagonal length of the indentation. Average hardness values of duplex and ferritic stainless steels at 1000, 1200 and 1400°C are shown in Figure 3.11 (b) and 3.11 (c) respectively and the values obtained are higher compared with previous literatures [7, 8]. Density, hardness and volume fractions of austenite and ferrite phases in duplex stainless steel at different sintered temperature are tabulated in Table 3.4.

It was observed that hardness value decreases with increase in applied indentation load for ferritic stainless steel but the variation is not so prominent for duplex steel. This variation of hardness values with increase in load is due to the indentation size effect (ISE) [9]. This is because of the errors which are directly related to the intrinsic structural factors of the test materials such as indentation elastic recovery, work hardening during indentation, surface dislocation pining etc [10, 11]. ISE also occurs due to the surface effect; strain gradient effect and non dislocation mechanisms based on mass transport by point defects.

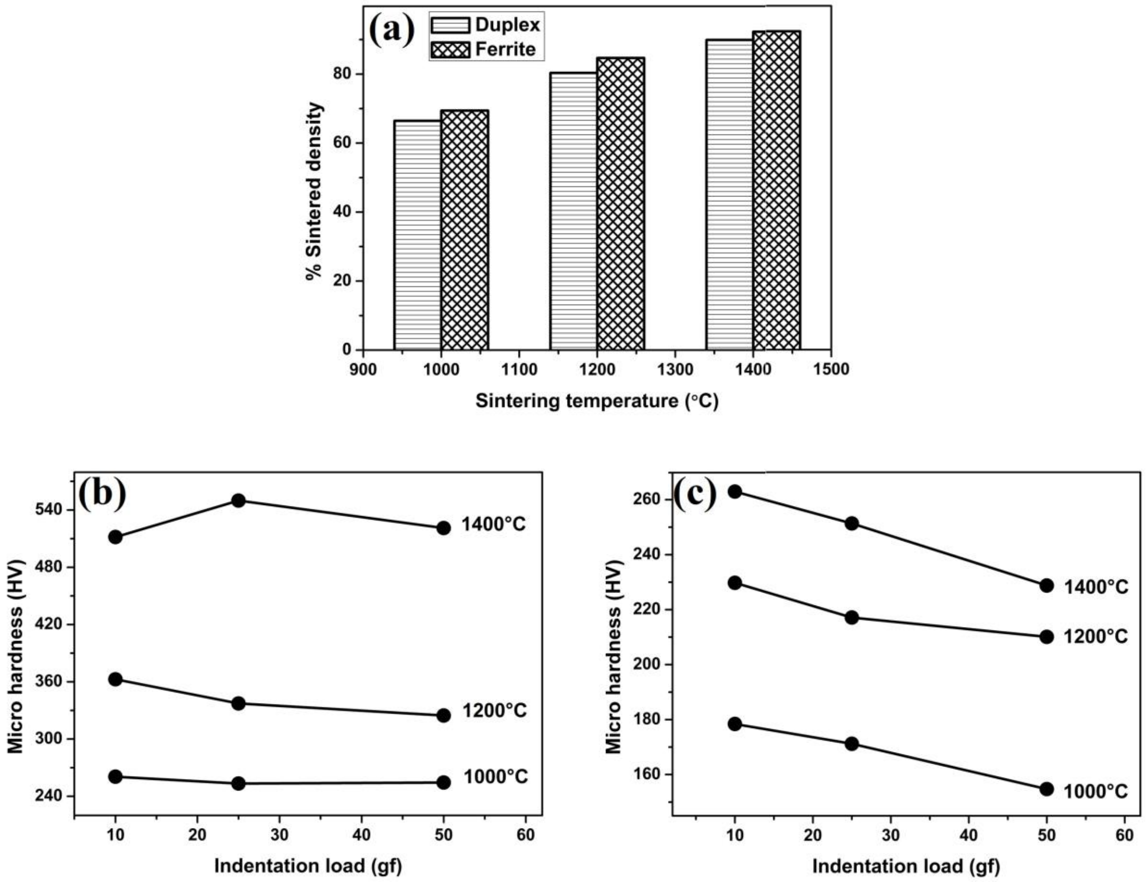

Figure 3.11 (a) Effect of sintering temperature on densities of duplex and ferritic stainless samples; Microhardness of (b) Duplex stainless steel (c) Ferritic stainless steel samples consolidated at 1000, 1200 and 1400°C for 1 hour with different indentation load

3.5 Summary and conclusions

Nano-structured duplex and ferritic stainless steel powders were prepared by mechanical alloying for 40h in Fritsch Pulverisette planetary mill. During milling, particle size increases initially due to repetitive welding of ductile iron and starts refining in the structure with the progress of milling. Lattice strain increases and crystallite size decreases with increase in milling time. Using DSC plots of 40h milled steel powders we calculated change in enthalpy, crystallization peaks, Curie temperature and also activation energy by Kissinger method. Increase in sintering temperature increases the density, hardness of the samples and decreases the amount of pores. Due to ISE both the stainless steel samples show reduced hardness with increasing indentation load. Both duplex and ferritic stainless steel shows maximum density and hardness at 1400°C. A density and microhardness value of 90% and 550HV were obtained for duplex stainless steel. Similarly, ferritic stainless steel exhibits 92% sintered density and 263HV microhardness value.

References

1) M. Sherif El-Eskandarany, H.A. Ahmed, Morphology and structural studies of amorphous of $Fe_{74}Cr_{18}Ni_8$ alloy prepared by the rod-milling technique, *J. Alloy. Compd.* 216 **(1994)** 213-220.

2) M.A. Meyers, A. Mishra, D.J. Benson, Mechanical properties of nanocrystalline materials, *Prog. Mater. sci.* 51 **(2006)** 427-556.

3) S. Raju, B. Jeya Ganesh, Aritra Banerjee, E. Mohandas, Characterisation of thermal stability and phase transformation energetics in tempered 9Cr–1Mo steel using drop and differential scanning calorimetry, *Mater. Sci. Eng. A.* 465 **(2007)** 29-37.

4) Zhong-jie Wang, Wen Ni, Yan Jia, Li-ping Zhu, Xiao-yan Huang, Crystallization behavior of glass ceramics prepared from the mixture of nickel slag, blast furnace slag and quartz sand, *J. Non-Cryst. Solids.* 56 **(2010)** 1554–1558.

5) H.E. Kissinger, Variation of peak temperature with heating rate in differential thermal analysis, *J. Res. Natl. Bur. Stand.* 57 **(1956)** 217–221.

6) Lauren Juliet Ayers, The hardening of type 316L stainless steel welds with thermal aging, Massachusetts Institute of Technology, **2012**.

7) Duyi Ye, Investigation of cyclic deformation behaviour in the surface layer of 18Cr–8Ni austenitic stainless steel based on Vickers microhardness measurement, *Mater. Chem. Phys.* 93 **(2005)** 495–503.

8) S. Picard, J.B. Memet, R. Sabot, J.L. Grosseau-Poussard, J.P. Riviere, R. Meilland, Corrosion behaviour, microhardness and surface characterisation of low energy, high current ion implanted austenitic stainless steel, *Mater. Sci. Eng. A.* 303 **(2001)** 163–172.

9) I. Manika, J. Maniks, Size effects in micro- and nanoscale indentation, *Acta. Mater.* 54 **(2006)** 2049–2056.

10) R. Shashanka, D. Chaira, Development of nano-structured duplex and ferritic stainless steel by pulverisette planetary milling followed by pressureless sintering, *Mater Charact.* 99 **(2015)** 220-229.

11) I.H. Bueckle, Use of the hardness test to determine other material properties, The Science of Hardness Testing and its Research Application. J. H. Westbrook and H. Conrad. Metal Park, OH. American Society for Metals, **(1973)** 453-494.

CHAPTER 4

Synthesis of nano-structured duplex and ferritic stainless steel powder by DDPM and consolidation by conventional sintering and SPS

4.1 Synthesis of nano-structured duplex and ferritic stainless steel powders by dual-drive planetary milling (DDPM)

4.1.1 Objectives and scope of the work

In the present work, nano-structured duplex and ferritic stainless steel powders were prepared in bulk by milling elemental powders in a specially designed dual-drive planetary mill (DDPM) for 10 hours. The progress of the milling and phase transition of stainless steel have been studied by means of x-ray diffraction. Annealing of milled powder at 750°C promotes ferritic to austenitic transformation in both argon and nitrogen atmosphere as limited transformation takes place after milling. However, nitrogen favours the transformation to a greater extent than argon. Lattice parameters obtained from both high resolution transmission electron micrographs (HRTEM) and Nelson-Riley method match with duplex and ferritic stainless steel.

4.1.2 Phase transformation study using XRD

4.1.2.1 Milling

The XRD traces of Fe-18Cr-13Ni and Fe-17Cr-1Ni powders milled in DDPM are shown in Figure 4.1.1 (a) & 4.1.1 (b) respectively. During planetary milling the sharp crystalline diffraction peaks of the parent powders begin to broaden progressively with increased milling time, ultimately resulting in the powder sample associated with maximum internal strain and refined grain size. The XRD spectral studies show elemental Cr and Ni peaks at 0h and they gradually go into the lattice of the Fe after 5h of milling. Hence, Ni and Cr peaks are absent finally after 10 hours of milling in both types of stainless steel. Duplex stainless steel milled in DDPM shows ferrite phase until 5h of milling and undergoes transformation to austenite phase at 10h. This is evidenced by the Nelson-Riley method of lattice parameter calculation. Until 5h of milling, the lattice parameter value was near to ferritic stainless steel but after 10h its value becomes very close to duplex stainless steel. Figure 4.1.1 (c) shows the XRD spectra of 10h milled duplex stainless steel powder scanned slowly in the range of 40 to 50°. The XRD spectra consists of three peaks corresponding to γ-Fe, Cr and α-Fe respectively [JCPDS file numbers: (47-1417), (88-2323) and (34-0396)]. This is due to the grains which are composed of large number of small regions where each plane spacing is substantially constant but differing at adjoining regions, these regions causes the various sharp diffraction lines [1]. Here, powder particles contain grains which are bent and the non uniform accumulated strain.

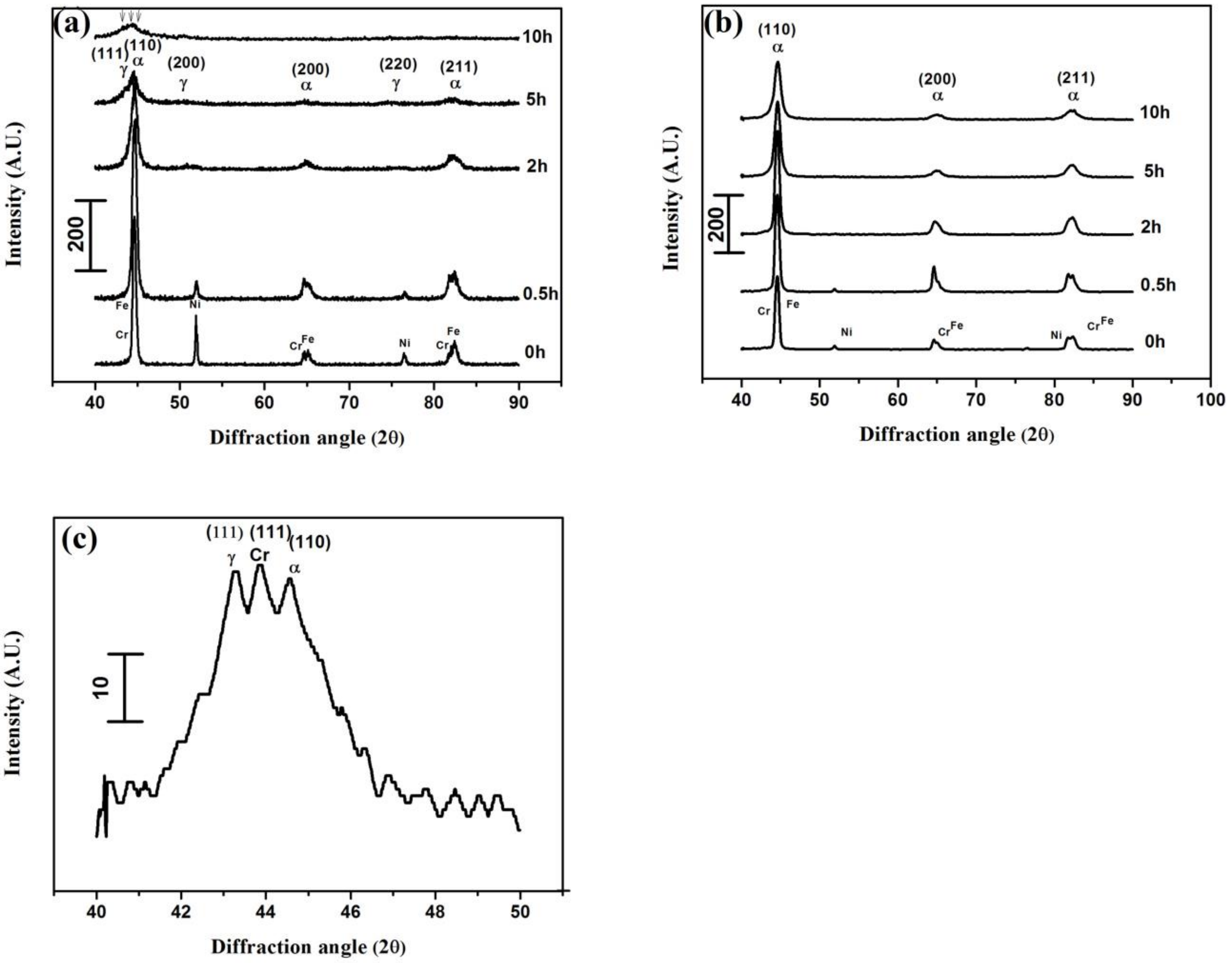

Figure 4.1.1 XRD spectra of (a) Fe–18Cr–13Ni alloy (b) Fe–17Cr–1Ni alloy milled for 10h in specially designed high energy planetary ball mill (c) Low scan range XRD spectra of Fe–18Cr–13Ni alloy milled for 10h in specially designed DDPM

4.1.2.2 Annealing under argon atmosphere

The effect of argon and nitrogen atmospheres during isothermal annealing has been thoroughly investigated. Figure 4.1.2 (a) and 4.1.2 (b) show the XRD traces of 10h DDPM milled Fe–18Cr–13Ni and Fe–17Cr–1Ni alloy powders after subsequent heat treatment at 750°C for 1h in argon atmosphere. The above annealed samples were furnace cooled to room temperature. The XRD spectra after annealing in argon atmosphere depicts the strong diffraction peaks of ferrite (α) and austenite (γ) with some weak peaks of iron oxide in both cases. The intensity of ferritic and austenitic peak is more in case of Fe-17Cr-1Ni and Fe-18Cr-13Ni alloys respectively. In Figure 4.1.2 (a) we can see sharp (110) plane in duplex stainless steel around 44.51°, this is due to the presence of ferritic stabilizer Ar. It is accepted from literatures that argon favours the ferritic transformation [2]. It is also found that, the XRD peaks are sharp and the intensity of ferritic and austenitic peaks increases as compared to unmilled powder due to supply of heat energy during annealing to the powders.

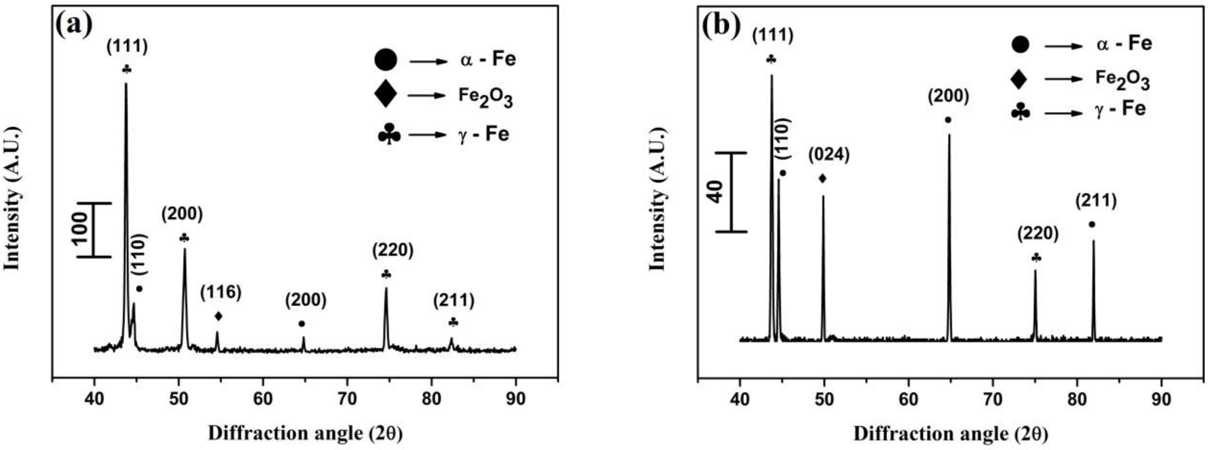

Figure 4.1.2 XRD traces of annealed samples of (a) Fe–18Cr–13Ni alloy (b) Fe–17Cr–1Ni alloy heat treated in Ar atmosphere at 750°C for 1h

4.1.2.3 Annealing under nitrogen atmosphere

Figure 4.1.3 (a) and 4.1.3 (b) shows the XRD traces of 10h DDPM milled Fe–18Cr–13Ni and Fe–17Cr–1Ni alloy powder heat treated at 750°C for 1h in nitrogen atmosphere. From the XRD graphs it is observed that austenitic (γ) peaks are dominant in case of Fe–18Cr–13Ni and strong ferritic (α) peak in case of Fe–17Cr–1Ni along with austenitic (γ) and traces of iron oxide phases. The presence of high amount of Ni in Fe–18Cr–13Ni alloy induces ferrite to austenite transformation. It is also widely accepted from literatures that nitrogen favours the austenitic transformation. Since a limited amount of austenite is generated during mechanical alloying, annealing of the powders promote α-Fe to γ-Fe transformation. If we compare the intensity of α and γ peak for a particular grade of stainless steel in both atmospheres then we can observe that nitrogen favours austenitic transformation to a greater extent than argon.

It has been reported that progress of milling of stainless steel powder under nitrogen atmosphere facilitates the ferrite-to-austenite transformation. Nitrogen atoms diffuse into the interstitial sites of ferrite crystallites and produce mismatch strains. Austenite has larger interstitial sites than ferrite, implying the nitrogen atoms to create less distortion and volume mismatch. In addition, austenite has smaller interfacial energy compared to ferrite. Apart from the nitrogen effect, refinement of the structure to the nano metric scale favours the austenitic transition during milling. The grain refinement increases the volume fraction of interfaces (grain boundaries), where the density of grain boundaries reaches $10^{19}cm^{-3}$ [3].

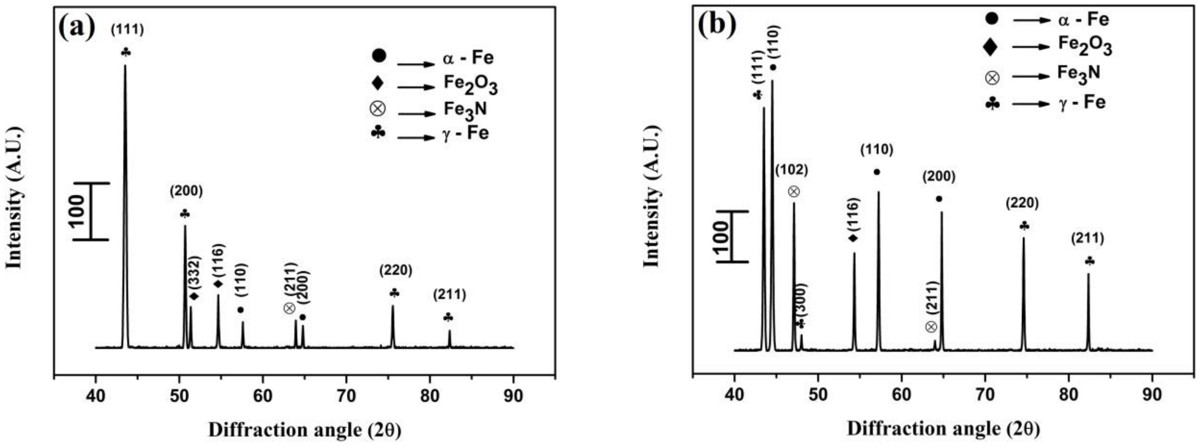

Figure 4.1.3 XRD traces of annealed samples of (a) Fe–18Cr–13Ni alloy (b) Fe–17Cr–1Ni alloy heat treated in nitrogen atmosphere at 750°C for 1h

Although the presence of alloying elements such as Cr and Ni enhance the solubility of nitrogen in iron lattice, the dissolved nitrogen in milled powders are still higher than the equilibrium level. We determined the amount of nitrogen dissolved in both duplex and ferritic stainless steel after annealing under nitrogen atmosphere using CHNS analyzer. The duplex stainless steel contains 4.18% of nitrogen, whereas ferritic stainless steel contains 3.73% of nitrogen. The annealing of milled powder under nitrogen in the above samples could be related to other effective parameters such as structural defects which are increased constantly through milling process. This eventually leads to a grain size reduction to nano range and the surface area of powder particles are exposed to nitrogen gas environment. During milling, different phenomena occur due to the transfer of energy into powder mixtures including distortion of crystallite lattice, fracturing and cold welding of powder particles, an increase in structural defects, a reduction of grain size and solid state amorphization or phase transformation. The reduction of grain size to a nano meter scale leads to increase in the volume fraction of grain boundaries which include many point and line defects, especially dislocations. Consequently, shorter diffusion path and more defect storage sites cause possible higher nitrogen content. An increase in the lattice defects increases ε (strain) and decreases d (grain size) (an enhancement of ε/d). Hence change of ε/d values could indicate the presence of preferable sites for nitrogen absorption as reported.

4.1.2.4 Lattice parameter calculation

Lattice parameters were successfully calculated by using Nelson-Riley (N-R) extrapolation relation as [1],

$$\frac{cos^2\theta}{\sin\theta}+\frac{cos^2\theta}{\theta}$$

In lattice parameter calculation, three strong XRD peaks of each duplex and ferritic stainless steel powders were taken and N-R functions were calculated for each peak. Then lattice parameter for each peak was calculated and the values were fitted in a straight line and extrapolated the straight line to y-axis. The point of intersection on y-axis gives the true lattice parameter value. The lattice parameter values of DDPM milled duplex and ferritic stainless steel powders are in good agreement with the standard values. The calculated lattice parameter values were plotted in graph as shown in Figure 4.1.4 (a). The final 10h milled duplex stainless steel powder shows single peak clearly remaining others are broadened due to decrease in crystallite size with milling time and hence Nelson-Riley plot cannot be obtained. From figure, it is clear that duplex composition shows ferritic phase till 5h of milling because the calculated lattice parameter value is close to ferritic lattice parameter. Hence we calculated lattice parameter of high energy planetary ball milled duplex stainless steel powder after 10h milling by using the equation as follows:

$$a=d\sqrt{h^2+k^2+l^2} \tag{1}$$

After 10h of milling we can see increase in the lattice parameter value. The calculated lattice parameters of duplex and ferritic stainless steel powder after 10h of milling is 3.51Å and 2.86Å respectively and these values are very close to the ideal lattice parameter of FCC iron (3.51Å) and BCC iron (2.86Å).

4.1.2.5 Crystallite size and lattice strain calculation

Considerable broadening of diffraction peaks will occur mainly due to instrumental errors, decrease in particle size and increase in lattice strain. This peak broadening errors can be minimized by using Williamson-Hall equation. Williamson and Hall proposed a method for de-convoluting size and strain broadening by looking at the peak width as a function of 2θ. Using XRD data, we determined crystallite size and lattice strain using Williamson-Hall equation [4] as follows:

$$\beta cos\theta = \frac{0.94\lambda}{D} + 4\eta \sin\theta \tag{2}$$

Where, β is full width half maxima (FWHM), D is crystallite size and η is lattice strain.

Here, Williamson-Hall plot is plotted with sinθ on the x-axis and β cosθ on the y-axis (β in radians). From the linear fit, crystallite size and strain are extracted from intercept and slope respectively. Here, three strong peaks of both duplex and ferritic stainless steel were used for the determination of crystallite size and lattice strain. We also calculated crystallite sizes of both the samples by using Scherrer equation individually as follows:

$$D = \frac{0.94\lambda}{\beta \cos\theta} \tag{3}$$

Where, β is full width half maxima (FWHM), D is crystallite size and λ is the wavelength of the target used. The differences in crystallite size as well as strain calculated from Williamson-Hall method were represented graphically in Figure 4.1.4 (b) and 4.1.4 (c) for duplex and ferritic stainless steel powder.

There is no much difference in crystallite size calculated from both Williamson-Hall method as well as Scherrer method respect to austenite and ferrite. From the graph we can conclude that as milling time increases, the crystallite size decreases and it attains a saturation level after 10h, where further refinement of crystallite size is quite difficult. However, lattice strain goes on increasing with increased milling time. The crystallite size and lattice strain cannot be calculated for duplex stainless steel using Williamson-Hall method after 10h of milling, because all the peaks were broadened and not visible except (111) plane. Hence, we calculated crystallite size of DDPM milled duplex stainless steel powder by Scherrer method. However, the same can be calculated for ferritic stainless steel by Williamson-Hall method as all the peaks are visible after 10h. The strong collision between ball-powder-jar reduces the crystallite size to nano level and increases strain continuously. Table 4.1 show the summary of crystal size, lattice strain and lattice parameter. Tjong et al. examined the effect of volume fraction of interfaces with respect to grain size and they found that, volume fraction of the interface increases with nano metric grain size and this result in the increased stored energy [5]. Meng et al. predicted that as the grain size of pure iron reaches below 14nm then austenite phase become more stable [6]. The crystallite sizes of prepared duplex and ferritic stainless steel powders are well below 11nm so we can expect intense phase transformation during annealing.

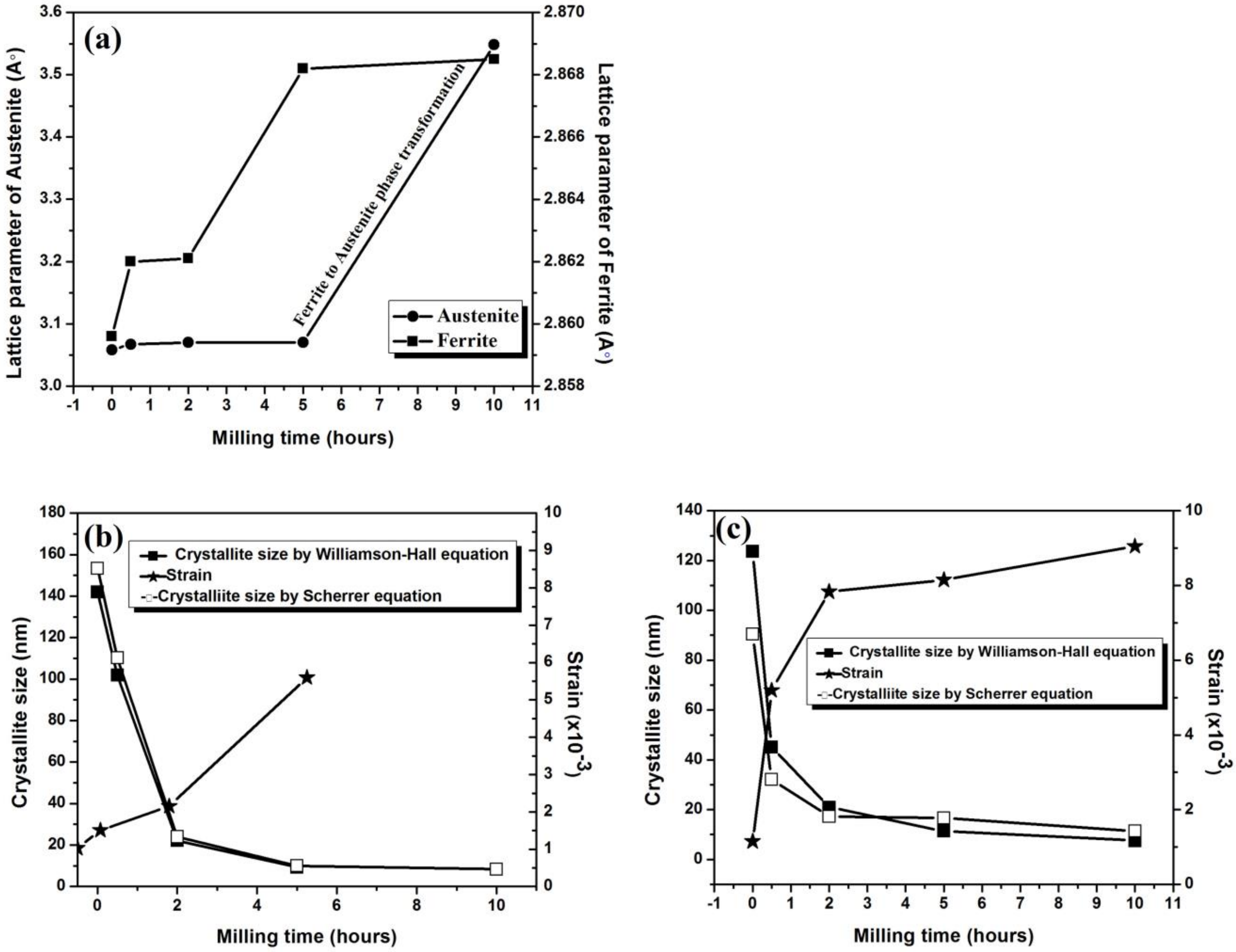

Figure 4.1.4 (a) Variation of lattice parameter with different milling time. Graphical representation of variation of strain, crystallite size with milling time of (b) Fe–18Cr–13Ni alloy (c) Fe–17Cr–1Ni alloy milled respectively for 5h and 10h in DDPM

4.1.3 Microstructure study

4.1.3.1 Scanning electron microscopy (SEM)

The SEM was used to study the morphology of mechanically alloyed duplex and ferritic stainless steel powder at various stages of milling. SEM micrographs of Fe-18Cr-13Ni and Fe-17Cr-1Ni powder milled in DDPM were presented in Figure 4.1.5 (a-d) and Figure 4.1.6 (a-d) respectively. The powder particles were bulky and random in size before milling. As milling begins, particles start to agglomerate to form plate like morphology up to 0.5h due to the soft nature of iron. But as milling proceeds further, the ductile powder particles get work hardened; Ni and Cr are entrapped into Fe and powder particles are refined. Further extended milling decreases inter lamellar spacing and brittle particles get uniformly dispersed in lamellae. Increase in the milling time from 0.5h to 10h decreases particle size and results in the formation of very fine with regular arrangement and spherical stainless steel powder. From the micrographs it is found that particle size of final 10h milled powder is around 10-15µm in both types of stainless steels.

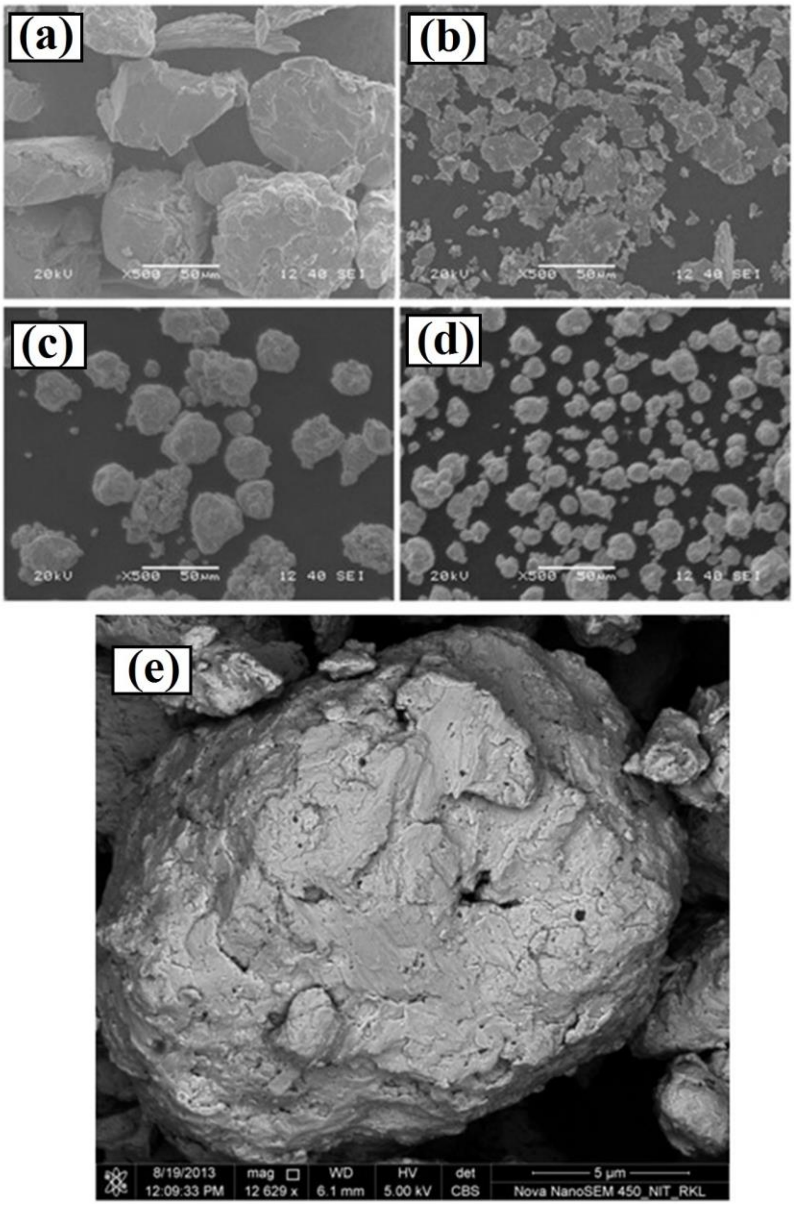

Figure 4.1.5 SEM micrographs of Fe–18Cr–13Ni alloy milled in high energy planetary mill for (a) 0h (b) 0.5h (c) 5h (d) 10h (e) FESEM BSE image of duplex stainless steel powder milled for 10h in DDPM containing grey spots of Cr and Ni diffused in to Fe lattice

Figure 4.1.5 (e) and 4.1.6 (e) show the BSE images of duplex and ferritic stainless steel powder milled in DDPM for 10h. The microstructure shows a uniform dispersion of Cr and Ni atoms in the Fe matrix in the form of grey spots as shown. From the figure we can observe river like layers confirming the diffusion of brittle Cr in to ductile Fe matrix during milling.

A standard EDX spectrum of 10h milled duplex and ferritic stainless steel powder samples were shown in Figure 4.1.7 (a) and 4.1.8 (a) respectively. The EDX studies were used to carry out the quantitative analysis and it confirms the presence of higher Ni content in duplex than ferrite. This affirms that chemical composition of 10h milled both stainless steel powder is close to as received powders. Figure 4.1.7 (b), 4.1.7 (c) and 4.1.7 (d) shows the elemental distribution of Fe, Cr and Ni in case of duplex stainless steel powder.

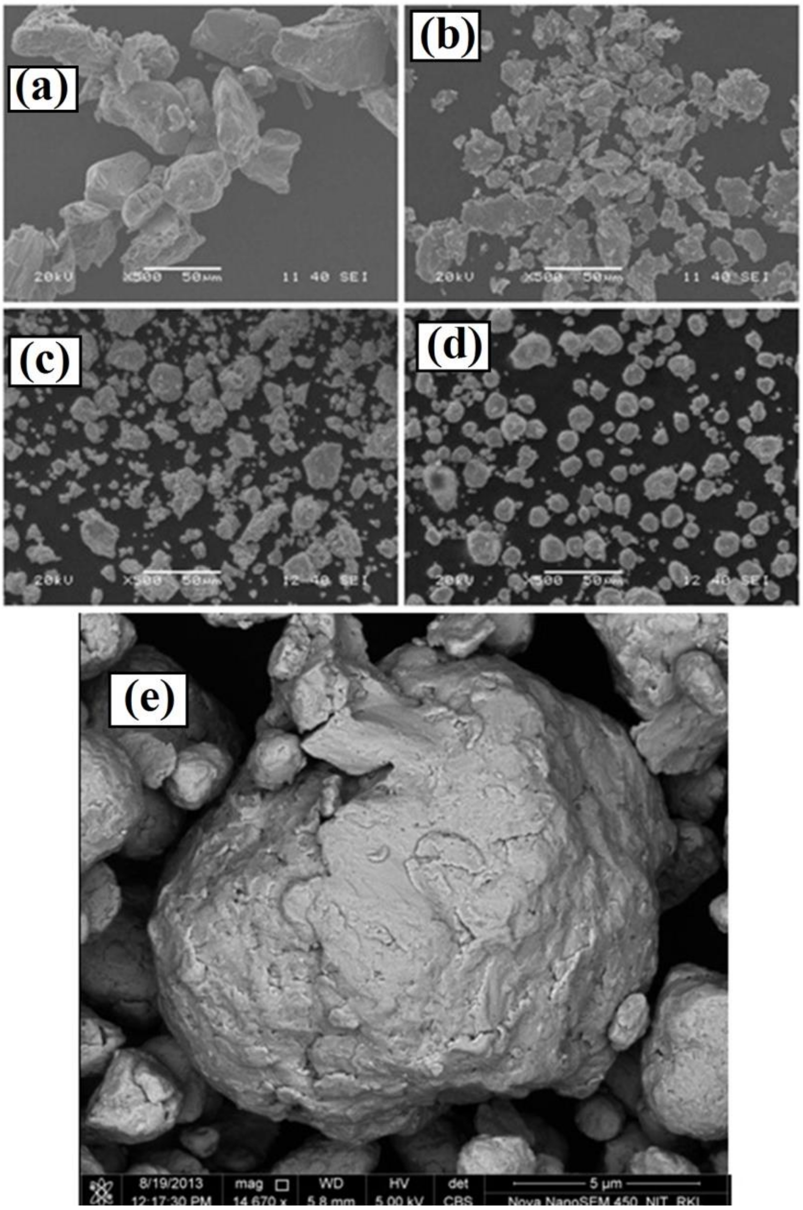

Figure 4.1.6 SEM micrographs of Fe–17Cr–1Ni alloy milled in high energy planetary mill for (a) 0h (b) 0.5h (c) 5h (d) 10h (e) FESEM BSE image of ferritic stainless steel powder milled for 10h in DDPM containing grey spots of Cr and Ni diffused in to Fe lattice

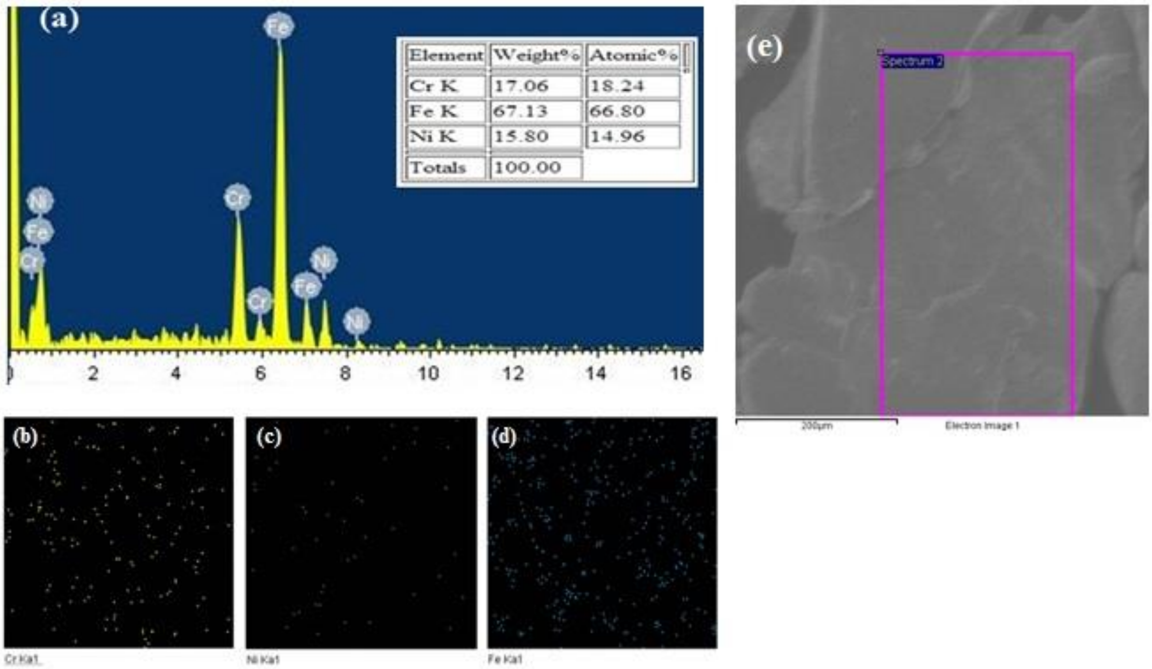

Element	Weight%	Atomic%
Cr K	17.06	18.24
Fe K	67.13	66.80
Ni K	15.80	14.96
Totals	100.00	

Figure 4.1.7 EDX spectra of (a) Fe–18Cr–13Ni alloy and its elemental mapping containing (b) Cr (c) Ni and (d) Fe (e) Image from which EDS and mapping was taken

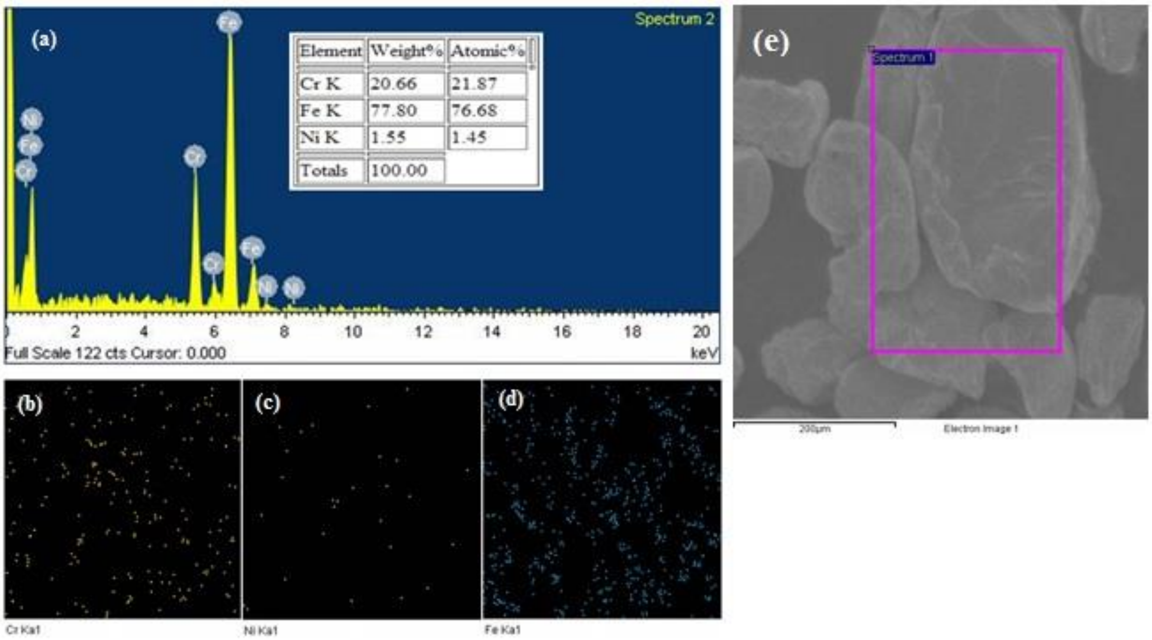

Element	Weight%	Atomic%
Cr K	20.66	21.87
Fe K	77.80	76.68
Ni K	1.55	1.45
Totals	100.00	

Figure 4.1.8 EDX spectra of (a) Fe–17Cr–1Ni alloy and its elemental mapping containing (b) Cr (c) Ni and (d) Fe (e) Image from which EDS and mapping was taken

Similarly, Figure 4.1.8 (b), 4.1.8 (c) and 4.1.8 (d) show the elemental distribution of Fe, Cr and Ni in ferritic stainless steel powder. From elemental mapping it is clear that elements are uniformly distributed between themselves and justify the composition of both types of powders.

4.1.3.2 High resolution transmission electron microscopy (HRTEM)

Microstructure analysis of duplex and ferritic stainless steel powders of high energy DDPM 10h milled and annealed powder (in nitrogen atmosphere for 1h) were performed by HRTEM. The diffraction pattern, lattice spacing and microstructure of the samples were studied successfully.

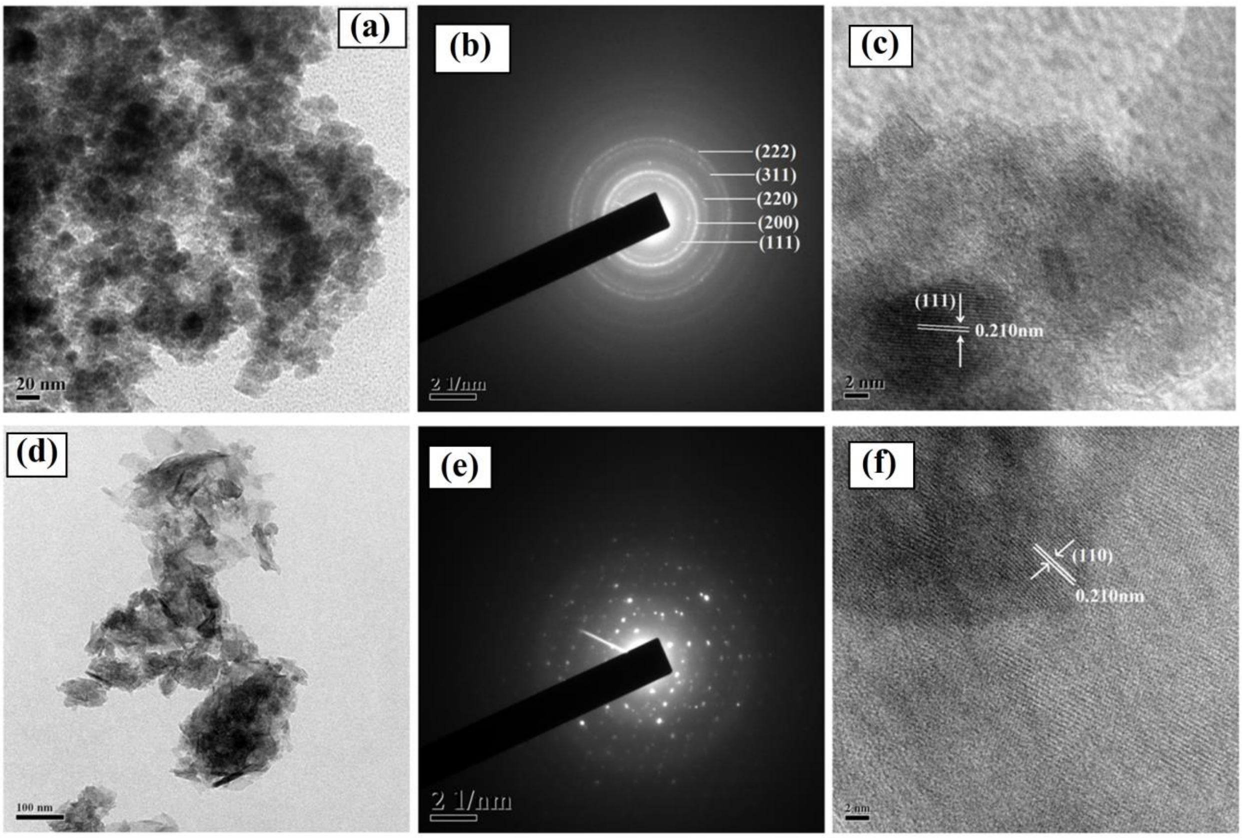

Figure 4.1.9 TEM images of DDPM milled duplex stainless steel powder (a) TEM image (b) SAED pattern (c) HRTEM to measure lattice spacing. Similarly, for ferritic stainless steel powder (d) TEM image (e) SAED pattern (f) HRTEM image

Figure 4.1.9 (a-f) shows the bright field TEM micrographs, SAED patterns and lattice images of 10h milled duplex and ferritic stainless steel powders respectively. It can be seen that spherical crystallites (black) with size around 10- 20nm are present in duplex stainless steel (Figure 4.1.9 a). Figure 4.1.9 (b) shows the SAED ring pattern which represents different crystallographic planes of austenite. Figure 4.1.9 (c) shows lattice spacing of 2.10Å for austenite (111) plane. Figure 4.1.9 (d) shows the BF micrograph of milled ferritic stainless steel. The micrographs show that particles are agglomerated and size is around 20-40nm. SEM and HRTEM results show a large difference in the particle sizes due to wide size distribution of milled powder starting from nano to micron size. During TEM sample preparation, milled powders were dispersed in ethanol by sonicating the mixture for 2h to reduce agglomeration. Large particles settle down and hence TEM shows the images of very fine and small particles which were dispersed properly. However, SEM shows the images of both small and large particles of size ranging from micron to nano level as there is no pre-treatment like TEM. The SAED pattern of Figure 4.1.9 (e) contains blurred ring structures with spotty appearance, which confirms the amorphization of ferritic stainless steel powder during milling. The amorphization process of ferritic stainless steel powder was occurred due to the severe plastic deformation and subsequent structural refinement during milling. This increases the concentration of defects, decreases the constancy of the crystalline structure and boost amorphization [6-8]. Figure 4.1.9 (f) shows the lattice spacing of 2.10Å for ferritic (110) plane.

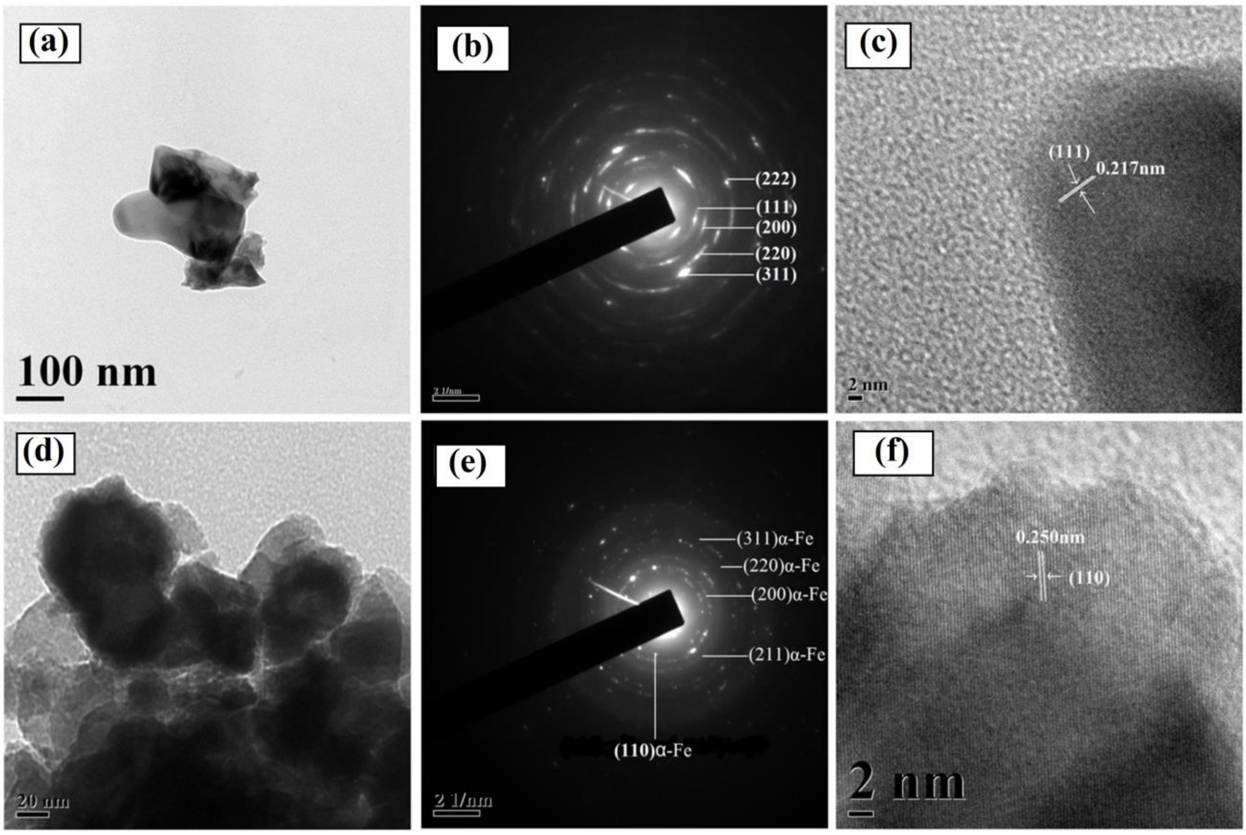

Figure 4.1.10 TEM images of annealed (N_2 atmosphere for 750°C for 1h) duplex stainless steel powder (a) TEM image (b) SAED pattern (c) HRTEM to measure lattice spacing. Similarly, for ferritic stainless steel powder (d) TEM image (e) SAED pattern (f) HRTEM image

Figure 4.1.10 (a-f) shows the BF images, SAED patterns and lattice images of duplex and ferritic stainless steel powder annealed at 750°C in nitrogen atmosphere for 1h. The BF images show that there is increase in size of crystal (around 100 nm) due to annealing (Figure

4.1.10 a). Figure 4.1.10 (b) shows SAED ring pattern correspond to FCC austenite (111) plane as well as BCC (110), (200), (211), (220) and (310) ferrite planes. This is due to the dissolution of austenitic stabilizers such as Ni and N_2 in to the iron lattice during milling and annealing respectively. The presence of Cr in the ferritic stainless steel composition increases the solubility of N_2 in α-Fe during annealing. Hence, we can expect phase transformation from α-Fe to γ-Fe. Lattice parameters of milled and annealed powders were calculated from lattice spacing and tabulated in Table 4.1.

Table 4.1 Summary of crystal size, lattice strain, particle size and lattice parameter

Condition	**Type of stainless steel**	**Crystallite size (nm)**			**Lattice strain (%)**	**Particle size (μm)**		**Lattice parameter (Å)**	
		W-H method	**Scherrer method**	**TEM**		**Particle size analysis**	**SEM**	**XRD**	**TEM**
Milled for 10h	Duplex	9 (after 5h milling)	8	13	0.6	22	21	3.52	3.65
	Ferrite	8	11	41	0.9	16	16	2.87	2.97
Annealed at 750°C in N_2 for 1h	Duplex		26	114				3.60	3.73
	Ferrite		37	47				2.87	2.89

4.1.4 Particle size analysis

The particle size distribution of duplex and ferritic stainless steel powder milled in DDPM mill after time intervals of 0, 0.5, 2, 5 and 10h are shown in Figure 4.1.11 (a) and 4.1.11 (b) respectively. The cumulative size distribution curves shift toward left side as milling progresses indicating refinement and reduction of powder particles. From the figures we can observe that particle size goes on decreasing with increase in milling time in both duplex and ferritic stainless steel powder. The variation of median particle size with increase in milling time in both duplex and ferritic stainless steel powders were shown in Figure 4.1.11 (c). The median particle size decreases from 80 to 22μm during milling from 0h to 10h in case of duplex stainless steel powder. Similarly, powder median size reduces from 56 to 16μm for ferritic stainless steel.

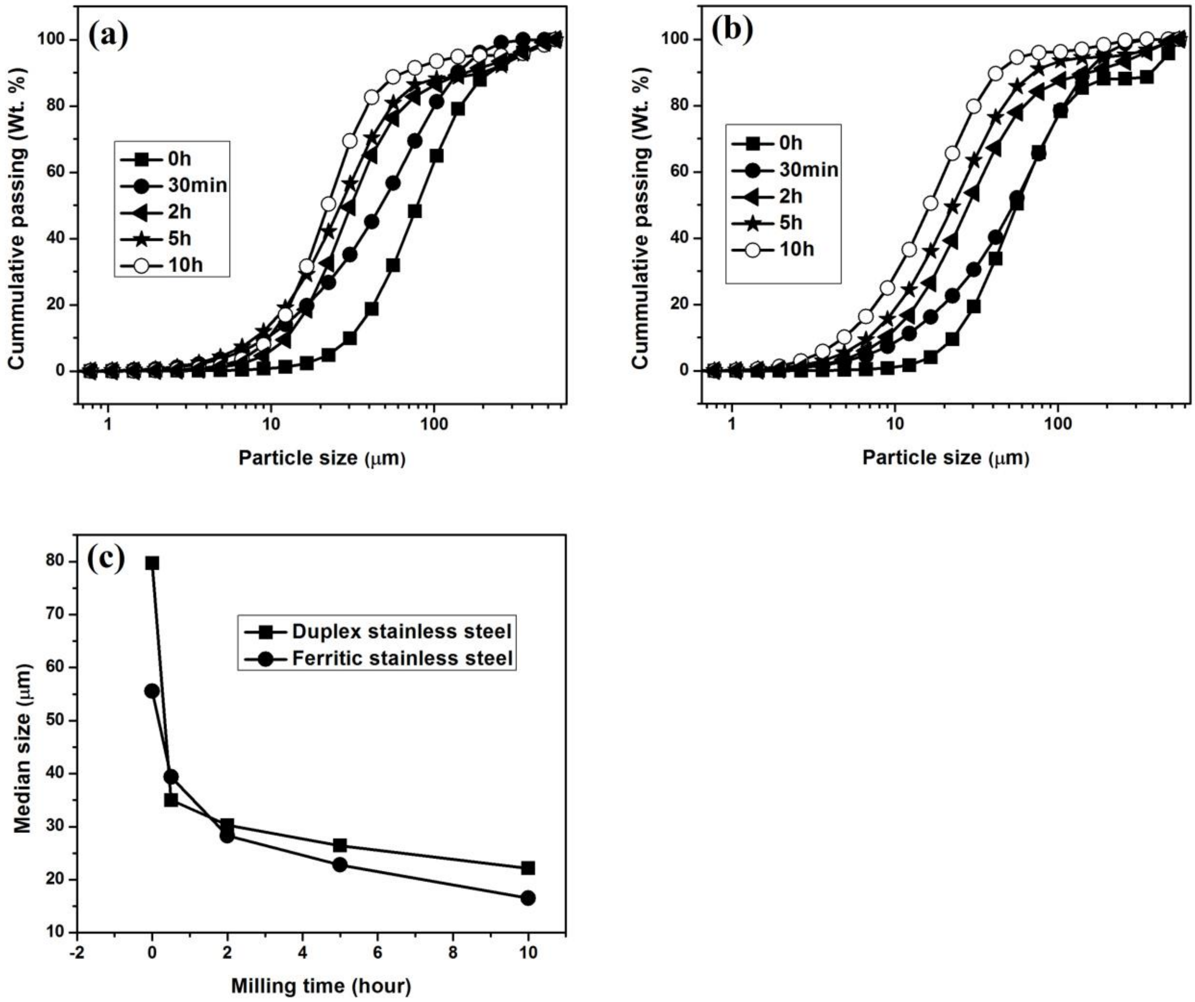

Figure 4.1.11 Particle size distribution of (a) Fe–18Cr–13Ni alloy (b) Fe–17Cr–1Ni alloy milled in specially designed planetary ball mill at different time intervals (c) Variation of median size with milling time

4.1.5 Thermal analysis

Differential scanning calorimetry (DSC) was performed by continuous heating of both duplex and ferritic stainless steel powders from 25 - 1000°C at the heating rate of 10°C/minute under argon atmosphere. Figure 4.1.12 (a) and 4.1.12 (b) shows the DSC graphs of duplex and ferritic stainless steel powder milled in specially designed ball mill and it shows exothermic peaks at 874 and 854°C respectively. The exothermic peaks represent crystal growth, lattice strain release and amorphous to crystalline phase transition during annealing with an enthalpy change of 52.80kJ/mol and 93.32kJ/mol in case of duplex and ferrite respectively. Eskandarany et al. [9] observed exothermic peak at 1240K with an enthalpy change of 16.88KJ/mole for amorphous $Fe_{74}Cr_{18}Ni_8$ powder prepared by rod milling after 300 hours of milling. Similarly, Oleszak et al. [10] found exothermic peak at 670°C with total heat evolved

20-40J/g depending on milling time for nano crystalline duplex stainless steel powder prepared by planetary milling.

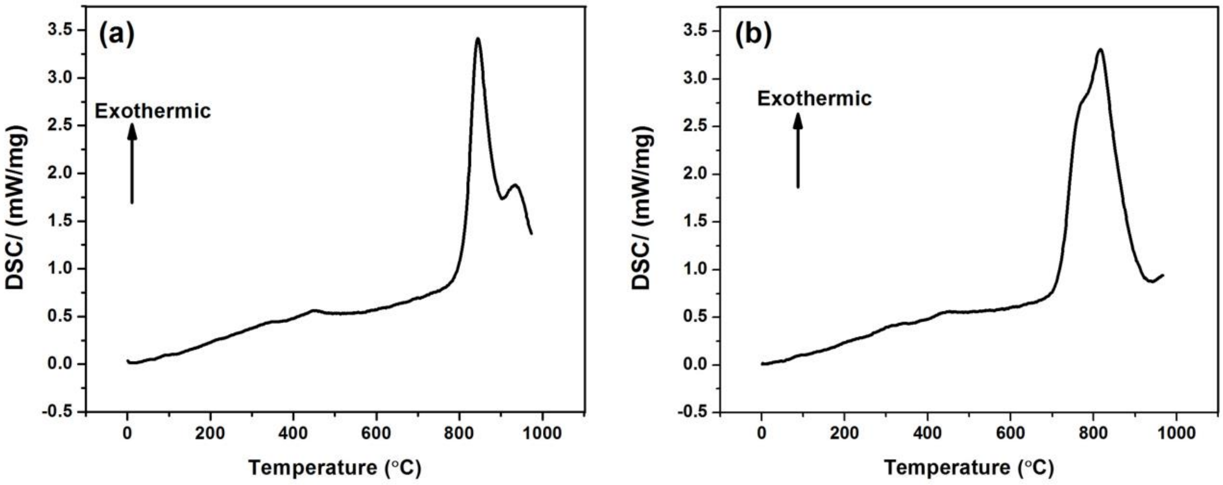

Figure 4.1.12 DSC graphs of (a) Fe–18Cr–8Ni alloy (b) Fe–17Cr–1Ni alloy milled in specially designed planetary ball mill after 10hours

4.1.6 BET surface area measurement

Quantachrome/AUTOSORB-1 model was used to measure the total surface area of the DDPM milled 0h and 10h duplex stainless steel powder samples by standard volumetric nitrogen adsorption method at 77K.

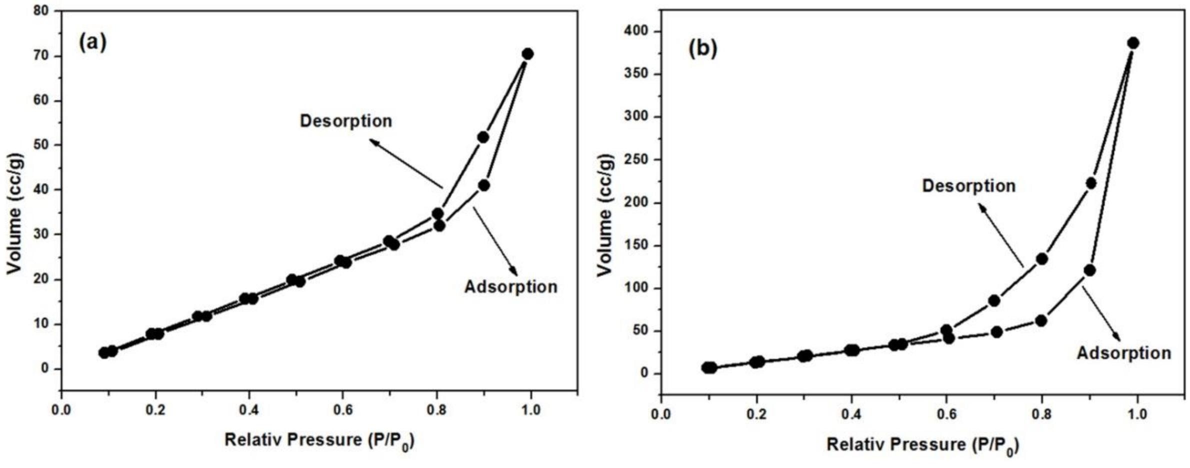

Figure 4.1.13 Adsorption-Desorption curves of duplex stainless steel powder milled for (a) 0h (b) 10h respectively

Figure 4.1.13 (a) and 4.1.13 (b) shows the adsorption–desorption isotherm of N_2 gas at 77K of nano-structured duplex stainless steel after 0 and 10h milling respectively. Surface area and total pore volume of 0h milled duplex stainless steel powder are 7.65m^2/g and 0.109g/cc respectively. Similarly, the values for 10h milled duplex stainless steel powder are 39.26m^2/g and 0.598g/cc respectively. Before milling, surface area and pore volumes are very less and they start to increase with milling. This is due to the increased volume fraction, plastic deformation and refinement of size.

4.1.7 Summary and conclusions

The following conclusions can be made from the present investigation:

1. It is found that only 10h is required to get nano-structured duplex and ferritic stainless steel powder in specially designed DDPM as compared to 40h in P5 mill.
2. The duplex composition was showing ferritic phase till 5h of milling and became duplex after 10h in DDPM.
3. The powder particles were of micron range and of random size before milling and as milling starts there will be slight increase in the particle size due to the repeated welding of ductile iron during milling. As milling continues, particles become strain hardened and spherical. After 10h of milling, the crystallite size reduced to 9 and 11nm in case of duplex and ferritic stainless steel respectively. The lattice strain goes on increasing in both cases.
4. Annealing of the powders at 750°C promote ferritic to austenitic transformation in both argon and nitrogen atmosphere. However, nitrogen favors austenitic transformation to a greater extent as compared to argon.
5. Thermal analysis study shows the exothermic peak, which represent crystallization of amorphous powder, crystal growth and lattice strain release during heating.
6. BET surface area measurements show the increase in surface area after milling due to the nano sized particles.
7. Although bulk efficient synthesis of nano structured duplex and ferritic stainless powder is the main focus of the present work, but there is a need for further research to scale-up the issues. There is plenty of scope for improved design of the milling system with enhanced energy efficiency to make dual drive planetary milling a viable commercial technique for bulk production.

References

1) B.D. Cullity, S.R. Stock, Elements of X-Ray diffraction, Pearson, Paperback, **2003**, ISBN-13: 9780131788183.

2) T. Haghir, M.H. Abbasi, M.A. Golozar, M. Panjepour, Investigation of α to γ transformation in the production of a nanostructured high-nitrogen austenitic stainless steel powder via mechanical alloying, *Mater. Sci. Eng. A.* 507 **(2009)** 144–148.

3) F. Tehrani, M.H. Abbasi, M.A. Golozar, M. Panjepour, The effect of particle size of iron powder on α to γ transformation in the nanostructured high nitrogen Fe–Cr–Mn–Mo stainless steel produced by mechanical alloying, *Mater. Sci. Eng. A.* 528 **(2011)** 3961–3966.

4) R. Jenkins, R.L. Snyder, Introduction to X-ray powder diffractometry, J. Wiley & Sons Inc, New York, **1996**.

5) S.C. Tjong, H. Chen, Nanocrystalline materials and coatings, *Mater. Sci. Eng. R.* 45 **(2004)** 1–88.

6) Q. Meng, N. Zhou, Y. Rong, S. Chen, T.Y. Hsu, Xu Zuyao, Size effect on the Fe nanocrystalline phase transformation, *Acta. Mater.* 50 **(2002)** 4563–4570.

7) P. S. Gilman, and J. S. Benjamin, Mechanical Alloying, *Ann. Rev. Mater. Sci.* 13 **(1983)** 279-300.

8) R. Shashanka, D. Chaira, Phase transformation and microstructure study of nano-structured austenitic and ferritic stainless steel powders prepared by planetary milling *Powder. Technol.* 259 **(2014)** 125–136.

9) M. Sherif E-Eskandarany, H.A. Ahmed, Morphology and structural studies of amorphous of $Fe_{74}Cr_{18}Ni_8$ alloy prepared by the rod-milling technique, *J. Alloys Compd.* 216 **(1994)** 213-220.

10) D. Oleszak, Grabias, A. Pekała, M. Swiderska-Sroda, A.T. Kulik, Evolution of structure in austenitic steel powders during ball milling and subsequent sintering, *J. Alloys. Compd.* 434-435 **(2007)** 340–343.

4.2 Optimization of milling parameters for the synthesis of nano-structured duplex and ferritic stainless steel powders

4.2.1 Objectives and scope of the work

Nano-structured duplex and ferritic stainless steel powders were prepared by high energy planetary milling of elemental Fe, Cr and Ni powders. Here, we have studied the effect of process controlling agent (PCA) such as stearic acid (SA), effect of ball to powder weight ratio (BPR 6:1and 12:1) and milling speed (64 and 75% critical speed) during planetary milling of elemental Fe–18Cr–13Ni (duplex) and Fe–17Cr–1Ni (ferritic) powders for 10h in a dual drive planetary mill (DDPM). We have found that all these mill parameters have great influence in tuning the final particle morphology, size and phase evolution during milling. It was found that addition of PCA, a BPR of 12:1 and 75% critical speed is more effective in reducing particle size and formation of duplex and ferritic stainless steel after 10h milling of elemental powder compositions than their counterparts.

4.2.2 Preparation of duplex and ferritic stainless steel powder

The effect of different milling parameters like process controlling agents (stearic acid), mill speed, BPR and milling atmosphere (dry and wet milling) were studied. In all cases, powders were milled in DDPM for 10h under toluene atmosphere (wet milling) and argon atmosphere (dry milling) to prevent oxidation. It was ensured that all the balls and powders were immersed in toluene. All milling experiments were carried out in DDPM consisting of 1kg chrome steel balls of 8 mm diameter kept in steel jar of 1000ml volume. A volume of 30% jar was filled with balls and powders.

4.2.2.1 Effect of stearic acid

Duplex and ferritic stainless steel powder samples were prepared by milling the elemental compositions of Fe, Cr and Ni powders in DDPM at a mill speed of 64% critical speed (CS) with 6:1 BPR for 10h in presence of SA and in the absence of SA under toluene atmosphere (wet milling). Before starting milling operation, 1wt. % of SA was added to Fe–18Cr–13Ni and Fe–17Cr–1Ni powder compositions separately in two different jars of DDPM.

4.2.2.2 Effect of ball to powder weight ratio

The wet milling was carried out at BPR of 6:1 and 12:1 using 1wt. % SA as PCA in both ferritic and duplex steel. Here, mill was run at 64% of CS.

4.2.2.3 Effect of milling speed

Wet milling was carried out at 64 and 75% CS. The main shaft speed was kept constant at 275 rpm, whereas jar speed was varied. The jar speeds were kept at 620 and 726 rpm for 64% and 75% CS respectively. Here, milling was carried out at BPR of 6:1.

4.2.2.4 Effect of dry and wet milling

We studied the effect of milling media on the synthesis of duplex and ferritic stainless steel powder samples milled in DDPM at 300rpm mill speed and 6:1 BPR for 10h. The disadvantage of dry milling is the particle agglomeration due to sudden decrease in the particle size, hence we added 1wt. % of SA along with Fe–18Cr–13Ni and Fe–17Cr–1Ni composition for milling. The duplex and ferritic stainless steel powders were prepared by dry and wet milling and characterized by XRD, SEM and particle size analysis techniques.

4.2.2.1 Effect of stearic acid

4.2.2.1.1 X-Ray diffraction study

Figure 4.2.1 (a) and 4.2.1 (b) show XRD spectra of Fe-18Cr-13Ni (duplex composition) and Fe-17Cr-1Ni (ferritic composition) milled for various times in DDPM in presence of SA. As milling proceeds, the sharp crystalline peaks of elemental Fe, Cr and Ni starts broadening continuously with milling time and they move into the lattice of Fe. This process starts just after 2h of milling in case of duplex and after 30 minutes in case of ferritic stainless steel. There is a shift of α-Fe (110) peak (Figure 4.2.1 a) towards lower angle side during milling from 0 to 10h. This displacement of (110) peak is due to the formation of austenite phase along with ferrite phase and confirms the presence of dual phase duplex stainless steel. Figure 4.2.1 (c) and 4.2.1 (d) show XRD spectra of 10h milled duplex and ferritic stainless steel powders with and without the addition of SA respectively. XRD spectra of duplex and ferritic steels without SA show sharp and high intense crystalline peaks confirming higher crystallite size and lower strain. Whereas stainless steel samples with the addition of SA show broad and low intense peaks due to lower crystallite size and higher internal strain.

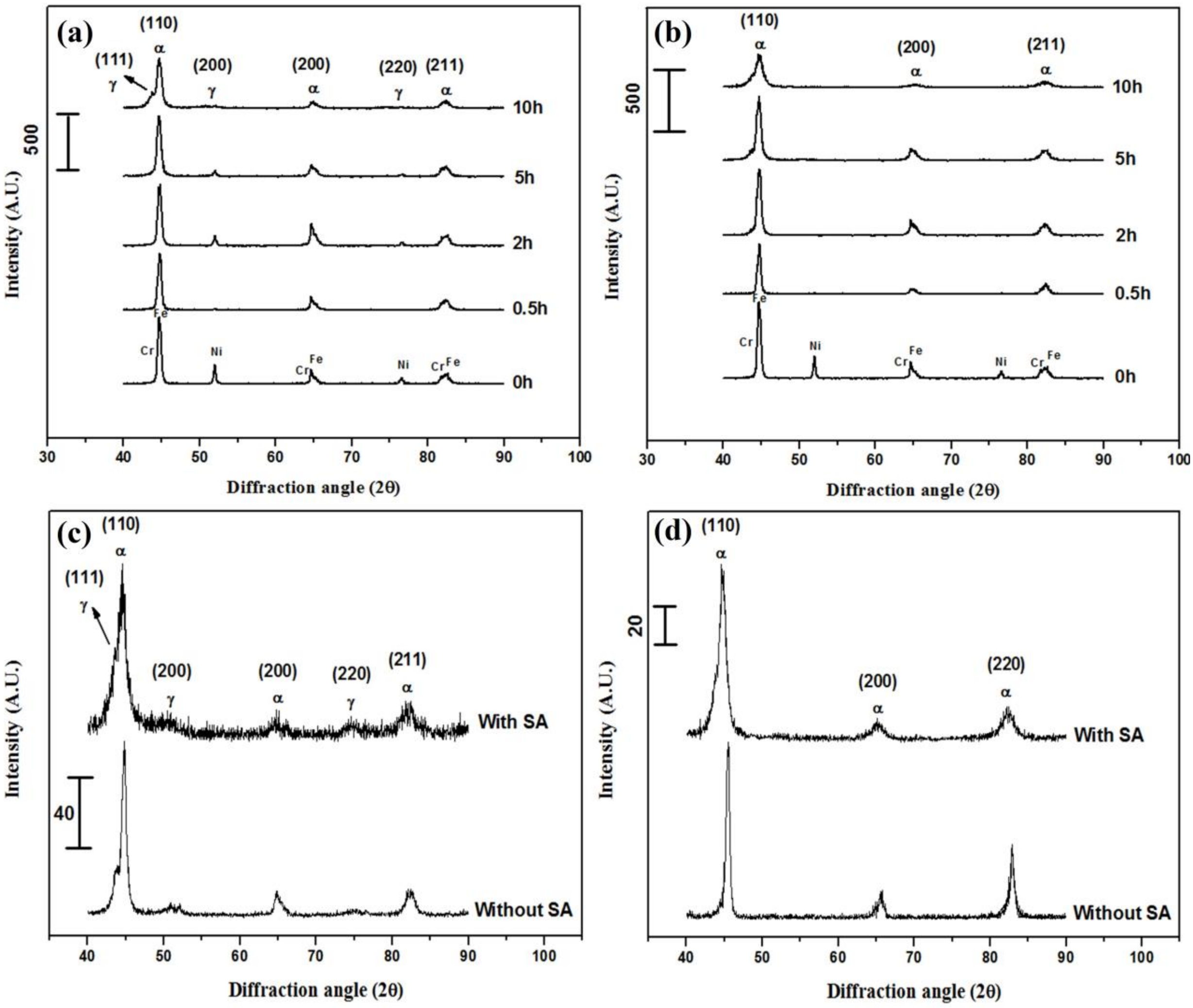

Figure 4.2.1 XRD spectra of 0 to 10h milled (a) Duplex stainless steel (b) Ferritic stainless steel in presence of 1wt. % SA. XRD spectra of only 10h milled (c) Duplex stainless steel (d) Ferritic stainless steel in presence and absence of SA

4.2.2.1.1 (a) Lattice parameter calculation

Nelson-Riley (N-R) extrapolation method was used to calculate lattice parameter by selecting three high intense XRD peaks of each duplex and ferritic stainless steel powders milled for different time periods. Figure 4.2.2 (a) and 4.2.2 (b) show the graphs of true lattice parameter values versus milling time of both duplex and ferritic stainless steel powder milled with and without SA respectively. Due to the large amount of defects generated during milling of both the stainless steel powders, an increasing trend of lattice parameter with milling time is observed. The lattice spacing value of austenite present in duplex and pure ferritic stainless steel powder milled with SA is 3.43Å and 2.87Å respectively. Similarly, the lattice parameter of duplex and ferritic stainless steel prepared without adding SA are 3.07Å and 2.86Å respectively. Both the stainless steels show higher lattice parameter value when SA is added as PCA during milling. Addition of SA increases the amount of defects such as dislocations, stacking fault, vacancy and it decreases crystal size more readily. Liu et al. reported that addition of SA decreases the milling time required to form Fe-Cr-Ni solid solution [1].

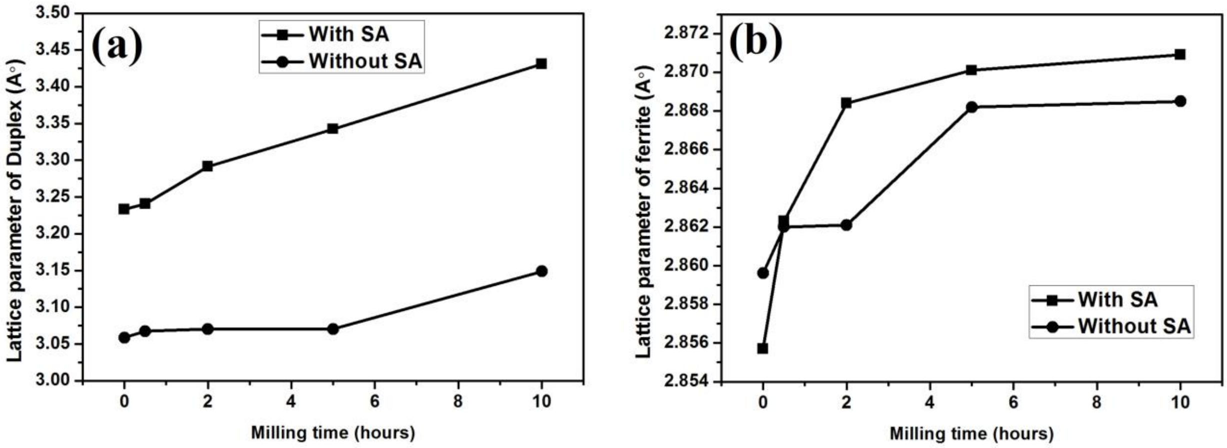

Figure 4.2.2 Graphical representation showing the effect of milling time on the lattice parameter (calculated from Nelson-Riley extrapolation method) of (a) Duplex stainless steel (b) Ferritic stainless steel in presence and absence of SA

4.2.2.1.1 (b) Crystallite size and lattice strain calculation

Figure 4.2.3 (a) and 4.2.3 (b) depict the crystallite size and lattice strain of duplex and ferritic stainless steel powders with the addition of SA. From the figure it is clear that crystallite size decreases and strain increases with milling time. Refinement of crystallite size reaches a saturation level at higher milling time and further refinement becomes quite difficult. Due to more and more interaction of powder-ball, powder-powder and powder-jar surface, the lattice strain increases continuously even after 10h of milling. Strong and frequent collision of ball-powder-jar reduces the crystallite size from 124nm to 7nm in case of duplex and from 121nm to 10nm in case of ferritic steel after 10h of milling. Similarly, lattice strain increases from 0.25 to 0.99% and from 0.1 to 0.94% respectively in case of duplex and ferritic stainless steel. We calculated crystallite size and lattice strain of duplex and ferritic stainless steel milled in the absence of SA using Williamson-Hall equation. Crystallite size and lattice strain of 10h milled duplex stainless steel are 10nm and 0.72% respectively. Similarly, ferritic stainless steel exhibits crystallite size of 8nm and lattice strain of 0.90% after 10h of milling.

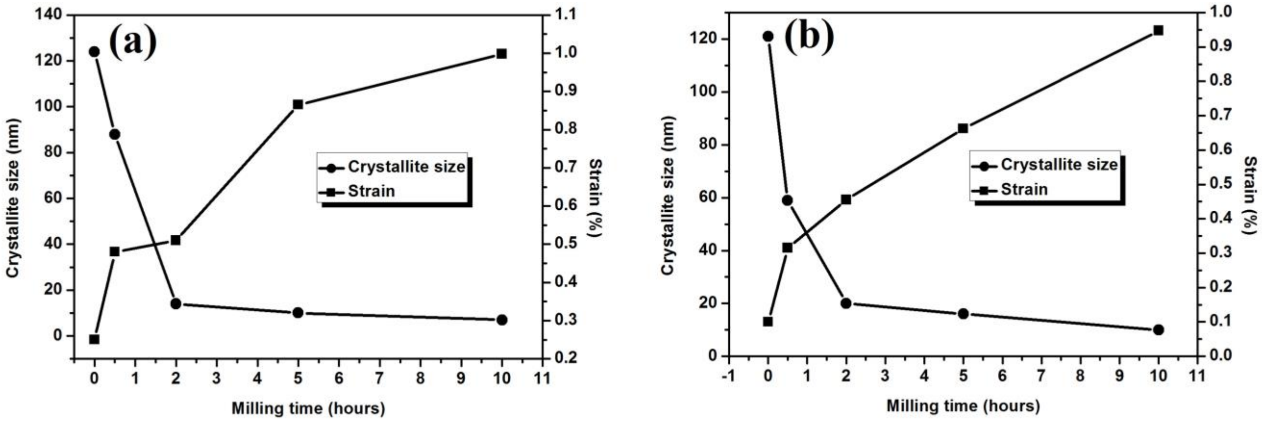

Figure 4.2.3 Graphical representation showing the variation of crystallite size and strain (Calculated from Williamson-Hall method) with milling time of (a) Duplex stainless steel (b) Ferritic stainless steel milled in presence of SA

4.2.2.1.2 Scanning electron microscopy (SEM)

SEM micrographs of duplex stainless steel powder milled at different intervals of time for 0 to 10h with SA and 10h powder sample without SA are shown in Figure 4.2.4. Similarly, SEM micrographs of ferritic stainless steel powder milled at different milling time from 0 to 10h (with SA) and 10h powder sample without SA are shown in Figure 4.2.5.

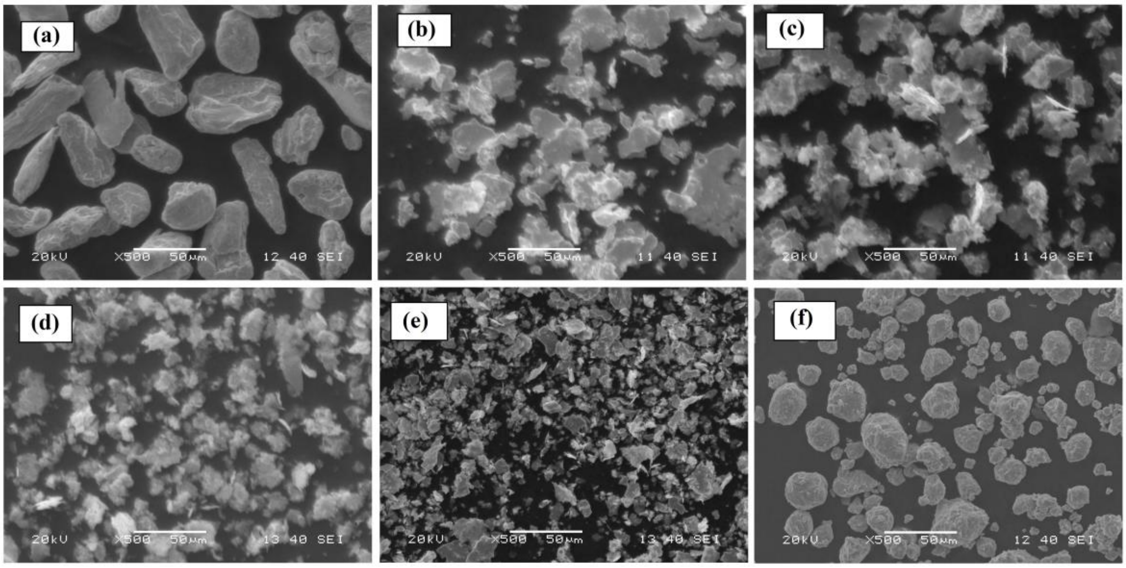

Figure 4.2.4 SEM images of duplex stainless steel powder milled for (a) 0h (b) 0.5h (c) 2h (d) 5h (e) 10h in presence of SA; (f) 10h in the absence of SA

Final 10h powder samples of both the stainless steels milled with SA show lesser particle size as compared to SA free samples. An amount of 1wt. % SA is sufficient to cover the newly yielded surface area of the stainless steel powder particles and prevention of excessive cold-welding. This results in a quick balance between the rate of cold-welding, alloying and fracturing.

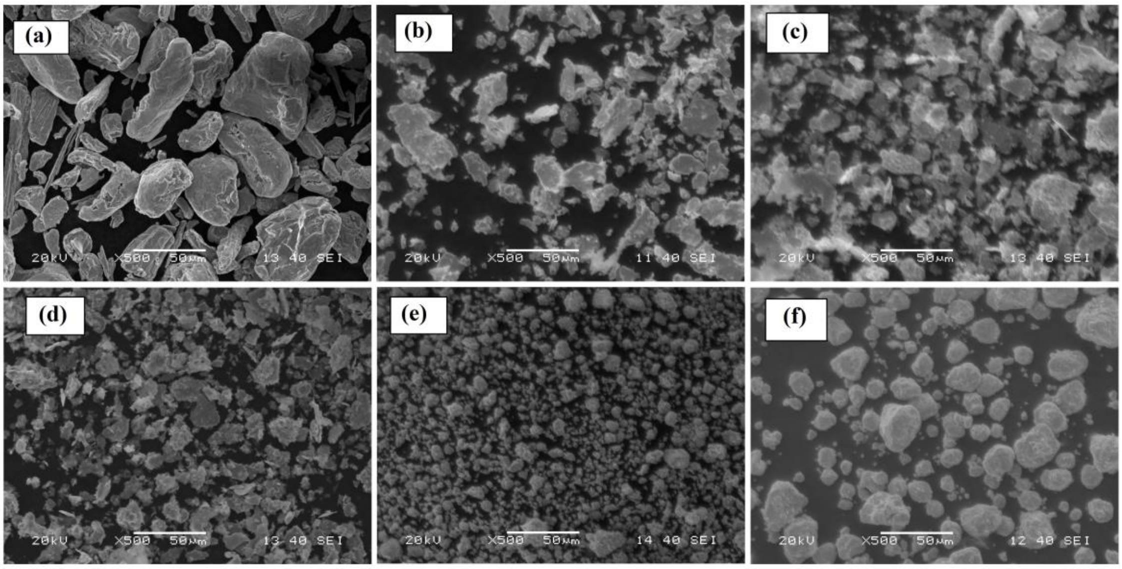

Figure 4.2.5 SEM images of ferritic stainless steel powder milled for (a) 0h (b) 0.5h (c) 2h (d) 5h (e) 10h in presence of SA; (f) 10h in the absence of SA

Elemental powder particles are large and irregular before milling but as milling starts particles start to form flat flakes and cold welded due to ductile nature of Fe. Meanwhile, SA covers the surface of the flakes and reduces the further cold welding with increase in milling time. As milling progress further, the ductile powder particles get work hardened and contain uniformly diffused Cr and Ni atoms in Fe lattice. The work hardened stainless steel fractured in to small particles with milling. This refinement of particle size reaches a saturation and further refinement of particles become more difficult after 10h. The stainless steel powders milled in presence of SA have irregular shape and lesser particle size compared to stainless steel milled in the absence of SA.

4.2.2.1.3 Particle size analysis

Particle size distribution of duplex stainless steel milled at different intervals of time from 0 to 10h with SA and 10h powder sample without SA are shown in Figure 4.2.6 (a). Similarly, particle size distribution of ferritic stainless steel powder sample is shown in Figure 4.2.6 (b). From the figure it is clear that the stainless steel powders milled with SA show lower particle size than without SA stainless steel samples. As the milling time increases from 0 to 10h, the particle size decreases and this is evidenced by the shift of cumulative size distribution curves towards left side. The reduction of mean particle size is due to the addition of SA which suppresses the excessive cold welding during milling by making a layer on the stainless steel powder particles. The rate of particle refinement during milling mainly depends upon PCA, ball to powder weight ratio, milling time, milling speed, size of the balls used for milling, etc.

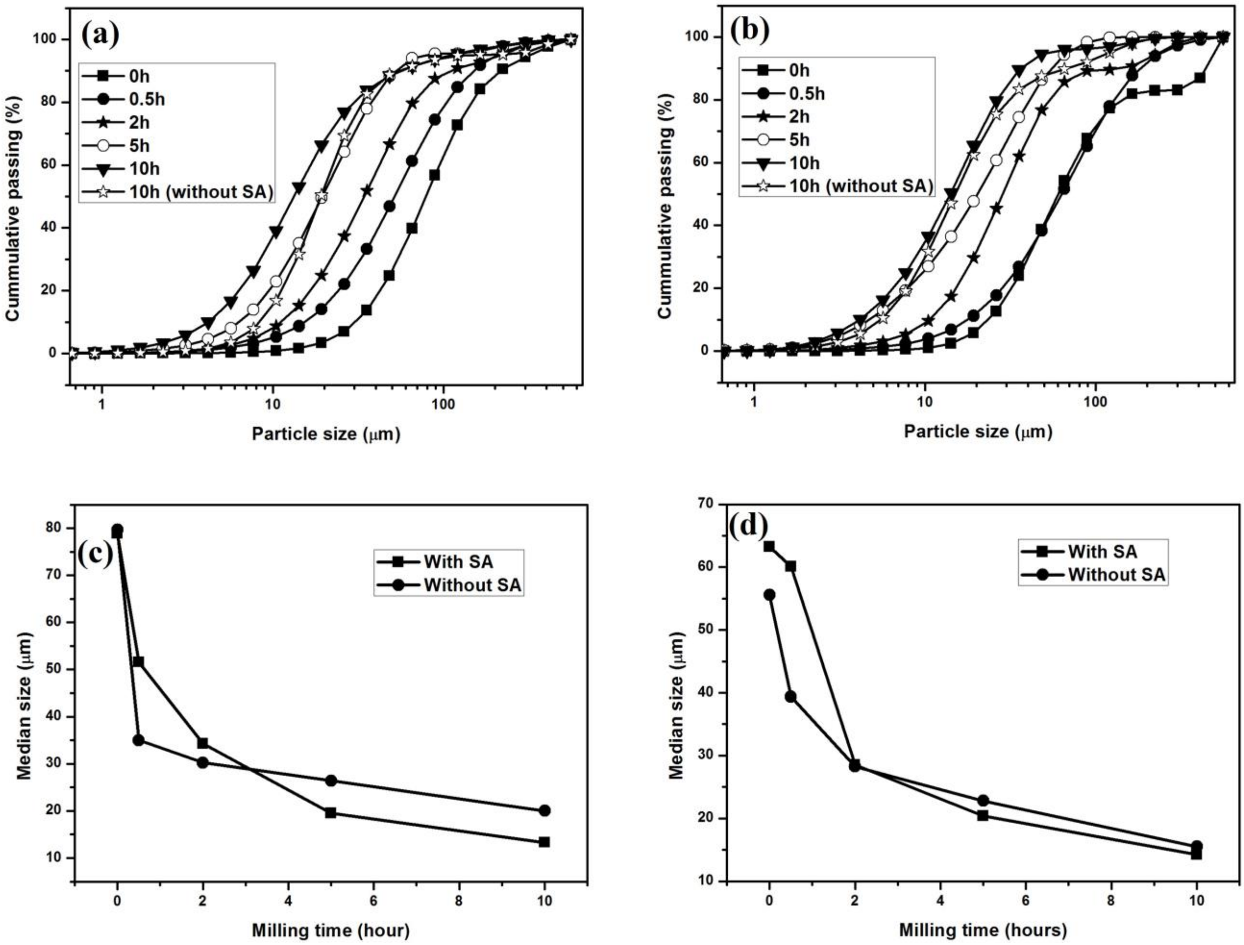

Figure 4.2.6 Particle size analysis of 0 to 10h milled (a) Duplex stainless steel (b) Ferritic stainless steel in presence of SA and 10h milled samples in the absence of SA; Median particle size of (c) Duplex stainless steel (d) Ferritic stainless steel in presence and absence of SA respectively

The effect of SA on the median particle size of duplex and ferritic stainless steel powders with milling time are represented in Figure 4.2.6 (c) and 4.2.6 (d) respectively. The median particle sizes of duplex and ferritic stainless steels milled in presence of SA are found to be 13 and 14μm respectively, whereas the median sizes are 20 and 16μm for without SA. Hence, SA serves as an effective process control agent to reduce the cold welding of stainless steel particles during milling. The particle size of duplex and ferritic steel is also supported by SEM results (Figure 4.2.4 and Figure 4.2.5).

Figure 4.2.7 depicts the schematic showing the effect of SA as PCA during planetary milling of stainless steel powders. Figure shows that each powder particle is coated with SA and prevents attraction between particles. Milled samples contain very fine stainless steel powders with high surface area and energy; as a result of which possibility of agglomeration is more. But SA acts as a protective coating on the each stainless steel powder particles and impedes the cold welding. During milling in toluene atmosphere, the hydrophilic head end covers the stainless steel powders and hydrophobic tail end repels the other SA coated stainless steel powder and thus decreases the chance of agglomeration as sown in the Figure 4.2.7.

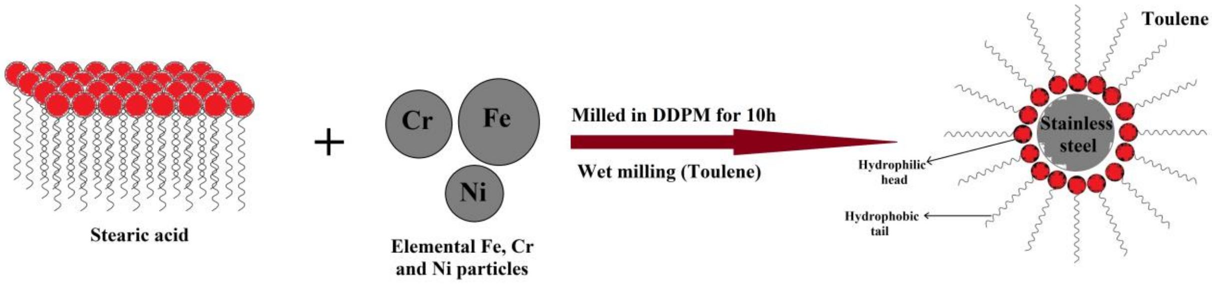

Figure 4.2.7 The mechanism of SA as PCA during mechanical alloying of stainless steel powders

4.2.2.2 Effect of ball to powder weight ratio

4.2.2.2.1 X-Ray diffraction study

Figure 4.2.8 (a) and 4.2.8 (b) show XRD spectra of duplex and ferritic stainless steel powder milled for different times in DDPM at BPR of 12:1. The sharp crystalline peaks of elemental Fe, Cr and Ni start broadening continuously with milling and gradually move into the Fe lattice. Figure 4.2.8 (c) and 4.2.8 (d) show XRD spectra of duplex and ferritic stainless steel powders milled for 10h at BPR of 6:1 and 12:1 respectively. It has been found that duplex and ferritic stainless steel powders milled at BPR of 12:1 show broad diffraction peaks than BPR of 6:1. It has also been noticed that γ-Fe (111) peak is prominent and resolved from α-Fe (110) peak at higher BPR in case of duplex steel after 10h of milling. The reason is higher energy input to elemental powder compositions due to large number of impacts and collisions at BPR of 12:1 than BPR 6:1. At BPR 6:1, the energy input is not sufficient and hence γ-Fe peak is absent even in case of duplex steel after 10h of milling.

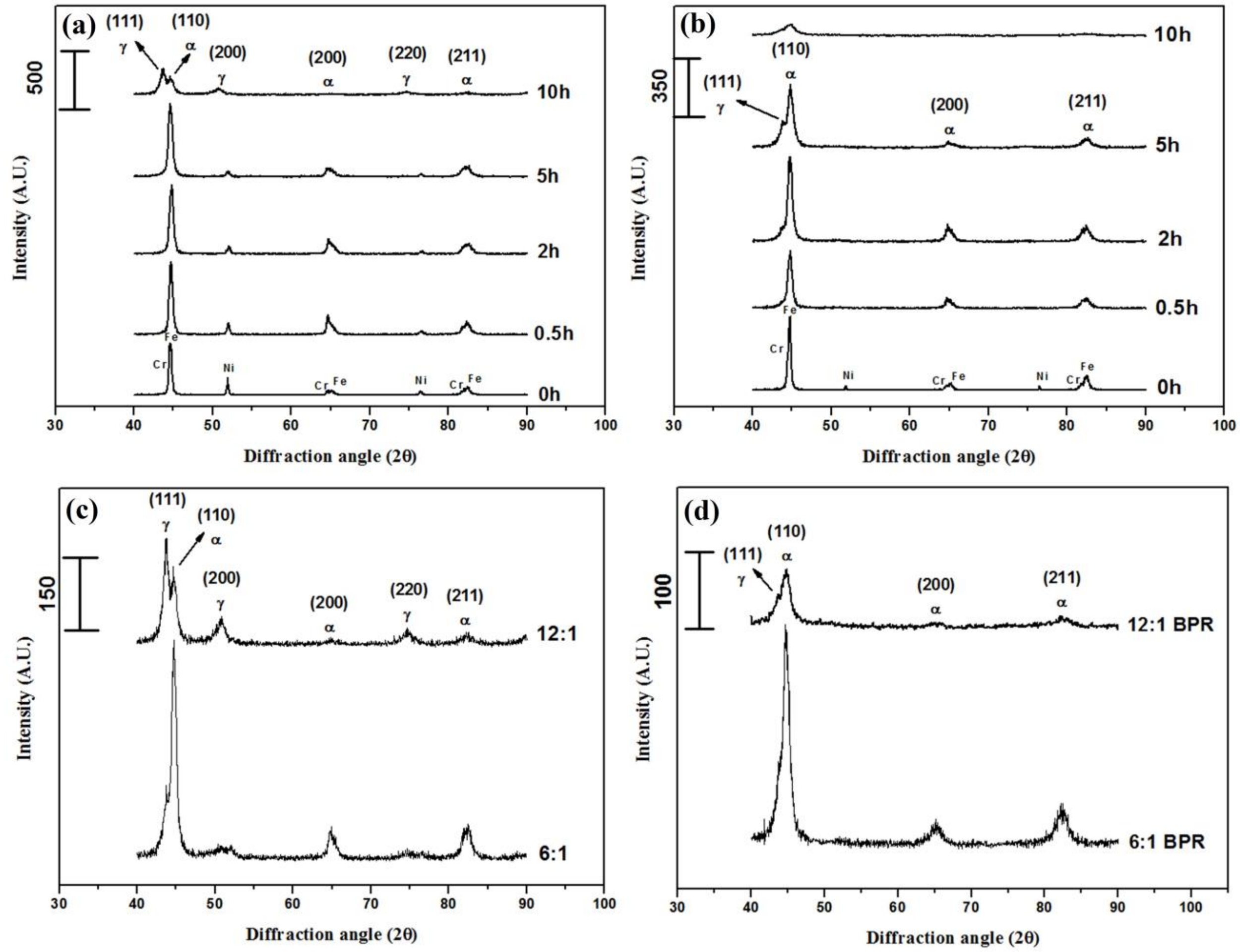

Figure 4.2.8 XRD spectra of 0 to 10h milled (a) Duplex stainless steel (b) Ferritic stainless steel at 12:1 BPR. XRD spectra of only 10h milled (c) Duplex stainless steel (d) Ferritic stainless steel at 6:1 and 12:1 BPR respectively

4.2.2.2.1 (a) Lattice parameter calculation

True lattice parameter is calculated from Nelson-Riley method of extrapolation by plotting the graph of N-R function versus milling time. Figure 4.2.9 (a) and 4.2.9 (b) show true lattice parameter of duplex and ferritic stainless steel powder milled at 6:1 and 12:1 BPR respectively. It has been observed from the graphs that lattice parameter values of duplex and ferritic stainless steel samples are higher at BPR 12:1 as compared to 6:1. True lattice parameter values of austenite present in duplex and pure ferritic stainless steel powder milled for 10h at 12:1 BPR are 3.47Å and 2.87Å respectively and that of 6:1 BPR are 3.43Å and 2.87Å respectively. Higher lattice parameter value for both duplex and ferritic steel at BPR 12:1 is due to the large amount of defects and imperfections. Pandey at al. and Rahmanifard et al. reported that large amount of defects will be generated during milling and this increases the lattice parameter value [2, 3].

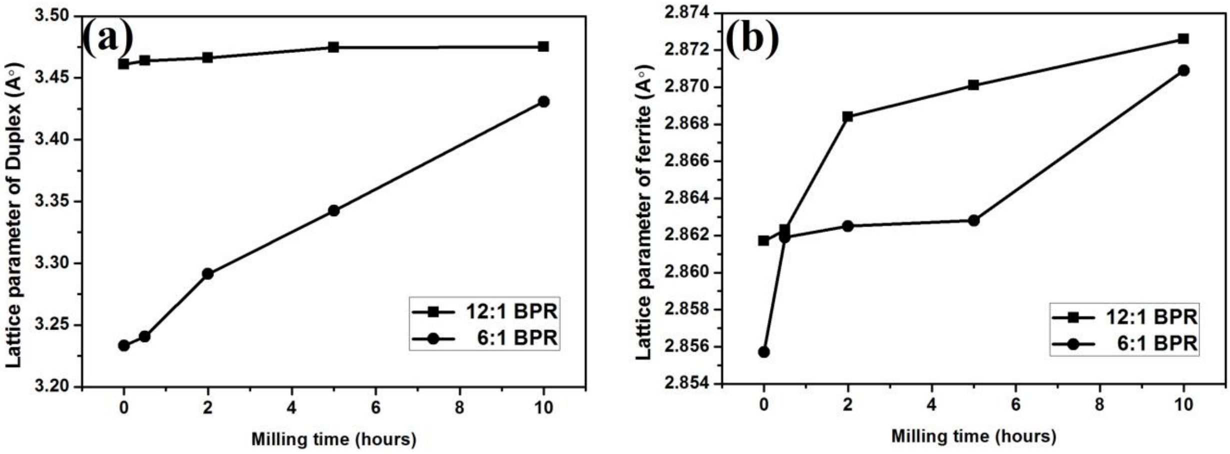

Figure 4.2.9 Graphical representation showing the effect of milling time on the lattice parameter (calculated from Nelson-Riley extrapolation method) of (a) Duplex stainless steel (b) Ferritic stainless steel milled at 6:1 and 12:1 BPR respectively

4.2.2.2.1 (b) Crystallite size and lattice strain calculation

Crystallite size and lattice strain of duplex and ferritic stainless steel powder samples are calculated by using Williamson-Hall equation. Figure 4.2.10 (a) and 4.2.10 (b) represent the crystallite size and lattice strain of duplex and ferritic stainless steel powder milled at 12:1 BPR.

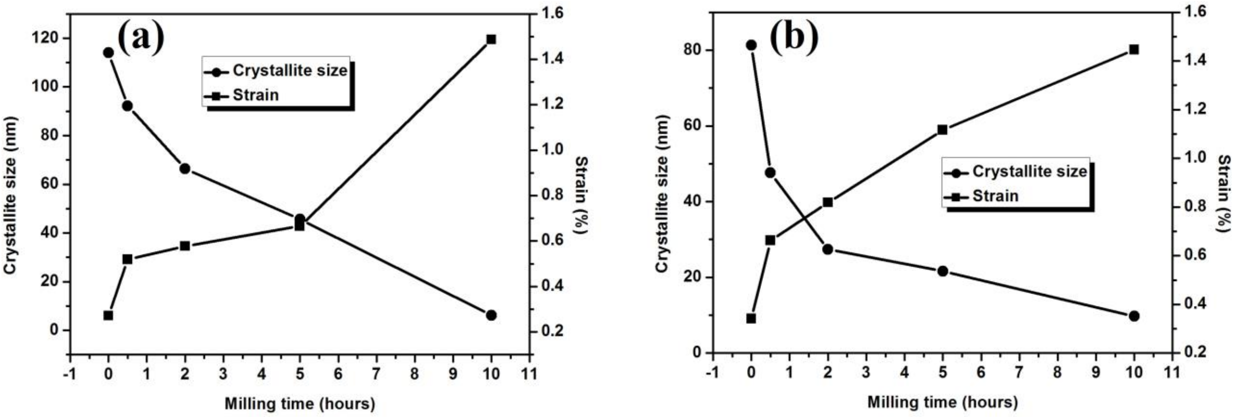

Figure 4.2.10 Graphical representation showing the variation of crystallite size and strain (Calculated from Williamson-Hall method) with milling time of (a) Duplex stainless steel (b) Ferritic stainless steel milled at 12:1 BPR

From the figures it is clear that strong and frequent collision of ball-powder-jar reduces the crystallite size and increases the lattice strain. Milling at 12:1 BPR, increases the interaction and impact energy of powder-ball, powder-powder and powder-jar surface. Whereas milling at 6:1 BPR, the impact energy of powder-ball-jar interaction is less. Hence, the crystallite size and strain of duplex stainless steel after milling for 10h at BPR of 6:1 are 7nm and 0.99%

respectively. Similarly, a crystallite size of 6nm and lattice stain of 1.48% is obtained for duplex stainless steel at 12:1 BPR. On the other hand, crystallite size and strain of ferritic stainless steel milled at 6:1 BPR condition show 10nm and 0.94% and at 12:1 BPR it shows 9nm and 1.44% respectively.

4.2.2.2.2 Scanning electron microscopy (SEM)

SEM micrographs of duplex and ferritic stainless steel powder samples milled at different intervals of time from 0 to 10h at 12:1 BPR and 10h samples milled at 6:1 BPR are shown in Figure 4.2.11 and Figure 4.2.12 respectively. Before milling, 1wt. % SA was added to both the stainless steel compositions.

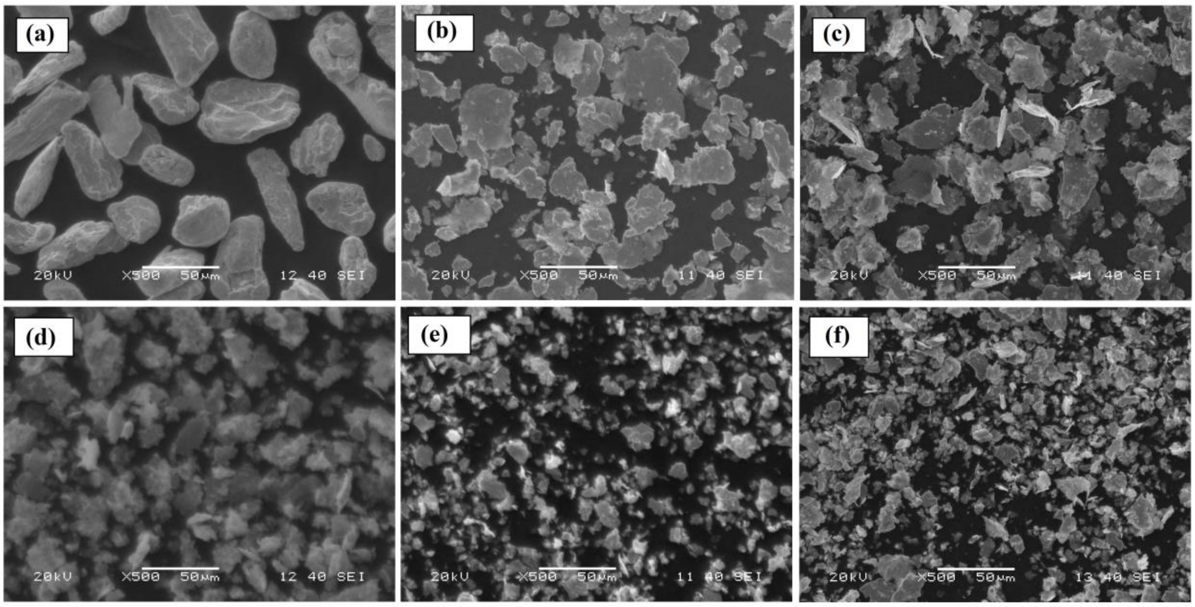

Figure 4.2.11 SEM images of duplex stainless steel powder milled for (a) 0h (b) 0.5h (c) 2h (d) 5h (e) 10h at 12:1 BPR; (f) 10h at 6:1 BPR

From Figure 4.2.11 it is found that powder particles are bulky and irregular in shape before milling and as milling continues it becomes flaky due to ductile nature of constituent powders. It has also been observed that size of the flakes gradually decrease with milling as particles become brittle. From Figure 4.2.12 it is evident that there is a gradual decrease in the particle size and gradual increase in the spherical shape with the milling time. The stainless steel powder samples milled at 12:1 BPR show lesser particle size and more regularity in their shape compared to powder samples milled at 6:1 BPR. This is due to the increased rate of collision of balls on powder samples at 12:1 BPR condition. Similar phenomena have also been reported by Ismail et al. and Mandal et al. [4, 5].

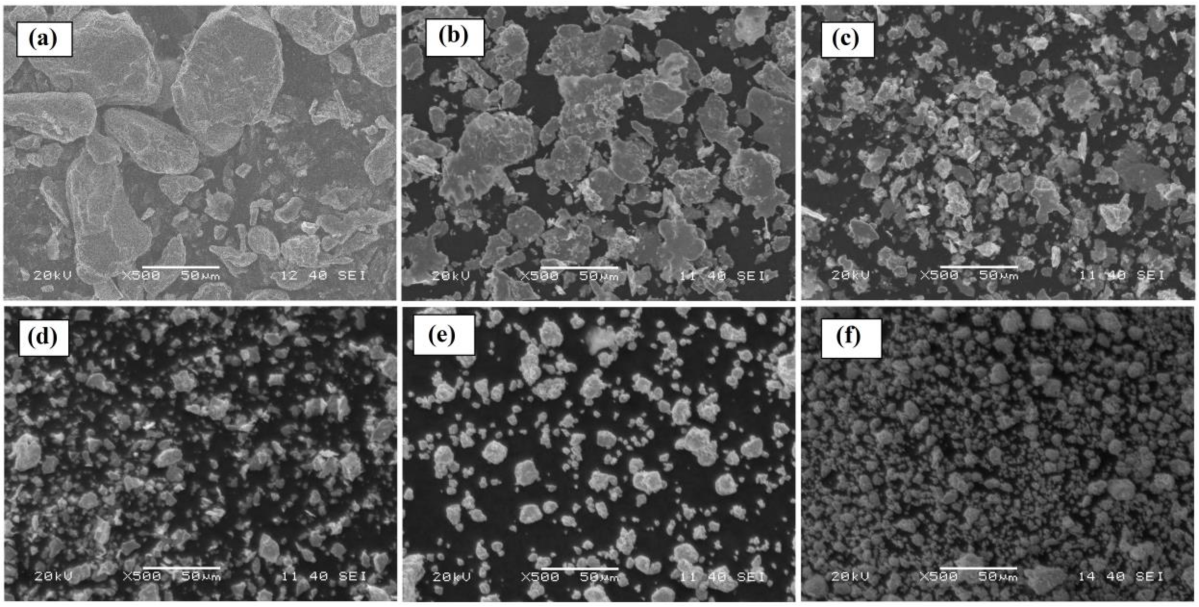

Figure 4.2.12 SEM images of ferritic stainless steel powder milled for (a) 0h (b) 0.5h (c) 2h (d) 5h (e) 10h at 12:1 BPR; (f) 10h at 6:1 BPR

4.2.2.2.3 Particle size analysis

Particle size distribution of duplex and ferritic stainless steel powders milled at 12:1 BPR for different intervals of time from 0 to 10h are shown in Figure 4.2.13 (a) and 4.2.13 (b) respectively. From the figure it is clear that cumulative size distribution curve shift towards left side indicating the decrease of the particle size with milling time. The rate of particle refinement during milling at 12:1 BPR is more than the 6:1 BPR milling condition. This is due to the maximum impact energy exerted by the balls on less quantity of powder sample. The effect of BPR on the median particle size of duplex and ferritic stainless steel powders with milling time are represented in Figure 4.2.13 (c) and 4.2.13 (d) respectively. The median particle size of duplex and ferritic stainless steel powder milled at 12:1 BPR condition is found to be 10 and 12µm whereas the median particle size is 13 and 14µm at 6:1 BPR condition.

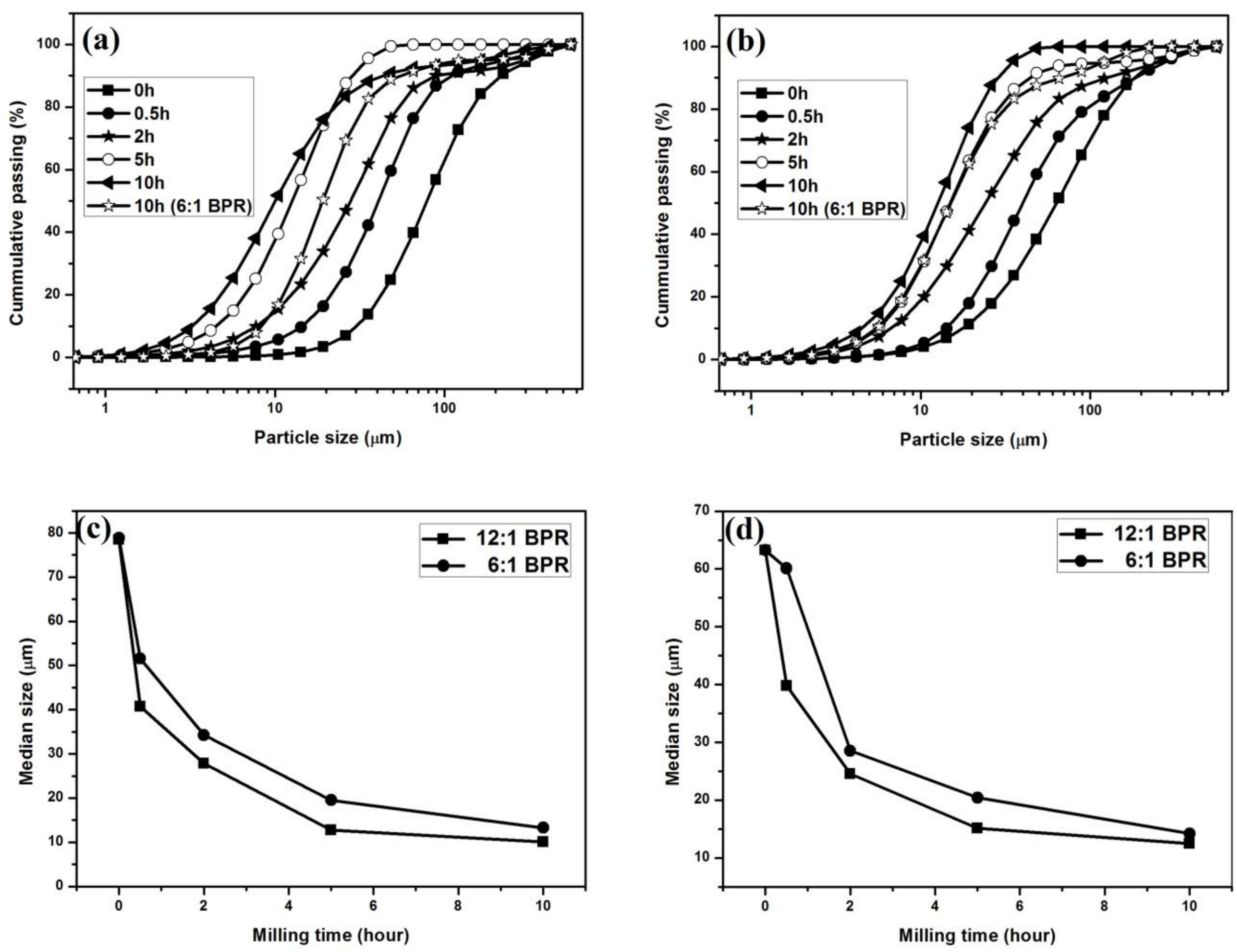

Figure 4.2.13 Particle size analysis of 0 to 10h milled (a) Duplex stainless steel (b) Ferritic stainless steel at 12:1 BPR and 10h milled samples at 6:1; Median particle size of (c) Duplex stainless steel (d) Ferritic stainless steel at 6:1 and 12:1 BPR respectively

4.2.2.3 Effect of milling speed

4.2.2.3.1 X-Ray diffraction study

The XRD spectra of duplex and ferritic stainless steel powders milled for various time periods at a mill speed of 75% CS are shown in Figure 4.2.14 (a) and 4.2.14 (b) respectively. We can see gradual decrease in the intensity of ferrite phase and shifting of peak towards lower diffraction angle confirms the formation of austenite phase. It is seen from both the graphs that intensity of individual elements (Fe, Cr, Ni) decreases gradually with milling. After 10h of milling, strong austenite peak is present along with ferrite peak for duplex stainless steel. However, weak peak of austenite is present along with strong ferrite peaks in case of ferritic stain steel. This is due to the presence of higher amount of austenite stabilizing element Ni in duplex than ferritic stainless steel. Figure 4.2.14 (c) and 4.2.14 (d) show XRD spectra of 10h milled duplex and ferritic stainless steel powders milled at a speed of 64 and

75% CS respectively. From the figures, it is confirmed that higher mill speed favours the phase transformation from α-Fe to γ-Fe. Meng et al. reported that, Fe with crystallite size less than 14nm makes austenite phase more stable [6]. At higher milling speed, phase transformation from α-Fe to γ-Fe is favoured. The higher mill speed increases impact energy of balls and thus increases the rate of collision between ball-powder-jar [7].

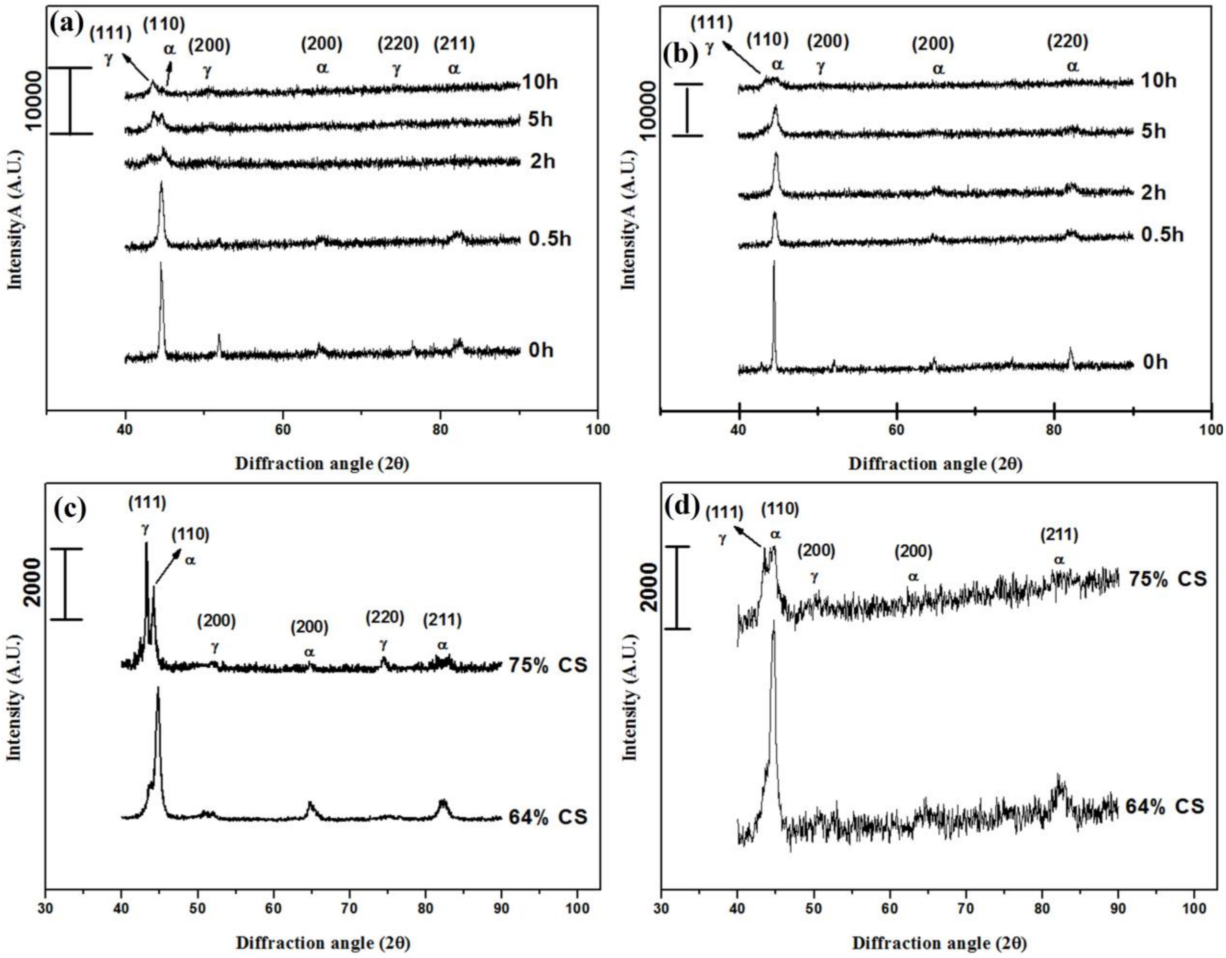

Figure 4.2.14 XRD spectra of 0 to 10h milled (a) Duplex stainless steel (b) Ferritic stainless steel at 75% CS. XRD spectra of 10h milled (c) Duplex stainless steel (d) Ferritic stainless steel at 64% and 75% CS respectively

4.2.2.3.1 (a) Lattice parameter calculation

Nelson-Riley extrapolation method is used to calculate true lattice parameter of 10h DDPM milled duplex and ferritic stainless steel samples at 75% CS. Figure 4.2.15 (a) and 4.2.15 (b) show true lattice parameter of duplex and ferritic stainless steel samples milled at 64% CS and 75% CS speed respectively.

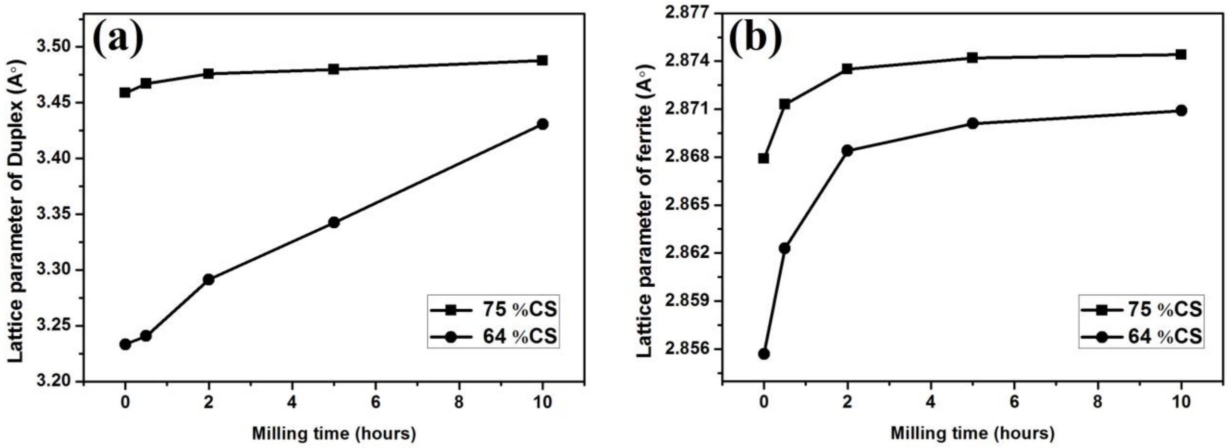

Figure 4.2.15 Graphical representation showing the effect of milling time on the lattice parameter (calculated from Nelson-Riley extrapolation method) of (a) Duplex stainless steel (b) Ferritic stainless steel milled at 64 and 75% CS respectively

At higher mill speed, the impact energy of collision and the amount of defects formation is more. Therefore, lattice parameter value at 75% CS milled duplex and ferritic stainless steel is more compared with 64% CS milled samples. True lattice parameter value of austenite present in duplex and pure ferritic stainless steel powder milled at 75% CS is 3.48Å and 2.87Å respectively and that of 64% CS milled samples is 3.43Å and 2.87Å respectively.

4.2.2.3.1 (b) Crystallite size and lattice strain calculation

Crystallite size and lattice strain of duplex and ferritic stainless steel powder samples are calculated by using Williamson-Hall equation. Figure 4.2.16 (a) and 4.2.16 (b) represent the crystallite size and lattice strain of duplex and ferritic stainless steel powder milled at 75% CS respectively. From the figures it is clear that crystallite size of both the stainless steel powders decreases with increase in milling time. Similarly, lattice strain value goes on increasing with milling time due to the formation of defects during milling. The crystallite size and strain of duplex stainless steel milled at 75% CS speed is 6nm and 1.06% and at 64% CS is 7nm and 0.99% respectively. Similarly, ferritic stainless steel has crystallite size of 7nm and lattice stain of 1.03% at 75% CS respectively and at 64% CS crystallite size and lattice strain is 10nm and 0.94% respectively. High mill speed involves high impact energy and results in more dislocations. As a result high lattice strain and low crystallite size are generated. The impact energy generated during 75% CS mill speed is more compared with the impact energy generated during 64% CS mill speed.

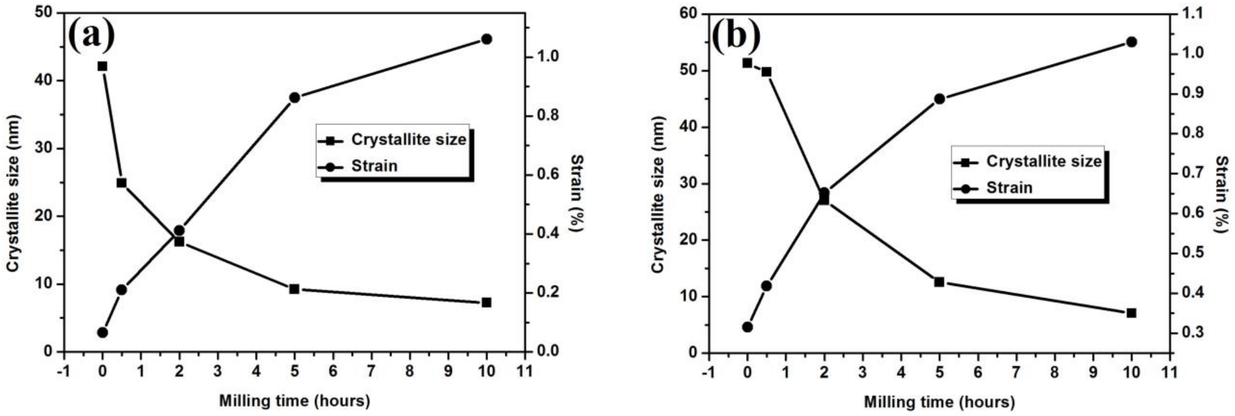

Figure 4.2.16 Graphical representation showing the variation of crystallite size and strain (Calculated from Williamson-Hall method) with milling time of (a) Duplex stainless steel (b) Ferritic stainless steel milled at 75% CS

4.2.2.3.2 Scanning electron microscopy (SEM)

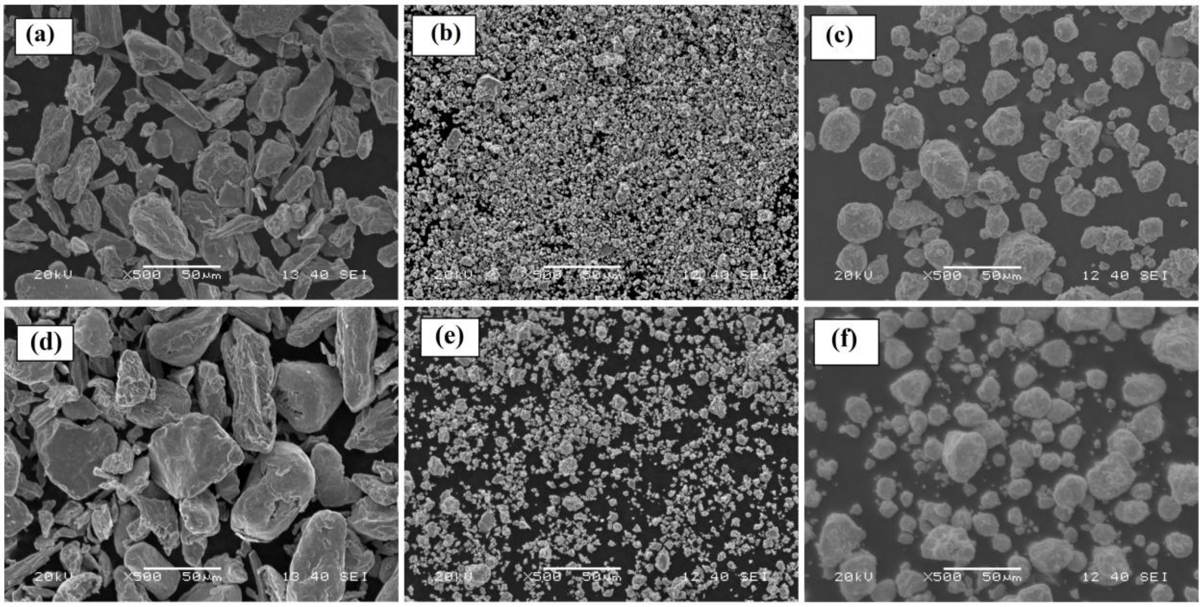

Figure 4.2.17 SEM images of duplex stainless steel powder milled for (a) 0h (b) 10h at a mill speed of 75% CS; (c) 10h at a mill speed of 64% CS; and ferritic stainless steel powder milled for (d) 0h (e) 10h at a mill speed of 75% CS; (f) 10h at a mill speed of 64% CS

Figure 4.2.17 (a) and 4.2.17 (b) represent the SEM micrographs of 0h and 10h milled duplex stainless steel powders at 75% CS. Figure 4.2.17 (c) shows the micrograph of duplex stainless steel milled for 10h at 64% CS. Similarly, Figure 4.2.17 (d) and 4.2.17 (e) represent SEM micrographs of ferritic stainless steel milled for 0h and 10h at 75% CS and Figure 4.2.17 (f) shows the ferritic stainless steel milled for 10h at 64% CS respectively. From SEM figures it is evident that stainless steel milled at 75% CS shows lesser particle size compared to stainless steel powders milled at 64% CS. At higher mill speed, rapid cold welding and work hardening occur due to high acceleration field. Therefore, particles gets work hardened at lesser time at 75% CS as compared to powders milled at 64% CS. Hence, they get more time to undergo fragmentation and this result in smaller particles with size of around 2 to 3µm in both the stainless steel powders.

4.2.2.3.3 Particle size analysis

Figure 4.2.18 (a) and 4.2.18 (b) depict the particle size distribution of 10h milled duplex and ferritic stainless steel powder samples at different mill speeds. Milling was carried out in the absence of SA and at mill speed of 64 and 75% CS respectively. From the figure it is confirmed that both types of stainless steel powders milled at 75% CS show lower particle size than the powder milled at 64% CS. At higher mill speed (75% CS), the rate of defects formation and solid solution formation is maximum. The median particle size of 10h milled duplex and ferritic stainless steel samples milled at 64% CS is found to be 20 and 16µm respectively, whereas the median size is 3.5 and 2.4µm at 75% CS. Therefore, milling speed variation is one of the most important milling parameters which control the particle morphology.

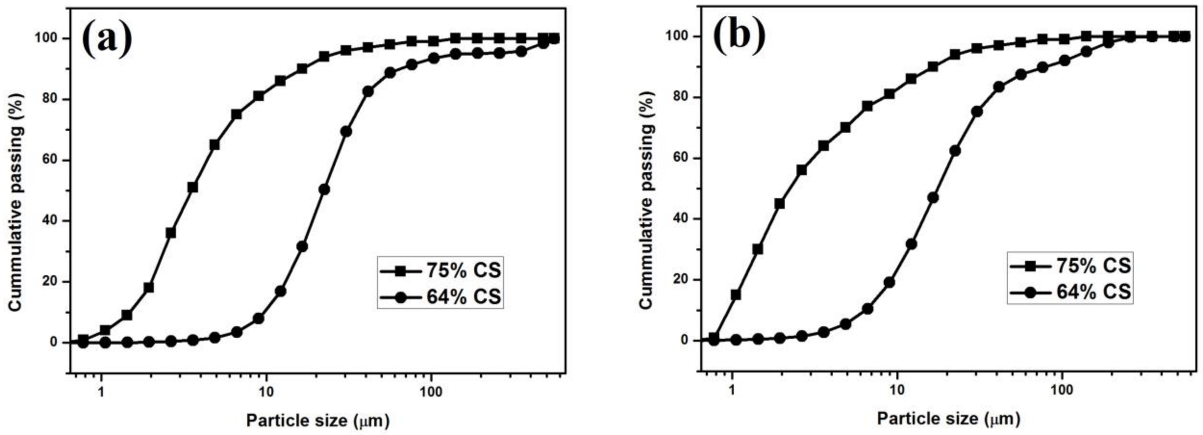

Figure 4.2.18 Particle size analysis of 10h milled (a) Duplex stainless steel (b) Ferritic stainless steel at a mill speed of 64 and 75% CS

4.2.2.4 Effect of wet and dry milling

4.2.2.4.1 X-Ray Diffraction study

The XRD spectra of duplex and ferritic stainless steel powders milled in argon atmosphere are shown in Figure 4.2.19 (a) and 4.2.19 (b) respectively. The dry milled duplex and ferritic stainless steel samples show very broad peaks with decreased intensity when compare with wet milled stainless steel samples as shown in the Figure 4.2.19 (c) and 4.2.19 (d) respectively. This due to the effective rate collision of balls with powder particles during dry milling when compared with wet milling. The impact energy generated during dry milling is more as the balls can freely move inside the jars as there is no liquid media to hinder the ball and particle movement. This increases the effective collision of ball-jar-powder; hence dry milling results in decreased crystallite size and increased strain when compared with wet milled samples.

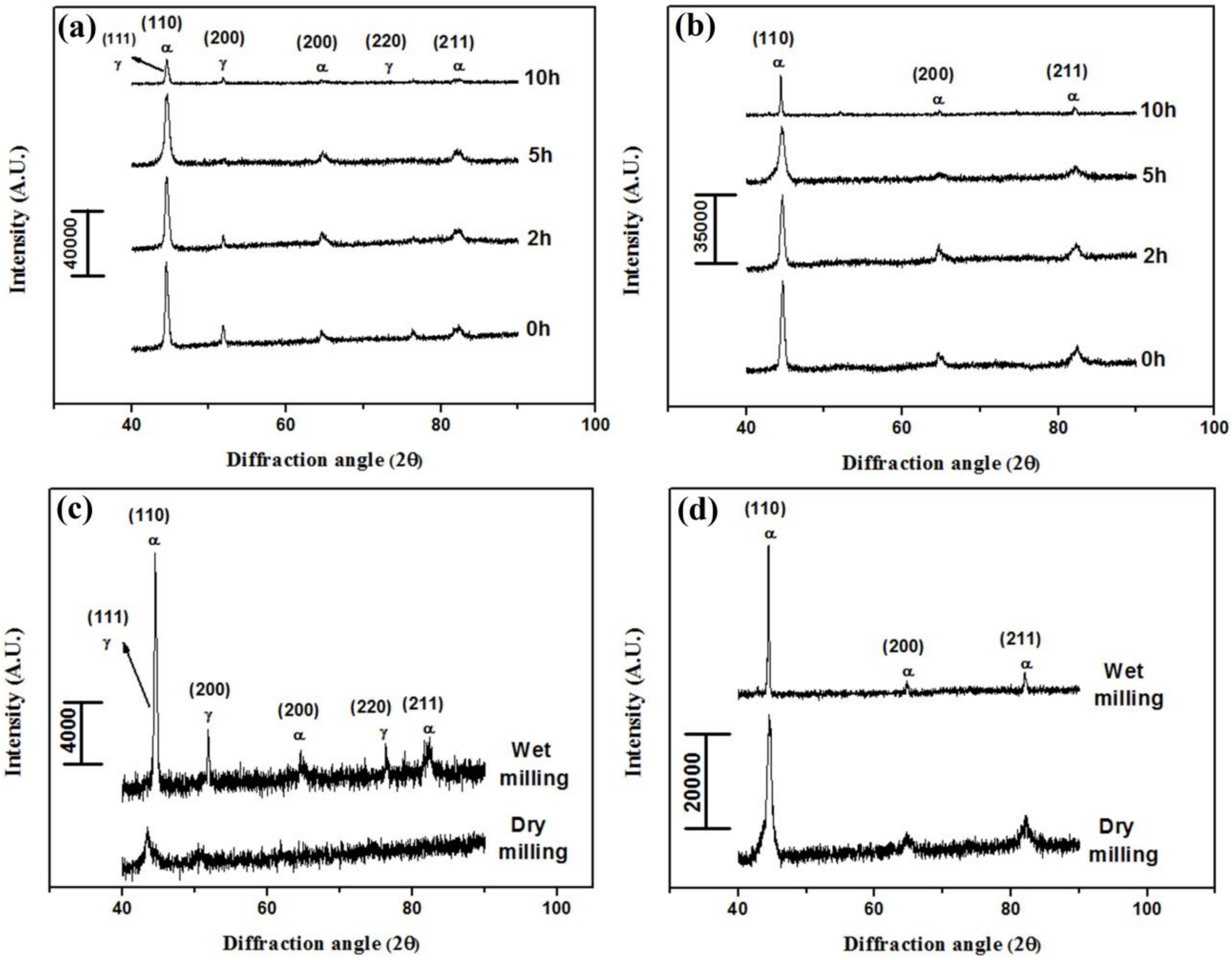

Figure 4.2.19 XRD spectra of 0 to 10h dry milled (a) Duplex stainless steel (b) Ferritic stainless in argon atmosphere; Comparison of 10h milled (c) Duplex stainless steel (d) Ferritic stainless steel by wet and dry milling

4.2.2.4.1 (a) Lattice parameter calculation

Nelson-Riley method of extrapolation method was used to calculate true lattice parameter of 10 hours dry milled duplex and ferritic stainless steel samples. Figure 4.2.20 (a) and 4.2.20 (b) show true lattice parameter of duplex and ferritic stainless steel samples milled in argon and toluene atmospheres respectively. In wet milling there is a hindrance of balls and powder collisions by toluene but this type of hindrance is absent in dry milling. This increases the impact energy of collision during dry milling. Hence, the amount of defects formed during dry milling is more than the defects formed during wet milling. Therefore, lattice parameter value of dry milled duplex and ferritic stainless steel is more compared with wet milled samples. True lattice parameter value of austenite present in duplex and pure ferritic stainless steel powder milled at argon atmosphere is 3.471Å and 2.875Å respectively and that of toluene atmosphere is 3.43Å and 2.870Å respectively.

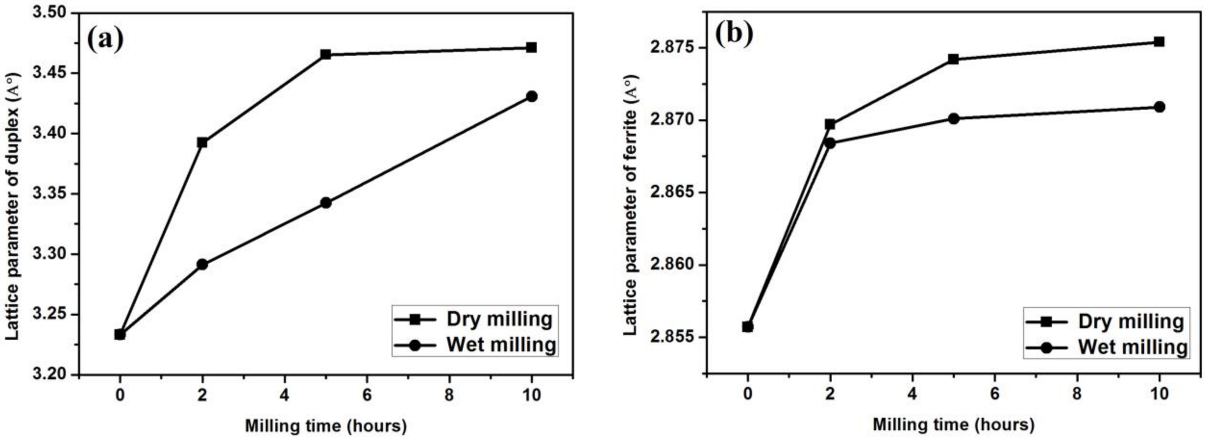

Figure 4.2.20 Graphical representation showing the effect of milling atmosphere on the lattice parameter (calculated from Nelson-Riley extrapolation method) of (a) Duplex stainless steel (b) Ferritic stainless steel during dry milling (argon) and wet milling (toluene) respectively

4.2.2.4.1 (b) Crystallite size and lattice strain calculation

Crystallite size and lattice strain of duplex and ferritic stainless steel powder samples were calculated by using Williamson-Hall equation. Figure 4.2.21 (a) and 4.2.21 (b) represents the crystallite size and lattice strain of duplex and ferritic stainless steel powder milled in argon and toluene atmospheres respectively. From the figure it is clear that crystallite size of dry milled duplex and ferritic stainless steel is less compared to wet milled stainless steel samples. Similarly, lattice strain of both the stainless steel is more during dry milling than wet milling. This is because dry milling involves high impact energy, results in more dislocations and hence high lattice strain. The impact energy generated during dry milling is more compared with the impact energy generated during wet milling. The crystallite size and strain of duplex stainless steel milled in argon atmosphere is 6nm and $21.8X10^{-3}$ and in toluene atmosphere is 7nm and $9.98X10^{-3}$ respectively. Similarly, dry milled ferritic stainless steel has crystallite size of 8nm and lattice stain of $30X10^{-3}$ and wet milled ferritic stainless steel has crystallite size of 10nm and lattice strain of $9.47X10^{-3}$ respectively.

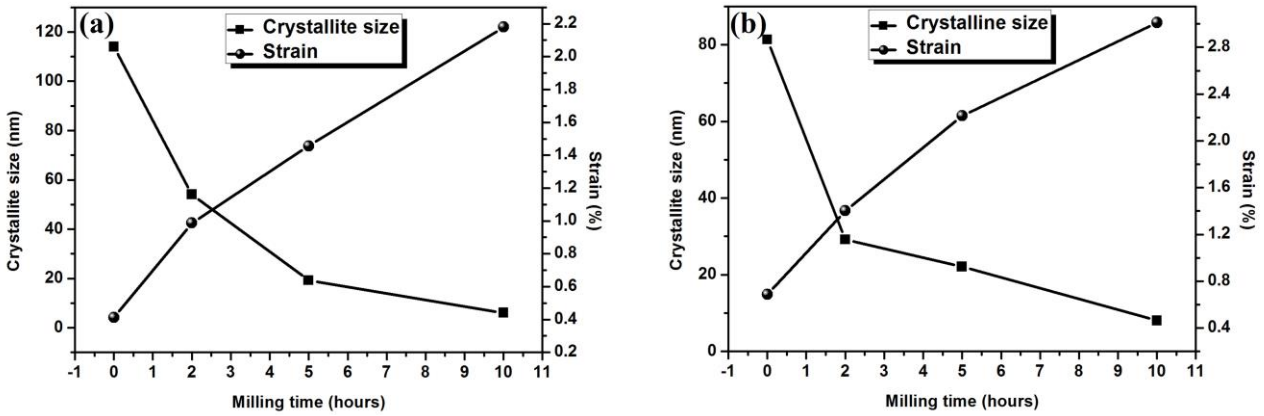

Figure 4.2.21 Graphical representation showing the variation of crystallite size and strain (Calculated from Williamson-Hall method) with milling time of (a) Duplex stainless steel (b) Ferritic stainless steel milled at argon atmosphere

4.2.2.4.2 Scanning electron microscopy (SEM)

Figure 4.2.22 (a-d) and 4.2.22 (f-i) represent the SEM micrographs of 0, 2, 5 and 10h milled duplex and ferritic stainless steel powders under argon atmosphere. Figure 4.2.22 (e) and 4.2.22 (j) show the micrograph of duplex and ferritic stainless steel milled for 10h in toluene atmosphere.

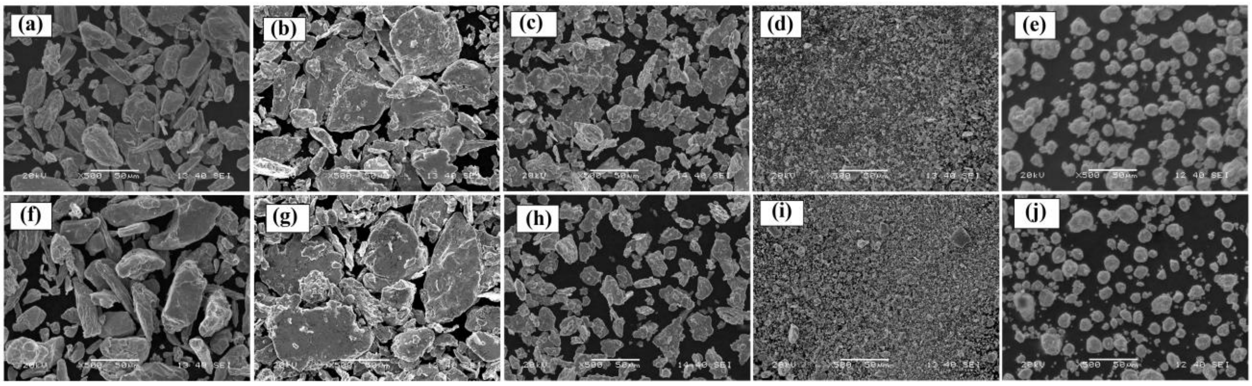

Figure 4.2.22 SEM images of duplex stainless steel powders milled for (a) 0h (b) 2h (c) 5h (d) 10h at argon atmosphere, and (e) 10h at toluene atmosphere. SEM images of ferritic stainless steel powder milled for (f) 0h (g) 2h (h) 5h (i) 10h at argon atmosphere, and (j) 10h at toluene atmosphere

From SEM figures it is evident that stainless steel milled in argon (dry milling) atmosphere shows lesser particle size compared to stainless steel powders milled in toluene (wet milling) atmosphere. In wet milling, the balls and powder collisions had been hindered by toluene due to its viscous nature when compared to argon gas. As results of which the milling at argon atmosphere increases the free movement of balls and impact energy of collision. This in turn increases the rapid cold welding, work hardening and fine fragmentation of stainless steel particles readily at less time.

4.2.2.4.3 Particle size analysis

Figure 4.2.23 (a) and 4.2.23 (b) depict the particle size distribution of 0 to 10h milled duplex and ferritic stainless steel powder samples in argon atmosphere and 10h milled stainless steel samples in toluene atmosphere. From the figure it is confirmed that both the types of stainless steel powders during dry milling show extremely lesser particle size than wet milled powder samples. The median particle size of 10h dry milled duplex and ferritic stainless steel samples are found to be 3 and 2μm respectively, whereas the median size is 20 and 16μm during wet milling.

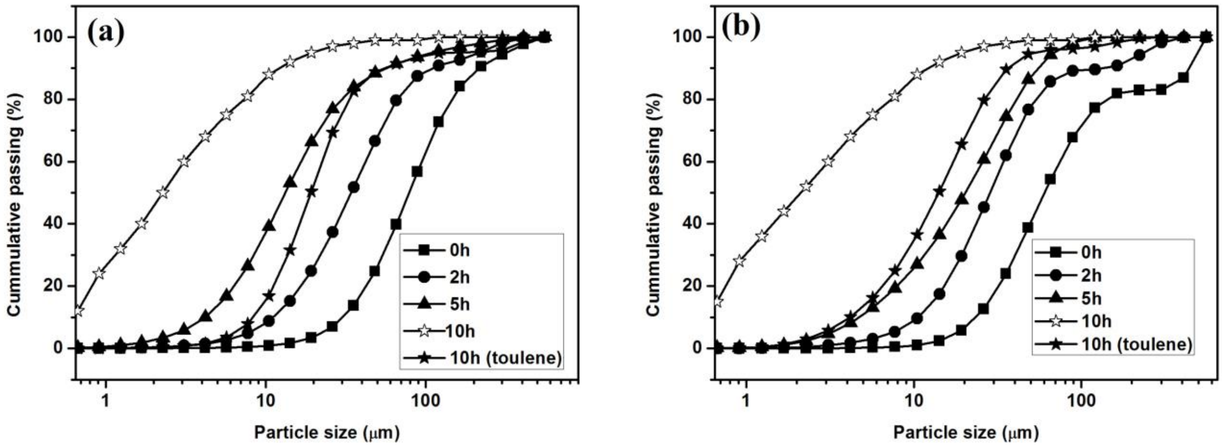

Figure 4.2.23 Particle size analysis of 0 to 10h milled (a) Duplex stainless steel (b) Ferritic stainless steel during dry milling and 10h wet milled samples

4.2.3 Summary and conclusions

Nano-structured duplex and ferritic stainless steel powders were prepared by DDPM after 10h of milling. Particle size of both the stainless steel particles becomes less when milled in presence of SA and shape of the powders is irregular as compared to stainless steel powder milled in the absence of SA. Milling of stainless steel samples carried out at 12:1 BPR shows reduced particle size as well as low crystallite size and higher lattice strain compared to 6:1 BPR milling conditions. XRD spectrum of duplex stainless steel milled at 12:1 BPR show rapid phase transformation from α-Fe to γ-Fe than 6:1 due to the high impact energy, increased defects and frequent collision of ball-powder-jar. Milling at 75% CS is found to be more efficient in refining the particle and crystallite size of both the stainless steel samples compared to milling carried out at 64% CS. The shape of the stainless steel powders milled at

75%CS is more regular and spherical than the stainless steel milled at 64% CS mill speed due to the increased defects and acceleration field of the mill at higher mill speed. We successfully studied the phase transformation, particle size and morphology at different milling parameters and concluded that all these parameters have great influence in refining and improvement in powder quality. Dry milled stainless steel shows lesser particle size than wet milled samples.

References

1) X.J. Liu, Z.Z. Xu, H. Xiao, D.K. Park, K.W. Kim, Y.C. Kim, S.H. Yeon, I.S. Ahn, The effect of process control agents and ball to powder rations on the electrochemical characteristics of mechanically alloyed SnS_2 anode materials, *Powder. Technol.* 259 **(2014)** 117–124.

2) Abhishek Pandey, K. Jayasankar, P. Parida, M. Debata, B.K. Mishra, S. Saroja, Optimization of milling parameters, processing and characterization of nano-crystalline oxide dispersion strengthened ferritic steel, *Powder. Technol.* 262 **(2014)** 162–169.

3) R. Rahmanifard, H. Farhangi, A.J. Novinrooz, Optimization of mechanical alloying parameters in 12YWT ferritic steel Nanocomposite, *Mater. Sci. Eng. A.* 527 **(2010)** 6853–6857.

4) I. Ismail, M. Hashim, K. A. Matori, R. Alias, J. Hassan, Milling time and BPR dependence on permeability and losses of $Ni0.5Zn0.5Fe_2O_4$ synthesized via mechanical alloying process, *J. Mag. Mater.* 323 **(2011)** 1470–1476.

5) T. Mandal, B.K. Mishra, A. Garg, D. Chaira, Optimization of milling parameters for the mechanosynthesis of nanocrystalline hydroxyapatite, *Powder. Technol.* 253 **(2014)** 650–656.

6) Q. Meng, N. Zhou, Y. Rong, S. Chen, T.Y. Hsu, Xu Zuyao, Size effect on the Fe nanocrystalline phase transformation, *Acta. Mater.* 50 **(2002)** 4563–4570.

7) R. Shashanka, D. Chaira, Optimization of milling parameters for the synthesis of nano-structured duplex and ferritic stainless steel powders by high energy planetary milling, *Powder. Technol.* 278 **(2015)** 35-45.

4.3 Fabrication of nano-Y_2O_3 dispersed and Y_2O_3 free duplex and ferritic stainless steel by conventional and spark plasma sintering methods

4.3.1 Objectives and scope of the work

Our aim is to study microstructural evolution, mechanical properties and phase transformation of yittria dispersed and yittria free duplex and ferritic stainless steel fabricated by conventional sintering and SPS methods. Microstructure, density and hardness values of all the stainless steel samples fabricated by SPS and conventional sintering methods at 1000°C were compared. The effect of sintering temperature and atmosphere on phase transformation, microstructure and mechanical properties were evaluated during conventional sintering. The effect of nano yittria addition was also studied successfully.

4.3.2 Fabrication of stainless steel

Planetary milled duplex and ferritic stainless steels powders were mixed separately with 1wt. % nano-Y_2O_3 powder particles (average size <100 nm) in a turbula shaker mixer for 3 hours. Yittria dispersed and yittria free duplex and ferritic stainless steel powder samples were consolidated by both conventional and SPS methods. All the stainless steel samples were compacted using hydraulic press at 700MPa and polyvinyl alcohol as binder. Compacted stainless steel samples were conventionally sintered at 1000, 1200 and 1400°C respectively in a tubular furnace with holding time of 1h each at argon atmosphere to study effect of temperature. In a separate set of experiments, conventional sintering was carried out at 1000°C in nitrogen atmosphere for 1h to study effect of sintering atmosphere. Spark plasma sintering was carried out at a pressure of 50MPa and 1000°C temperature in vacuum for 5 minutes in a 20mm diameter graphite die (SCM 1050, Sumitomo Coal Mining Co, Ltd Japan).

4.3.3 Conventional sintering

4.3.3.1 Effect of sintering temperature

4.3.3.1.1 Phase analysis by XRD

The XRD spectra of duplex and ferritic stainless steel samples sintered at 1000, 1200 and 1400°C is shown in Figure 4.3.1 (a) & 4.3.1 (b) respectively. XRD spectra of conventionally consolidated duplex and ferritic stainless steel samples show sharp and crystalline diffraction peaks of ferrite and austenite phases. The sharpness and crystallinity of diffraction peaks increases with increase in sintering temperature from 1000 to 1400°C. During milling, the stainless steel powder has undergone many transformations like structural defects; amorphization; reduction in crystallite size and increase in volume fraction of grain boundaries. This increases the number of defect storage sites, shorter diffusion paths and attains non-equilibrium state as reported by Gojic et al. [1]. But during sintering of stainless steel, the powder particles diffuse and rearrange themselves in a regular manner and this increases the crystallinity of stainless steel. The rate of diffusion, grain growth and the atomic periodicity increases with increasing sintering temperature. Figure 4.3.1 (c) and 4.3.1 (d) depict the XRD spectra of conventionally consolidated yittria dispersed duplex and ferritic stainless steel samples at 1000, 1200 and 1400°C respectively.

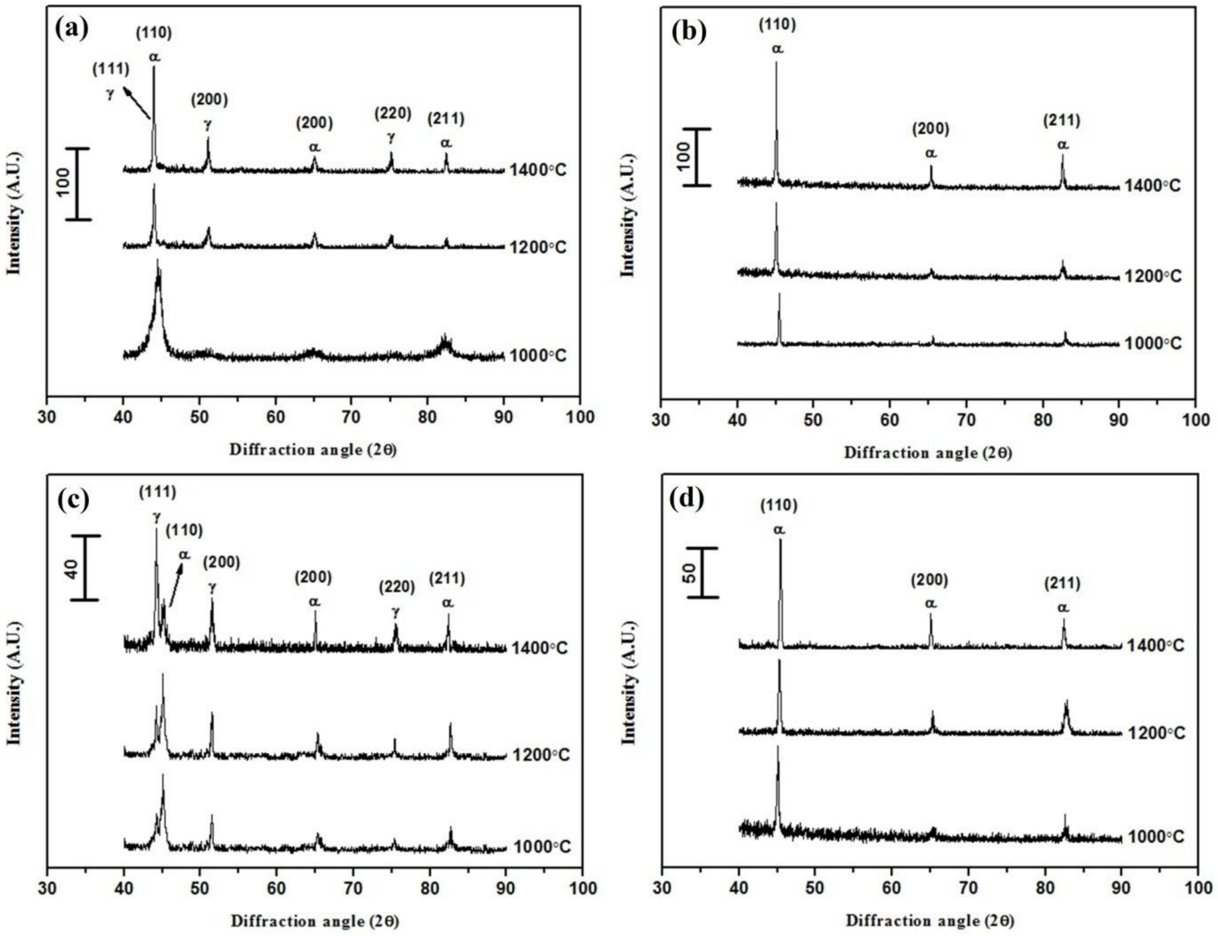

Figure 4.3.1 XRD spectra of (a) Duplex (b) Ferritic stainless steel (c) Yittria dispersed duplex (d) Yittria dispersed ferritic stainless steel samples sintered at 1000, 1200 and 1400°C in argon atmosphere

Both the stainless steel samples show high intense, sharp crystalline diffraction peaks as shown in the figures. Yittria dispersed duplex stainless steel shows phase transformation from α-Fe to γ-Fe during sintering and results in more dominant austenite phase at higher temperature. Figure 4.3.1 (c) clearly shows the phase transformation of α-Fe to γ-Fe by resolving both austenite and ferrite peaks at 1000°C. The intensity and percentage volume of austenite phase increases with increase in sintering temperature. At 1400°C, the austenite peak become more dominant than ferrite peak in case of yittria dispersed duplex stainless steel. Yittria dispersed duplex stainless steel shows more intense and predominant austenite peaks than yittria free duplex stainless steel where phase transformation is limited even at higher temperature. The phase transformation is due to the dispersion of Y_2O_3 in stainless steel but mechanism of Y_2O_3 during phase transformation is still unknown. The phase transformation may be due to the diffusion of yittria atoms in to the smaller interstitial sites of ferrite crystallites and a form mismatch strains and thus initiates phase transformation. The refinement of ferrite crystallite to nano level can also initiate phase transformation. Both the XRD spectra show no sigma phases, carbides or nitride precipitations of secondary phases.

4.3.3.1.2 Microstructure and phase analysis

Figure 4.3.2 depicts the FESEM image of as received Y_2O_3 nanoparticles. The yittria nanoparticles are regular and spherical shape with average particle size of around 40nm.

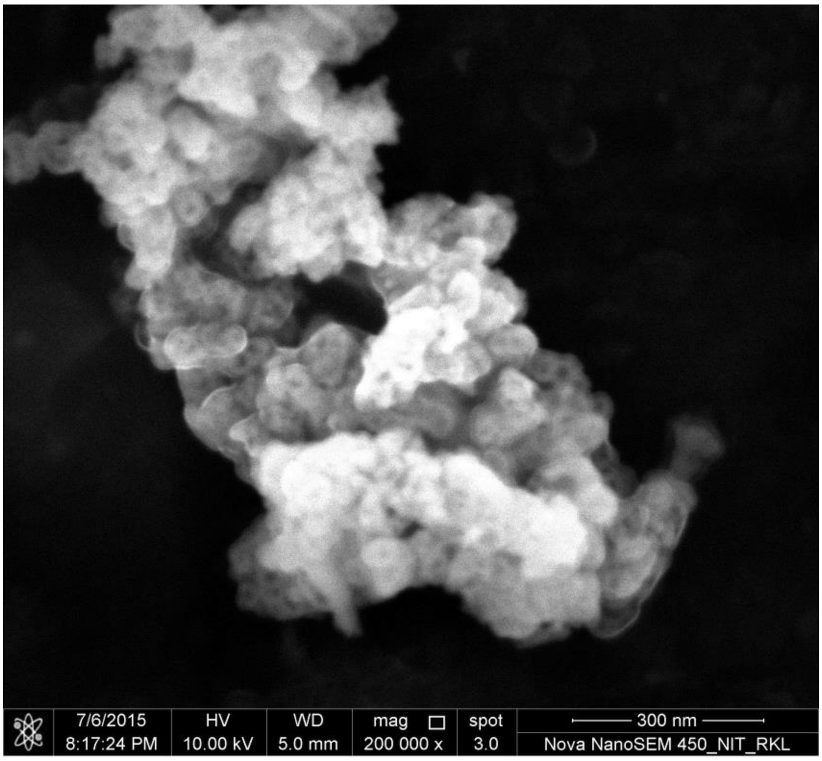

Figure 4.3.2 FESEM microstructure of as received Y_2O_3 nanoparticles

Figure 4.3.3 (a) and 4.3.3 (b) show the optical micrographs of duplex and ferritic stainless steel samples consolidated at 1000, 1200 and 1400°C respectively.

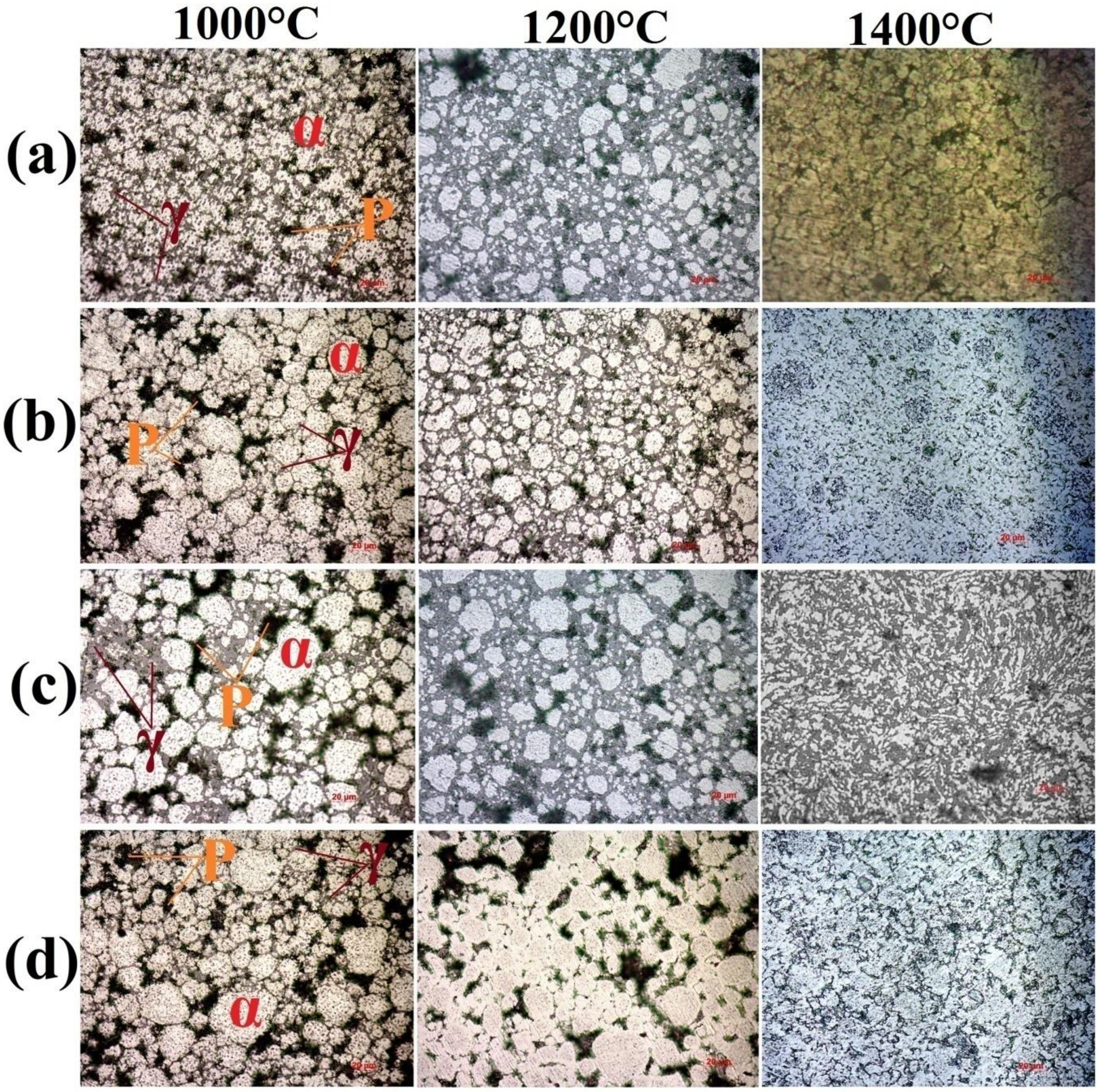

Figure 4.3.3 Optical microstructure of (a) Duplex (b) Ferritic stainless steel (c) Yittria dispersed duplex (d) Yittria dispersed ferritic stainless steel samples sintered at 1000, 1200 and 1400°C in argon atmosphere (P- Pores)

From the microstructures it is observed that, number of pores decreases and density increases with increase in sintering temperature from 1000 to 1400°C. This is due to the release of strain, decrease in defect storage sites, grain growth and increase in crystallinity due to the diffusion of atoms to form a regular cubic geometry. At 1400°C, material dissolution takes place primarily at the interior of both the stainless steel samples. At 1400°C, the part of the very fine stainless steel powders melts and forms pendular bonds at their particle contacts due to the weak and semi-solid bonding between the particles. German [2] reported that, the low viscous liquid flows freely through capillary action and results in rapid viscous flow during sintering. Therefore, stainless steel sintered at 1400°C exhibits low porosity ratio, high density and maximum hardness. Figure 4.3.3 (c) and 4.3.3 (d) represents the optical micrographs of yittria dispersed duplex and ferritic stainless steel samples sintered at 1000, 1200 and 1400°C respectively. Increase in sintering temperature from 1000 to 1400°C decreases the number of pores and increases the density as well as austenite phase in both the stainless steels as shown in Figure 4.3.3. XRD spectra of Figure 4.3.1 (c) and 4.3.1 (d) also prove that increase in sintering temperature increases the austenite phase. Therefore, we have carried out an investigation to study the extent of volume fraction of ferrite and austenite phase in both yittria dispersed and yittria free stainless steel. The volume fractions of both ferrite and austenite phases were calculated by Axio Vision Release software. It is concluded that the amount of austenite phase increases with increase in sintering temperature from 1000 to 1400°C due to the phase transformation of ferrite to austenite at higher temperatures. Amount of austenite phase increases from 51 to 65 volume fractions during sintering from 1000 to 1400°C in case of duplex and from 57 to 72 volume fractions in case of yittria dispersed duplex stainless steel. Similarly, austenite phase increases from 33 to 58 volume fractions in ferritic stainless steel and from 41 to 62 volume fractions in yittria dispersed ferritic stainless steel during sintering from 1000 to 1400°C. In the micrographs, ferrite (α-white), austenite (γ-grey) and pores (P-black) are shown.

4.3.3.1.3 Density and hardness study

Figure 4.3.4 (a) represents the effect of sintering temperature on the densities of duplex, ferritic, yittria dispersed duplex and yittria dispersed ferritic stainless steel samples respectively. Density of all the four stainless steel samples increases with increase in sintering temperature from 1000 to 1400°C. At higher temperature, the rate of diffusion is more effective and the atoms rearrange themselves in a very dense pattern. A maximum density of more than 94% is achieved for both yittria dispersed duplex and ferritic stainless steel samples sintered at 1400°C. This is due to the accommodation of yittria nanoparticles in the interstices of micron sized stainless steel particles. Jain et al. [3] reported that, the added yittria nanoparticles have a tendency to increase the propensity for grain boundary added diffusion. They also reported that, the addition of more percentage of yittria nanoparticles increases the possibility of yittria-yittria interaction rather than yittria-stainless steel interaction and agglomerates at grain boundaries and decreases the strength of stainless steel. Optical microstructure of all the stainless steel samples confirm that increase in sintering temperature decreases the number of pores and increases the density. Density of duplex and ferritic stainless steel varies from 71 to 91% and from 73 to 93% respectively at sintering temperature of 1000 to 1400°C. Similarly, density of yittria dispersed duplex and ferritic stainless steel varies from 78 to 94% and from 80 to 96% respectively.

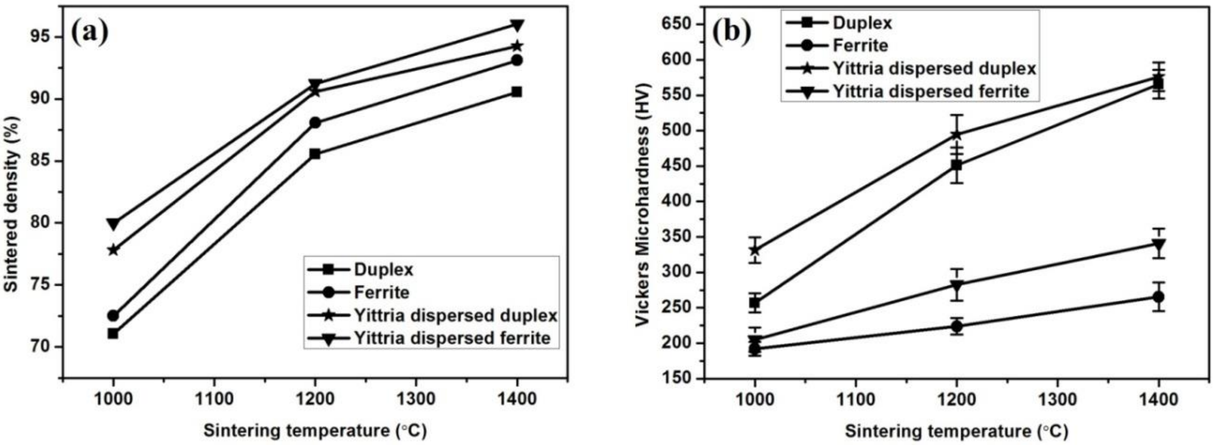

Figure 4.3.4 Graph of (a) Sintered density (b) Vickers microhardness of stainless steel samples sintered at 1000, 1200 and 1400°C in argon atmosphere

Figure 4.3.4 (b) represents the microhardness values of yittria dispersed and yittria free stainless steel samples measured at 25gf indentation load. At higher sintering temperature, density increases due to the less number of voids and hence harder is the material. Yittria dispersed duplex and ferritic stainless steel samples show more hardness values than yittria free duplex and ferritic stainless steels respectively. Addition of yittria in stainless steel increases the bonding strength, density and hinders grain growth. Finally, yittria dispersed stainless steel exhibits higher hardness than yittria free stainless steel. The Vickers microhardness values of duplex and ferritic stainless steel changes from 257 to 567HV and 192 to 265HV respectively for variation of sintering temperature from 1000 to 1400°C. Similarly, yittria dispersed duplex and ferritic stainless steel show change in hardness values from 332 to 576HV and 205 to 341HV respectively.

Figure 4.3.5 (a), 4.3.5 (b), 4.3.5 (c) and 4.3.5 (d) shows the effect of indentation load on microhardness of duplex, ferritic, yittria dispersed duplex and ferritic stainless steel samples sintered at 1000, 1200 and 1400°C respectively. The Vickers microhardness measurements of all the stainless steel samples were carried out at three different loads of 10, 25 and 50gf with a dwell time of 10 seconds. For each stainless steel sample, at least 5 trials of indentation were made and the average values of the diagonal lengths of indentation marks were measured as hardness. From the Figure 4.3.5 (a) to 4.3.5 (d) it is observed that hardness values of respective stainless steel samples decreases with increase in applied indentation load. This is due to the indentation size effect (ISE) and it occurs due to the surface effect; strain gradient effect based on mass transport by point defects.

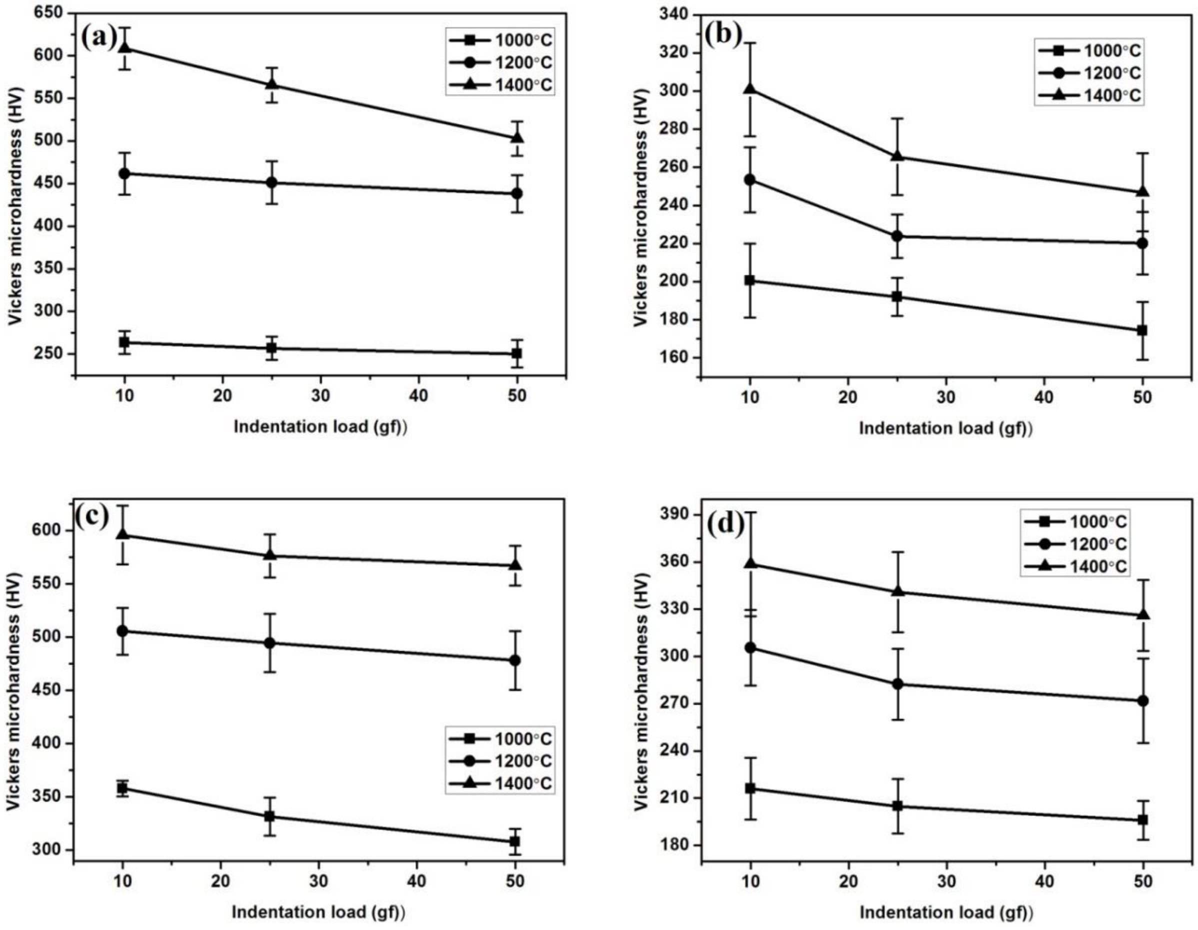

Figure 4.3.5 Effect of indentation load (10, 25 and 50gf) on Vickers microhardness of (a) Duplex (b) Ferritic stainless steel (c) Yittria dispersed duplex (d) Yittria dispersed ferritic stainless steel samples sintered at 1000, 1200 and 1400°C in argon atmosphere

4.3.3.1.4 Compressive strength study

Figure 4.3.6 shows the compressive stress-strain curves of yittria dispersed and yittria free duplex and ferritic stainless steel samples sintered at 1000°C. Yittria dispersed stainless steel shows maximum resistance to deformation than yittria free stainless steel as shown in the figure. As we know that, yittria dispersed stainless steel exhibits maximum density and hardness values and hence more stress is required to deform them. Pasebani et al. [4] reported that, addition of yittria increases strengthening, inhibits dislocation motion, increases the deformation resistance, controls the recovery and re-crystallization process, inhibits the grain growth and thus increases the grain boundary strengthening. As a result of which yittria dispersed stainless steel sintered at 1000°C shows maximum compressive strength than yittria free stainless steels.

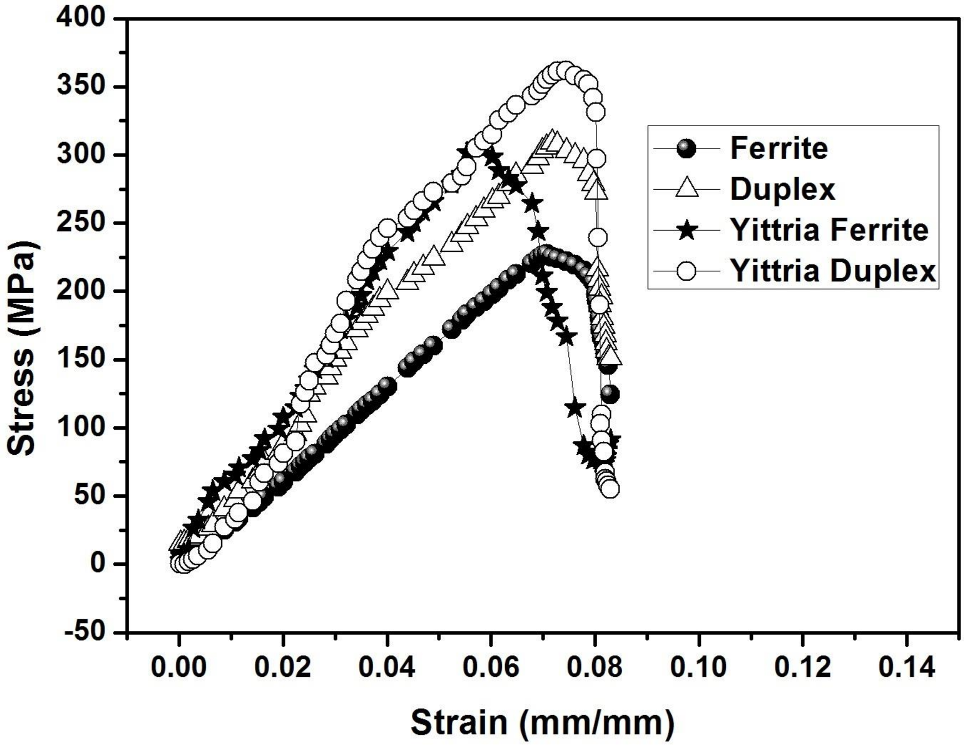

Figure 4.3.6 Compressive stress–strain curves of the yittria dispersed and yittria free duplex and ferritic stainless steel samples sintered at 1000°C in argon atmosphere

Yittria dispersed duplex and ferritic stainless steels exhibit the maximum compressive stress of 360MPa and 308MPa respectively. Whereas yittria free duplex and ferritic stainless steel possess maximum yield stress of 312MPa and 225MPa respectively. The values of volume fractions, density, hardness and compressive strength of austenite and ferrite phases of yittria dispersed and yittria free stainless steel samples sintered in argon atmosphere are tabulated in Table 4.2.

Table 4.2 Volume fractions, density and hardness of austenite and ferrite phases of stainless steel samples sintered in argon atmosphere at different sintering temperature

Sample	**Sintering temperature (°C)**	**Volume fraction (%)**		**Theoretical density (g/cc)**	**Sintered density (%)**	**Vickers microhardness (HV)**	**Compressive strength (MPa)**
		Austenite	**Ferrite**				
Duplex stainless steel	1000	51	49	7.84	71.05	257	312
	1200	62	38		85.55	451	-
	1400	65	35		90.56	567	-
Ferritic stainless steel	1000	33	67	7.75	72.5	192	225
	1200	44	56		88.08	224	-
	1400	58	42		93.12	265	-
Yittria duplex stainless steel	1000	57	43	7.80	77.81	332	360
	1200	65	35		90.6	495	-
	1400	72	27		94.28	576	-
Yittria ferritic stainless steel	1000	41	58	7.70	79.99	205	308
	1200	52	48		91.23	282	-
	1400	62	38		96.05	341	-

4.3.3.2 Effect of sintering atmosphere

4.3.3.2.1 Phase analysis by XRD

Figure 4.3.7 (a) and 4.3.7 (b) represent the XRD spectra of duplex and ferritic stainless steel samples sintered conventionally at 1000°C in nitrogen atmosphere. Both the stainless steels show sharp and crystalline diffraction peaks due to the diffusion and rearrangement of atoms. From the XRD graphs it is confirmed that austenite peaks are more dominant in duplex and ferrite peaks in ferritic stainless steel along with austenite and traces of iron nitride phases. Ferritic stainless steel sintered in nitrogen atmosphere shows α-Fe to γ-Fe phase transformation but phase transformation is absent in ferritic stainless steel sintered at argon atmosphere. It is widely accepted that nitrogen favours the α-Fe to γ-Fe phase transformation and therefore sintering atmosphere plays an important role in phase transformation. Limited amount of austenite phase forms during milling, hence sintering of stainless steel compacts can promote α-Fe to γ-Fe. Austenite has large interstitial sites and smaller interfacial energy whereas ferrite has smaller interstitial sites and larger interfacial energy. During sintering in nitrogen atmosphere, N_2 atoms diffuse in to the larger interstitial sites of austenite and form very less distortion and volume mismatch. But in case of ferrite, N_2 atoms diffuse in to the interstitial sites and create mismatch strains. Presence of alloying elements like Cr and Ni in ferritic stainless steel increases the solubility of N_2 atoms in Fe lattice. Ferritic stainless steel contains alloying elements like Cr and Ni and they increase the solubility of nitrogen atoms in Fe lattice. During milling, many processes like introduction of structural defects, distortion of crystallite lattice and refinement in grain size, fracturing and cold welding of powder particles take place. This results in maximum defect storage sites and shorter diffusion path. Therefore, during sintering N_2 atoms can easily diffuses in to Fe lattice through shorter diffusion paths and piled in defect storage sites.

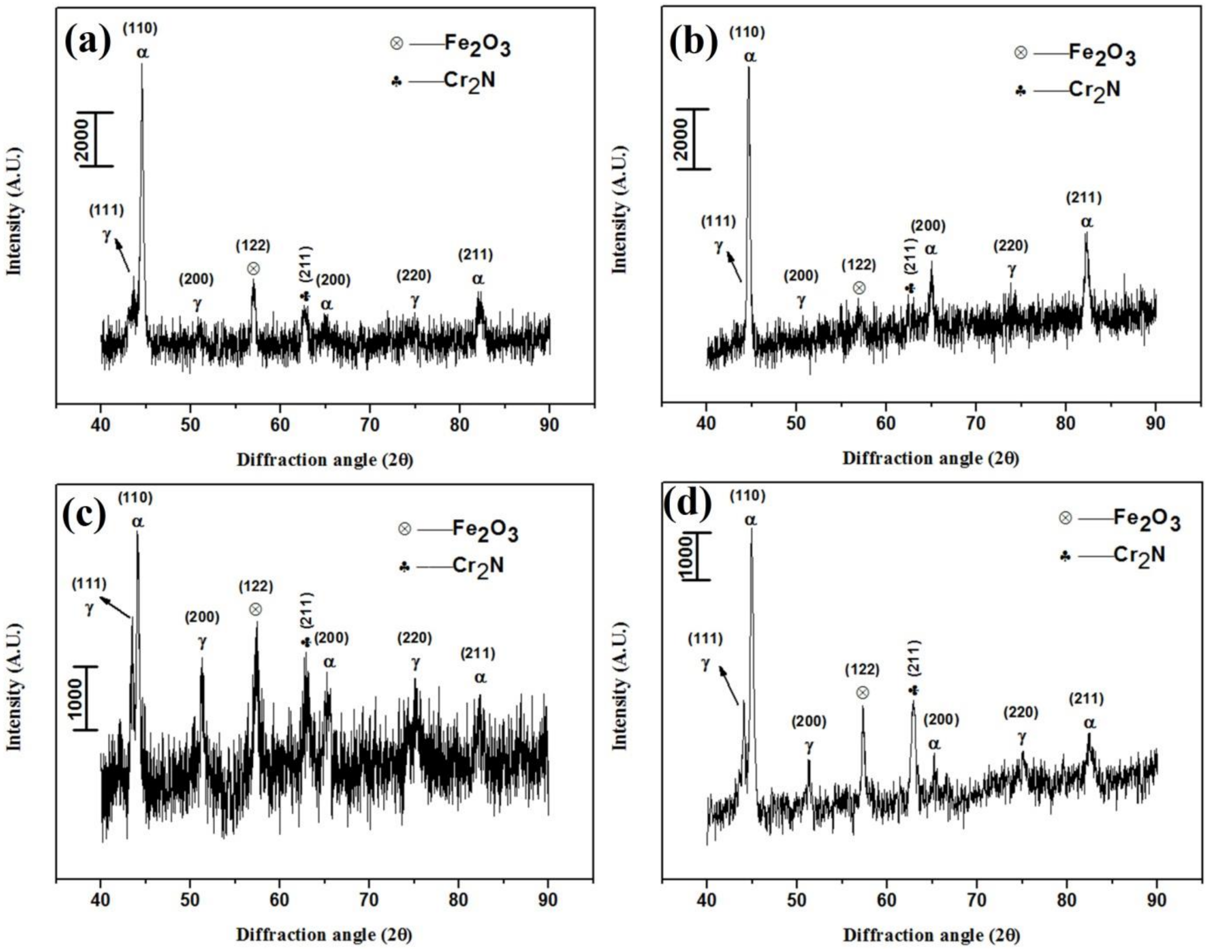

Figure 4.3.7 XRD spectra of (a) Duplex (b) Ferritic stainless steel (c) Yittria dispersed duplex (d) Yittria dispersed ferritic stainless steel samples sintered at 1000°C in nitrogen atmosphere

Tehrani et al. [5] reported that, the increased ratio of lattice strain and grain size increases the preferable lattice storage sites for nitrogen absorption and thereby enhances the α-Fe to γ-Fe phase transformation. All the above explanations provide evidence that nitrogen acts as austenitic stabilizer. Figure 4.3.7 (c) and 4.3.7 (d) depict the XRD spectra of yittria dispersed duplex and ferritic stainless steel samples conventionally sintered at 1000°C in nitrogen atmosphere. Yittria dispersed ferritic stainless steel shows phase transformation from α-Fe to γ-Fe in presence of nitrogen atmosphere. But phase transformation is absent in case of yittria dispersed ferritic stainless steel sintered in argon atmosphere at 1000°C. XRD spectra of all the four stainless steel samples sintered at nitrogen atmosphere show secondary iron nitride phase, which enhances the hardness of the material.

4.3.3.2.2 Microstructure and phase analysis

Optical micrographs of yittria dispersed and yittria free duplex and ferritic stainless steel samples consolidated at 1000°C in nitrogen atmosphere are shown in Figure 4.3.8 (a), 4.3.8 (b), 4.3.8 (c) and 4.3.8 (d) respectively.

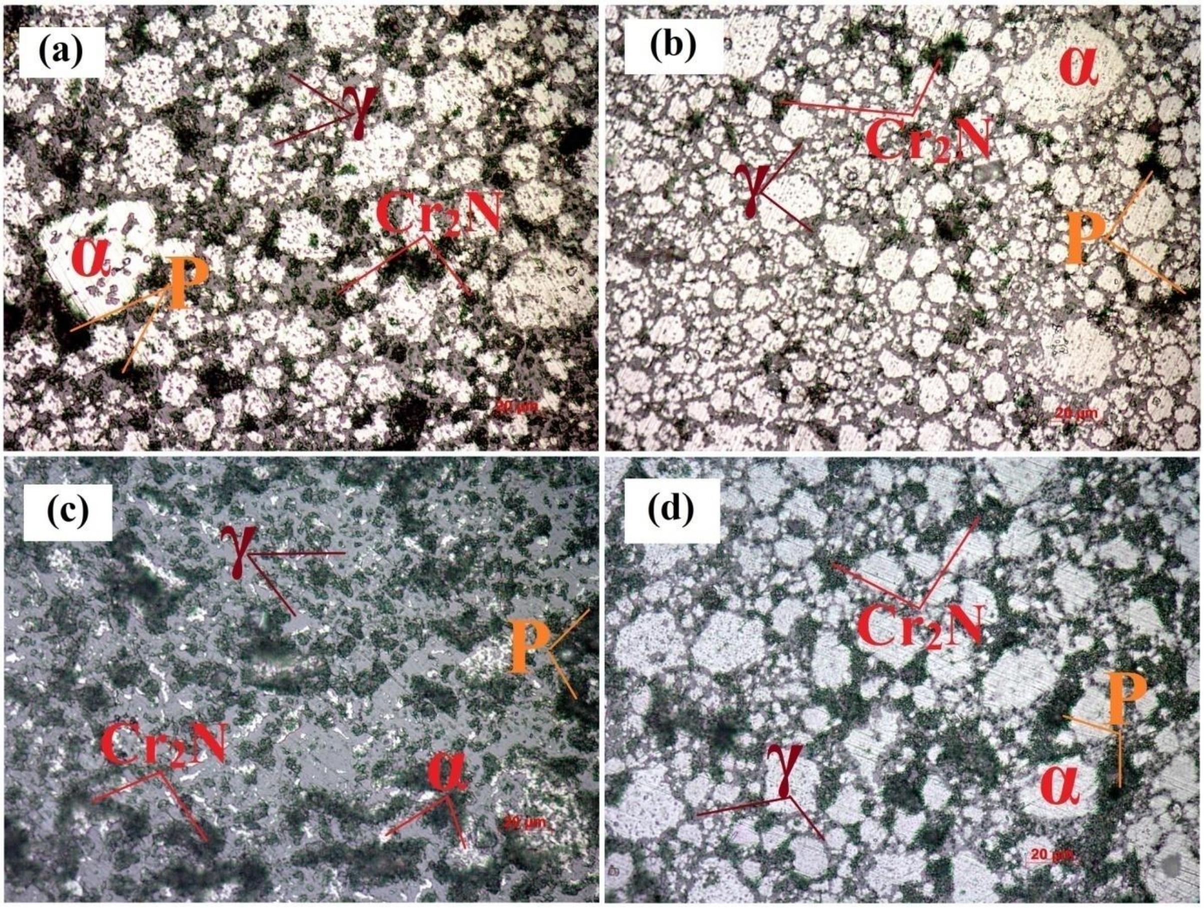

Figure 4.3.8 Optical microstructure of (a) Duplex (b) Ferritic stainless steel (c) Yittria dispersed duplex (d) Yittria dispersed ferritic stainless steel samples sintered at 1000°C in nitrogen atmosphere (P- Pores)

All the microstructures show a low porosity ratio which improves the mechanical properties significantly. Whereas stainless steel samples sintered at 1000°C in argon atmosphere possess a high ratio of porosity with irregular shapes. Stainless steel samples sintered in nitrogen atmosphere forms secondary phase like chromium nitrides at grain boundaries of Fe matrix as shown in the micrographs and forms tri-phase structure. But secondary phases are absent in stainless steel samples sintered in argon atmosphere at 1000°C and it shows only bi-phase structure. Presence of chromium nitride and phase transformation from α-Fe to γ-Fe has been confirmed by XRD spectra. As we have discussed earlier, nitrogen acts as austenitic stabilizer, therefore stainless steel samples sintered in nitrogen atmosphere show more volume fraction of austenite than the stainless steel sintered in argon atmosphere.

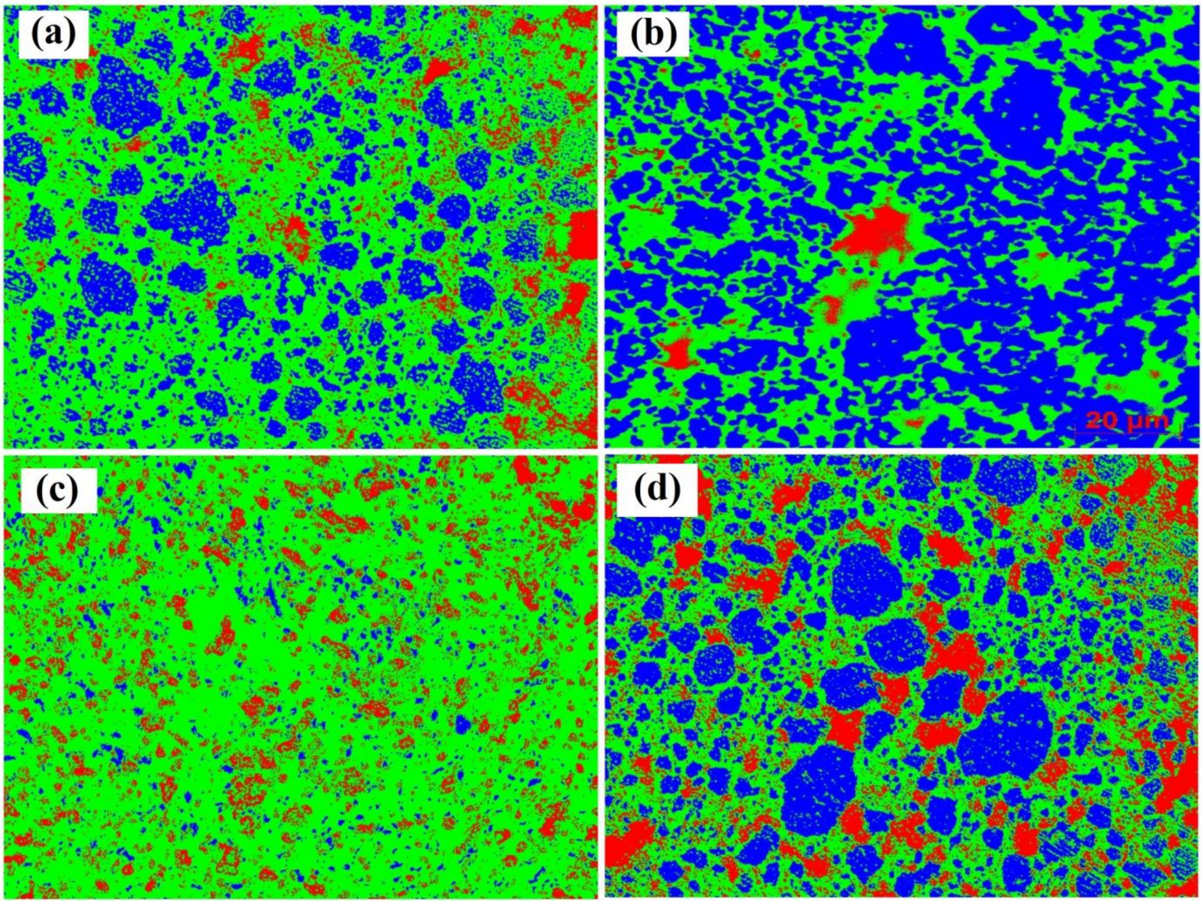

Figure 4.3.9 Phase analysis of (a) Duplex (b) Ferritic stainless steel (c) Yittria dispersed duplex (d) Yittria dispersed ferritic stainless steel samples sintered at 1000°C in nitrogen atmosphere (Ferrite-Blue, Austenite-Green, Chromium nitride-Red)

Figure 4.3.9 (a), 4.3.9 (b), 4.3.9 (c) and 4.3.9 (d) represent the volume fraction analysis of yittria free and yittria dispersed duplex and ferritic stainless steel respectively. In the micrographs, ferrite (Blue), austenite (Green) and chromium nitride (Red) are shown. Duplex and ferritic stainless steel sintered at nitrogen atmosphere show 63 and 40 volume fraction of austenite phase, whereas the same stainless steel sintered at argon atmosphere show 51 and 33 volume fraction of austenite phase respectively. Yittria dispersed duplex and ferritic stainless steel samples sintered at nitrogen atmosphere show 79 and 45 volume fraction of austenite phase. Similarly, yittria dispersed duplex and ferritic stainless steel sintered at argon atmosphere show 57 and 41 volume fraction of austenite phase respectively.

4.3.3.2.3 Density and hardness study

Figure 4.3.10 (a) represents the effect of sintering atmosphere on the densities of duplex, ferritic and yittria dispersed duplex and ferritic stainless steel samples respectively. Sintering was carried out in both argon and nitrogen atmospheres at 1000°C to study the effect of sintering atmosphere on density and hardness of yittria dispersed and yittria free stainless steel samples. It is found that conventional sintering carried out under nitrogen atmosphere results in higher values of density and hardness as compared to sintered at argon atmosphere. Kurgan [6] also reported similar kind of results. Duplex and ferritic stainless steel sintered in nitrogen atmosphere show 74 and 77% density respectively. Similarly, yittria dispersed duplex and ferritic stainless steel possess density of 80 and 82% respectively. From Figure 4.3.8 and Figure 4.3.8 it is found that secondary phase like Cr_2N is formed in all the stainless steel samples sintered under nitrogen atmosphere at 1000°C. Formation of secondary phase at grain boundaries improves the hardness, density and strength of the stainless steel significantly.

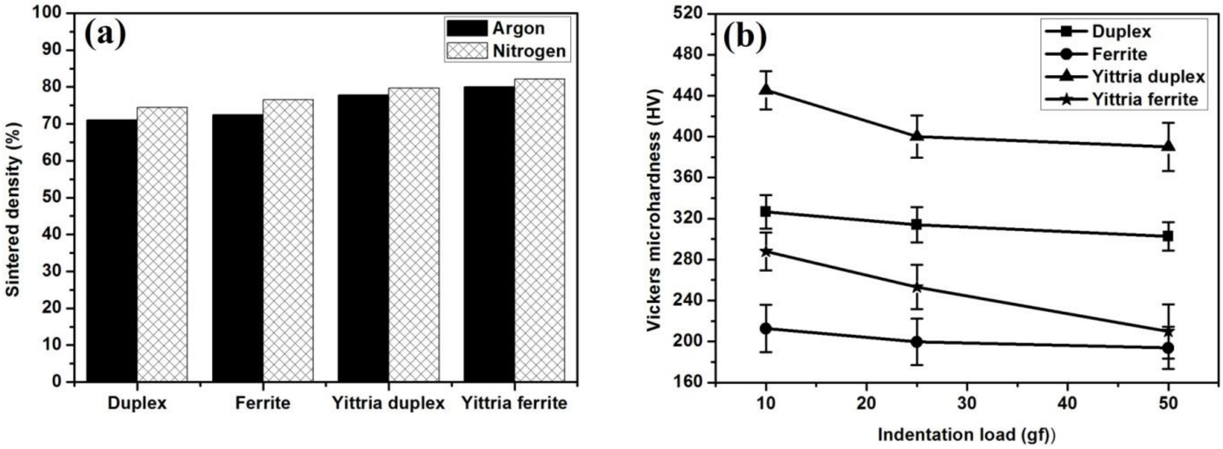

Figure 4.3.10 Graph of (a) Sintered density (Argon and Nitrogen) (b) Vickers microhardness of stainless steel samples sintered at 1000°C in nitrogen atmosphere

Figure 4.3.10 (b) represents the effect of indentation load on the microhardness of yittria dispersed and yittria free duplex and ferritic stainless steel sintered at 1000°C in nitrogen atmosphere. The Vickers microhardness measurements of stainless steel samples were carried out at 10, 25 and 50gf indentation load with a dwell time of 10 seconds. Figure 4.3.10 (b) shows the effect of indentation load on hardness and the hardness value decreases with increase in indentation load due to ISE. Addition of yittria nanoparticles in stainless steel enhances the bonding strength and therefore yittria dispersed stainless steel show more density and hardness values. The Vickers microhardness values of duplex and ferritic stainless steel sintered at nitrogen atmosphere are 314 and 200HV respectively. Similarly, yittria dispersed duplex and ferritic stainless steel show microhardness value of 400 and 253HV respectively. Whereas microhardness values of duplex and ferritic stainless steel sintered at argon atmosphere are 257 and 192HV respectively. Similarly, yittria dispersed duplex and ferritic stainless steel show microhardness value of 332 and 205HV respectively. This increased hardness in nitrogen atmosphere is due to the dissolution of nitrogen in to stainless steel samples during sintering. Presence of nitrogen not only increases solid solution strengthening but also increases grain size strengthening [7]. The values of volume fractions, density and hardness of austenite and ferrite phases of yittria dispersed and yittria free stainless steel samples sintered in nitrogen atmosphere are tabulated in Table 4.3.

Table 4.3 Volume fractions, density and hardness of austenite, ferrite and chromium nitride phases of yittria dispersed and yittria free stainless steel samples sintered in nitrogen atmosphere at 1000°C

Type of stainless steel	**Volume fraction (%)**			**Theoretical density (g/cc)**	**Sintered density (%)**	**Vickers microhardness (HV)**
	Austenite phase	**Ferrite phase**	**Cr_2N**			
Duplex stainless steel	63	28	8	7.84	74	314
Ferritic stainless steel	40	58	2	7.75	77	200
Yittria duplex stainless steel	79	7	13	7.80	80	400
Yittria ferritic stainless steel	45	35	18	7.70	82	253

4.3.4 Spark plasma sintering

4.3.4.1 Phase analysis by XRD

Figure 4.3.11 (a) and 4.3.11 (b) represent the XRD spectra of duplex, yittria dispersed duplex and ferritic, yittria dispersed ferritic stainless steel samples sintered at 1000°C by SPS method. From the Figure 4.3.11 (a) it is found that yittria dispersed duplex stainless steel shows maximum phase transformation from α-Fe to γ-Fe than duplex stainless steel. This is due to the dispersion of Y_2O_3 nanoparticles in to the smaller interstitial sites of ferrite crystallites and forms a mismatch strain and induces the phase transformation from α-Fe to γ-Fe. The refinement of ferrite crystallite to nano level can also initiate phase transformation. However, no difference in XRD spectra of ferritic and yittria dispersed ferritic stainless steel are visible from Figure 4.3.11 (b). There are no traces of secondary phases like sigma phase; carbides or nitrides precipitated diffraction peaks in all the stainless steel samples sintered by SPS method.

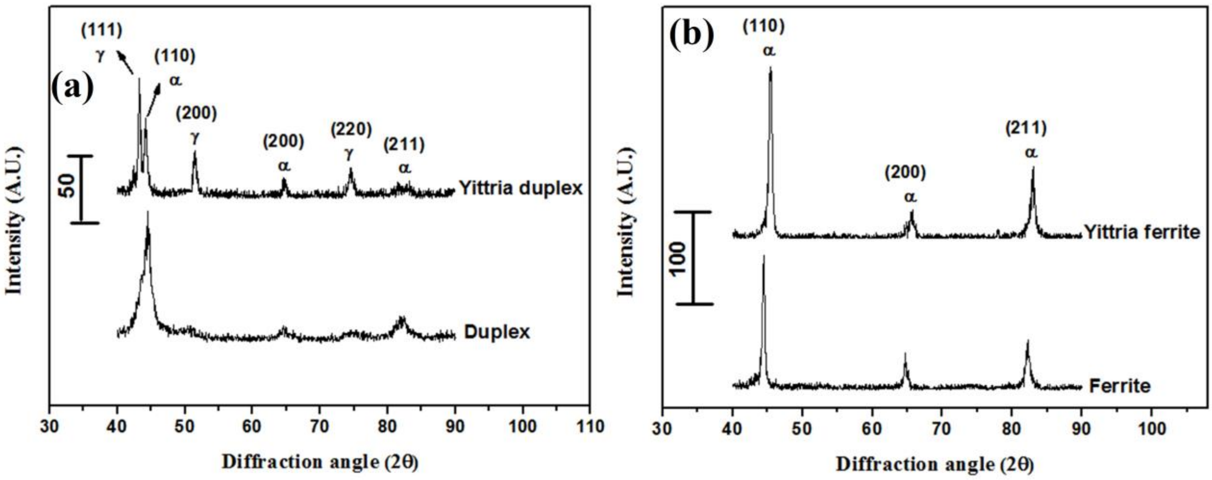

Figure 4.3.11 XRD spectra of (a) Duplex and yittria dispersed duplex (b) Ferritic and yittria dispersed ferritic stainless steel samples sintered at 1000°C by SPS

4.3.4.2 Microstructure and phase analysis

Figure 4.3.12 (a-d) shows the optical microstructures of yittria free and yittria dispersed ferritic and duplex stainless steel samples respectively consolidated at 1000°C by SPS method. From the optical micrographs it is confirmed that, yittria dispersed stainless steels forms less pores than yittria free duplex stainless steel. Tiwari et al. [8] reported that, the added nano yittria not only diffuses in to interstitial sites of duplex stainless steel but also to the grain boundary. This increases the densification process in yittria dispersed duplex stainless steel by grain boundary strengthening. This decreases the porosity ratios and hinders the grain size. The optical microstructure of yittria dispersed ferritic stainless steel show small, spherical grains with less porosity as shown in Figure 4.3.12 (b). On the other hand, microstructure of yittria free ferritic stainless steel depicts large spherical grains with more pores as shown in Figure 4.3.12 (a). The duplex and yittria dispersed duplex stainless steel contains acicular ferrite as shown in the Figure 4.3.12 (c) and 4.3.12 (d) respectively. The acicular ferrite is characterized by needle shaped chaotic grains of ferrite usually formed in the interior of austenite phase by nucleation on the inclusion. This chaotic order acts as obstacles for cleavage, crack propagation and hence increases the strength of stainless steel [9].

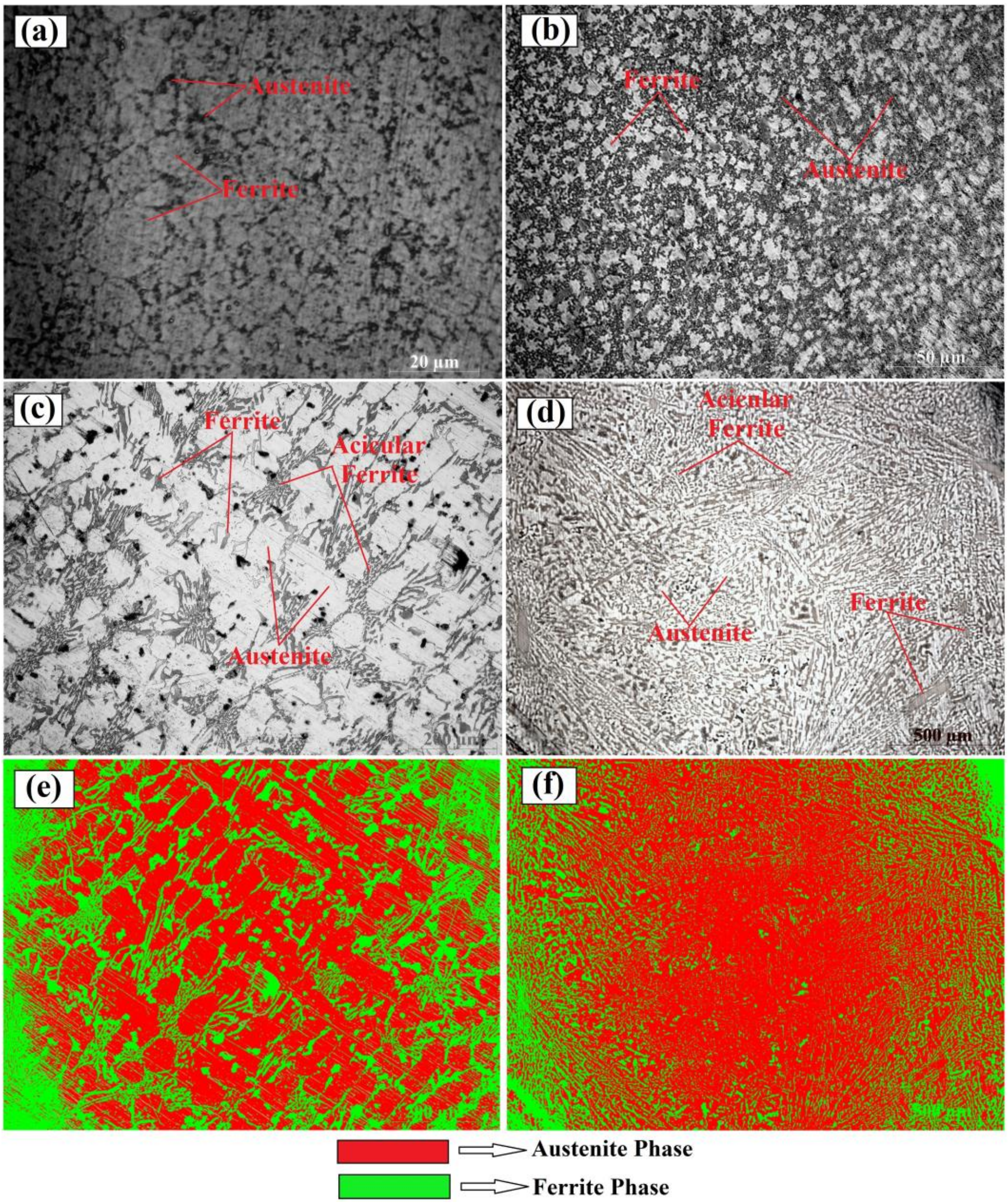

Figure 4.3.12 Optical microstructure of (a) Ferritic stainless steel (b) Yittria dispersed ferritic stainless steel (c) Duplex (d) Yittria dispersed duplex stainless steel samples sintered at 1000°C by SPS method; Phase analysis of (e) duplex and (f) yittria dispersed duplex stainless steel

Usually acicular ferrites are formed at the interior grains of pure austenite and hence ferritic and yittria dispersed ferritic stainless steels do not form acicular ferrites. The addition of yittria initiate phase transformation as explained in Figure 4.3.11, even microstructure analysis also gives evidence for phase transformation from α-Fe to γ-Fe. The addition of yittria increases the austenite phase in both duplex and ferritic stainless steels as shown in the figure. Therefore, we performed phase analysis by calculating volume fraction of both ferrite and austenite phases by using Axio Vision Release software. Figure 4.3.12 (e) and 4.3.12 (f) represents the phase analysis study of duplex and yittria dispersed duplex stainless steel respectively. Yittria dispersed duplex stainless steel contains 71% volume fraction of austenite; whereas duplex stainless steel contains 58% of austenite.

4.3.4.3 Density and hardness study

Figure 4.3.13 (a) depicts the densities of duplex, ferritic, yittria dispersed duplex and yittria dispersed ferritic stainless samples sintered by SPS method. Spark plasma sintered stainless steel samples comprise of ultrafine or nano crystalline materials [10]. Therefore, SPS stainless steel shows more density and hardness than conventionally sintered stainless steel samples (Figure 4.3.4). Tiwari et al. [8] reported that density, hardness and tribological properties of ferritic (434L) stainless steel can be improved by adding yttrium aluminium garnet (YAG). They concluded that, addition of 10wt. % YAG results in weak YAG-YAG bonding instead of strong YAG-stainless steel bonding and agglomerates at grain boundaries to reduce the hardness of stainless steel. They found that addition of small amount of YAG (5wt. %) results in strong YAG-stainless steel bonding. The percentage density of duplex and ferritic stainless steel sintered by SPS method is 91 and 92% respectively. Similarly, yittria dispersed duplex and ferritic stainless steel possess density of 93 and 95% respectively.

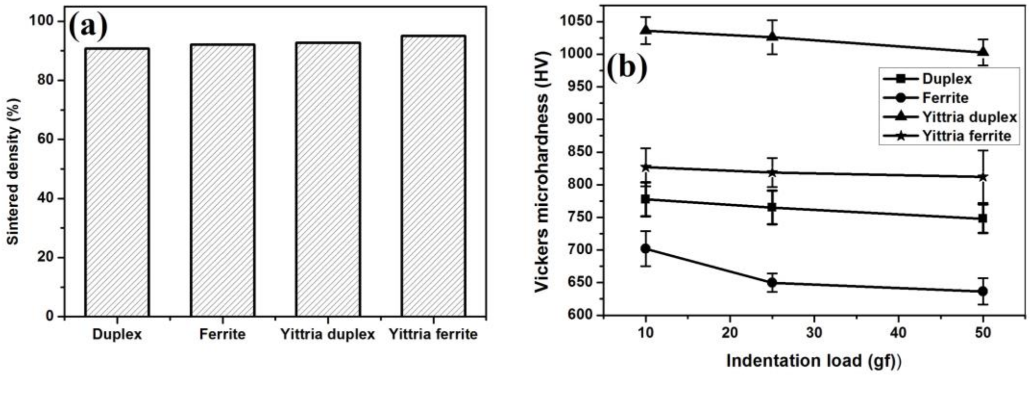

Figure 4.3.13 Graph of (a) Sintered density (b) Vickers microhardness of stainless steel samples sintered at 1000°C by SPS method

Figure 4.3.13 (b) represents the effect of indentation load on the microhardness of yittria dispersed and yittria free duplex and ferritic stainless steel sintered at 1000°C by SPS. The

Vickers microhardness measurements were carried out at 10, 25 and 50gf indentation load. At least 5 trials of indentations were made at each load and the average values of the diagonal lengths of indentation marks were measured as hardness for each stainless steel sample. From the figure it is clear that Vickers microhardness value decreases with increase in indentation load due to ISE effect. ISE occurs due to the some intrinsic structural factors such as indentation elastic recovery, work hardening during indentation and surface dislocation pining. Addition of yittria in stainless steel increases the bonding strength, density and hinders the grain growth. Finally, yittria dispersed stainless steel exhibits higher hardness than yittria free stainless steels. Yittria dispersed stainless steel show maximum microhardness than yittria free stainless steel samples due to the increase in bonding strength, density and reduction in grain growth after the addition of yittria nanoparticles. The Vickers microhardness values of duplex and ferritic stainless steel sintered by SPS method at 25gf indentation load is 765 and 650HV respectively. Similarly, yittria dispersed duplex and ferritic stainless steel show Vickers microhardness values of 1026 and 819HV respectively. Whereas microhardness values of duplex and ferritic stainless steel sintered by conventional method is 257 and 192HV respectively. Similarly, yittria dispersed duplex and ferritic stainless steel show microhardness value of 332 and 205HV respectively. Hardness and density values of yittria dispersed and yittria free stainless steel samples sintered by SPS method at 1000°C are tabulated in Table 4.4.

Table 4.4 Density and hardness of yittria dispersed and yittria free stainless steel samples sintered by SPS method at 1000°C

Samples	**Theoretical density (%)**	**Sintered density (%)**	**Vickers microhardness (HV)**
Duplex stainless steel	7.84	91	765
Ferritic stainless steel	7.75	92	650
Yittria Duplex stainless steel	7.80	93	1026
Yittria Ferritic stainless steel	7.70	95	819

4.3.4.4 Compressive strength study

The compression yield stress of yittria dispersed and yittria free duplex and ferritic stainless steels are studied. Figure 4.3.14 is the representation of the compression yield stress of yittria dispersed duplex stainless steel sample sintered at 1000°C. Yittria dispersed stainless steel exhibit higher yield stress than yittria free stainless steel [5]. The addition of yittria increases strengthening; hardness values, forms acicular structure which acts as obstacles for dislocation motion, increases the deformation resistance, controls the recovery and re-crystallization process, inhibits the grain growth and it also increases the grain boundary strengthening [5]. As a result of which yittria dispersed duplex stainless steel shows maximum yield stress than yittria free duplex stainless steels. Yittria dispersed duplex stainless steel exhibit the maximum compressive yield stress of 1205MPa and whereas, yittria free duplex stainless steel shows 960MPa.

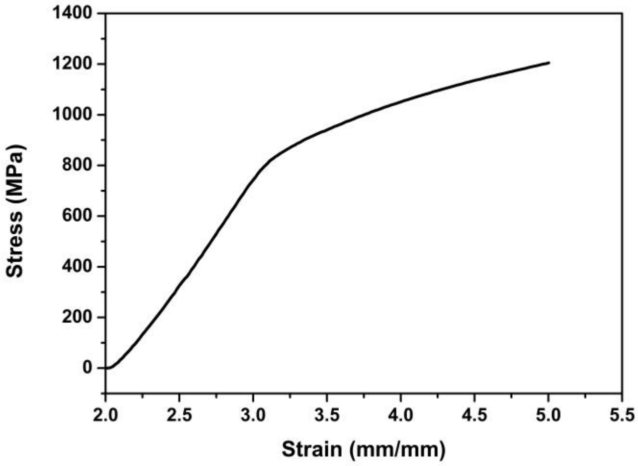

Figure 4.3.14 Compressive stress–strain curve representation of yittria dispersed duplex stainless steel sample

4.3.5 Summary and conclusions

Yittria dispersed and yittria free duplex and ferritic stainless steel samples were fabricated successfully by conventional sintering and SPS methods. The effect of sintering temperature and atmosphere on the microstructure, phase transformation, density and hardness of stainless steel during conventional sintering was studied. Increase in sintering temperature from 1000 to 1400°C increases the density, hardness and α-Fe to γ-Fe phase transformation of duplex and yittria dispersed duplex stainless steel. Conventional sintering in nitrogen atmosphere favours α-Fe to γ-Fe phase transformation and increases the density and hardness of stainless steel when compared with sintering in argon atmosphere. Spark plasma sintered stainless steels exhibit higher density, hardness and phase transformation due to retention of nano grains even after sintering.

References

1) M. Gojic, A. Nagode, B. Kosec, S. Koz uh, S. Savli, T. Holjevac Grguric, L. Kosec, Failure of steel pipes for hot air supply, *Eng. Failure. Anal.* 18 **(2011)** 2330–2335.

2) R.M. German, Sintering theory and practice, Wiley, New York, NY, **(1996)**.

3) J. Jain, A.M. Kar, A. Upadhyaya, Effect of YAG addition on sintering of P/M 316L and 434L stainless steels, *Mater. Lett.* 58 **(2004)** 2037– 2040.

4) S. Pasebani, A.K. Dutt, J. Burns, I. Charit, R.S. Mishra, Oxide dispersion strengthened nickel based alloys via spark plasma sintering, *Mater. Sci. Eng. A.* 630 **(2015)** 155–169.

5) F. Tehrani, M.H. Abbasi, M.A. Golozar, M. Panjepour, The effect of particle size of iron powder on to transformation in the nanostructured high nitrogen Fe–Cr–Mn–Mo stainless steel produced by mechanical alloying, *Mater. Sci. Eng. A.* 528 **(2011)** 3961–3966.

6) N. Kurgan, Effects of sintering atmosphere on microstructure and mechanical property of sintered powder metallurgy 316L stainless steel, *Mater. Des.* 52 **(2013)** 995–998.

7) R. Shashanka, D. Chaira, Effects of Nano-Y_2O_3 and Sintering Parameters on the Fabrication of PM Duplex and Ferritic Stainless Steels, *Acta. Metall. Sin. (Engl. Lett.)* 29 **(2016)** 58-71.

8) S.M. Tiwari, S. Balaji, A. Upadhyaya, Sintering and characterization of YAG dispersed ferritic stainless steels, *Mater. Sci. Eng. A.* 492 **(2008)** 60–67.

9) Bhadeshia, H.K.D. Hansraj, Honeycombe, R.W. Kerr, Steels: microstructure and properties (3rd ed.), Butterworth-Heinemann, **(2006)** 155, ISBN 978-0-7506-8084-4.

10) G. Marnier, C. Keller, J. Noudem, E. Hug, Functional properties of a spark plasma sintered ultrafine-grained 316L Steel, *Mater. Des.* 63 **(2014)** 633–640.

CHAPTER 5

Non-lubricated sliding wear behaviour of nano-yittria dispersed and yittria free duplex and ferritic stainless steel fabricated by powder metallurgy

5.1 Objectives and scope of the work

Wear is one of the major mechanical degradation of engineering materials where sliding between two contact surfaces takes place. During wear the dimension of the materials get reduced due to the loss of materials from contacting surfaces in the form of wear debris. This material loss leads to the more gaps between moving parts and ultimately results in reduced efficiency, maximum vibration, high noise and system malfunction. Wear debris may cause harmful contamination in food and beverage industries, it may block a valve in critical pipe lines, filters and also in electrical contacting points [1]. Therefore, greater efforts have been put forward by the researchers to reduce the wear of materials. Hence, it is very important to study the wear properties of stainless steels which are mainly used in electric motors, automobiles, mechanical joints of vibrating structures ranging from household applications to human body implants where there is relative movement between two contacting surfaces. Therefore, in the present investigation an attempt has been made to study the effect of sintering temperature, addition of dispersoids, sintering atmosphere on the wear resistance of stainless steel samples. In the present work we have consolidated yittria dispersed and yittria free duplex and ferritic stainless steel samples by conventional powder metallurgy method by optimizing the sintering temperatures and atmosphere. It involves the consolidation of stainless steel at different sintering temperatures (1000, 1200 and 1400°C) in argon and nitrogen (1000°C) atmospheres respectively and then fundamental study of non-lubricated sliding wear.

5.2 Effect of sintering temperature

5.2.1 Wear behaviour study

5.2.1.1 Effect of load on wear depth

Figure 5.1 (a) and 5.1 (b) represent the variation of wear depth with sliding time for duplex and ferritic stainless steel sintered at 1000, 1200 and 1400°C at 10N applied load. Ferritic stainless steel shows maximum wear depth than duplex stainless steel as shown in the figure. From the optical microstructure it is confirmed that dispersion of yittria in stainless steel decreases porosity ratio, increases the austenite phase and hinders the grain growth during sintering. As a result, density and hardness of stainless steel samples increases to a greater extent. Therefore, yittria dispersed duplex stainless steel shows lesser wear depth compared to yittria free duplex stainless steel.

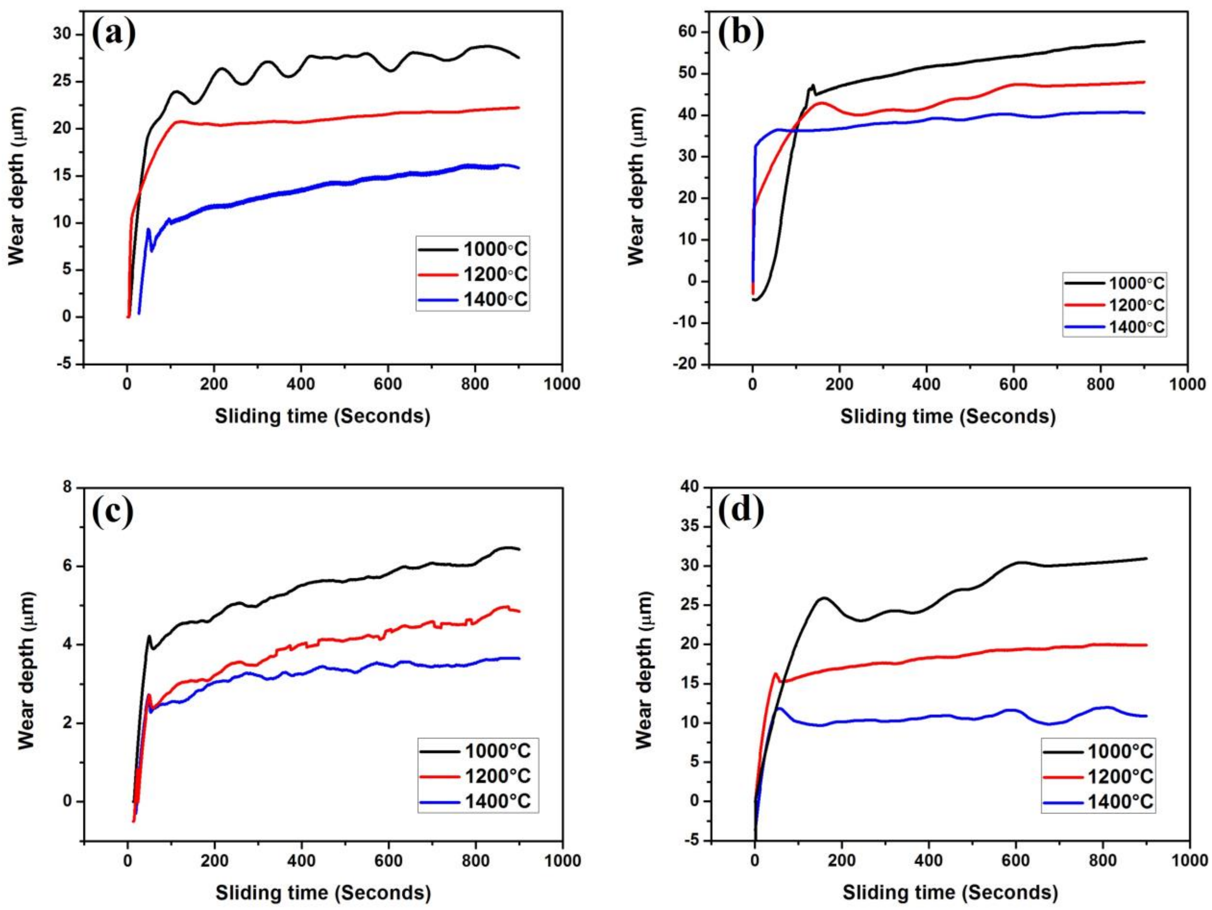

Figure 5.1 Variation of wear depth with sliding time of (a) Duplex (b) ferrite (c) yittria dispersed duplex (d) Yittria dispersed ferritic stainless steel samples sintered at 1000, 1200 and 1400°C at 10N applied load

Figure 5.1 (c) and 5.1 (d) depict the variation of wear depth with sliding time for a range of temperature 1000 to 1400°C in case of yittria dispersed duplex and yittria dispersed ferritic stainless steel at an applied load of 10N. The wear depth of duplex and yittria dispersed duplex stainless steel sintered at 1000°C is found to be 29 and 7μm respectively when tested at an applied load of 10N. Similarly, the wear depth of ferritic and yittria dispersed ferritic stainless steel sintered at 1000°C is found to be 58 and 31μm respectively. It has also been observed that wear depth decreases with increase in sintering temperature from 1000 to 1400°C. The reason is due to higher hardness and density at 1400°C as compared to 1000°C. The hardness value increases from 265 to 341HV and density from 80 to 96% for ferritic stainless steel after the addition of yittria nanoparticles when sintered at 1400°C for 1h under Ar atmosphere. Whereas in case of duplex steel, hardness value increases from 567 to 576HV and density from 78 to 95% after the addition of yittria nanoparticles.

We also investigated the effect of applied load (10N and 20N) on the wear behaviour of yittria dispersed and yittria free duplex and ferritic stainless steel. Figure 5.2 (a-d) represents the graph of wear depth vs. sliding time at 20N applied load in case of yittria dispersed and yittria free duplex and ferritic stainless steel. The well known relation between frictional force (F) and applied normal load (N) is represented by equation (1):

$$F = \mu N \qquad \textbf{(1)}$$

Where F is frictional force, N is normal load applied and μ is co-efficient of friction.

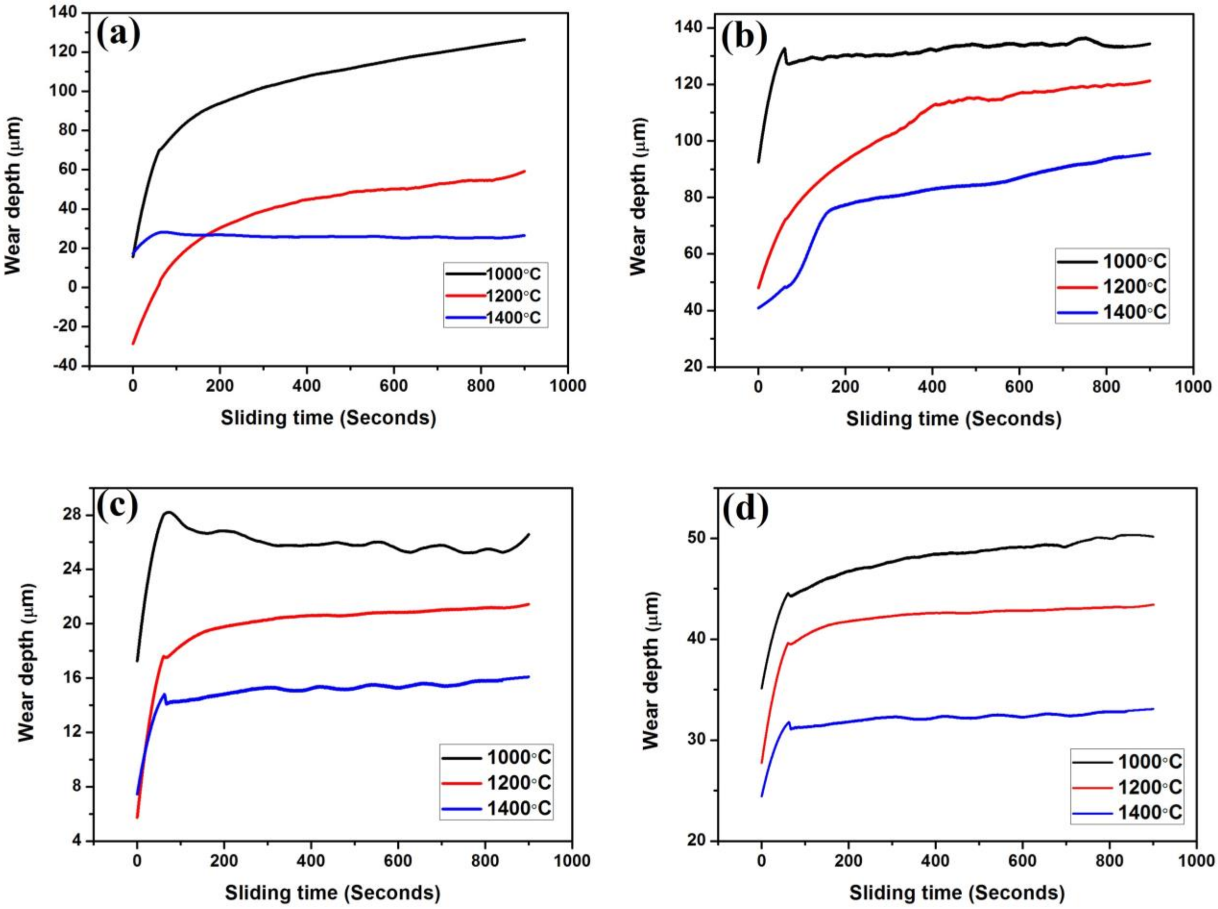

Figure 5.2 Variation of wear depth with sliding time of (a) Duplex (b) ferrite (c) yittria dispersed duplex (d) Yittria dispersed ferritic stainless steel samples sintered at 1000, 1200 and 1400°C at 20N applied load

Chowdhury et al. [2] studied the friction co-efficient of stainless steel 304 (SS 304) at 10, 15 and 20N applied loads using specially designed pin on disc wear tester at 1, 1.5 and 2m/s sliding velocity. They observed that magnitudes of friction coefficients are different for different materials depending on the sliding velocity and applied load. They reported that coefficient of friction decreases with the increase in applied load and it increases with increase in sliding velocity. The wear depth of duplex and yittria dispersed duplex stainless steel consolidated at 1000°C at 20N applied load is found to be 127 and 29µm. Similarly, the wear depth of ferritic and yittria dispersed ferritic stainless steel consolidated at 1000°C is 137 and 50µm respectively at 20N. All the stainless steels exhibit higher wear depth at 20N than 10N load. This is due to higher frictional force at higher load.

Figure 5.3 shows a typical front view depth of worn region of yittria dispersed duplex stainless steel sintered at 1000°C in argon atmosphere using 10N applied load. The wear depth of yittria dispersed duplex stainless steel measured from surface profilometer is 8µm; the value is in good agreement with the wear depth measured from graph of wear depth vs. sliding distance as shown in the Figure 5.1 (c).

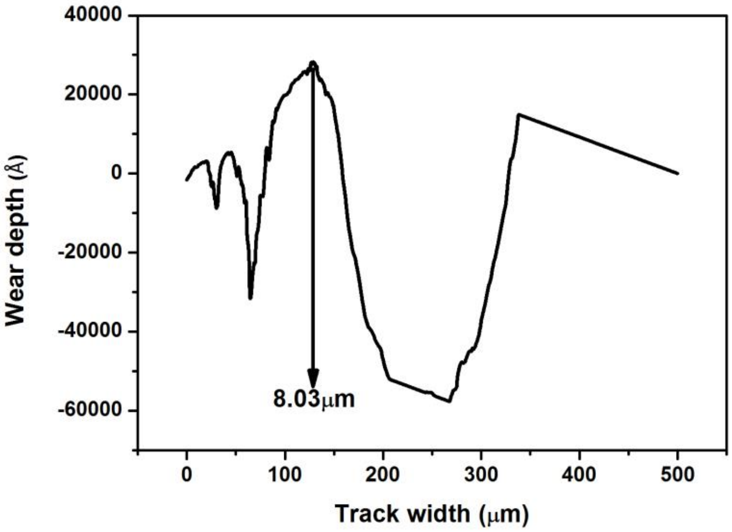

Figure 5.3 Surface profilometer data of depth of worn region of yittria dispersed duplex stainless steel sintered at 1000°C in argon atmosphere using 10N applied load

5.2.1.2 Mechanism of wear

SEM was used to study the wear mechanism and wear modes. Figure 5.4 (a-c) represents the SEM images of worn out surfaces at 10N applied load for duplex stainless steel sintered at 1000, 1200 and 1400°C respectively. SEM microstructures depict the clear indication of abrasive wear mechanism along with mild oxidation wear during wear study at 10N applied load. The effective oxidative wear increases with increase in sintering temperature as confirmed by SEM and EDS study. Figure 5.4 (d-f) represents the EDS spectra of duplex stainless steel sintered at 1000, 1200 and 1400°C temperature respectively. The EDS study reveals the presence of more oxygen percentage at higher sintering temperature as shown in the figures. The oxygen percentage increases from 5 to 37% with increasing sintering temperature from 1000 to 1400°C. Stainless steel sintered at 1400°C exhibits more hardness and density than stainless steel sintered at 1000 and 1200°C [3]. Therefore, wear debris produced by stainless steel sintered at higher temperature (1400°C) is of spherical particle shape. Whereas flake shaped wear debris is produced for the stainless steel sintered at lower temperature due to soft nature. The produced wear debris entrap in between the contacting surfaces and break up the contacting interface to sufficiently small sizes and rapidly oxidize both wear debris and wear track surfaces [4]. Quinn [5], Stott [6] and Jiang et al. [7] also observed similar kind of oxidative wear mechanisms.

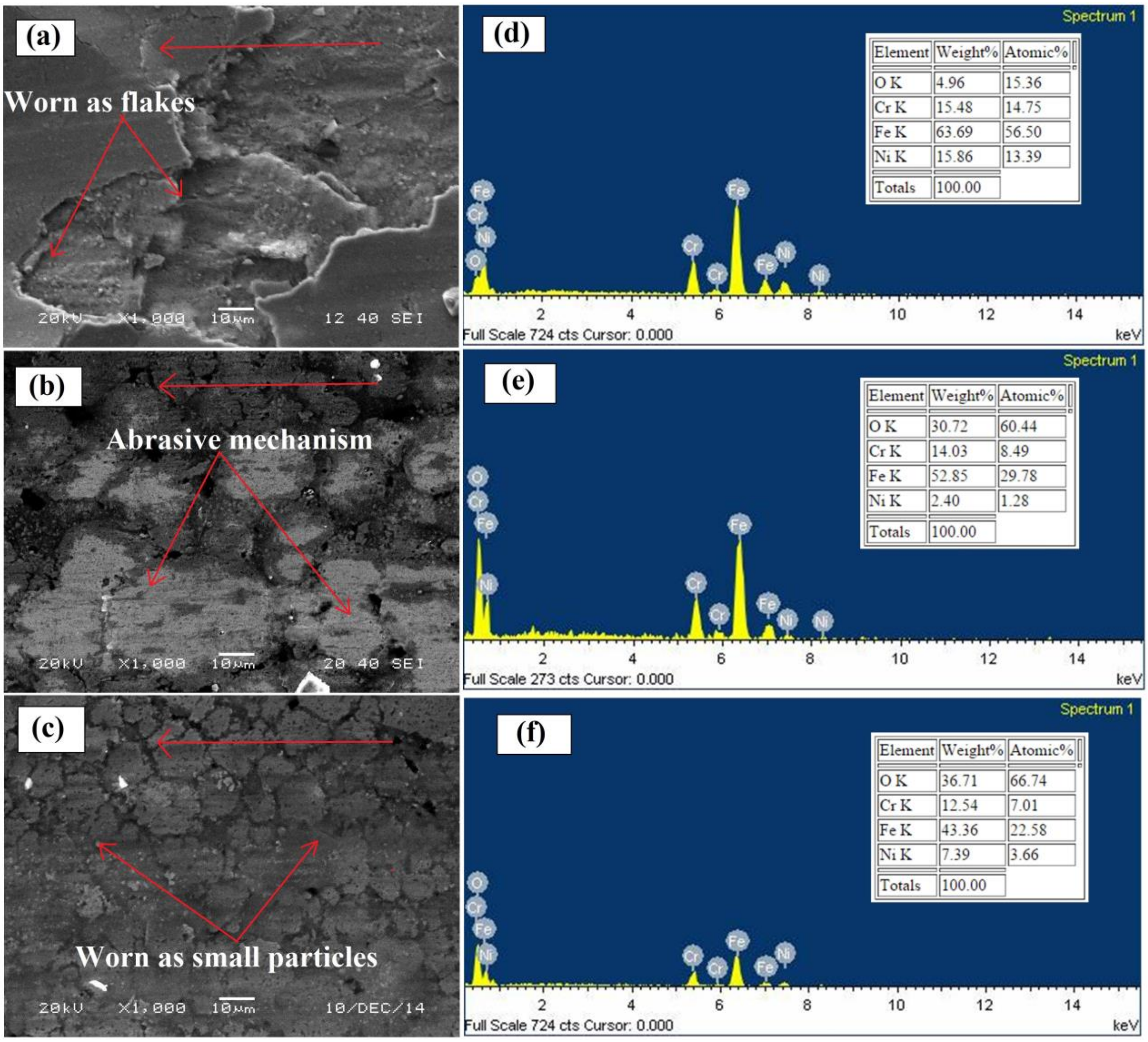

(d)

Element	Weight%	Atomic%
O K	4.96	15.36
Cr K	15.48	14.75
Fe K	63.69	56.50
Ni K	15.86	13.39
Totals	100.00	

(e)

Element	Weight%	Atomic%
O K	30.72	60.44
Cr K	14.03	8.49
Fe K	52.85	29.78
Ni K	2.40	1.28
Totals	100.00	

(f)

Element	Weight%	Atomic%
O K	36.71	66.74
Cr K	12.54	7.01
Fe K	43.36	22.58
Ni K	7.39	3.66
Totals	100.00	

Figure 5.4 SEM and EDS spectra of worn regions of duplex stainless steel at (a, d) 1000°C (b, e) 1200°C and (c, f) 1400°C respectively at 10N applied load

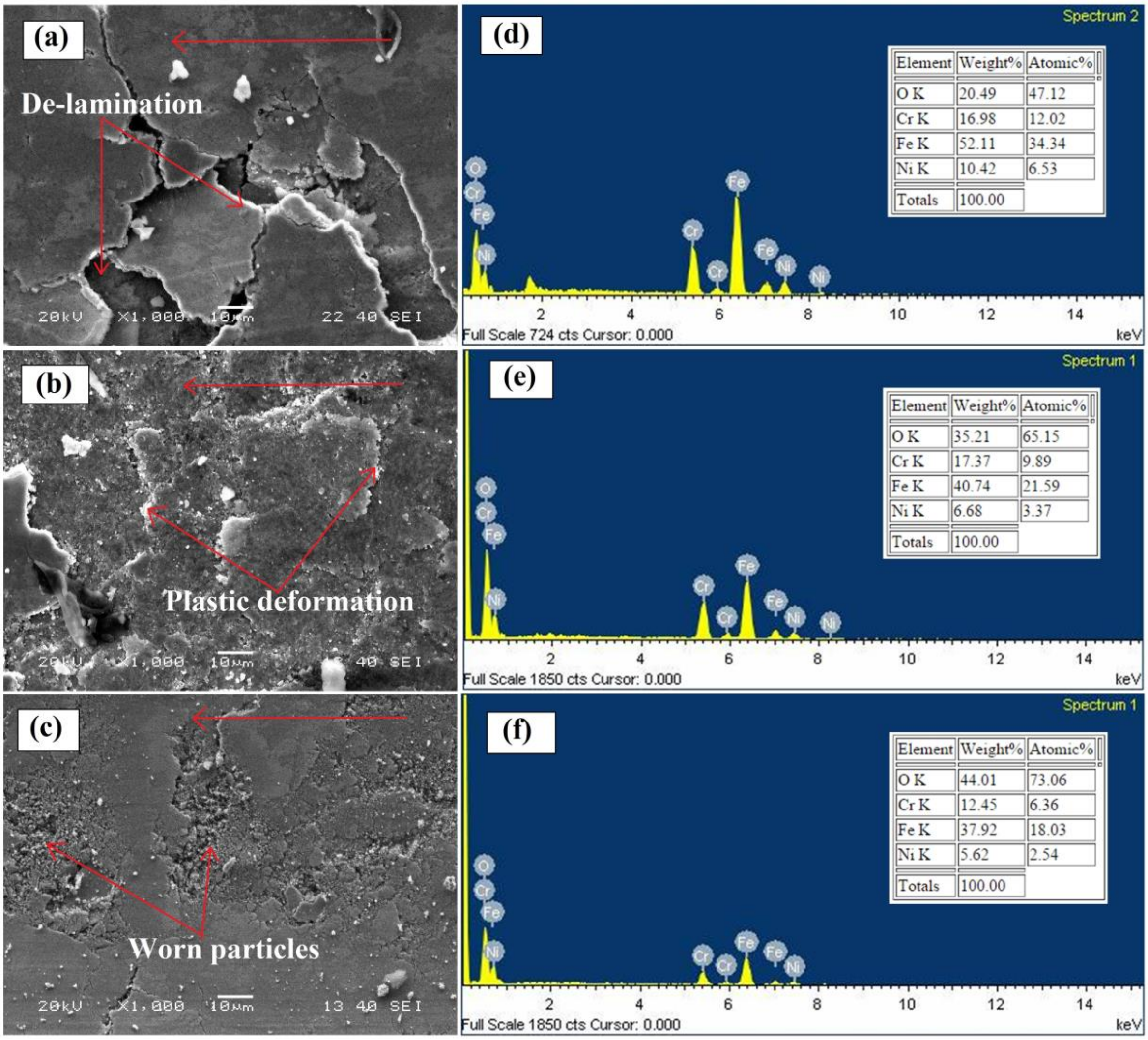

Element	Weight%	Atomic%
O K	20.49	47.12
Cr K	16.98	12.02
Fe K	52.11	34.34
Ni K	10.42	6.53
Totals	100.00	

Element	Weight%	Atomic%
O K	35.21	65.15
Cr K	17.37	9.89
Fe K	40.74	21.59
Ni K	6.68	3.37
Totals	100.00	

Element	Weight%	Atomic%
O K	44.01	73.06
Cr K	12.45	6.36
Fe K	37.92	18.03
Ni K	5.62	2.54
Totals	100.00	

Figure 5.5 SEM and EDS spectra of worn regions of duplex stainless steel at (a, d) 1000°C (b, e) 1200°C and (c, f) 1400°C respectively at 20N applied load

Figure 5.5 (a-c) represents the SEM images of worn out surfaces at 20N applied load for duplex stainless steel sintered at 1000, 1200 and 1400°C respectively. From the figures it is clear that the wear mechanism is abrasive and mild oxidation followed by ploughing and plastic deformation modes. Figure 5.5 (a) shows that de-lamination takes place due to the low hardness of stainless steel sintered at 1000°C. It has also been seen that worn out material is in the form of flake. However, stainless steel sintered at 1400°C shows the worn out material in the shape of plastically deformed particles. It is also evident that failure is severe at higher load (20N) as seen from micrographs as compared to 10N load due to higher frictional force. Figure 5.5 (d-f) shows the EDS spectra of duplex stainless steel sintered at 1000, 1200 and 1400°C temperature respectively. The oxygen percentage increases from 20 to 44% with increase in sintering temperature from 1000 to 1400°C for samples tested at 20N. The EDS analysis depicts the presence of more fraction of oxygen at 20N applied load than at 10N applied load due to maximum frictional force at 20N.

5.2.1.3 Microstructure and volume of wear debris

We investigated the morphology of wear debris of yittria dispersed and yittria free stainless steel samples sintered at 1000°C during wear study at 20N applied load. During 10N applied load, there was negligible amount of wear debris and hence wear debris were collected at 20N applied load to study the wear mechanism. Figure 5.6 (a-d) represents the wear debris of yittria dispersed and yittria free duplex and ferritic stainless steel respectively. Both yittria dispersed and yittria free ferritic stainless steel show flake shape wear debris which was generated by abrasive mechanism with ploughing mode due to their ductile nature and low hardness. Whereas, yittria dispersed and yittria free duplex stainless steels exhibit higher hardness and very less ductility. Therefore, they produce spherical particle shape wear debris which was produced by abrasive wear mechanism with plastic deformation mode. The EDS analysis was carried out to study the wear mechanism in detail. Figure 5.6 (e-h) represents the EDS spectra of wear debris of yittria dispersed and yittria free duplex and ferritic stainless steel respectively sintered at 1000°C temperature. From EDS it is confirmed that yittria dispersed and yittria free duplex stainless steels are more prone to oxidation as the oxygen percentage is more in both the cases. As explained earlier, the higher percentage of oxygen is due to large surface area of plastically deformed and hardened wear debris formed during wear study as shown in Figure 5.6 (a) and 5.6 (c). The wear debris of duplex and yittria dispersed duplex stainless steels contain 26 and 32% of oxygen by weight. Whereas ferritic and yittria dispersed ferritic stainless steel contain 24 and 25% of oxygen as shown in EDS.

Volume of wear debris is calculated by Archard equation [8] as follows:

$$Q = \frac{KWL}{H} \tag{2}$$

Where, ‘Q’ is the total volume of wear debris produced, ‘K’ is dimensionless constant, ‘W’ is total normal load, ‘L’ sliding distance and ‘H’ is the hardness of the softest contacting surface (Original surface hardness of stainless steel).

Volume of wear debris depends upon the hardness of materials; higher the hardness lower will be the volume of wear debris. Figure 5.7 (a) and 5.7 (b) depicts the volume of wear debris produced at applied load of 10N and 20N respectively for all the stainless steel samples sintered at 1000 to 1400°C.

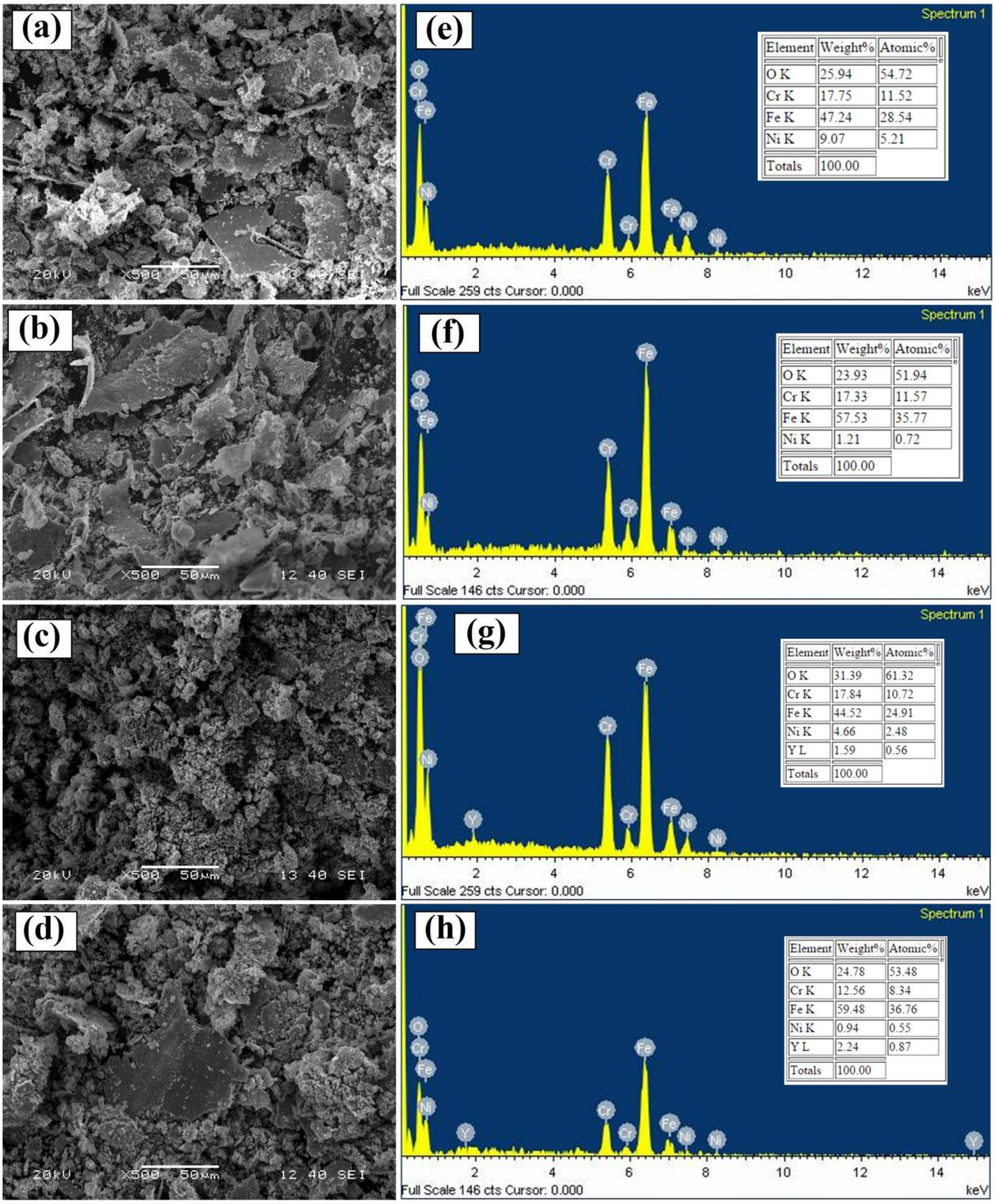

(e)

Element	Weight%	Atomic%
O K	25.94	54.72
Cr K	17.75	11.52
Fe K	47.24	28.54
Ni K	9.07	5.21
Totals	100.00	

(f)

Element	Weight%	Atomic%
O K	23.93	51.94
Cr K	17.33	11.57
Fe K	57.53	35.77
Ni K	1.21	0.72
Totals	100.00	

(g)

Element	Weight%	Atomic%
O K	31.39	61.32
Cr K	17.84	10.72
Fe K	44.52	24.91
Ni K	4.66	2.48
Y L	1.59	0.56
Totals	100.00	

(h)

Element	Weight%	Atomic%
O K	24.78	53.48
Cr K	12.56	8.34
Fe K	59.48	36.76
Ni K	0.94	0.55
Y L	2.24	0.87
Totals	100.00	

Figure 5.6 SEM and EDS spectra of wear debris produced by (a) Duplex, (b) Ferrite, (c) Yittria dispersed duplex and (d) Yittria dispersed ferritic stainless steel samples sintered at 1000°C at 20N load

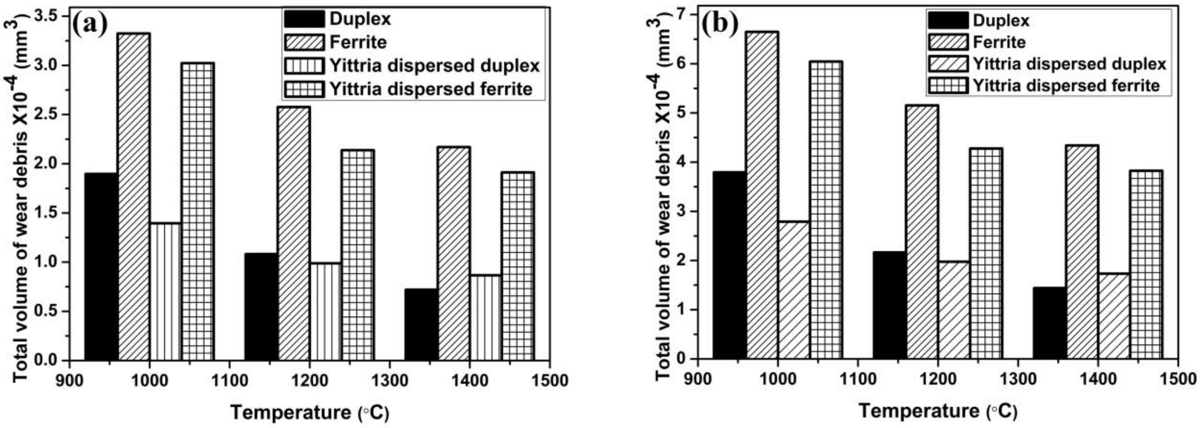

Figure 5.7 Volume of wear debris produced by yittria dispersed and yittria free stainless steels sintered at 1000 to 1400°C (a) 10N and (b) 20N applied load

Table 5.1 Values of wear depth and volume of wear debris produced at different sintering temperatures

Type of stainless steel	**Temperature (°C)**	**10N applied load**		**20N applied load**	
		Wear depth (μm)	**Wear volume (X 10^{-4}mm^3)**	**Wear depth (μm)**	**Wear volume (X 10^{-4}mm^3)**
Duplex stainless steel	1000	29±11%	1.9	127±15%	3.80
	1200	22±13%	1.08	61±13%	2.16
	1400	16±10%	0.72	27±14%	1.44
Ferritic stainless steel	1000	58±8%	3.32	137±15%	6.64
	1200	48±12%	2.57	122±11%	5.15
	1400	41±10%	2.17	96±12%	4.33
Yittria duplex stainless steel	1000	7±8%	1.4	27±12%	2.8
	1200	5±9%	0.98	22±9%	1.97
	1400	4±9%	0.87	16±10%	1.74
Yittria ferritic stainless steel	1000	31±14%	3.02	50±13%	6.04
	1200	20±13%	2.13	43±13%	4.27
	1400	12±10%	1.91	33±9%	3.82

From the figure it is confirmed that the volume of wear debris produced decreases with increase in sintering temperature and increases with increase in applied load from 10 to 20N. Yittria dispersed stainless steel samples produce less volume of wear debris when compared with yittria free stainless steel samples. Wang et al. [9] and Kim et al. [10] also calculated volume of austenitic stainless steel wear debris using Archard equation and they reported that increase in sintering temperature increases the density, hardness and wear resistance. They also observed that increase in applied load increases the volume of wear debris. The wear depth, volume of wear debris produced at different sintering temperature and different loads are tabulated in Table 5.1.

5.3 Effect of sintering atmosphere

5.3.1 Wear behaviour study

5.3.1.1 Effect of load on wear depth

The variation of wear depth with sliding time for all the stainless steel compacts sintered at 1000°C in nitrogen atmosphere at 10N and 20N applied load are shown in Figure 5.8 (a) and 5.8 (b) respectively. The wear depth of duplex, ferritic, yittria dispersed duplex and yittria dispersed ferritic stainless steel at 10N applied load is measured to be 14, 25, 6 and 17µm respectively. Similarly, the wear depth is 36, 76, 21 and 60µm respectively tested at 20N applied load.

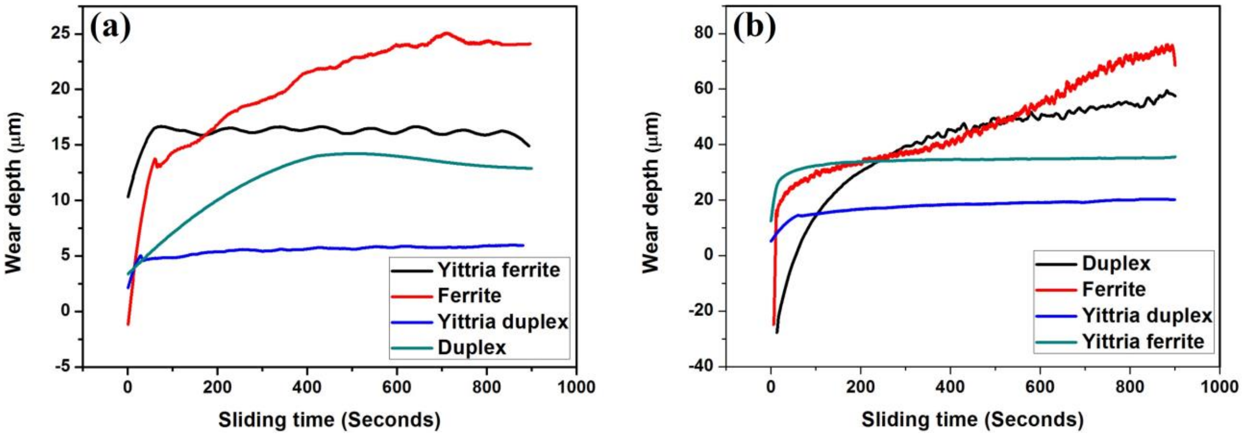

Figure 5.8 Variation of wear depth with sliding time of yittria dispersed and yittria free stainless steel samples sintered at 1000°C (nitrogen atmosphere) during (a) 10N, and (b) 20N applied loads

Stainless steel sintered at nitrogen atmosphere posses maximum wear resistance than the stainless steel sintered at argon atmosphere. This is due to the increased density and hardness, low porosity ratios, formation of hard chromium nitride phase and rapid phase transformation from ductile α-Fe to less ductile γ-Fe. As explained earlier, this is due to the diffusion of N_2 atoms in to the Fe lattice. Presence of yittria enhances the solubility of N_2 atoms in Fe lattice, therefore yittria dispersed stainless steel exhibits more volume percentage of austenite and Cr_2N phases than yittria free stainless steel. Eventually the wear depth of yittria dispersed stainless steel is less compared to wear depth of yittria free stainless steel samples. Figure 5.8 reveals that wear depth of the all the four stainless steel samples increase with increase in applied load from 10N to 20N.

Figure 5.9 shows a typical front view of worn region of yittria dispersed duplex stainless steel sintered at 1000°C in nitrogen atmosphere using 10N applied load. The wear depth of yittria dispersed duplex stainless steel measured from surface profilometer is found to be 7.7µm; the value is in good agreement with the wear depth measured from graph of wear depth vs. sliding distance as shown in Figure 5.8 (a). From the surface profilometer study, the wear depth of yittria dispersed duplex stainless steel sintered in argon atmosphere is found to be around 8µm; whereas the wear depth of yittria dispersed duplex stainless steel sintered in nitrogen atmosphere is around 7.7µm. This is due to the increase in the strength, presence of chromium nitride phase and phase transformation of ductile α-Fe to less ductile γ-Fe phase.

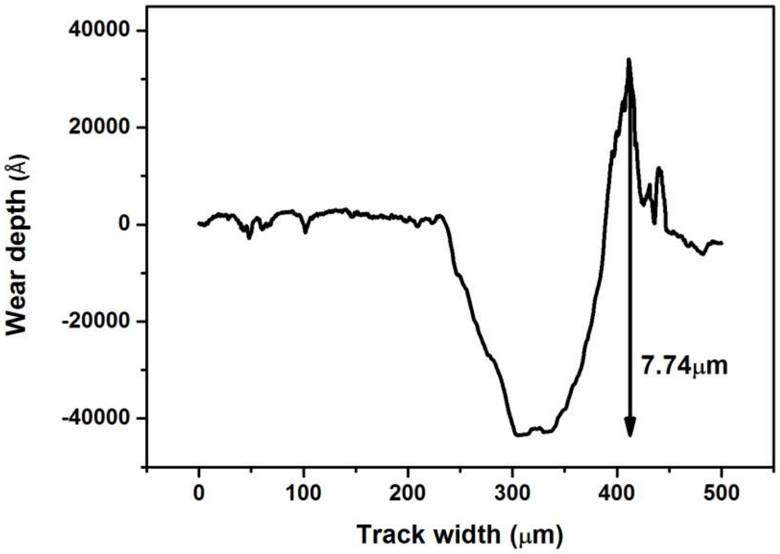

Figure 5.9 Surface profilometer data of depth of worn region of yittria dispersed duplex stainless steel sintered at 1000°C in nitrogen atmosphere using 10N applied load

5.3.1.2 Mechanism of wear

The effect of yittria on wear mechanism and wear modes of stainless steel has been investigated by using SEM. Figure 5.10 (a) and 5.10 (b) represent the SEM images of worn surface of duplex and yittria dispersed duplex stainless steel sintered in nitrogen atmosphere at 1000°C tested at 10N load. Conventional sintering carried out under nitrogen atmosphere results in higher values of density and hardness as compared to stainless steel sintered at argon atmosphere [11]. A Vickers microhardness value of 314 and 257HV are obtained for duplex stainless steel when sintered at 1000°C under N_2 and Ar atmosphere respectively. Similarly, Vickers microhardness of yittria dispersed duplex stainless steel sintered under N_2 and Ar atmosphere are found to be 400 and 332HV respectively. Therefore, stainless steels sintered under nitrogen atmosphere show maximum wear resistance than stainless steel sintered under argon atmosphere due to their higher hardness values. Presence of nitrogen not only increases the solid solution strengthening but also increases the grain size strengthening [12, 13]. As duplex stainless steel is less hard than yittria dispersed duplex stainless steel, hence it shows the less abrasive wear mechanism and mild oxidation wear as shown in the figure. On the other hand, yittria dispersed duplex stainless steel undergoes higher abrasive and intense oxidative wear with plastic deformation mode.

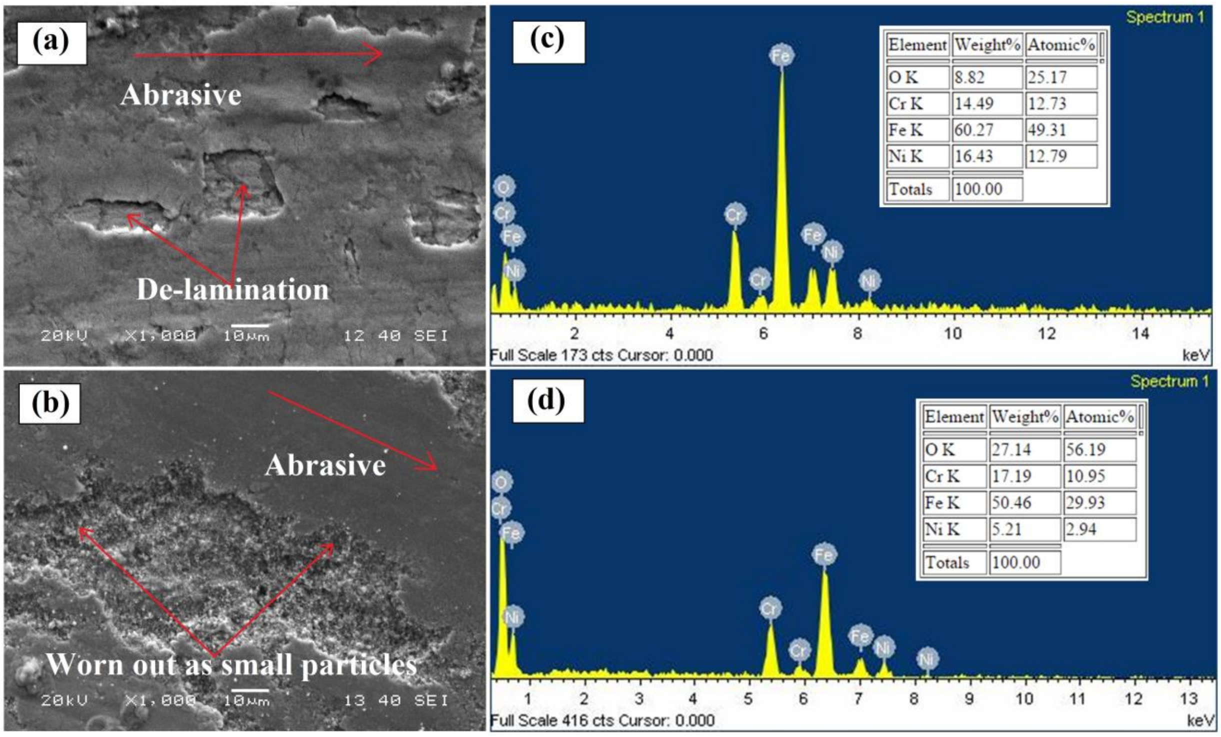

(c)

Element	Weight%	Atomic%
O K	8.82	25.17
Cr K	14.49	12.73
Fe K	60.27	49.31
Ni K	16.43	12.79
Totals	100.00	

(d)

Element	Weight%	Atomic%
O K	27.14	56.19
Cr K	17.19	10.95
Fe K	50.46	29.93
Ni K	5.21	2.94
Totals	100.00	

Figure 5.10 SEM and EDS spectra of worn regions of 1000°C nitrogen sintered (a, c) duplex stainless steel (b, d) Yittria dispersed duplex stainless steel at 10N applied wear load

Figure 5.10 (c) and 5.10 (d) represent the EDS spectra of duplex and yittria dispersed duplex stainless steel sintered at 1000°C temperature in nitrogen atmosphere. The EDS study reveals the presence of more oxygen percentage in yittria dispersed duplex stainless steel as shown in the figure. The amount of oxygen present in duplex and yittria dispersed duplex stainless steel tested at 10N load is 9 and 27% respectively. The hardness and density increases with the dispersion of yittria nano particles in to stainless steel [14, 15]. Therefore, wear debris produced in yittria dispersed duplex stainless steel is in the form of spherical particles instead of small flakes as produced by ferritic stainless steel. Both wear debris and worn out surface undergo rapid oxidation due to the entrapped fine wear debris between contacting surfaces. The oxidation elevates further due to the fine particle size and maximum surface area of worn particles and worn surface.

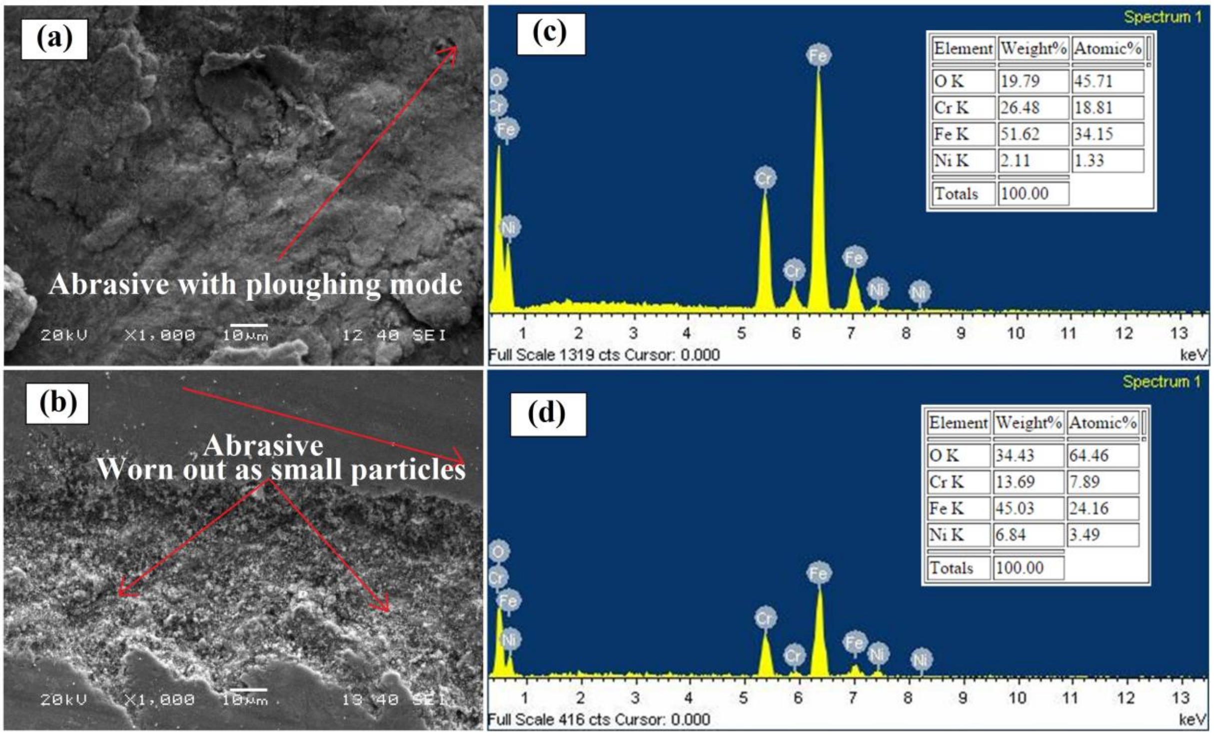

Element	Weight%	Atomic%
O K	19.79	45.71
Cr K	26.48	18.81
Fe K	51.62	34.15
Ni K	2.11	1.33
Totals	100.00	

Element	Weight%	Atomic%
O K	34.43	64.46
Cr K	13.69	7.89
Fe K	45.03	24.16
Ni K	6.84	3.49
Totals	100.00	

Figure 5.11 SEM and EDS spectra of worn regions of 1000°C nitrogen sintered (a, c) duplex stainless steel (b, d) Yittria dispersed duplex stainless steel at 20N applied wear load

Figure 5.11 (a) and 5.11 (b) represent the SEM images of worn surface of duplex and yittria dispersed duplex under 20N applied load sintered in nitrogen atmosphere at 1000°C. The duplex stainless steel undergoes abrasive wear along with oxidation wear with ploughing mode; and yittria dispersed duplex stainless steel undergoes abrasive wear and intense oxidation wear with plastic deformation mode. The plastic deformation mode is due to the maximum hardness of yittria dispersed duplex stainless steel. Figure 5.11 (c) and 5.11 (d) show the EDS spectra of duplex and yittria dispersed duplex stainless steel sintered at 1000°C temperature in nitrogen atmosphere. Oxygen percentage of yittria dispersed duplex stainless steel is 34% and that of duplex stainless steel is 20% at 20N applied load. From EDS figures it is clear that yttria dispersed duplex stainless steel undergo rapid oxidation due to fine worn particles.

5.3.1.3 Microstructure and volume of wear debris

Figure 5.12 (a) and 5.12 (b) represent the SEM micrographs of wear debris of duplex and yttria dispersed duplex stainless steel sintered at 1000°C under nitrogen atmosphere with wear load of 20N. It is observed from the micrographs that duplex stainless steel produces plastically deformed flake shape wear debris due to its soft ductile nature (compare to yttria dispersed duplex stainless steel). Whereas yttria dispersed duplex stainless steel produces spherical shaped wear debris due to its maximum hardness and brittle nature. Both types of stainless steels follow abrasive and oxidative mechanism with mild ploughing and intense plastic deformation modes respectively. Therefore, we investigated the amount of oxygen present in wear debris by using EDS to study the wear mechanism in detail.

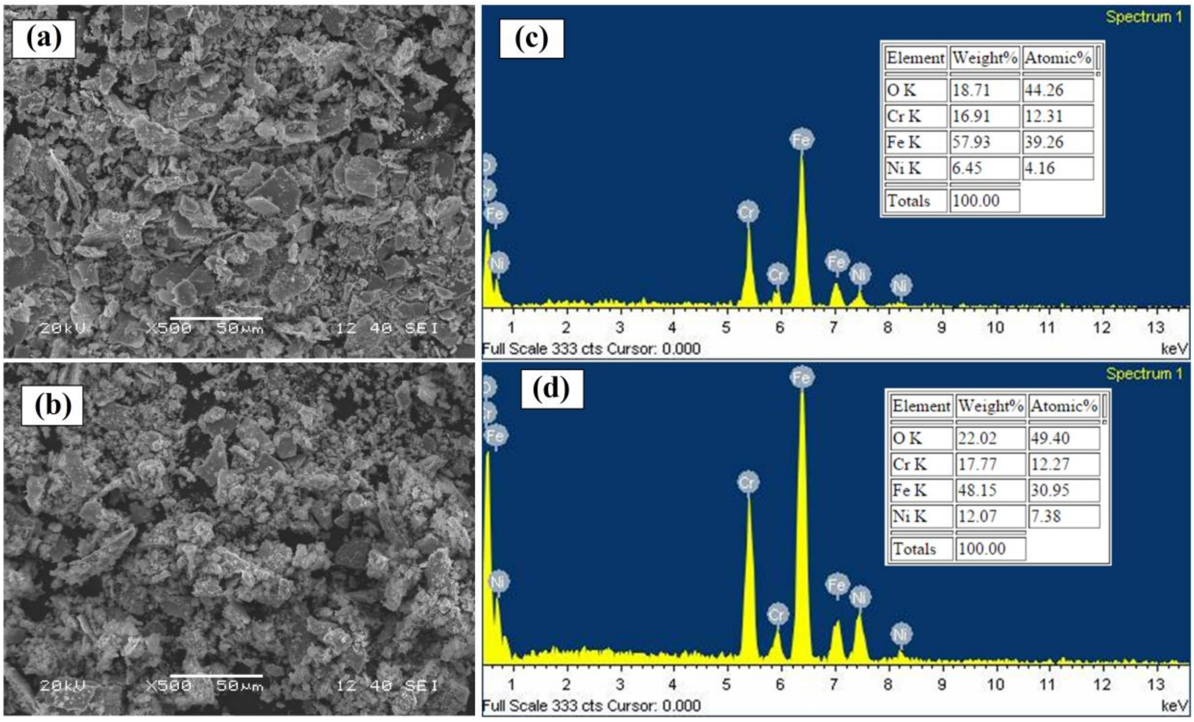

Element	Weight%	Atomic%
O K	18.71	44.26
Cr K	16.91	12.31
Fe K	57.93	39.26
Ni K	6.45	4.16
Totals	100.00	

Element	Weight%	Atomic%
O K	22.02	49.40
Cr K	17.77	12.27
Fe K	48.15	30.95
Ni K	12.07	7.38
Totals	100.00	

Figure 5.12 SEM and EDS spectra of wear debris produced by 1000°C nitrogen sintered (a, c) Duplex and (b, d) Yittria dispersed duplex stainless steel samples at 20N applied wear load

Figure 5.12 (c) and 5.12 (d) depicts the EDS spectra of wear debris of duplex and yittria dispersed duplex stainless steel produced at 20N applied load. The EDS studies reveal that yittria dispersed duplex stainless steel shows more weight percentage of oxygen than duplex stainless steel. This is due to the small sized wear debris of yittria dispersed duplex stainless steel than duplex stainless steel and hence undergoes oxidation readily. The wear debris of duplex stainless steel contains 19% of oxygen and that of yittria dispersed duplex stainless steel contains 22% of oxygen by weight.

Volumes of wear debris are calculated by Archard equation. Figure 5.13 depicts the volume of wear debris produced by yittria dispersed and yittria free stainless steel at applied load of 10N and 20N.

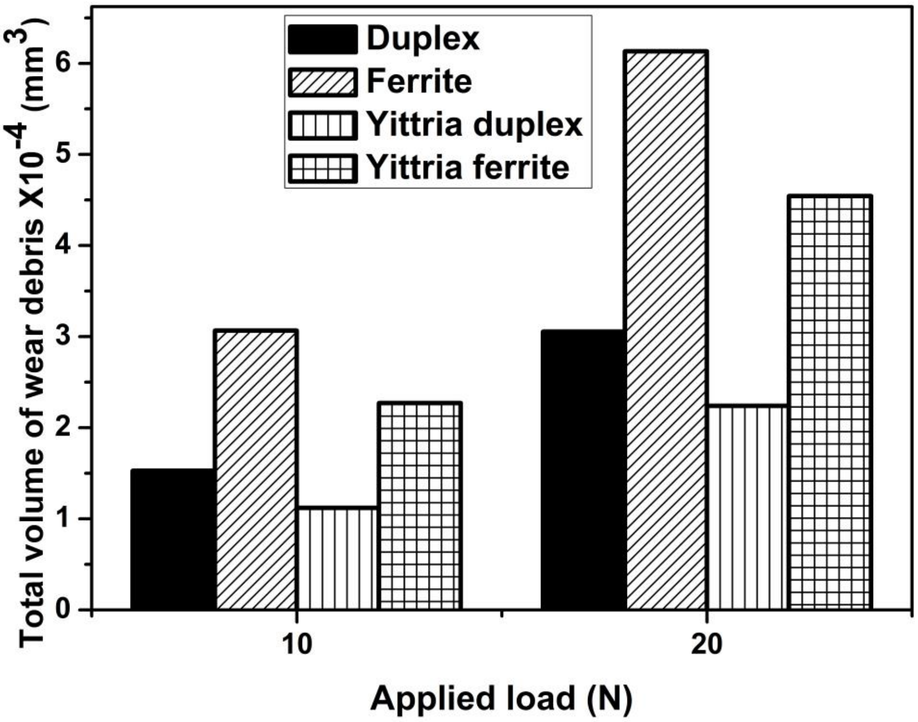

Figure 5.13 Volume of wear debris produced by yittria dispersed and yittria free stainless steel at 10N and 20N applied load sintered at 1000°C in nitrogen atmosphere

From the figure it is evident that volumes of wear debris produced depends upon the applied load and wear resistance of materials. Yittria dispersed stainless steels are more wear resistant, hence they produce less volume of wear debris than yittria free stainless steels. Wear study of all the stainless steels at 10N applied load produce less volume of wear debris than the stainless steels at 20N applied load. The volume of wear debris is also calculated experimentally from the weight of wear debris produced and density of the respective stainless steel. The volume of wear debris produced follows linear trend as that of Archard equation. Wear volume increases from 0.20 to 0.49mm^3 with increases in applied load from 10N to 20N in case of duplex stainless steel. Similarly, it increases from 0.1 to 0.24 mm^3 in case of yittria dispersed duplex stainless steel. The wear depth, volume of wear debris produced at different sintering atmosphere and different loads are tabulated in Table 5.2.

Table 5.2 Values of wear depth and volume of wear debris produced at nitrogen sintering atmosphere at 1000°C temperature

Type of stainless steel	**10N applied load**			**20N applied load**		
	Wear depth (μm)	**Wear Volume (Archard equation) (X $10^{-4}mm^3$)**	**Wear volume (Experiment) (mm^3)**	**Wear depth (μm)**	**Wear Volume (Archard equation) (X $10^{-4}mm^3$)**	**Wear volume (Experiment) (mm^3)**
Duplex stainless steel	13±11%	1.52	0.20	59±11%	3.05	0.49
Ferritic stainless steel	24±11%	3.06	0.43	76±9%	6.13	0.78
Yittria duplex	6±12%	1.12	0.10	21±5%	2.24	0.24
Yittria ferrite	16±10%	2.27	0.31	35±8%	4.54	0.58

5.4 Spark plasma sintering

5.4.1 Wear behaviour study

5.4.1.1 Effect of load on wear depth

Figure 5.14 (a) and 5.14 (b) represent the variation of wear depth with sliding time for yittria dispersed and yittria free duplex and ferritic stainless steel measured at 40 and 60N applied load respectively. We studied the effect of applied load (40 and 60N) on the wear properties of yittria dispersed and yittria free duplex and ferritic stainless steel samples.

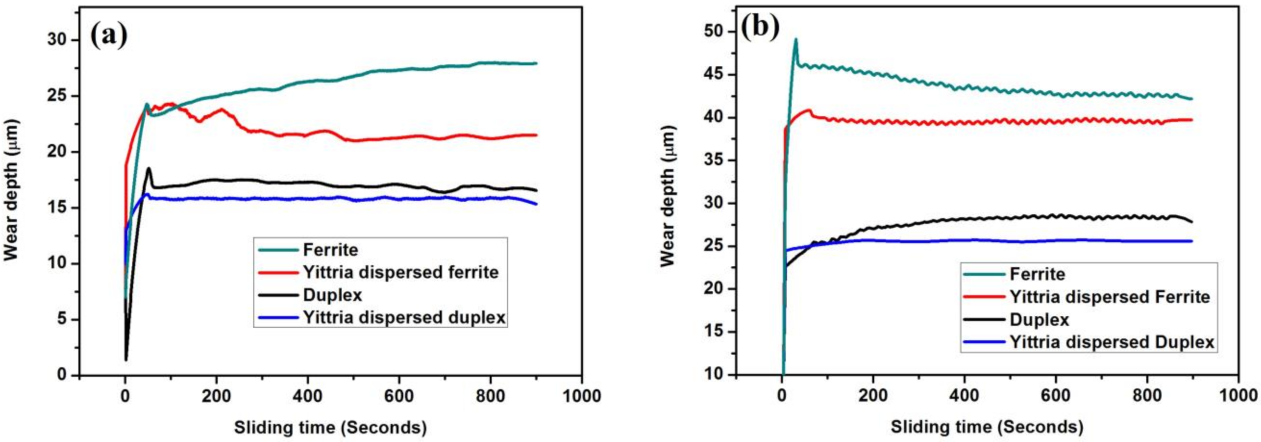

Figure 5.14 Variation of wear depth of yittria dispersed and yittria free duplex and ferritic stainless steel against sliding time at a applied load of (a) 40N (b) 60N respectively

From the Figure 5.14 it is confirmed that increase in applied load from 40 to 60N decreases the wear resistance of all the four stainless steels. The equation (1) explicates that increase in normal applied load increases the frictional force as shown in the Figure 5.14. Chowdhury et al. [2] reported that co-efficient of friction decreases with the increase in applied load and it increases with increase in sliding velocity. Therefore, increase in applied load increases the wear depth and thereby decreases the wear resistance as shown in the Figure 5.14 (a) and 5.14 (b). The wear depth of duplex, ferritic, yittria duplex and yittria ferritic stainless steels at 40N applied load were found to be 19, 28, 16 and 24µm respectively. Similarly, at 60N applied load the wear depth were found to be 29, 49, 26 and 41µm respectively.

We also investigated the effect of yittria dispersion on the wear resistance of duplex and ferritic stainless steel. We also know that addition of yittria in stainless steel improves the density and hardness through a strong yittria-stainless steel bonding. Therefore, the impingement of Rockwell indenter is less on yittria dispersed stainless steel than yittria free stainless steel. Hence, yittria dispersed stainless steel shows lesser wear depth than respective yittria free stainless steel as shown in the figure.

5.4.1.2 Mechanism of wear

The morphology of worn surface and wear debris produced by the yittria dispersed and yittria free stainless steel have been investigated using SEM to study the wear mechanism and wear modes. Figure 5.15 (a-d) represents the SEM images of worn surface of yittria dispersed and yittria free duplex and ferritic stainless steel respectively at 40N applied load. From the SEM microstructures of worn surface it is found that all the four stainless steels follow abrasive wear mechanism with ploughing mode. The degree of ploughing depends upon the strength of the material; stronger the material, lesser will be the ploughing impression. Yittria dispersed stainless steels undergo mild ploughing compared to their respective yittria free stainless steels due to their hard nature (confirmed by hardness study). On the other hand, we also investigated the effect of applied load on the morphology of wear surface.

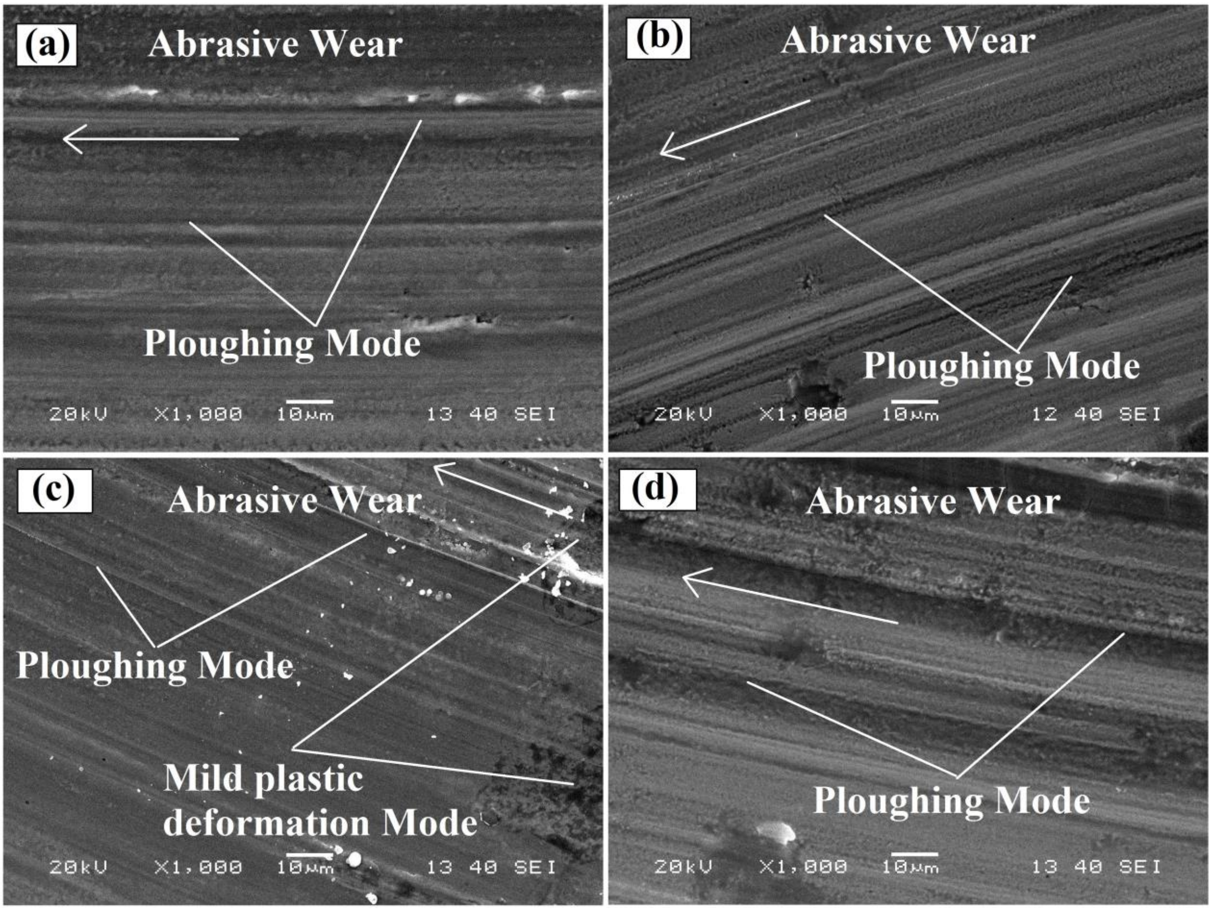

Figure 5.15 SEM worn surface of (a) Duplex (b) Ferritic (c) Yittria dispersed duplex (d) Yittria dispersed ferritic stainless steel respectively at 40N applied load

Figure 5.16 (a-d) represents the SEM microstructure of worn surfaces of yittria dispersed and yittria free duplex and ferritic stainless steel at 60N applied load. From the SEM microstructure (Figure 5.15 and Figure 5.16) it is observed that the impact of wear during 60N applied load is more compared to wear during 40N applied load. As seen from the micrographs that the failure is severe at 60N applied load than 40N due to the high frictional force. All the stainless steel samples at a load of 60N follow abrasive and mild oxidative mechanism along with ploughing and plastic deformation modes as shown in the Figure 5.16. The stainless steels with maximum density and hardness undergo oxidation easily because the material worn out as small particles instead of flakes likes ductile materials. The surface area and surface energy of these small particles is higher than flakes; hence these wear debris undergo oxidation very easily. The produced wear debris trammel in between the two contacting surfaces and break the contacting interface to very small sizes and rapidly oxidize both wear debris and wear track surfaces [4]. Therefore, we performed EDS to quantify the amount of oxygen present on the wear surface.

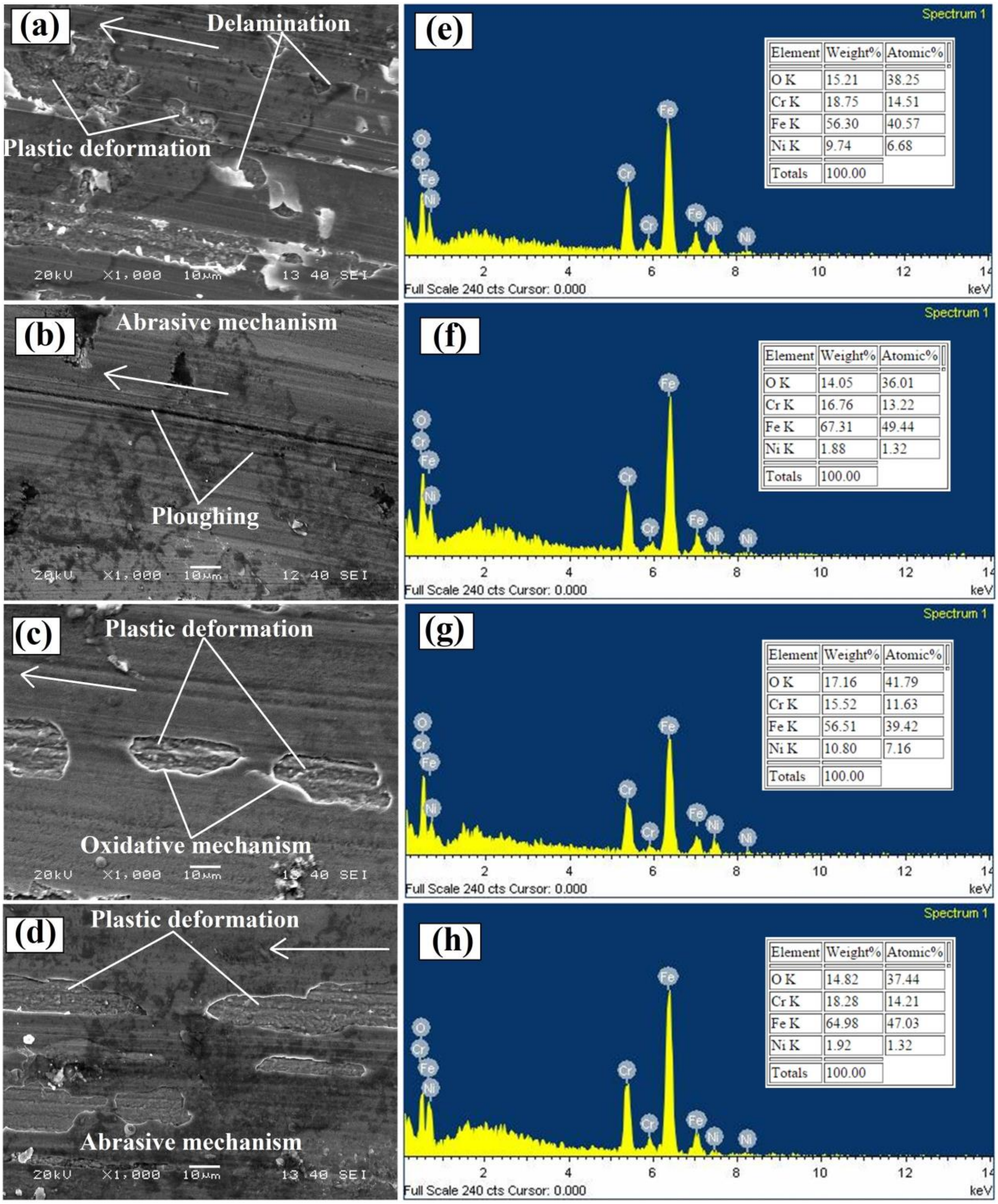

(e)

Element	Weight%	Atomic%
O K	15.21	38.25
Cr K	18.75	14.51
Fe K	56.30	40.57
Ni K	9.74	6.68
Totals	100.00	

(f)

Element	Weight%	Atomic%
O K	14.05	36.01
Cr K	16.76	13.22
Fe K	67.31	49.44
Ni K	1.88	1.32
Totals	100.00	

(g)

Element	Weight%	Atomic%
O K	17.16	41.79
Cr K	15.52	11.63
Fe K	56.51	39.42
Ni K	10.80	7.16
Totals	100.00	

(h)

Element	Weight%	Atomic%
O K	14.82	37.44
Cr K	18.28	14.21
Fe K	64.98	47.03
Ni K	1.92	1.32
Totals	100.00	

Figure 5.16 SEM and EDS spectra of worn surface of (a, e) Duplex (b, f) Ferritic (c, g) Yittria dispersed duplex (d, h) Yittria dispersed ferritic stainless steel respectively at 60N applied load

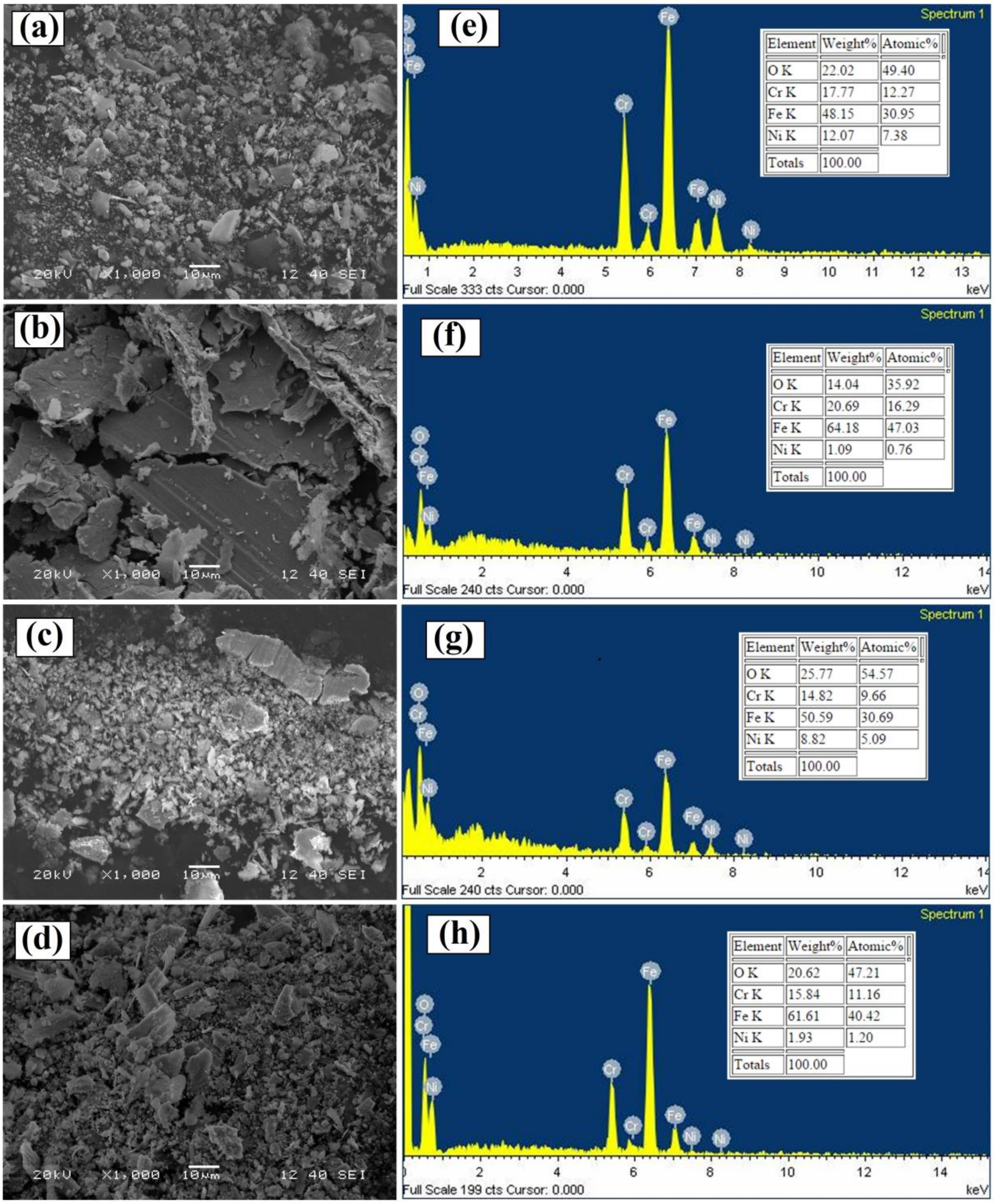

(e)

Element	Weight%	Atomic%
O K	22.02	49.40
Cr K	17.77	12.27
Fe K	48.15	30.95
Ni K	12.07	7.38
Totals	100.00	

(f)

Element	Weight%	Atomic%
O K	14.04	35.92
Cr K	20.69	16.29
Fe K	64.18	47.03
Ni K	1.09	0.76
Totals	100.00	

(g)

Element	Weight%	Atomic%
O K	25.77	54.57
Cr K	14.82	9.66
Fe K	50.59	30.69
Ni K	8.82	5.09
Totals	100.00	

(h)

Element	Weight%	Atomic%
O K	20.62	47.21
Cr K	15.84	11.16
Fe K	61.61	40.42
Ni K	1.93	1.20
Totals	100.00	

Figure 5.17 SEM and EDS spectra of wear debris of (a, e) Duplex (b, f) Ferritic (c, g) Yittria dispersed duplex (d, h) Yittria dispersed ferritic stainless steel respectively at 60N applied load

Figure 5.16(e-h) represents the EDS spectra of worn surfaces of duplex, ferritic, yittria duplex and yittria ferritic stainless steel tested at 60N applied load. The oxygen percentage of duplex and yittria dispersed duplex stainless steel is found to be 15 and 17% respectively. Similarly, the oxygen percentage of ferritic and yittria dispersed ferritic stainless steel is found to be 14 and 15% respectively. Figure 5.17 (a-d) represents the SEM micrographs of wear debris of duplex, ferritic, yittria duplex and yittria ferritic stainless steel produced at 60N applied load. Duplex and yittria dispersed duplex stainless steels are hard and brittle and produce wear debris in the form of small particles with maximum surface area. But, ferritic and yittria dispersed ferritic stainless steel produce wear debris as big flake like structure due to their soft and ductile nature. Therefore, oxygen percentage of wear debris produced by ferritic and yittria dispersed ferritic stainless steel is less compared to duplex and yittria dispersed duplex stainless steel. Figure 5.17 (e-h) represents the EDS spectra of wear debris of duplex, ferritic, yittria duplex and yittria ferritic stainless steel produced at 60N applied load. The wear debris of duplex and yittria dispersed duplex stainless steel show oxygen percentage of 22 and 26% respectively. Similarly, the oxygen percentage of ferritic and yittria dispersed ferritic stainless steel is found to be 14 and 21% respectively. During 40N applied load, the loss of wear debris is very negligible therefore wear debris were collected at 60N applied load to study the wear mechanism.

5.5. Summary and conclusions

The following conclusions can be made from the present investigation:

a) There is an increase in density, hardness, rate of phase transformation (α-Fe to γ-Fe) and finally increase in wear resistance of stainless steel when temperature for conventional sintering increases from 1000 to 1400°C.

b) Wear depth increases with increase in applied load from 10 to 20N for conventional sintered stainless steels.

c) Conventional sintering conducted in nitrogen atmosphere at 1000°C increases the volume percentage of austenitic, density and hardness than sintering under argon atmosphere.

d) Stainless steel sintered under nitrogen atmosphere exhibits more wear resistance than the stainless steel sintered under argon atmosphere.

e) The wear debris produced in duplex and ferritic steels are flake shape due to soft nature, whereas particle shape wear debris is generated in case of yittria dispersed duplex steel.

f) Wear mechanisms in both types of stainless steels are mainly abrasive and oxidative nature.

g) The amount of oxygen present on worn surfaces in duplex stainless steel at 10N applied load varies from 5 to 37% and at 20N load it varies from 20 to 44% with increase in sintering temperature from 1000 to 1400°C. The worn surface of duplex stainless steel sintered in nitrogen atmosphere at 1000°C show oxygen percentage of 9 at 10N and 20 at 20N applied loads respectively.

h) Stainless steel sintered through SPS method show great improvement in wear resistance properties when compared to conventionally sintered stainless steel samples.

References

1) C.X. Li, Surface Engineering, Wear and Wear Mechanism, The University of Birmingham, UK.

2) M.A. Chowdhury, D.M. Nuruzzaman, B.K. Roy, P.K. Dey, M.G. Mostafa, M.S. Islam, Md. Rashed Mia, Experimental Investigation on Friction and Wear of Stainless Steel 304 Sliding Against Different Pin Materials, *World Applied Sciences Journal.* 22 **(2013)** 1702-1710.

3) R. Shashanka, D. Chaira, Development of nano-structured duplex and ferritic stainless steels by pulverisette planetary milling followed by pressureless sintering, *Mater. Charact.* 99 **(2015)** 220–229.

4) M.C.M. Farias, R.M. Souza, A. Sinatora, D.K. Tanaka, The influence of applied load, sliding velocity and martensitic transformation on the unlubricated sliding wear of austenitic stainless steels, *Wear.* 263 **(2007)** 773–781.

5) T.F.J. Quinn, Review of oxidational wear, part 1: The origins of oxidational wear, *Tribol. Int.* 16 **(1983)** 257–271.

6) F.H. Stott, The role of oxidation in the wear of alloys, *Tribol. Int.* 31 **(1998)** 61–71.

7) J. Jiang, F.H. Stott, M.M. Stack, Some frictional features associated with the sliding wear of the nickel-base alloy N80A at temperatures to 250° C, *Wear.* 176 **(1994)** 185–194.

8) J. F. Archard, W. Hirst, The Wear of Metals under Unlubricated Conditions, *Proc. R. Soc. A.* 236 **(1956)** 397–410.

9) B. Wang, B. Yao, Z. Han, Annealing Effect on Wear Resistance of Nanostructured 316L Stainless Steel Subjected to Dynamic Plastic Deformation, *J. Mater. Sci. Technol.* 28 **(2012)** 871–877.

10) Hun Kim, Jong Hyun Choi, Jun Ki Kim, Hyun Seon Hong, Seon Jin Kim, Reciprocating sliding wear of Inconel 600 tubing in room temperature air, *J. Alloy. Compd.* 351 **(2003)** 309–313.

11) N. Kurgan, Effects of sintering atmosphere on microstructure and mechanical property of sintered powder metallurgy 316L stainless steel, *Mater. Des.* 52 **(2013)** 995–998.

12) J. Abenojar, F. Velasco, A. Bautista, M. Campos, J.A. Bas, J.M. Torralba, Atmosphere influence in sintering process of stainless steels matrix composites reinforced with hard particles, *Compos. Sci. Technol.* 63 **(2003)** 69–79.

13) E. Salahinejad, R. Amini, M.J. Hadianfard, Contribution of nitrogen concentration to compressive elastic modulus of 18Cr–12Mn–*x*N austenitic stainless steels developed by powder metallurgy, *Mater. Des.* 31 **(2010)** 2241–2244.

14) S.K. Karak, C.S. Vishnu, Z. Witczak, W. Lojkowski, J. Dutta Majumdar, I. Manna, Studies on wear behavior of nano-Y_2O_3 dispersed ferritic steel developed by mechanical alloying and hot isostatic pressing, *Wear.* 270 **(2010)** 5–11.

15) R. Shashanka. D. Chaira, Effect of sintering temperature and atmosphere on non-lubricated sliding wear of nano-yttria dispersed and yttria free duplex and ferritic stainless steel fabricated by powder metallurgy, *Tribol. T.* **(2016)** DOI:10.1080/10402004.2016.1168897.

CHAPTER 6

Corrosion study of spark plasma sintered duplex and ferritic stainless steel samples by linear sweep voltammetric method

6.1 Objectives and scope of the work

The microstructure and corrosion behaviour of spark plasma sintered yittria dispersed and yittria free duplex and ferritic stainless samples were studied. Corrosion studies were carried out in 0.5, 1 and 2M concentration of NaCl and H_2SO_4 solutions at different quiet time of 2, 4, 6, 8 and 10 seconds. Corrosion studies were performed for yittria free and yittria dispersed duplex and ferritic stainless steel samples by linear sweep voltammetry (LSV) method. Yittria dispersed stainless steel samples show more resistance to corrosion than yittria free stainless steel samples. The addition of yittria in stainless steel samples increases the corrosion resistance. Increase in reaction time from 2 to 10 seconds decreases the pitting potential because experimental setup remains active for 2, 4, 6, 8, 10 individual seconds and after that LSV starts showing readings. Hence more seconds means more reaction and less corrosion resistance. Similarly, as concentration of NaCl and H_2SO_4 increases from 0.5M to 2M the corrosion resistance decreases due to the availability of more Cl^{-} and SO_4^{-} ions at higher concentration. Corroded samples were then characterized by FESEM and optical microscopy to confirm the presence of corrosion region.

6.2 Corrosion study of yittria dispersed and yittria free stainless steel samples by LSV

Pitting corrosion is a process of localized accelerated dissolution of metal caused due to the result of a breakdown of the protective passive film on metal surface. The important steps involved in pitting process are breakdown of the passive film, metastable pitting and pit growth. The mechanism of pitting corrosion involves the dissolution of protective passive film and gradual acidification of the electrolyte caused by its insufficient aeration [1]. This increases the pH of the pits by increasing the anion concentration.

6.2.1 Mechanism of pitting corrosion in stainless steel

In other words, Pitting corrosion is a process of depleting passive layer of the stainless steel aroused by an electrolyte rich in chloride and or sulphides. Figure 6.1 depicts the mechanism of pitting corrosion process in stainless steel. There is a formation of protective Cr_2O_3 passive layer. But in presence of anions and proper voltage the passive layer breaks and the voltage required to deplete the passive layer is called as pitting voltage. After breaking of Cr_2O_3 layer, initiation of pit starts. This increases the anion concentration (Cl^{-}) in the electrolyte and pit grows further. But in some cases, re-passivation of pit takes place and this partially improves the corrosion resistant properties of stainless steel.

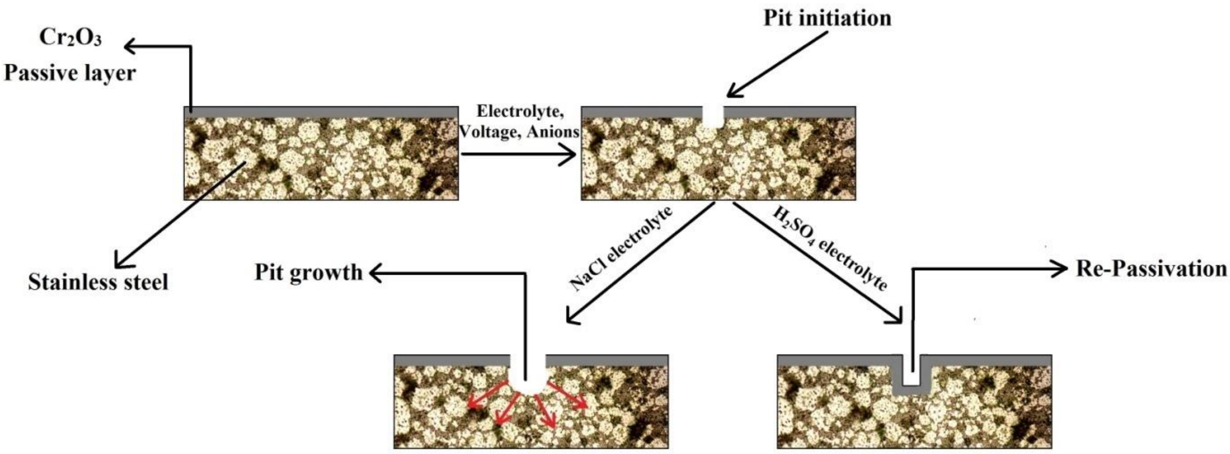

Figure 6.1 Mechanism of pitting corrosion in stainless steel samples

Some of the reactions responsible for corrosion in stainless steel at NaCl electrolytes are shown below.

Anodic reaction: $Fe \longrightarrow Fe^{2+} + 2e^{-}$ (Dissolution of Iron)

$Fe^{2+} + 2H_2O \longrightarrow FeOH^{+} + H_3O^{+}$

Formation of $FeOH^{+}$ is mainly responsible for the sudden increase in current due to the dissolution of Fe metal.

Cathodic reaction: $O_2 + 2H_2O + 4e^{-} \longrightarrow 4OH^{-}$

Main reaction: $Fe^{2+} + 2Cl^{-} \longrightarrow FeCl_2$

$FeCl_2 + 2H_2O \longrightarrow Fe(OH)_2 + 2HCl$

Formation of $Fe(OH)_2$ increases the pH of the electrolyte inside a pit from 6 to 2, which induces further corrosion process.

But in case of H_2SO_4, re-passivation of passive layer takes place due to the following reactions,

Anodic reaction: $Fe \longrightarrow Fe^{2+} + 2e^{-}$ (Dissolution of Iron)

Cathodic reaction: $2H^{+} + 2e^{-} \longrightarrow H_2$

The main corrosion reaction gives the products iron sulphate and hydrogen gas as shown below.

Main reaction: $Fe + H_2SO_4 \longrightarrow FeSO_4 + H_2$

There is a formation of $FeSO_4$ thin layer on the stainless steel surface, which acts as a passive protective layer for corrosion. But the liberated hydrogen gas scrub off the $FeSO_4$ layer and causes corrosion [2].

6.2.2 Effect of concentration of NaCl electrolyte solution

In the present work we studied the effect of reaction time (quiet time) and the effect of different concentration of NaCl electrolyte on pitting corrosion. The NaCl electrolytes of concentrations 0.5, 1 and 2M were prepared in double distilled water to study corrosion. All the consolidated stainless steel samples were polished to 4/0 grade finish and cleaned with distilled water before the experiment in each case. The stainless steel (working electrode) whose corrosion properties to be studied was kept inside the electrochemical cell containing NaCl electrolyte, counter electrode and reference electrode.

LSV was performed at a sweeping potential from 0.9 to 0V (adjusted according to the pitting potential) with different quiet time of 2, 4, 6, 8 and 10seconds. A curve of current and potential is obtained for each individual quiet time at constant concentration. Figure 6.2 (a-d) represent the LSV curve of current versus voltage variation of yittria dispersed and yittria free duplex and ferritic stainless steel samples at 0.5M NaCl electrolyte at different quiet time. As the potential sweeps from 0.9 to 0V, the current increases sharply a particular potential and that potential is called as pitting potential (E_P). The sharp increase in current is due to the availability of more electrons after passing through Cr_2O_3 layer. This results in pitting and it grows if the metal is unprotected.

The pitting corrosion process is evidenced by the LSV measurement method by sudden and drastic increase in pitting current (I_P) as shown in the Figure 6.2. E_P values of yittria duplex and ferritic stainless steel samples are found to be 1.45V and 0.64V respectively. Similarly, yittria free duplex and ferritic stainless steel samples have E_P value of 0.63V and 0.57V respectively. Yittria dispersed stainless steel samples show more E_P value than yittria free samples due to the presence of oxygen active yittria [3-6], which imparts more strength to interfacial bonding and forms strong oxide layer. Hence, more potential is required to break the oxide layer. Therefore, yittria dispersed stainless steel samples show maximum pitting potential. Higher the pitting potential more is the corrosion resistance [7].

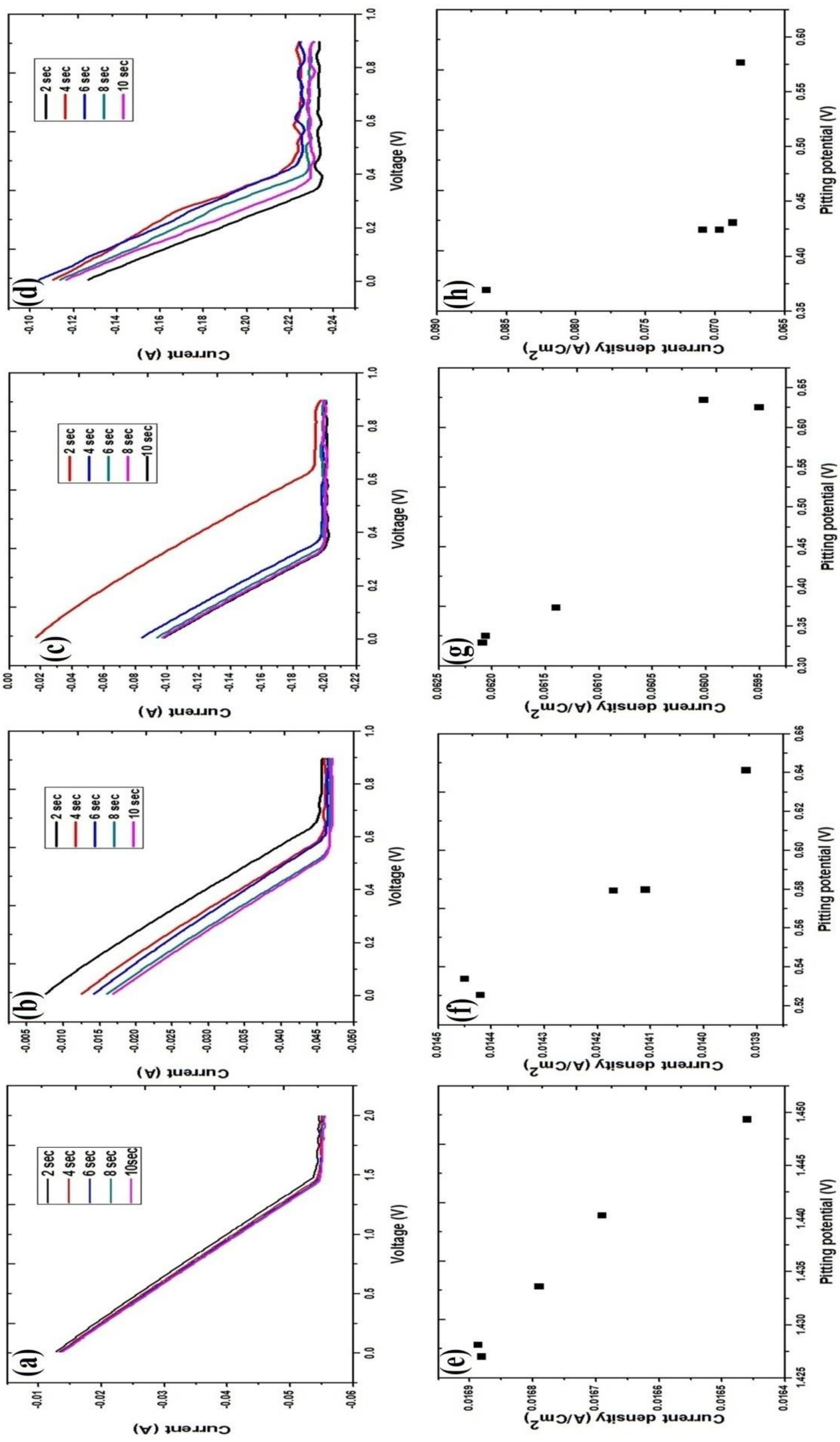

Figure 6.2 Potentiometric curves and current density vs. pitting potential graphs of (a)(e) Yittria dispersed duplex stainless steel, (b)(f) Yittria dispersed ferritic stainless steel, (c)(g) duplex stainless steel, (d)(h) ferritic stainless steel respectively at 0.5M NaCl solution

The effect of current density on E_P for all the four stainless steel samples was studied successfully. The current density was calculated using equation (1) as follows.

$$J = \frac{I}{A} \qquad \textbf{(1)}$$

Where, J is the current density, I is the pitting current and A is the area of working electrode used. Figure 6.2 (e-h) shows the effect of current density on E_P in case of yittria dispersed and yittria free duplex and ferritic stainless steel respectively. As the current density decreases both E_P and I_P increases. Similarly, whole experimental procedure was repeated for the same stainless steel samples but at 1M and 2M NaCl concentrations respectively.

Figure 6.3 (a-d) and Figure 6.3 (e-h) show the current vs. voltage graphs and current density vs. E_P curves of yittria dispersed and yittria free duplex and ferritic stainless steel samples at 1M NaCl concentration. E_P values of yittria dispersed duplex and ferritic stainless steel samples at 1M NaCl are 0.67V and 0.43V respectively and for yittria free duplex and ferritic stainless steel samples have E_P value of 0.57V and 0.19V respectively.

Similarly, Figure 6.4 (a-d) and Figure 6.4 (e-h) show the current versus voltage graphs and current density versus E_P curves of yittria dispersed and yittria free duplex and ferritic stainless steel samples at 2M NaCl concentration. Yittria dispersed duplex and ferritic stainless steel samples posses E_P value of 0.63V and 0.43V respectively. Similarly, for yittria free duplex and ferritic stainless steel samples have E_P value of 0.24V and 0.18V respectively. From the graphs it is clear that as the concentration of NaCl electrolyte increases from 0.5 to 2M, pitting potential for all the four stainless steel samples decrease due to the accelerated rate of corrosion reactions at higher concentrations.

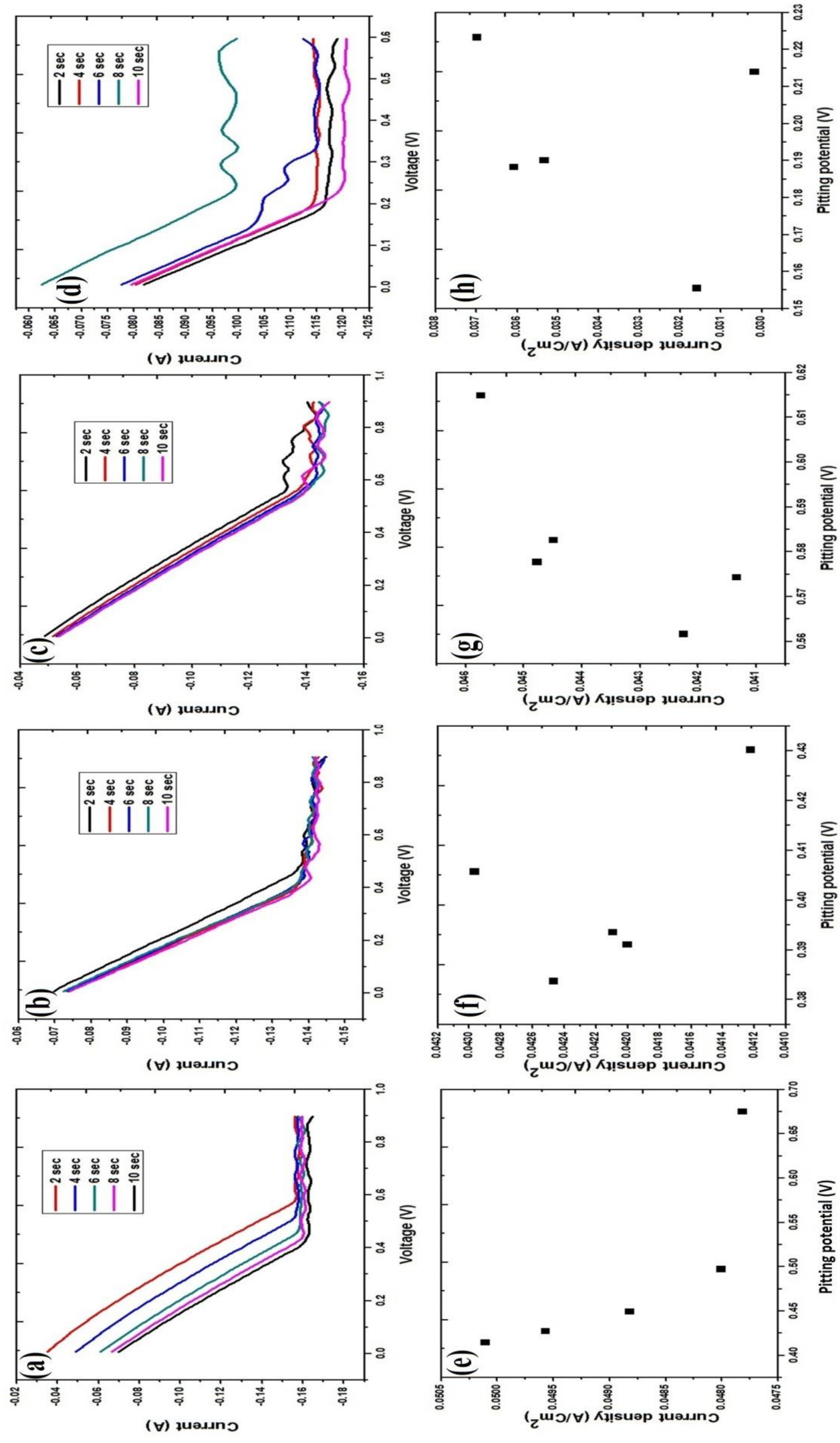

Figure 6.3 Potentiometric curves and current density vs. pitting potential graphs of (a)(e) Yittria dispersed duplex stainless steel, (b)(f) Yittria dispersed ferritic stainless steel, (c)(g) duplex stainless steel, (d)(h) ferritic stainless steel respectively at 1M NaCl solution

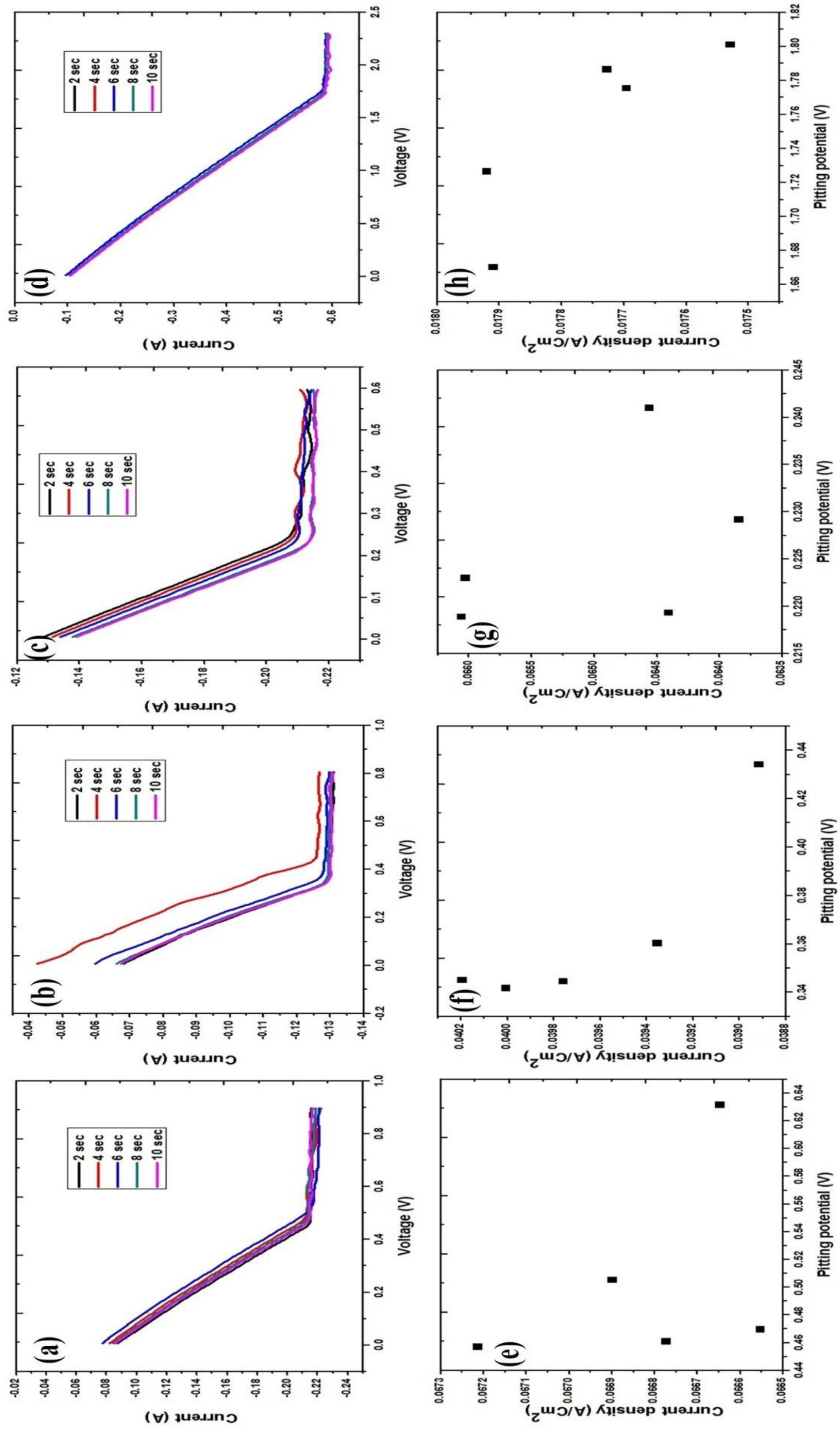

Figure 6.4 Potentiometric curves and current density vs. pitting potential graphs of (a)(e) Yittria dispersed duplex stainless steel, (b)(f) Yittria dispersed ferritic stainless steel, (c)(g) duplex stainless steel, (d)(h) ferritic stainless steel respectively at 2M NaCl solution

6.2.3 Effect of concentration of H_2SO_4 electrolyte solution

The corrosion studies were carried out in same electrochemical experimental set up and same condition as the corrosion studies conducted in NaCl electrolyte. But here NaCl electrolyte was replaced by H_2SO_4 electrolyte to study the effect of acid electrolyte on corrosion of stainless steel samples. The H_2SO_4 electrolytes of 0.5, 1 and 2M concentrations were prepared in double distilled water and used for the corrosion study of yittria dispersed and yittria free duplex and ferritic stainless steel samples.

A sweeping potential of 0.6 to 0V (adjusted according to the pitting potential) was applied in LSV with different quiet time of 2, 4, 6, 8 and 10seconds. A voltammetric curve was obtained for each individual quiet time at particular constant concentration. LSV curve of current versus voltage variation in yittria dispersed and yittria free duplex and ferritic stainless steel samples at 0.5M H_2SO_4 electrolyte after 2, 4, 6, 8 and 10seconds are shown in Figure 6.5 (a-d) respectively. From the figures it is clear that there is a sharp and sudden increase in the current between the potential 0.6 to 0V. E_P values of yittria duplex and ferritic stainless steel samples are 0.30V and 0.23V respectively at 0.5M H_2SO_4 electrolyte. Similarly, yittria free duplex and ferritic stainless steel samples have E_P value of 0.18V and 0.14V respectively. The mechanism of corrosion in H_2SO_4 and NaCl solutions are almost same for all the four SPS consolidated stainless steel samples. The only difference is extent of pitting, pitting potential and pitting current values. Pitting potential value obtained under H_2SO_4 electrolyte setup is comparatively low compared to the results obtained during NaCl electrolyte.

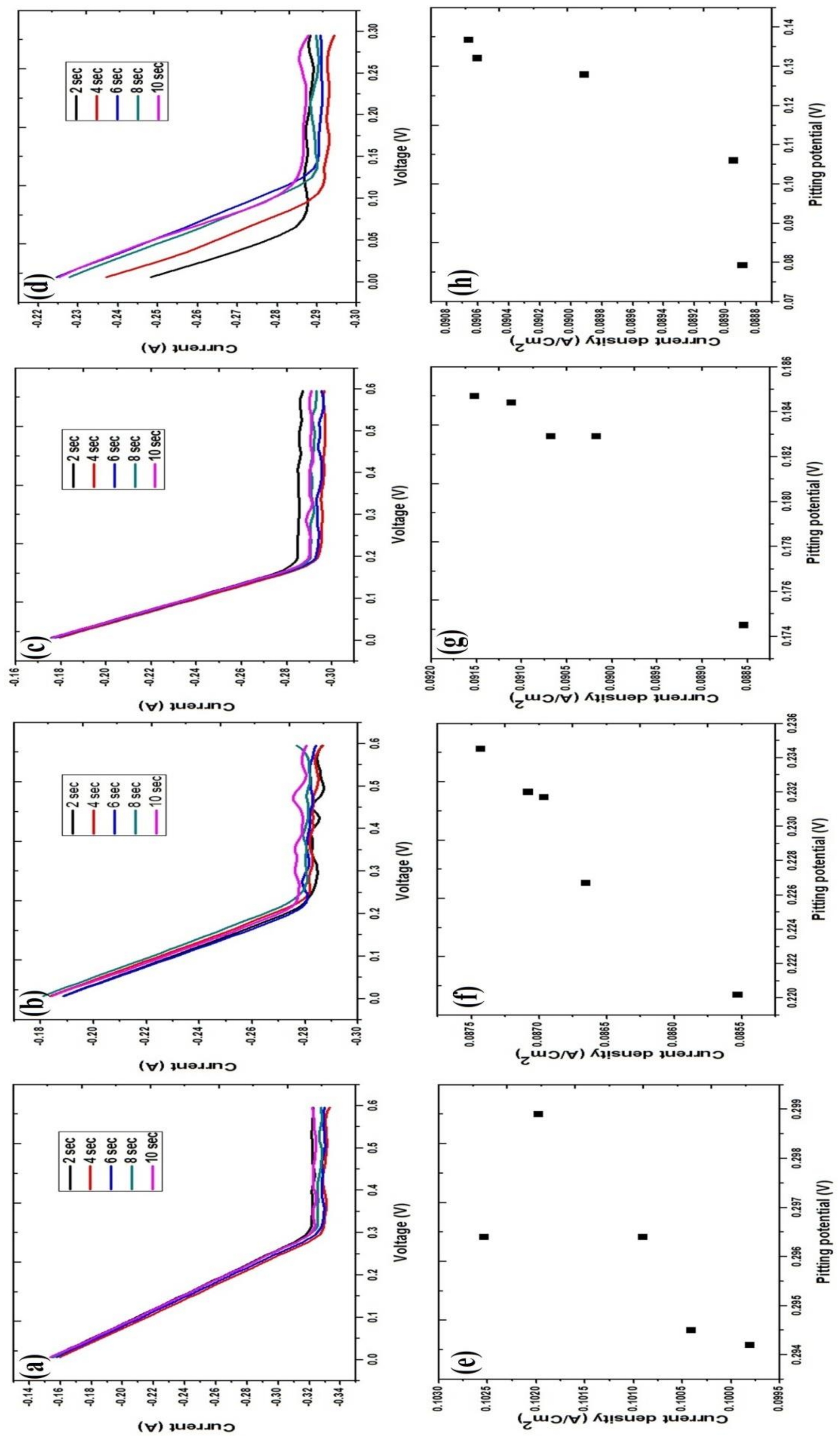

Figure 6.5 Potentiometric curves and current density vs. pitting potential graphs of (a)(e) Yittria dispersed duplex stainless steel, (b)(f) Yittria dispersed ferritic stainless steel, (c)(g) duplex stainless steel, (d)(h) ferritic stainless steel respectively at 0.5M H_2SO_4 solution

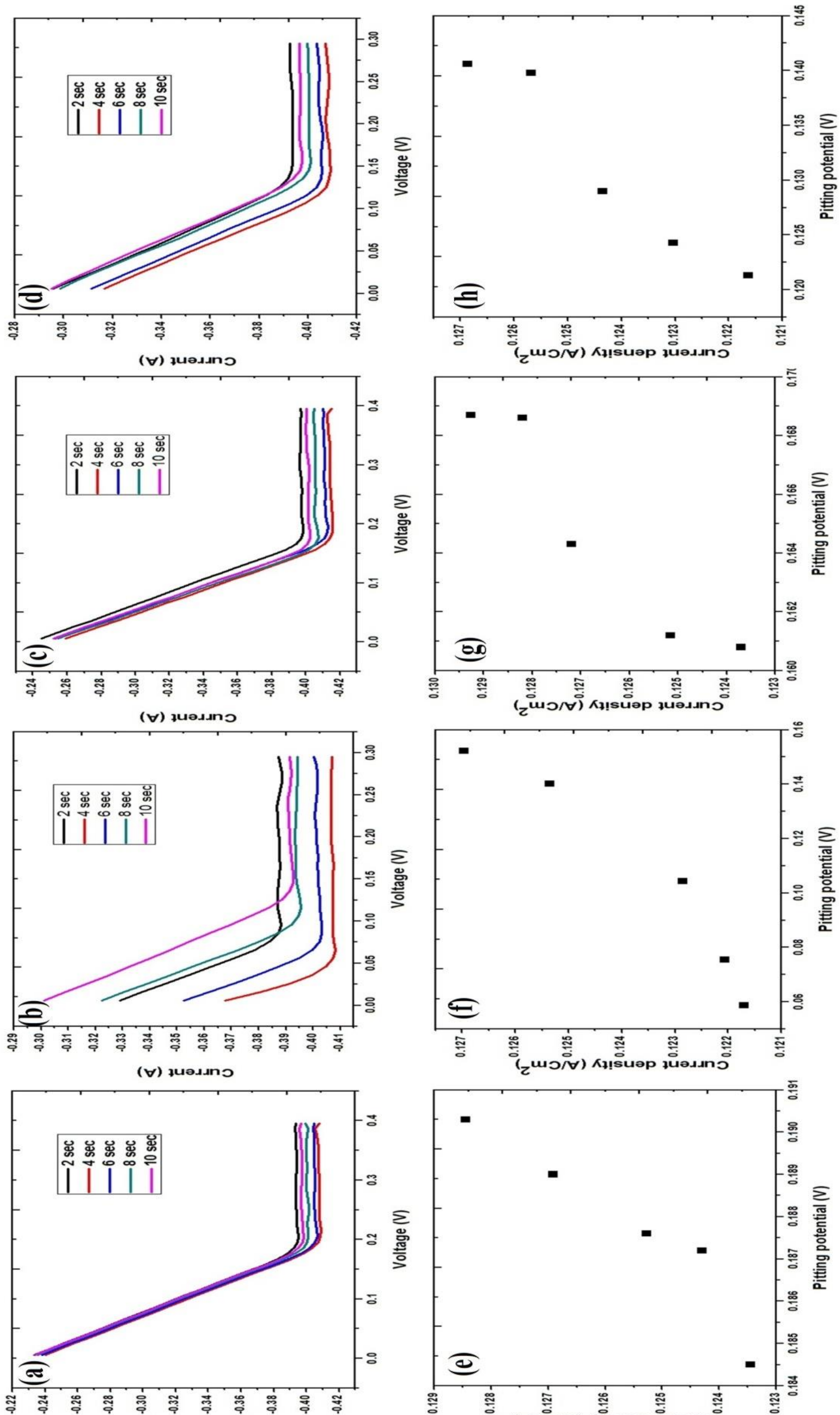

Figure 6.6 Potentiometric curves and current density vs. pitting potential graphs of (a)(e) Yittria dispersed duplex stainless steel, (b)(f) Yittria dispersed ferritic stainless steel, (c)(g) duplex stainless steel, (d)(h) ferritic stainless steel respectively at 1M H_2SO_4 solution

Stainless steel samples undergo corrosion easily in presence of H_2SO_4 than NaCl electrolyte [8]. This is due to the maximum acidic nature of H_2SO_4 than NaCl. In the beginning of the experiment itself H_2SO_4 reacts with stainless steel vigorously in presence of voltage and nucleates hydrogen bubbles during active dissolution of passive layer in acid media [9].

Current density was calculated using equation (1) and successfully studied the effect of current density on E_P. Figure 6.5 (e-h) represent the effect of current density on E_P of yittria dispersed and yittria free duplex and ferritic stainless steel respectively. As the current density decreases the pitting potential of all the samples also decreases with increase in pitting current. We successfully studied the effect of E_P at 1M and 2M H_2SO_4 concentrations by maintaining the same procedure as explained above. Figure 6.6 (a-d) and Figure 6.6 (e-h) show the current versus voltage graphs and current density versus E_P curves of yittria dispersed and yittria free duplex and ferritic stainless steel samples at 1M H_2SO_4 solution. E_P values of yittria dispersed duplex and ferritic stainless steel samples at 1M H_2SO_4 are found to be 0.19V and 0.15V respectively. Similarly, yittria free duplex and ferritic stainless steel samples show E_P values of 0.17V and 0.14V respectively. Figure 6.7 (a-d) and Figure 6.7 (e-h) show the current versus voltage graphs and current density versus E_P curves of yittria dispersed and yittria free duplex and ferritic stainless steel samples at 2M H_2SO_4 solution. Yittria dispersed duplex and ferritic stainless steel samples posses E_P value of 0.080V and 0.067V respectively. Similarly, yittria free duplex and ferritic stainless steel samples have E_P value of 0.028V and 0.013V respectively. From the graphs it is clear that as the concentration of H_2SO_4 increases from 0.5 to 1M both pitting potential and current density increases.

In case of 0.5 and 1M H_2SO_4 electrolyte the formed protective $FeSO_4$ layer bounds strongly to the surface of stainless steel along with Cr_2O_3 layer and hence hydrogen gas liberated in these concentrations is not enough to break the oxide layer to form a pit and initiate corrosion. Hence at 0.5 and 1M H_2SO_4 solution, the corrosion studies concluded with higher E_P and maximum current density. But in case of 2M H_2SO_4 solution, the hydrogen gas liberated is sufficient to scrub off the $FeSO_4$ layer at very low potential. Finally, all the four stainless steel samples show low pitting potential value at 2M H_2SO_4. The values of E_P and current density with different electrolytes are tabulated in Table 6.1.

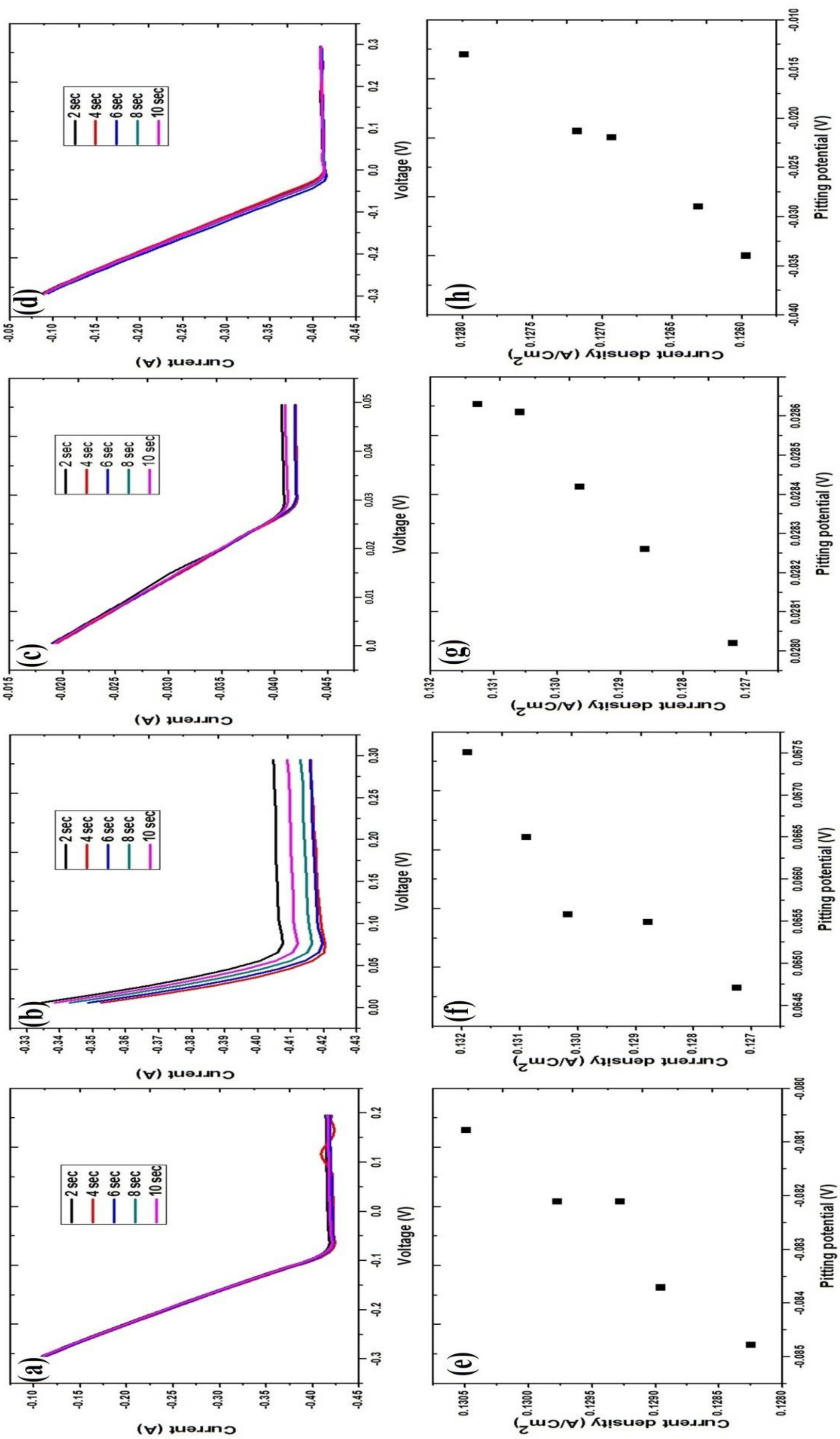

Figure 6.7 Potentiometric curves and current density vs. pitting potential graphs of (a)(e) Yittria dispersed duplex stainless steel, (b)(f) Yittria dispersed ferritic stainless steel, (c)(g) duplex stainless steel, (d)(h) ferritic stainless steel respectively at 2M H_2SO_4 solution

6.2.4 Microstructural analysis of SPS consolidated stainless steel samples after corrosion study

Figure 6.8 depicts the FESEM images of yittria dispersed and yittria free duplex and ferritic stainless steel samples. From FESEM images we can see the grey colour corroded regions clearly in all the samples. Figure 6.9 shows the EDS analysis of corroded regions of yittria dispersed duplex stainless steel. Quantification at these corroded regions confirms the presence of 27% oxygen as shown in the figure.

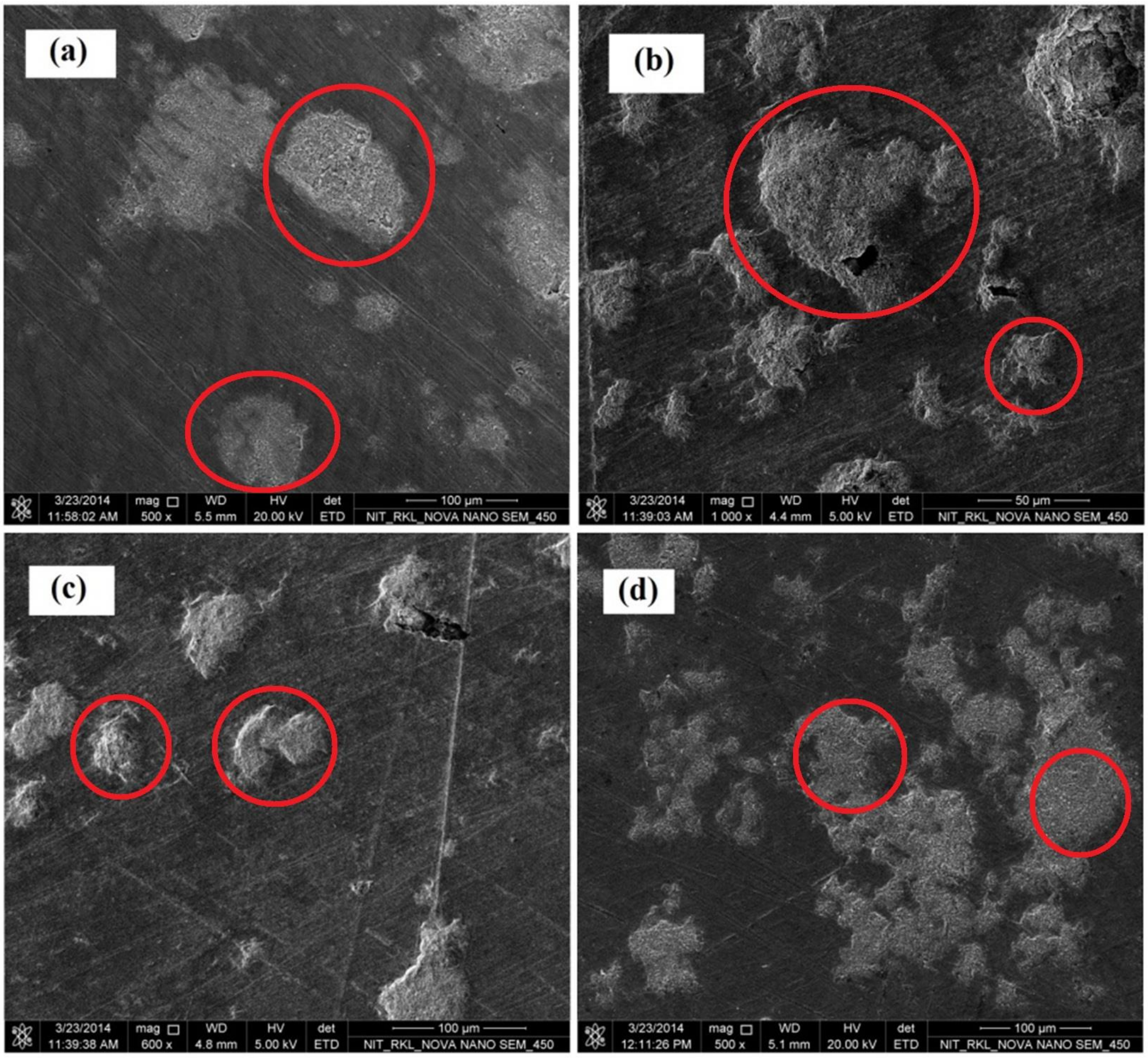

Figure 6.8 FESEM images of (a) Yittria dispersed duplex stainless steel (b) Yittria dispersed ferritic stainless steel (c) duplex stainless steel (d) ferritic stainless steel after corrosion in 2M H_2SO_4 solution (The grey colour regions marked by rings are corroded regions)

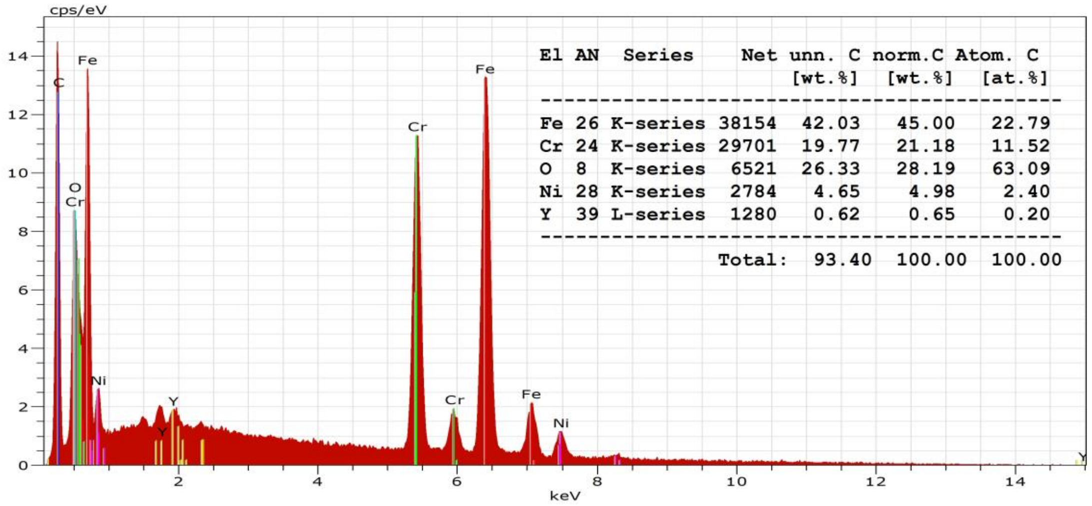

```
El AN  Series    Net unn. C norm.C Atom. C
                      [wt.%]  [wt.%]  [at.%]
--------------------------------------------
Fe 26 K-series 38154  42.03   45.00   22.79
Cr 24 K-series 29701  19.77   21.18   11.52
O   8 K-series  6521  26.33   28.19   63.09
Ni 28 K-series  2784   4.65    4.98    2.40
Y  39 L-series  1280   0.62    0.65    0.20
--------------------------------------------
               Total:  93.40  100.00  100.00
```

Figure 6.9 EDS analysis of corroded regions of yittria dispersed duplex stainless steel

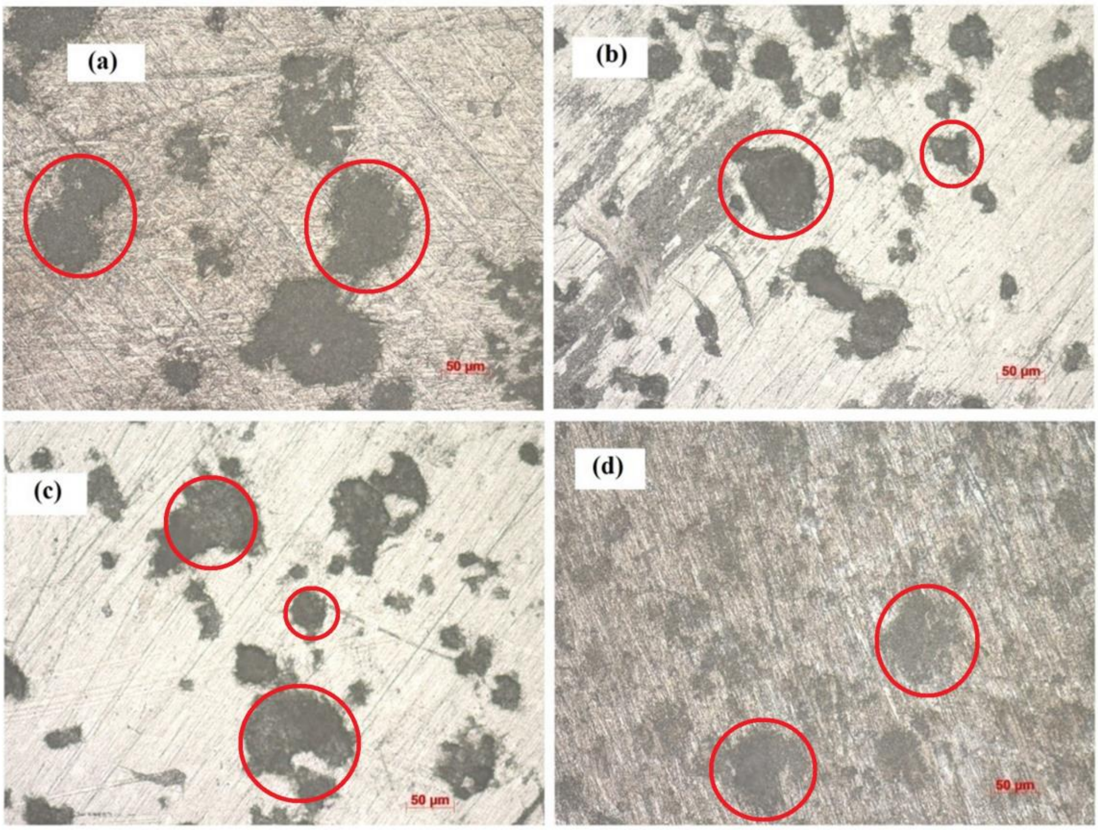

Figure 6.10 Optical microstructure study of (a) Yittria dispersed duplex stainless steel (b) Yittria dispersed ferritic stainless steel (c) duplex stainless steel (d) ferritic stainless steel after corrosion in 2M H_2SO_4 solution (The grey colour regions marked by rings are corroded regions)

Optical image analysis was carried out to study the microstructure of corroded yittria dispersed and yittria free duplex and ferritic stainless steel. Figure 6.10 and Figure 6.11 show the microstructure and phase analysis of stainless steel after corrosion. The black coloured region is corroded region containing iron oxide. All the stainless steel samples are having black region in the microstructure confirming the occurrence of corrosion during electrochemical measurement. Microstructural analysis was conducted to those stainless steel samples whose corrosion studies were performed by LSV method at 2M H_2SO_4 solution.

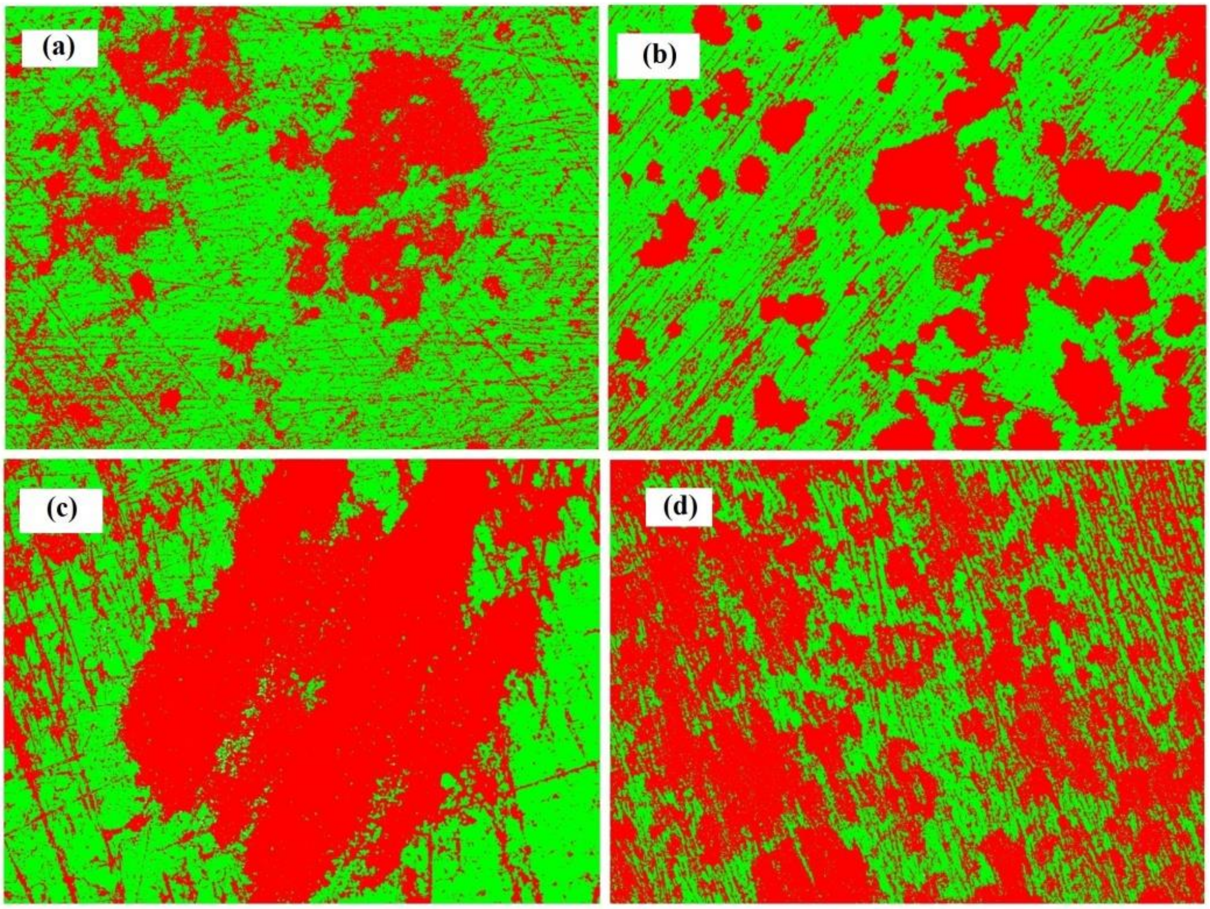

Figure 6.11 Optical phase analysis of (a) Yittria dispersed duplex stainless steel (b) Yittria dispersed ferritic stainless steel (c) duplex stainless steel (d) ferritic stainless steel after corrosion in 2M H_2SO_4 solution using Axio Vision Release software (Red clour=Corroded region, Green colour=Stainless steel surface)

According to corrosion studies, the rate of corrosion is more in yittria free stainless steel samples than yittria dispersed samples and it is confirmed by microstructural analysis. Phase analysis was carried out to study the volume fraction of iron oxide present in stainless steel samples. The presence of iron oxide volume percentage is more in yittria free stainless steel samples than yittria dispersed samples and the values are tabulated in Table 6.1. The volume fraction of iron oxide phase was determined by Axio Vision Release software. In Figure 6.11, red colour region corresponds to corroded (iron oxide) stainless steel part and green colour corresponds to unaffected stainless steel. There is a gradual decrease in the corrosion from yittria dispersed stainless steel to yittria free stainless steel samples.

Table 6.1 The values of E_P, I_P in NaCl and H_2SO_4 electrolytes at different concentrations

Condition	**Type of stainless steel**	**Volume fraction of Fe_2O_3 (%)**	**Concentration (M)**	**NaCl**		**H_2SO_4**	
				E_P (V)	**J (mA/cm^2)**	**E_P (V)**	**J (mA/cm^2)**
Yittria dispersed stainless steel	Duplex stainless steel	36.99	0.5	1.45	16.46	0.30	102.54
			1	0.67	47.81	0.19	128.45
			2	0.63	66.64	0.08	130.50
	Ferritic stainless steel	41.73	0.5	0.64	13.92	0.23	87.43
			1	0.43	41.22	0.15	126.97
			2	0.42	38.91	0.06	131.90
Yittria free stainless steel	Duplex stainless steel	60.55	0.5	0.63	60.02	0.18	91.52
			1	0.57	41.33	0.16	129.26
			2	0.24	64.56	0.02	131.25
	Ferritic stainless steel	64.10	0.5	0.57	86.45	0.14	90.66
			1	0.19	35.33	0.14	126.87
			2	0.18	17.52	0.01	128.0

6.3 Summary and conclusions

Mechanically alloyed duplex and ferritic stainless steel samples dispersed with yittria and without yittria were consolidated by SPS method at a load of 50MPa and 1000°C temperature under vacuum for 5 minutes. We successfully studied the corrosion properties of consolidated stainless steel samples by LSV method at different concentrations of NaCl and H_2SO_4 solutions. As the concentration of NaCl and H_2SO_4 electrolytes increases from 0.5 to 2M then pitting potential for all the four stainless steel samples decrease due to the accelerated rate of corrosion reactions at higher concentrations. In case of NaCl, E_P decreases with increasing current density but in case of H_2SO_4, E_P increases with increasing current density due to the formation of $FeSO_4$ protective layer along with Cr_2O_3 layer. At 0.5M NaCl, pitting potential (E_P) of yittria dispersed duplex and ferritic stainless steel samples are found to be 1.45V and 0.64V and yittria free duplex and ferritic stainless steel samples show E_P value of 0.63V and 0.57V respectively. Similarly, E_P value for yittria dispersed duplex and ferritic stainless steel samples at 0.5M H_2SO_4 are 0.30V and 0.23V respectively and yittria free duplex and ferritic stainless steel samples show E_P value of 0.18V and 0.14V respectively. Microstructural analysis by FESEM and optical microscope show corroded regions of stainless steel samples. Volume fraction of iron oxide (corrosion) present in yittria dispersed duplex and ferritic stainless steel samples are 37 and 41.73% respectively and that of yittria free duplex and ferritic stainless steel samples are 60.55 and 64.10% respectively.

References

1) F. Yuan Ma, Corrosive Effects of Chlorides on Metals, In Tech China, Pitting Corrosion, Prof. Nasr Bensalah (Ed.), **(2012)**, ISBN: 978-953-51-0275-5.

2) Sulphuric Acid on the Web, Knowledge for the Sulphuric Acid Industry, Corrosion, June 6, **(2005)**.

3) R. Liu, D.Y. Li, Effects of yttrium and cerium additives in lubricants on corrosive wear of stainless steel 304 and Al alloy 6061, *J. Mater Sci.* 35 **(2000)** 633– 641.

4) E. J. Felten, High-Temperature Oxidation of Fe-Cr Base Alloys with Particular Reference to Fe-Cr-Y Alloys, *J. Electrochem. Soc.* 108 **(1961)** 490–495.

5) C. S. Wukusick, J. F. Collins, An Iron-Chromium-Aluminum Alloy Containing Yttrium, *Mat. Res. Standard.* 4 **(1964)** 637–646.

6) J. M. Francis, W. H. Whitlow, The effect of yttrium on the high temperature oxidation resistance of some Fe-Cr base alloys in CO_2, *Corros. Sci.* 5 **(1965)** 701–710.

7) E. Blasco-Tamarit, D.M. García-Garcia, J. Garcia Anton, Imposed potential measurements to evaluate the pitting corrosion resistance and the galvanic behaviour of a highly alloyed austenitic stainless steel and its weldment in a LiBr solution at temperatures up to 150°C, *Corros. Sci.* 53 **(2011)** 784–795.

8) J.A. Cabral-Miramontes, J.D.B. Sánchez, C.A.P. Salas, G.K.P. Basulto, D.N. Mendoza, P.C.Z. Robledo, F.A. Calderón, J.G.C. Nava, Corrosion Behavior of AISI 409Nb Stainless Steel Manufactured by Powder Metallurgy Exposed in H2SO4 and NaCl Solutions, *Int. J. Electrochem. Sci.* 8 **(2013)** 564 – 577.

9) D.A. Jones, Principles and Prevention of Corrosion. New York, EE.UU. Maxwell Macmillan International Editions, **(1992)**.

CHAPTER 7

Electrochemical investigations of duplex and yittria dispersed duplex stainless steel at carbon paste electrode in detecting folic acid: A cyclic voltammetry study

7.1 Objectives and scope of the work

A carbon paste electrode (CPE) modified by nano structured duplex and yittria duplex stainless steel powder was used for the detection of folic acid (FA). Cyclic voltammograms evidenced better response of FA compared to bare CPE. Yittria duplex modified carbon paste electrode (YDMCPE) showed an excellent sensitivity than duplex modified carbon paste electrode (DMCPE) towards the oxidation of FA in 0.2M phosphate buffer (PBS) at 7.2 pH. Electro catalytic properties of analyte were investigated at 2, 4, 6, 8, 10 and 12mg concentrations of modifier. Stainless steel powders with 4mg modified carbon paste electrode show maximum anodic peak current and hence it is used as the modifier to study the electrochemical properties of FA analyte. We also studied the effect of scan rate, effect of concentration of both modifiers and analyte, effect of pH on anodic peak potential by using cyclic voltammetric technique. The above studies show that the duplex modified electrode exhibit splendid sensitivity towards FA and its response is fast, stable, reliable and resistant to material fouling and this can be applied for the real sample analysis in medical, pharmaceutical and biotechnological sectors. The adsorption-controlled processes and kinetic parameters of the duplex modified electrode were determined using electrochemical approaches.

7.2 Importance of folic acid (FA)

Folic acid (FA) is a part of vitamin B complex usually found in enriched foods, vitamin pills and employed in the treatment of megaloblastic anaemia during pregnancy, childhood, stroke, ischaemic heart disease or colorectal cancer and liver diseases [1]. Deficiency of FA causes gigantocytic anaemia, associated with leucopoenia, devolution of mentality, psychosis, etc [2]. Some of the common methods used to determine FA are ELISA (enzyme-linked immunosorbent assays) [3], capillary electrophoresis [4], high performance liquid chromatography with UV [5], micro-emulsion electro kinetic chromatography [6], spectrophotometer after coupling reaction with specific compounds [7], liquid chromatography with tandem mass spectroscopy, biosensor based determination [8]. Among all, cyclic voltammetric determination of FA is gaining more attention in analyzing electrochemical response of FA due to the low cost method, maximum sensitivity and more accurate measurements [9].

7.3 Fabrication of stainless steel carbon paste electrode

Milling of the duplex composition (Fe-18Cr-13Ni) was carried out in a specially designed DDPM. The electrochemical experiments were carried out using electrochemical work station CHI-660c model. All the experiments were carried out in a conventional three electrode system composed of working electrode (carbon paste electrode of 3mm diameter), a platinum wire as counter electrode and Ag/AgCl saturated KCl electrode as reference electrode. The carbon paste electrode (CPE) was prepared by hand-mixing of graphite powder and silicon oil at a ratio 70:30 by wt. in an agate mortar. The homogeneous carbon paste electrode was packed into a cavity of a homemade carbon paste electrode (3.0 mm in diameter). The duplex modified carbon paste electrode (DMCPE) and yittria dispersed duplex modified carbon paste electrode (YDMCPE) were prepared by mixing 2, 4, 6, 8, 10 and 12mg stainless steel powder individually with graphite powder and silicon oil. Surface was smoothed by rubbing slowly on a piece of weighing paper. The electrical contact was provided by copper wire connected to the paste at tube end. The bare CPE was prepared by without adding modifier.

7.4 Electrochemical investigation of DMCPE at FA

7.4.1 Cyclic voltammetric measurements

Figure 7.1 represents the cyclic voltammogram of BCPE and 4mg DMCPE. The dotted curve and straight line curve represents the cyclic voltammogram of 2mM FA at BCPE and DMCPE respectively. The anodic peak current of BCPE is 10µA and that of DMCPE is 12.60µA respectively. This is due to modification of electrode by duplex stainless steel. Any modifier added to carbon paste increases the surface area and surface active sites. This increases the electron transfer rate between carbon paste and electrolyte. Therefore, modified carbon paste electrode shows higher redox potential than bare carbon paste electrode. Hence, DMCPE can be used as folic acid sensor for detection of folic acid. We also studied the effect of scan rate, effect of concentration and effect of pH on the anodic peak current and potential.

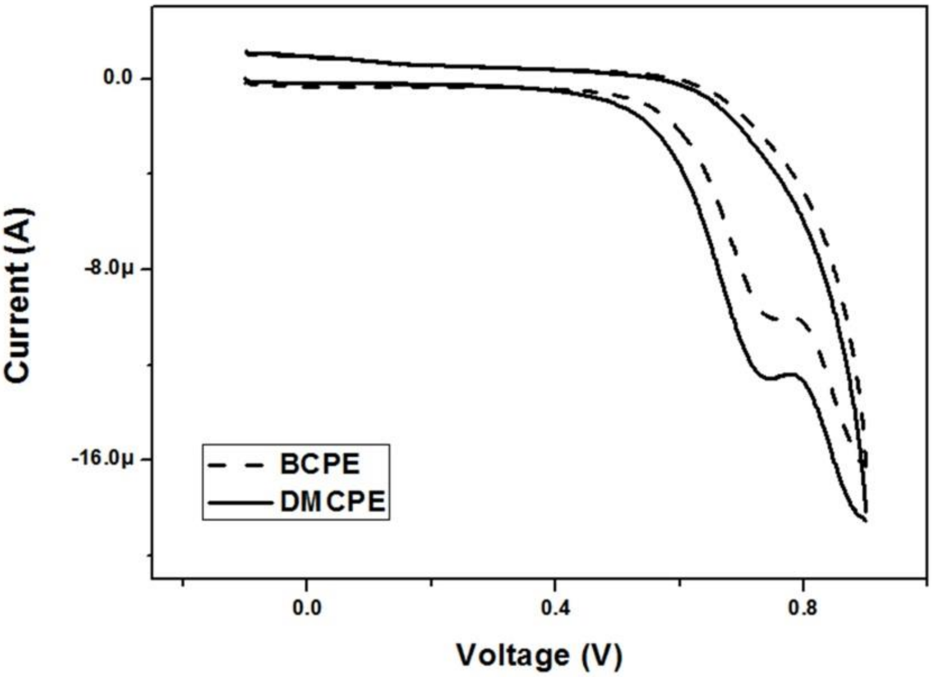

Figure 7.1 Cyclic voltammogram of bare carbon paste electrode (BCPE) and 4mg DMCPE in 2mM FA at $100mVs^{-1}$ and in PBS of pH 7.2

7.4.1.1 Effect of scan rate

Kinetic studies of electrode reactions can be investigated by varying the scan rates; hence scan rate effect is a very important parameter used to study the stability of the electrode. The effect of scan rate was performed by increasing the scan rate from 50 to $300mVs^{-1}$ for 2mM FA in phosphate buffer solution (PBS) of pH 7.2. Cyclic voltammogram of 2mM FA in 4mg DMCPE at different scan rates was shown in Figure 7.2 (a). The oxidation peak current and anodic peak potential increases linearly with increase in the scan rate from 50 to $300mVs^{-1}$. This linear increase of anodic peak current can be explained by Randles Sevick equation as follows [10]:

$$i_P = (2.69\times10^5)An^{3/2}D^{1/2}\upsilon^{1/2}C_o \qquad \textbf{(1)}$$

Where, 'i_p' is the peak current, 'n' is the stoichiometric number of electrons involved in the electrode reaction, 'A' is the area of electrode (cm^2), 'D' is the diffusion coefficient (cm^2s^{-1}), 'C_o' is the concentration (mol/ cm^3) and 'υ' is the scan rate (Vs^{-1}). According to the equation (1), peak current (i_p) is not only directly proportional to scan rate but also on area of electrode, diffusion coefficient, concentration and number of electrons involved in the electrode reaction.

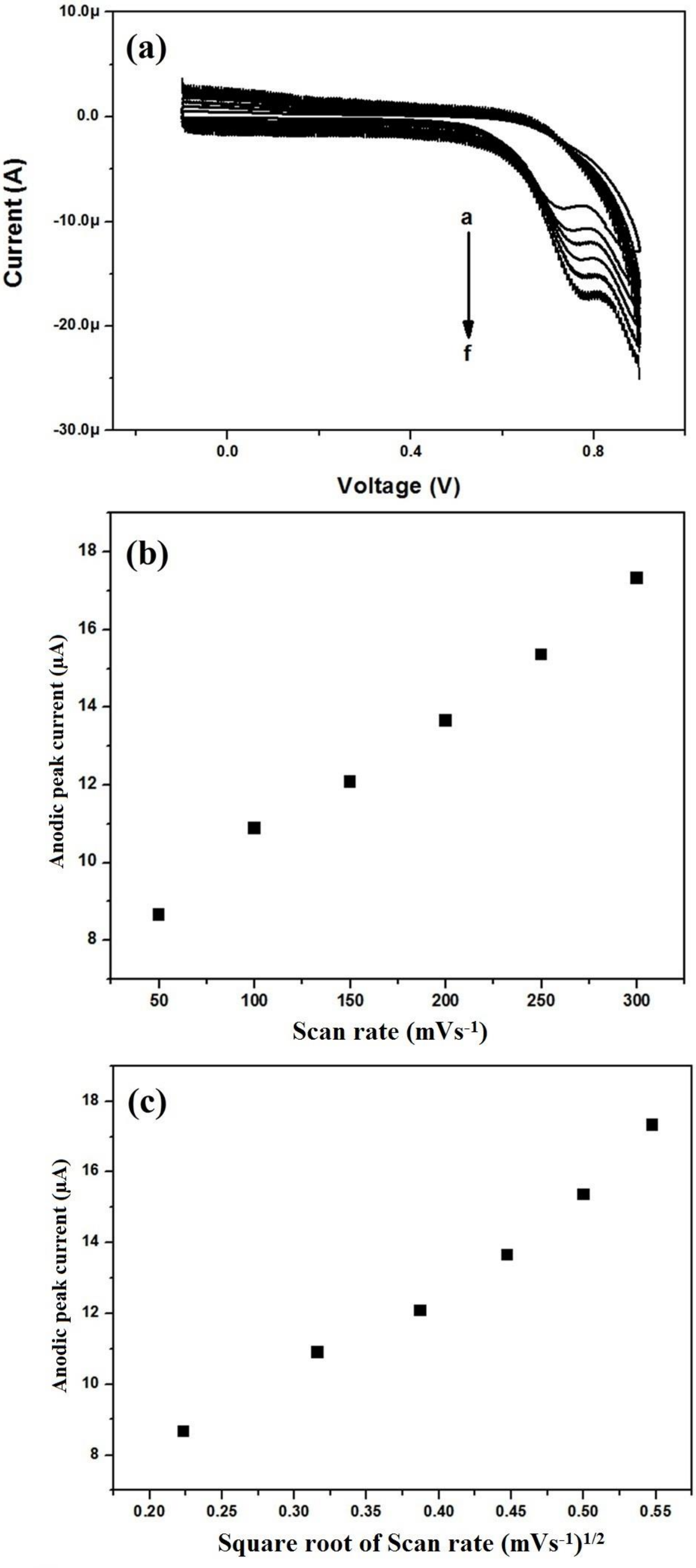

Figure 7.2 (a) Cyclic voltammogram of 2mM FA using 4mg DMCPE at 50 to 300mVs^{-1} scan rate (a=50, b=100, ..., f=300mVs^{-1}) in PBS of pH 7.2 (b) Plot of anodic peak current vs. scan rate (c) Plot of anodic peak current vs. square root of scan rate

Hence, anodic peak current increases linearly with increase in scan rate as shown in the Figure 7.2 (a). The oxidation peak current at 50mVs^{-1} is found to be 8.67µA and at 300mVs^{-1} is17.32µA respectively. Figure 7.2 (b) shows the plot of anodic peak current vs. different scan rate. The anodic peak current increases linearly with correlation coefficient 0.9931. Hence, this indicates that the electrode process is adsorption controlled [4]. During adsorption controlled reaction, the atoms or molecules adhere on the carbon paste electrode and increases the surface active sites of carbon paste electrode. As a result, transfer of electrons between surface active sites of carbon paste electrode and electrolyte increases and hence peak current increases linearly. The values of anodic peak current vs. scan rate are plotted and analyze the result by linear fit to get adjacent R-square (R^2) value. If the value $R^2 \approx 1$, then the electrode reaction is adsorption controlled. In Figure 7.2 (b), the anodic peak current increases linearly with $R^2=0.9931 \approx 1$ and therefore the electrode reaction is adsorption controlled. Similarly, linear increase in peak current with square root of scan rate gives diffusion controlled reaction (only when $R^2 \approx 1$). But Figure 7.2 (c) depicts the plot of anodic peak current vs. square root of scan rate with correlation coefficient 0.9880. This value is not equal to 1, therefore the electrode reaction is adsorption controlled.

7.4.1.2 Effect of concentration of folic acid

Electro catalytic behaviour of 4mg DMCPE was studied by varying the concentrations of FA. Figure 7.3 (a) depicts the cyclic voltammogram of FA at 2 to 2.6mM concentration at phosphate buffer solution (PBS) of pH 7.2 and scan rate of 100mVs^{-1}.

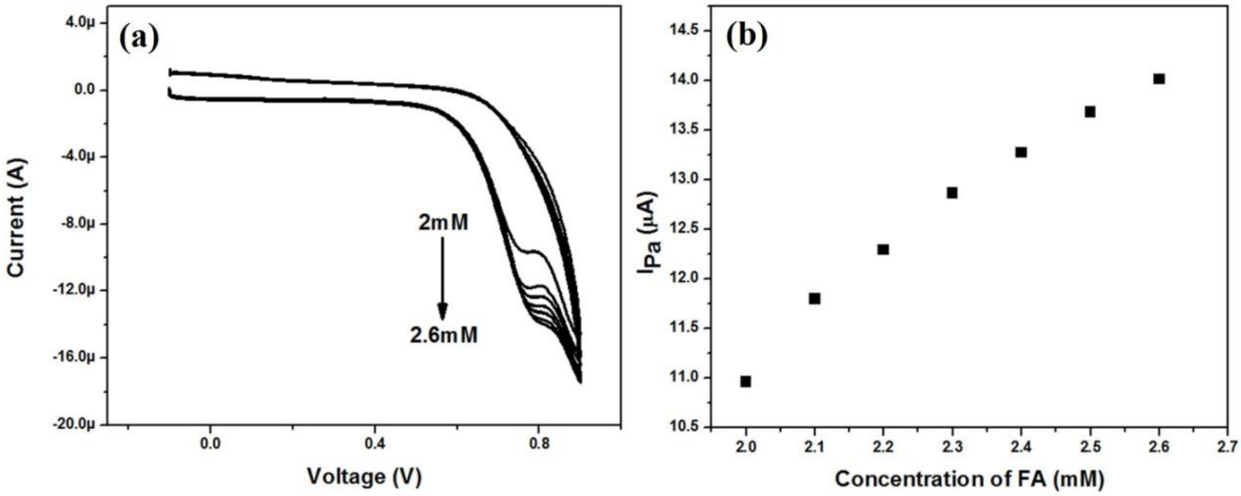

Figure 7.3 (a) Cyclic voltammogram of 2 to 2.6mM concentration of FA at 100mVs^{-1} in PBS of pH 7.2 using 4mg DMCPE (b) Plot of anodic peak current vs. concentration of FA

From the figure it is evident that, as the concentration of FA increases from 2 to 2.6mM (Increment of 0.1mM) then anodic peak current also increases along with anodic peak potential. Anodic peak potential at 2mM FA is found to be 768mV and at 2.6mM FA is 812mV respectively. Figure 7.3 (b) depicts the plot of anodic peak current vs. different concentration of FA. Plot shows the linear relationship between anodic peak current and different concentration of FA with correlation coefficient of 0.9757. The anodic peak current at 2mM FA is 10.96µA and at 2.6mM FA concentration it has been increased to 14.01µA. The increase in peak current is due to the availability of more FA molecules at higher concentration, hence more number of electrons involved in electrode reactions.

7.4.1.3 Effect of pH

The electro catalytic response of 4mg DMCPE in 2mM FA at different pH of PBS was studied successfully. Generally, redox potential shift towards the lower potential side at higher pH. Figure 7.4 (a) depicts the cyclic voltammogram of 2mM FA at different pH from 5.7 to 8. From the voltammogram it is evident that the oxidation peak potential of 2mM FA shifts towards a lower potential side with the increase of pH value. Because, FA undergoes oxidation very easily at higher pH values, higher the pH value higher will be the oxidation rate of FA. Figure 7.4 (b) represents the plot of different pH vs. anodic peak potential of 2mM FA at scan rate of 100mVs^{-1}. The Anodic peak potential decreases linearly from pH 5.7 to 8 with correlation coefficient of 0.9487. The oxidation peak potential at pH 5.7 is 753mV and at pH 8 it is decreased to 578mV respectively.

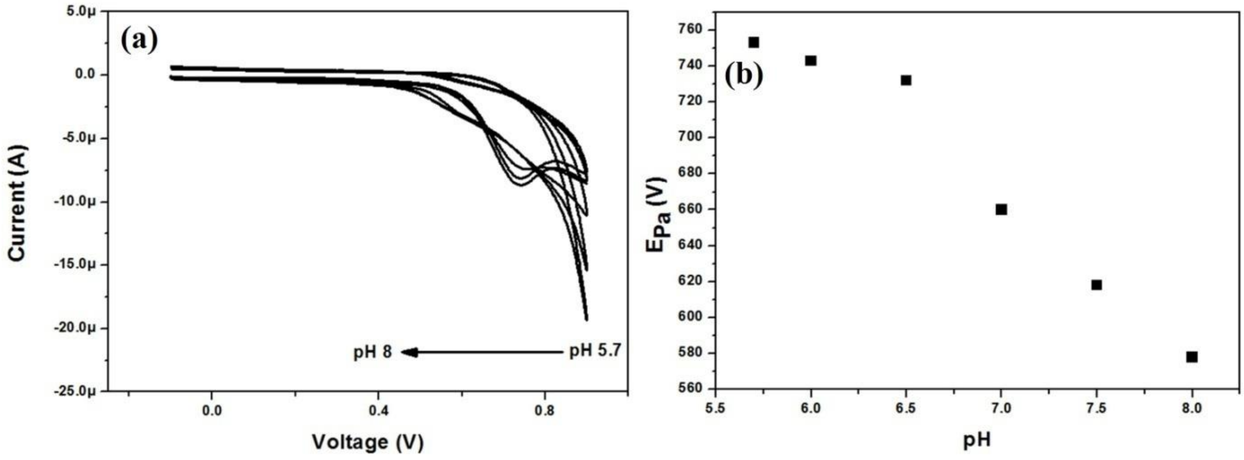

Figure 7.4 (a) Cyclic voltammogram of 2mM FA at different pH of PBS buffer solutions at 100mVs^{-1} using 4mg DMCPE (b) Plot of anodic peak current vs. pH from values 5.7 to 8

7.5 Electrochemical investigation of YDMCPE at FA

7.5.1 Microstructure study

Figure 7.5 (a) and 7.5 (b) shows the SEM images of BCPE and YDMCPE respectively. Figure depicts irregular surface of BCPE due to the graphite flakes and DMCPE surface is flat and regular shape with graphite flakes and yittria dispersed duplex stainless steel powder. This difference in surface appearance is due to the use of modifier, which results in easy movement of electrons from carbon paste to electrolyte and vice versa.

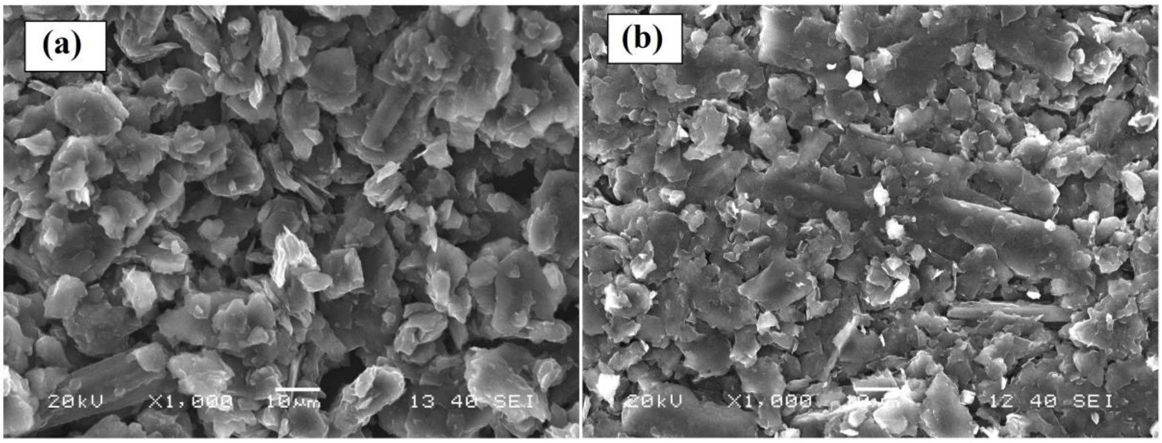

Figure 7.5 SEM micrographs of (a) BCPE and (b) YDMCPE

7.5.2 Cyclic voltammetric measurements

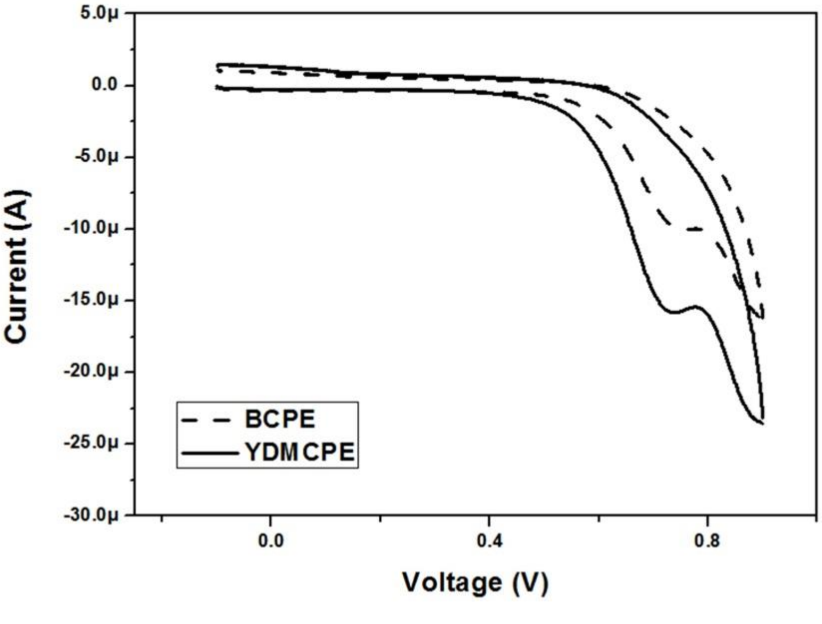

Figure 7.6 Cyclic voltammogram of bare carbon paste electrode (BCPE) and 8mg YDMCPE in 2mM FA at $100mVs^{-1}$ and in PBS of pH 7.2

Figure 7.6 depicts the cyclic voltammogram of BCPE and 8mg YDMCPE. The oxidation peak current of 8mg YDMCPE at 2mM FA shows maximum current sensitivity than BCPE and 4mg DMCPE. The anodic peak current of BCPE is 10µA, DMCPE is 12.60µA (Figure 7.1) and YDMCPE is 15.87µA respectively.

7.5.2.1 Effect of scan rate

Figure 7.7 (a) shows the cyclic voltammogram of 2mM FA at a scan rate of 50 to 300mVs^{-1} in PBS of pH 7.2. From the figure it is found that both anodic peak current and potential increases with increase in scan rate. The anodic peak potential increases from 724 to 780mV at 50 to 300mVs^{-1} respectively. Figure 7.7 (b) depicts the plot of scan rate vs. anodic peak current of 2mM FA at 100mVs^{-1} in PBS of pH 7.2 and it varies from 9.92µA at 50mVs^{-1} to 22.05µA at 300mVs^{-1} respectively. The correlation coefficient of the plot is 0.9937 and this reveals that electrode process is diffusion controlled. Similarly, Figure 7.7 (c) represents the plot of square root of scan rate vs. anodic peak current of 2mM FA and the correlation coefficient is found to be 0.9749.

7.5.2.2 Effect of Concentration of Folic acid

The anodic peak current of FA increases linearly with increase in the concentration of FA in an electrochemical cell. This is due to the availability of more FA molecules at higher concentration; hence electron transfer takes place readily between electrolyte and electrode. This in turn increases the anodic peak current at higher concentration of folic acid. Figure 7.8 (a) represents the cyclic voltammogram of 8mg YDMCPE at 2 to 2.6mM FA concentration. From the voltammogram it is found that anodic peak potential increase linearly with increase in concentration of FA. The oxidation potential increases from 764 to 778mV at 2mM to 2.6mM FA concentrations. Figure 7.8 (b) shows the plot of anodic peak current vs. concentration of FA and it shows linear relationship with correlation coefficient of 0.9850. The anodic peak current increases from 14.95µA to 18.49µA at 2mM to 2.6mM FA concentrations.

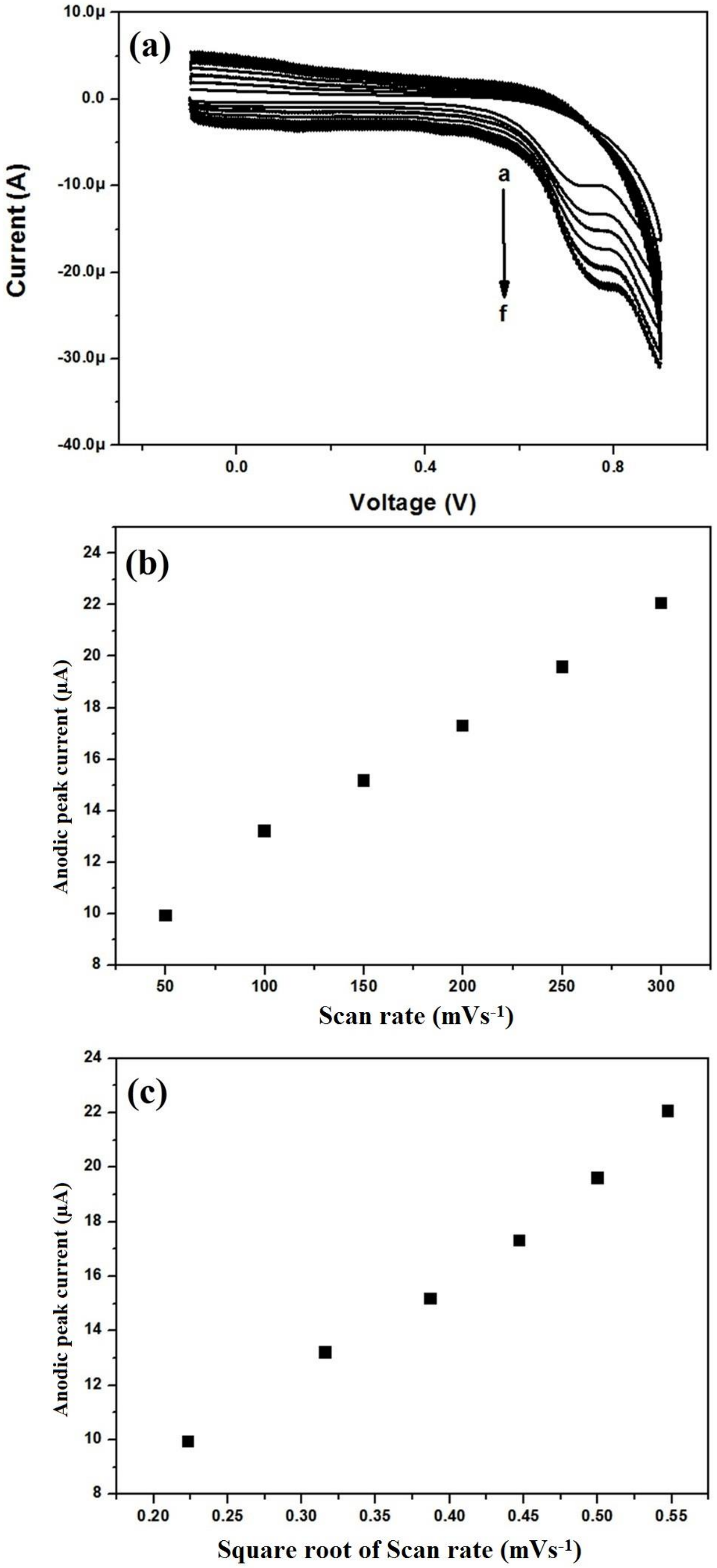

Figure 7.7 (a) Cyclic voltammogram of 2mM FA using 8mg YDMCPE at 50 to 300mVs^{-1} scan rate (a=50, b=100, ..., f=300mVs^{-1}) in PBS of pH 7.2 (b) Plot of anodic peak current vs. scan rate (c) Plot of anodic peak current vs. square root of scan rate

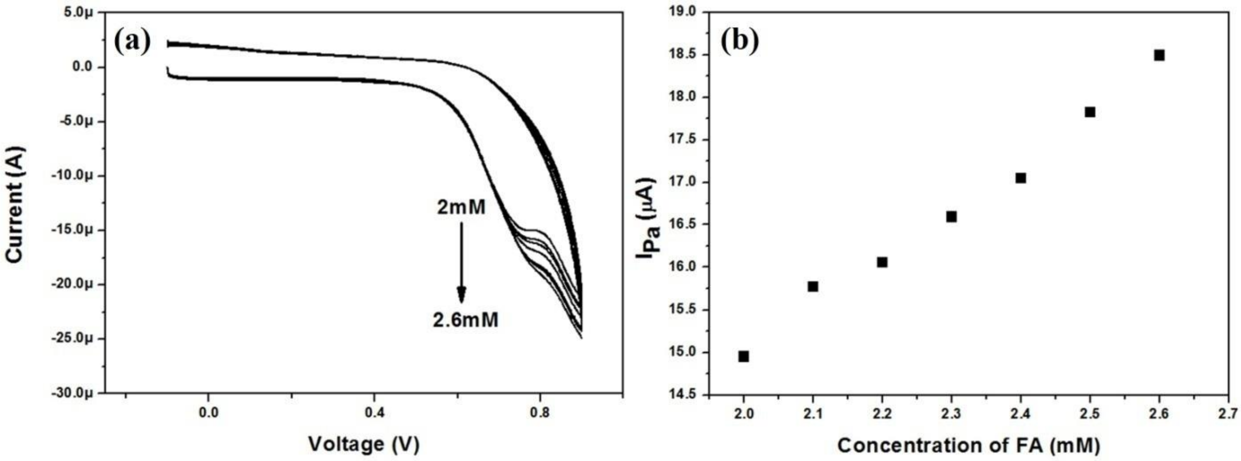

Figure 7.8 (a) Cyclic voltammogram of 2 to 2.6mM concentration of FA at 100mVs^{-1} in PBS of pH 7.2 using 8mg YDMCPE (b) Plot of anodic peak current vs. concentration of FA

7.5.2.3 *Effect of pH*

It is very important to know the optimum pH value at which the electrodes show maximum sensitivity, selectivity and less material fouling during electrochemical measurements. Therefore, we studied the electrochemical response of YDMCPE at pH 5.7 to 8 using 2mM FA at a scan rate of 100mVs^{-1}.

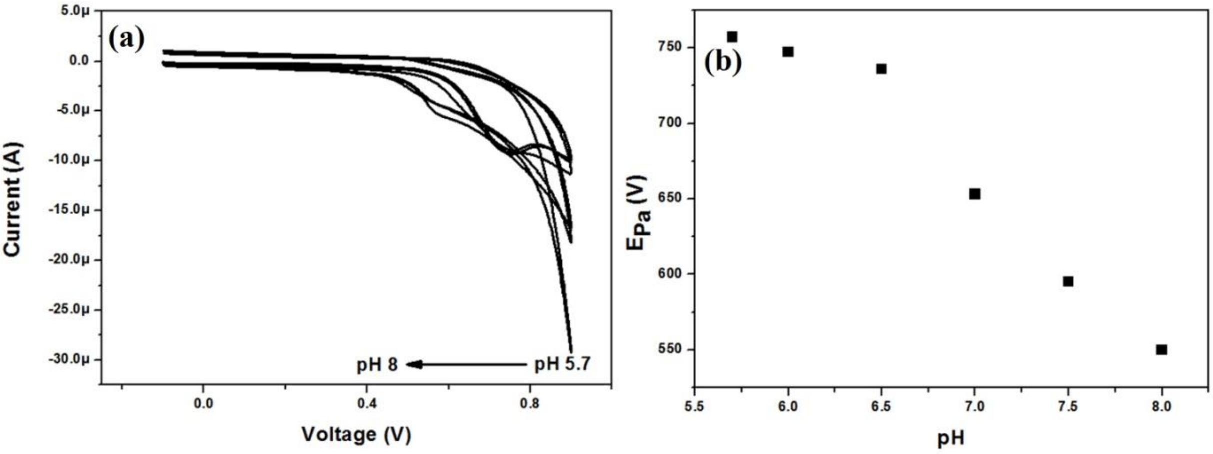

Figure 7.9 (a) Cyclic voltammogram of 2mM FA at different pH of PBS buffer solutions at 100mVs^{-1} using 8mg YDMCPE (b) Plot of anodic peak current vs. pH (pH= 5.7 to 8)

Figure 7.9 (a) represents the voltammogram of 2mM FA at different pH values of 0.2M PBS. The anodic peak potentials of 2mM FA were shifted towards lower potential side with the increase of pH value as show in the voltammogram. This is due to the higher oxidation rate of FA at higher pH values. Figure 7.9 (b) represents the plot of pH vs. anodic peak potential of FA. Oxidation peak potential of FA decreases linearly from pH 5.7 to 8 with correlation coefficient of 0.9407 as shown in the plot. At pH 5.7, the oxidation peak potential is 757mV and at pH 8 it is decreased to 550mV respectively.

7.6 Summary and conclusions

The prepared duplex stainless steel powder was mixed with 1wt. % nano structured Y_2O_3 powder particles by turbula shaker mixer for 2h. We successfully fabricated DMCPE and YDMCPE for detecting folic acid. The 4mg concentration of duplex and 8mg yittria dispersed duplex stainless steel powders show maximum current sensitivity. YDMCPE shows strong electro catalytic activity towards the oxidation of FA than DMCPE. High selectivity, easy preparation and high sensitivity of the voltammetric response made these electrodes a very useful sensor in determining FA. The entire electrode reactions at the above bioactive compound are adsorption controlled reactions. YDMCPE and DMCPE can be used as sensor in medical field for the diagnosis of FA deficiency diseases. Although we reported very efficient YDMCPE as a sensor for detecting the bioactive compounds, there is still a need for further research to scale-up the issues.

References

1) F.J. Al-Shammary, K.A. Al-Rashood, N.A. Mian, M.S. Mian, Analytical profile of folic acid, *Anal. Profiles. Drug. Sub.* 19 **(1990)** 221–259.

2) H.X. Guo, Y.Q. Li, L.F. Fan, X.Q. Wu, M.D. Guo, Voltammetric behavior study of folic acid at phosphomolybdic-polypyrrole film modified electrode, *Electrochim. Acta.* 51 **(2006)** 6230–6237.

3) J. Alaburda, A.P. De Almeida, L. Shundo, V. Ruvieri, M. Sabino, Determination of folic acid in fortified wheat flours, *J. Food. Comp. Anal.* 21 **(2008)** 336–342.

4) S.L. Zhaoa, H.Y. Yuan, C. Xie, D. Xiao, Determination of folic acid by capillary electrophoresis with chemiluminescence detection, *J. Chromatogr. A.* 1107 **(2006)** 290–293.

5) L.A. Kozhanova, G.A. Fedorova, G.I. Baram, Determination of Water and Fat Soluble Vitamins in Multivitamin Preparations by High-Performance Liquid Chromatography, *J. Anal. Chem.* 57 **(2002)** 40–45.

6) R.H.F. Cheung, J.G. Hughes, P.J. Marriott, D.M. Small, Investigation of folic acid stability in fortified instant Asian noodles by use of capillary electrophoresis, *Food. Chem.* 112 **(2009)** 507–514.

7) P. Nagaraja, H.R. Arun kumar, R.A. Vasantha, H.S. Yathirajan, Spectrophotometric determination of folic acid in pharmaceutical preparations by coupling reactions with iminodibenzyl or 3-aminophenol or sodium molybdate–pyrocatechol, *Anal. Biochem.* 307 **(2002)** 316–321.

8) M.B. Caselunghe, J. Lindeberg, Biosensor-based determination of folic acid in fortified food, *Food. Chem.* 70 **(2000)** 523–532.

9) V.D. Vaze, A.K. Srivastava, Electrochemical behavior of folic acid at calixarene based chemically modified electrodes and its determination by adsorptive stripping voltammetry, *Electrochim. Acta.* 53 **(2007)** 1713–1721.

10) Crouch, R. Stanley, Skoog, A. Douglas, Principles of instrumental analysis, Cengage Learning, **(2006),** ISBN 0-49501-201-7.

CHAPTER 8

Summary and Conclusions

In this thesis, nano-structured duplex and ferritic stainless steel powders were prepared from elemental Fe, Cr and Ni powders by high energy planetary milling and then detailed characterization of the powders were conducted. Here, both stainless steel powders were prepared by Fritsch Pulverisette planetary milling and indigenously built dual drive planetary milling (DDPM) and also a comparative study was carried out. Then the powders were consolidated separately by conventional sintering and spark plasma sintering (SPS) techniques. The corrosion behaviour of consolidated samples by linear sweep voltammetric method was studied. The possibility of stainless steel powder as an electrochemical sensor application was also evaluated. We have studied the effect of milling parameters such as types of mill, ball to powder weight ratios (BPR), process controlling agents (PCA), mill speed, milling time and milling atmosphere on the morphology, phase transformation and particle size of stainless steel powders.

The oxygen active compound like Y_2O_3 nanoparticles (size <100 nm) were dispersed into both duplex and ferritic stainless steel and its effect was studied successfully. Yittria dispersed and yittria free stainless steel powders were consolidated by conventional sintering and SPS techniques separately. The effect of sintering temperatures and sintering atmospheres on the hardness, density, microstructures, phase transformation and wear resistance properties were investigated systematically. The electro catalytic properties of yittria dispersed and yittria free stainless steel powders towards biologically active compounds were studied. The corrosion studies of spark plasma sintered stainless steels were carried out by using linear sweep voltammetry.

Nano-structured duplex and ferritic stainless steel powders were prepared by milling for 40h in Fritsch Pulverisette planetary mill. During milling, particle size increases initially due to repetitive welding of ductile iron and starts refining in the structure with the progress of milling. Lattice strain increases and crystallite size decreases with increase in milling time. Using DSC plots of 40h milled steel powders we calculated change in enthalpy, crystallization peaks, Curie temperature and also activation energy by Kissinger method. Increase in sintering temperature increases the density, hardness of the samples and decreases porosity level. Due to indentation size effect (ISE) both the stainless steel samples show reduced hardness with increasing indentation load. Both duplex and ferritic stainless steel sintered at 1400°C show maximum density and hardness. A density and microhardness value of 90% and 550HV were obtained for duplex stainless steel. Similarly, ferritic stainless steel exhibits 92% sintered density and 263HV microhardness value.

It was found that only 10h is sufficient to prepare nano-structured duplex and ferritic stainless steel powder in specially designed DDPM as compared to 40h in P5 mill. The duplex composition was showing ferritic phase till 5h of milling and becomes duplex after 10h in DDPM. The powder particles were of micron range and of random size before milling and as milling starts there will be slight increase in the particle size due to the repeated welding of ductile iron during milling. As milling continues, particles become strain hardened and spherical. After 10h of milling, the crystallite size reduced to 9 and 11nm in case of duplex and ferritic stainless steel respectively. The lattice strain goes on increasing in both the cases. Annealing of the powders at 750°C promotes ferritic to austenitic transformation in both argon and nitrogen atmosphere. However, nitrogen favours austenitic transformation to a greater extent as compared to argon. Thermal analysis study shows the exothermic peak, which represent crystallization of partial amorphous powder, crystal growth and lattice strain release during heating. Although bulk efficient synthesis of nano-structured duplex and ferritic stainless steel powder is the main focus of the present work, but there is a need for further research to scale-up the issues. There is plenty of scope for improved design of the milling system with enhanced energy efficiency to make dual drive planetary milling a viable commercial technique for bulk production.

Nano-structured duplex and ferritic stainless steel powders were prepared by optimizing the milling parameters. Particle size of both the stainless steel powder particles become less when milled in presence of stearic acid (SA) and shape of the powder is irregular as compared to stainless steel powder milled in the absence of SA. Milling of stainless steel samples carried out at 12:1 BPR shows reduced particle size as well as low crystallite size and higher lattice strain compared to 6:1 BPR milling conditions. XRD spectrum of duplex stainless steel milled at 12:1 BPR shows rapid phase transformation from α-Fe to γ-Fe than 6:1 due to the high impact energy, increased defects and frequent collision of ball-powder-jar. Milling at 75% critical speed (CS) is found to be more efficient in refining the particles and crystallite size of both the stainless steel samples compared to milling carried out at 64% CS. The shape of the stainless steel powders milled at 75%CS is more regular and spherical than the stainless steel milled at 64% CS mill speed due to the increased defects and acceleration field of the mill at higher mill speed. We successfully studied the phase transformation, particle size and morphology at different milling conditions and concluded that all these parameters have great influence in refining particle size and morphology of powders. It was also noticed that dry milled stainless steel showed lesser particle size than wet milled samples.

Yittria dispersed and yittria free duplex and ferritic stainless steel samples were consolidated successfully by conventional sintering and SPS methods. It was found that increase in sintering temperature from 1000 to 1400°C increases the density, hardness and α-Fe to γ-Fe phase transformation of duplex and yittria dispersed duplex stainless steel. Conventional sintering in nitrogen atmosphere favours α-Fe to γ-Fe phase transformation and increases the density and hardness of stainless steel when compared with sintering in argon atmosphere. Spark plasma sintered stainless steel show maximum density, hardness and phase transformation due to retention of nano grains even after sintering.

Non-lubricated sliding wear resistance of stainless steel samples against diamond indenter was studied. It was found that wear depth increases with increase in applied load from 10 to 20N in all the stainless steels. Stainless steel sintered under nitrogen atmosphere exhibits more wear resistance than the stainless steel sintered under argon atmosphere. The wear debris produced in duplex and ferritic steels are flake shape due to soft nature, whereas, spherical particle shaped wear debris is generated in case of yittria dispersed duplex steel. Wear mechanisms in both types of stainless steels are mainly abrasive and oxidative nature. The amount of oxygen present on worn surfaces in duplex stainless steel at 10N applied load varies from 5 to 37% and at 20N load it varies from 20 to 44% with increase in sintering temperature from 1000 to 1400°C. The worn surface of duplex stainless steel sintered in nitrogen atmosphere at 1000°C shows oxygen percentage of 9 at 10N and 20 at 20N applied loads respectively.

Mechanically alloyed duplex and ferritic stainless steel samples dispersed with yittria and without yittria were consolidated by SPS method at a load of 50MPa and 1000°C temperature under vacuum for 5 minutes. XRD and microstructural analysis were performed for consolidated stainless steel samples before corrosion study. From XRD it is confirmed that yittria acts as austenitic stabilizer but more research should be conducted to study the actual role of yittria as austenitic stabilizing agent. We successfully studied the corrosion properties of consolidated stainless steel samples by LSV method at different concentration of NaCl and

H_2SO_4 solutions. As the concentration of NaCl and H_2SO_4 electrolytes increase from 0.5 to 2M then pitting potential for all the four stainless steel samples decrease due to the accelerated rate of corrosion reactions at higher concentrations. In case of NaCl, pitting potential (E_P) decreases with increasing current density but in case of H_2SO_4, E_P increases with increasing current density due to the formation of $FeSO_4$ protective layer along with Cr_2O_3 layer. At 0.5M NaCl, pitting potential (E_P) of yittria dispersed duplex and ferritic stainless steel samples are found to be 1.45V and 0.64V and that of yittria free duplex and ferritic stainless steel samples show E_P value of 0.63V and 0.57V. Similarly, E_P value of yittria dispersed duplex and ferritic stainless steel samples at 0.5M H_2SO_4 are 0.30V and 0.23V respectively and that of yittria free duplex and ferritic stainless steel samples show E_P value of 0.18V and 0.14V. Microstructural analysis by FESEM and optical microscopy show corroded regions of stainless steel samples. Volume fraction of iron oxide (corrosion) present in yittria dispersed duplex and ferritic stainless steel samples are 37 and 41.73% respectively and that of yittria free duplex and ferritic stainless steel samples are 60.55 and 64.10% respectively.

The prepared duplex stainless steel powder was mixed with 1wt. % nano-structured Y_2O_3 powder particles by turbula shaker mixer for 2h. We successfully fabricated duplex modified carbon paste electrode (DMCPE) and yittria duplex modified carbon paste electrode (YDMCPE) for detection of folic acid (FA). The 4mg concentration of duplex and 8mg yittria dispersed duplex stainless steel powders show maximum current sensitivity. YDMCPE shows strong electro catalytic activity towards the oxidation of FA than DMCPE. High selectivity, easy preparation and high sensitivity of the voltammetric response made these electrodes a very useful sensor in determining FA. The entire electrode reactions at the above bioactive compound are adsorption controlled reactions. YDMCPE and DMCPE can be used as sensor in medical field for the diagnosis of FA deficiency diseases. Although we reported the use of YDMCPE as a sensor for detecting the bioactive compounds, there is still a need for further research to scale-up the issues. There is always a plenty of scope to fabricate sensitive, selective and material fouling resistant electrodes. YDMCPE and DMCPE satisfy the above needs with excellent performance.

CONTRIBUTION FROM THE PRESENT WORK

- Nano-structured duplex and ferritic stainless steel powders were prepared by both pulverisette planetary milling and high energy dual drive planetary milling (DDPM) from elemental Fe, Cr and Ni powders.

- Optimized milling parameters such as BPR, milling speed, PCA, milling time, milling atmosphere, types of milling to prepare duplex and ferritic stainless steel powders and studied their effects on particle size, morphology and phase transformation during milling.

- Yittria dispersed and yittria free stainless steel powders were consolidated by both pressureless conventional sintering and SPS to investigate the hardness, density, microstructures, phase transformation and wear resistance properties.

- The electro catalytic properties of yittria dispersed and yittria free stainless steel powders towards biologically active compounds were studied. The duplex modified electrode exhibits resplendent sensitivity towards the detection of folic acid and their responses are fast, stable, reliable and resistant to material fouling and this can be applied for the real sample analysis in medical, pharmaceutical and biotechnological sectors.

- Stainless steels consolidated by SPS process exhibit enhancement in physical and mechanical properties than conventionally sintered stainless steels.

- Linear sweep voltammetry is a new method to study pitting corrosion resistance properties of duplex and ferritic stainless steel. The yittria dispersed stainless steel exhibit higher corrosion resistance than yittria free stainless steels.

FUTURE WORK

- Performing SPS at different sintering temperature to study the microstructure, phase transformation, mechanical properties and surface properties in detail.
- The addition of other dispersoids such as titanium oxide, lanthanum oxide and tungsten individually to stainless steel during milling and study their effect on microstructure, mechanical properties, corrosion properties, wear behaviour study etc.
- To study the corrosion properties of P/M stainless steel by optimizing the electrochemical conditions such as electrolyte types (acidic and basic electrolytes), different concentration of electrolytes, use of different types of corrosion inhibitors, reaction time etc.
- TEM analysis of SPS and conventionally sintered yittria dispersed stainless steel to investigate the effect of yittria and phase analysis in detail.
- Study of electrocatalytic properties of P/M stainless steel using cyclic voltammetry in detecting other bio-active compounds.

Appendix 1

A comparison on synthesis of nano-structured duplex and ferritic stainless steel powders by DDPM and pulverisette planetary milling

In the present work, nano-structured duplex and ferritic stainless steel powders were prepared by milling elemental Fe, Ni and Cr powders in a specially designed dual-drive planetary mill (DDPM) and Fritsch pulverisette planetary mill (P5 mill). Here, we report that only 10 hours is sufficient to prepare both types of stainless steel powders in DDPM. Whereas 40 hours is required to prepare the stainless steel powders in Fritsch pulverisette planetary mill. From the available literature it is found that large milling time (>100 h) is required to prepare stainless steel powder and very small amount of powder can be prepared (<50 g) in pulverisette type planetary mills. But the specially designed DDPM is one of the highly efficient mills to prepare nano-structured stainless steel powder compared with other traditional mills as it has a very high acceleration field (73g) as compared to 25g in Fritsch pulverisette planetary mill.

Table 1 Comparison on synthesis of stainless steel by DDPM and P5 mills

Type of mill	Milling time (hours)	Milling media	Composition	Crystallite size (nm)	Lattice strain (%)	Mean Particle size (µm)	Lattice parameter (Å)	Particle morphology
P5 Mill	40	Jar volume: 500ml, 300g chrome steel balls, 6:1 BPR, Toluene atmosphere	Duplex	8	0.92	15	3.53	Contains both spherical and irregular particles
			Ferrite	7	0.71	18	2.88	
DDPM	10	Jar volume: 1200ml, 1000g chrome steel balls, 6:1 BPR, Toluene atmosphere	Duplex	7	0.56	22	3.51	Spherical particles with more regularity
			Ferrite	8	0.91	16	2.86	

The DDPM consists of a gyratory shaft and cylindrical jars and both rotate simultaneously in opposite directions at high speed and we can control their speed of rotation by a frequency regulator. This allows ball to move strongly and rigorously, which led to large impact energy between the balls and the materials. Single run of the DDPM can easily synthesize more than 500 g of powder in one batch but that is limited to around 50g in P5 mill. We compared the microstructural evolution, particle size, shape, phase transformation of duplex and ferritic stainless steel powders prepared by DDPM and P5 mills. The specially designed DDPM is found to be more efficient and cost effective technique to prepare duplex and ferritic stainless steel powders when compared with P5 mill. Table 1 depicts the comparison on synthesis of stainless steel by DDPM and P5 mills. Now a day many different types of planetary mills are available in the market and all are having different efficiency to refine the structure of materials. Some of the researchers investigated the microstructural evolution, particle shape and size of duplex and ferritic stainless steel powders by optimizing the milling parameters and their results are tabulated in Table 2.

Table 2 Synthesis of duplex, austenite and ferritic stainless steel powders by different investigators

References	**Type of stainless steel**	**Type of mill**	**Milling time (hours)**	**Milling media**	**Crystallite size (nm)**	**Particle size (μm)**	**Particle morphology**
[1]	Duplex	Planetary ball mill	60	Jar volume: 120ml, 6:1 BPR, Argon atmosphere,	15	-	-
[2]	Austenite	Retsch PM100	100	Jar volume: 500ml, 25:1 BPR, 300rpm mill speed, Nitrogen atmosphere,	< 10	200	Irregular shape with agglomeration
[3]	Yittria dispersed austenite	High energy planetary mill	50	Different ball sizes 20, 10 and 6mm, 5:1 BPR, 300rpm mill speed, Nitrogen atmosphere,	13	100	Nearly spherical with different sizes
[4]	Austenite	Retsch PM100	100	Balls with 20mm diameter, 25:1 BPR, 300rpm mill speed, Nitrogen atmosphere	7	7	Irregular shape and sizes
[5]	Ferritic stainless steel	Sepahan planetary ball mill	120	Jar volume: 150ml, Balls with 20 and 12mm diameter, 20:1 BPR, 500rpm mill speed, argon atmosphere	10	-	-
[6]	Yittria dispersed ferritic stainless steel	Simoloyer CM20 horizontal ball mill	48	15:1 BPR, 240rpm mill speed, Ar-H_2 mixture atmosphere	-	60	Spherical shape with a smooth surface

References

1) M.H. Enayati, M.R. Bafandeh, Phase transitions in nanostructured Fe–Cr–Ni alloys prepared by mechanical alloying, *J. Alloy. Compd.* 454 **(2008)** 228–232.

2) T. Haghir, M.H. Abbasi, M.A. Golozar, M. Panjepour, Investigation of α to γ transformation in the production of a nanostructured high-nitrogen austenitic stainless steel powder via mechanical alloying, *Mater. Sci. Eng. A.* 507 **(2009)** 144–148.

3) M. Wang, H. Sun, L. Zou, G. Zhang, S. Li, Z. Zhou, Structural evolution of oxide dispersion strengthened austenitic powders during mechanical alloying and subsequent consolidation, *Powder. Technol.* 272 **(2015)** 309–315.

4) F. Tehrani, M.H. Abbasi, M.A. Golozar, M. Panjepour, The effect of particle size of iron powder on α to γ transformation in the nanostructured high nitrogen Fe–Cr–Mn–Mo stainless steel produced by mechanical alloying, *Mater. Sci. Eng. A.*528 **(2011)** 3961–3966.

5) E. Salahinejad, M.J. Hadianfard, M. Ghaffari, R. Amini, Sh. Bagheri Mashhadi, A.K. Okyay, Microstructural characterization of medical-grade stainless steel powders prepared by mechanical alloying and subsequent annealing, *Adv. Powder. Tech.* 24 **(2013)** 605–608.

6) S. Noh, B.K.. Choi, S.H. Kang, T.K. Kim, Influence of mechanical alloying atmospheres on the microstructures and mechanical properties of 15Cr ODS steels, *Nucl. Eng. Technol.* 46 **(2014)** 857-862.

Appendix 2

Comparison of duplex and ferritic stainless steels fabricated by DDPM and pulverisette planetary milling followed by conventional sintering

Table 3 Comparative investigation of stainless steel prepared by DDPM and P5 mill followed by conventional sintering at 1000, 1200 and 1400°C respectively

Type of mill	Type of stainless steel	Sintering temperature (°C)	Volume fraction (%)		Sintered density (%)	Vickers microhardness at 25gf (HV)
			Austenite	Ferrite		
P5 Mill	Duplex	1000	44	52	66	253
		1200	57	40	80	337
		1400	60	38	90	550
	Ferrite	1000	-	96	69	171
		1200	-	97	85	217
		1400	-	97	92	251
DDPM	Duplex	1000	51	49	71	257
		1200	62	38	86	451
		1400	65	35	91	567
	Ferrite	1000	33	67	73	192
		1200	44	56	88	224
		1400	58	42	93	265
	Yittria Duplex	1000	57	43	78	332
		1200	65	35	91	495
		1400	72	27	94	576
	Yittria Ferrite	1000	41	58	80	205
		1200	52	48	91	282
		1400	62	38	96	341

We reported a very fast and efficient method of fabrication of nano-Y_2O_3 dispersed and Y_2O_3 free nano-structured duplex and ferritic stainless steel by DDPM and P5 milling of elemental Fe, Cr and Ni powders and then consolidation by conventional pressureless sintering. Table 3 depicts the comparative results of stainless steels obtained from DDPM and P5 mill followed by conventional sintering. Table 4 depicts the comparative results of some of the researchers performed at similar conditions.

Table 4 Comparative results of some of the researchers performed at similar conditions

References	**Type of stainless steel**	**Sintering conditions**	**Sintering temperature (°C)**	**Sintered density (%)**	**Microhardness (HV)**
[1]	YAG dispersed austenitic stainless steel	Conventional sintering, H_2 atmosphere	1200	85	140
			1400	98	290
[2]	Austenitic stainless steel	Compacted at 600MPa, Conventional sintering, H_2 atmosphere	1200	83	97
			1300	86	109
			1400	90	126
[3]	Austenitic stainless steel	Compacted at 800MPa, Conventional sintering, N_2 atmosphere for 30min	1200	80	234
			1250	83	249
			1300	88	320
[4]	YAG dispersed Ferritic stainless steel	Compacted at 600MPa, Conventional sintering, H_2 atmosphere for 1h	1200	83	140
			1400	93	250
[5]	Duplex stainless steel	Electric muffle furnace for 30min and water quenched	1100		232
			1200		239
			1300		257
			1350		243
[6]	Duplex stainless steel	Compacted at 700MPa, Conventional sintering, Argon atmosphere for 1h	1000	66	253
			1200	80	337
			1400	90	550

References

1) J. Jain, A.M. Kar, A. Upadhyaya, Effect of YAG addition on sintering of P/M 316L and 434L stainless steels, *Mater. Lett.* 58 **(2004)** 2037– 2040.

2) S. Pandya, K.S.Ramakrishna, A.R. Annamalai, A. Upadhyaya, Effect of sintering temperature on the mechanical and electrochemical properties of austenitic stainless steel, *Mater. Sci. Eng. A.* 556 **(2012)** 271–277.

3) N. Kurgan, Effect of porosity and density on the mechanical and microstructural properties of sintered 316L stainless steel implant materials, *Mater. Design.* 55 **(2014)** 235–241.

4) S.M. Tiwari, S. Balaji, A. Upadhyaya, Sintering and characterization of YAG dispersed ferritic stainless steels, *Mater. Sci. Eng. A.* 492 **(2008)** 60–67.

5) K. Vijayalakshmi, V. Muthupandi, R. Jayachitra, Influence of heat treatment on the microstructure, ultrasonic attenuation and hardness of SAF 2205 duplex stainless steel, *Mater. Sci. Eng. A.* 529 **(2011)** 447– 451.

6) R. Shashanka, D. Chaira, Development of nano-structured duplex and ferritic stainless steels by pulverisette planetary milling followed by pressureless sintering, *Mater. Charact.* 99 **(2015)** 220–229.

Appendix 3

Comparison of experimental results of spark plasma sintered stainless steels with the results of other investigators

Table 5 Stainless steel fabricated by SPS method by various researchers

References	Type of stainless steel	Sintering conditions	Sintering temperature (°C)	Sintered density (%)	Microhardness (HV)
[1]	Ferritic stainless steel	SPS in vacuum, <6Pa load for 5min	1000	99	501
[2]	ODS ferritic stainless steel	SPS in Ar atmosphere, 45MPa load for 5min	1050	97	-
[3]	Yittria dispersed ferritic stainless steel	SPS, 80MPa load for 1h	1050	97	380
[4]	Yittria dispersed ferritic stainless steel	SPS, 30MPa load for 5min	900	98	850
[5]	Austenitic stainless steel	SPS in vacuum, 50MPa for 5min	1000	99.5	237
[6]	Nickel free austenitic stainless steel	SPS in vacuum, 40MPa load for 8min	1000	99	260
[Our Results]	Yittria dispersed duplex stainless steel	SPS in vacuum, 50MPa for 5min	1000	93	1026
[Our Results]	Yittria dispersed ferritic stainless steel	SPS in vacuum, 50MPa for 5min	1000	95	819
[Our Results]	Duplex stainless steel	SPS in vacuum, 50MPa for 5min	1000	91	765
[Our Results]	Ferritic stainless steel	SPS in vacuum, 50MPa for 5min	1000	92	650

We fabricated planetary milled duplex and ferritic stainless steel by SPS. In another set of experiment we dispersed 1wt. % of yittria nanoparticles in to milled duplex and ferritic stainless steel by using turbula mixer for 3h and then consolidated by SPS method at a temperature of 1000°C and a load of 50MPa for 5min in vacuum. Table 5 depicts the comparison of stainless steel fabricated by SPS method by various researchers with our results.

References

1) N.H. Wei, H.E. Hang, L.G. Qiang, L. Jing, Preparation of Nanocrystalline 430L Stainless Steel by HEBM and SPS, *J. Iron. Steel. Res. Int.* 15 **(2008)** 73-76.

2) Y.P. Xia, X.P. Wang, Z. Zhuang, Q.X. Sun, T. Zhang, Q.F. Fang, T. Hao, C.S. Liu, Microstructure and oxidation properties of 16Cr–5Al–ODS steel prepared by sol–gel and spark plasma sintering methods, *J. Nucl. Mater.* 432 **(2013)** 198–204.

3) K.N. Allahar, J. Burns, B. Jaques, Y.Q. Wu, I. Charit, J. Cole, D.P. Butt, Ferritic oxide dispersion strengthened alloys by spark plasma sintering, *J. Nucl. Mater.* 443 **(2013)** 256–265.

4) A. Pandey, K. Jayasankar, P. Parida, M. Debata, B.K. Mishra, S. Saroja, Optimization of milling parameters, processing and characterization of nano-crystalline oxide dispersion strengthened ferritic steel, *Powder. Technol.* 262 **(2014)** 162–169.

5) G. Marnier, C. Keller, J. Noudem, E. Hug, Functional properties of a spark plasma sintered ultrafine-grained 316L Steel, *Mater. Design.* 63 **(2014)** 633–640.

6) Z. Xu, C. Jia, C. Kuang, K. Chu, X. Qu, Spark plasma sintering of nitrogen-containing nickel-free stainless steel powders and effect of sintering temperature, *J. Alloy. Compd.* 484 **(2009)** 924–928.

Thesis dissemination

International journal publications

1) R. Shashanka, D. Chaira, Phase transformation and microstructure study of nano-structured austenitic and ferritic stainless steel powders prepared by planetary milling **Powder Technology,** 259 (2014) 125–136.

2) R. Shashanka, D. Chaira, Development of nano-structured duplex and ferritic stainless steel by pulverisette planetary milling followed by pressureless sintering, **Materials Characterization,** 99 (2015) 220-229.

3) R. Shashanka, D. Chaira, Optimization of milling parameters for the synthesis of nano-structured duplex and ferritic stainless steel powders by high energy planetary milling, **Powder Technology,** 278 (2015) 35-45.

4) R. Shashanka, D. Chaira, B.E. Kumara Swamy, Electrocatalytic Response of Duplex and Yittria Dispersed Duplex Stainless Steel Modified Carbon Paste Electrode in Detecting Folic Acid Using Cyclic Voltammetry, **International Journal of Electrochemical Science,** 10 (2015) 5586 – 5598.

5) R. Shashanka, D. Chaira, B.E. Kumara Swamy, Electrochemical investigation of duplex stainless steel at carbon paste electrode and its application to the detection of dopamine, ascorbic and uric acid, **International Journal of Scientific & Engineering Research,** 6 (2015) 1863–1871.

6) R. Shashanka, D. Chaira, Effects of Nano-Y2O3 and Sintering Parameters on the Fabrication of PM Duplex and Ferritic Stainless Steels, **Acta Metallurgica Sinica (English Letters),** 29 (2016) 58-71.

7) R. Shashanka, D. Chaira, B.E. Kumara Swamy, Fabrication of yttria dispersed duplex stainless steel electrode to determine dopamine, ascorbic and uric acid electrochemically by using cyclic voltammetry, **International Journal of Scientific & Engineering Research,** 7 (2016) 1275-1285.

8) R. Shashanka. D. Chaira, Effect of sintering temperature and atmosphere on non-lubricated sliding wear of nano-yttria dispersed and yttria free duplex and ferritic stainless steel fabricated by powder metallurgy, **Tribology Transactions,** (2016) DOI:10.1080/10402004.2016.1168897.

9) R. Shashanka. D. Chaira, Effect of Y2O3 addition on non-lubricated sliding wear behaviour of duplex stainless steel, **Transactions of PMAI,** 41 (2015) 17-25.

10) R. Shashanka, D. Chaira, B.E. Kumara Swamy, Effect of Y_2O_3 on corrosion study of spark plasma sintered duplex and ferritic stainless steel samples by linear sweep voltammetric method, **Journal of Analytical & Bioanalytical Techniques** (Accepted for publication).

11) R. Shashanka, D. Chaira, Fast fabrication of nano-Y_2O_3 dispersed duplex and ferritic stainless steels by spark plasma sintering, (under review) **Metallurgical and Materials Transactions B.**

Conference proceedings

1) R. Shashanka. D. Chaira, “Synthesis and characterisation of nano-structured ferritic and austenitic stainless steel powder by high energy planetary milling”. OPJIT **International Journal of Innovation and Research,** 3 (2014) 19-25. ISSN 2319-4340.
2) S. Gupta, R. Shashanka, D. Chaira, Synthesis of nano-structured duplex and ferritic stainless steel powders by planetary milling: An experimental and simulation study, 4th National Conference on Processing and Characterization of Materials, **IOP Conf. Series: Materials Science and Engineering**, 75 (2015) 012033.

3) A.K. Nayak, R. Shashanka, D. Chaira, Effect of Nanosize Yittria and Tungsten Addition to Duplex Stainless Steel During High Energy Planetary Milling, 5th National Conference on Processing and Characterization of Materials, **IOP Conf. Series: Materials Science and Engineering**, 115 (2016) 012008.

Conferences attended and published abstracts

1) 5th National Symposium for Materials Research Scholars MR-13, IIT Bombay, 8-9th May 2013.

2) International Conference on Metallurgical and Materials Processes, Products and Applications, O.P. Jindal Institute of Technology, Raigarh, 8-10th January 2014.

3) 52nd National Metallurgists day and 68th Annual Technical meeting, Indian Institute of Metals NMD ATM-2014, COEP, Pune, 12-15th November.

4) PM 15 International Conference on Powder Metallurgy and Particulate Materials and 41st Annual Technical Meeting, IIT Bombay, 19-21st January 2015.

5) International conference on Powder Metallurgy and Particulate Materials, POWDERMET-2015, San Diego, California, USA, May 17-20th 2015.

6) PM 16 International Conference on Powder Metallurgy and Particulate Materials and 42nd Annual Technical Meeting, Hotel Hyatt Regency, Pune, 18-20th January 2016.

Awards and Achievements

1) Rewarded first prize for poster presentation at IIM, NMD ATM-2014, COEP, Pune, 12-15th November.
2) First recipient of the prestigious “India’s best powder metallurgy student of the year award-2015” by Powder Metallurgy Association of India (PMAI) at an International conference on Powder Metallurgy and Particulate Materials-2015 (PM-15) held at IIT Bombay.
3) Won a full paid sponsorship of PMAI to attend POWDERMET-2015 conference held at San Diego, USA.

Biography of the scholar

Shashanka was born in Birur, Chikmagalur district, Karnataka, India on 18th November 1986. He finished his schooling from Shree Akkamahadevi Primary School and intermediate from K.L.K. Govt. College, Birur. He completed Bachelor of Science in Industrial Chemistry from Sahyadri Science College, Shimoga in 2007, one of the premier science colleges in Karnataka. He pursued his Master of Science (M.Sc) in Industrial Chemistry from Kuvempu University, Shankaraghatta, Karnataka in 2009. During his M.Sc days, he was attracted a lot towards Nano technology and he pursued M.Tech degree in Nanoscience and Technology from Kuvempu University, Shankaraghatta, Karnataka in 2011. During his M.Tech he participated in several conferences and won "Best poster presentation" award at Tumkur University in a National conference on "Chemistry of materials-2011". His M.Tech project was on "Electrochemical generation of CuO nanoparticles by a Cyclic voltammetric technique" in the Dept. of Industrial Chemistry, Kuvempu University under the guidance of Dr. B.E. Kumara Swamy. Apart from studies, he is a good sports person too. He played a several state level volleyball tournaments and had won handsome number of best player awards. He enrolled himself to pursue PhD in the department of Metallurgical and Materials Engineering, National Institute of Technology, Rourkela in November 2011 in a CSIR funded project under the supervision of Dr. Debasis Chaira, Assistant Professor, NIT Rourkela. He was involved in research relating to synthesis of nano-structured stainless steel powders (Austenitic, ferritic and duplex stainless steel powders) by mechanical alloying method and their characterizations. He prepared nano-structured stainless steel powders at different milling parameters (Mill speed, ball to powder weight ratio, process controlling agents) and studied phase transformation, particle size and morphology etc. He also investigated the consolidation of stainless steel powders at different sintering parameters (Different sintering systems, sintering atmospheres, different temperatures) and studied their mechanical, wear, corrosion and electro catalytic properties. He has published papers in frontier journals such as Powder Technology, Materials Characterization, International Journal of Electrochemical Science and many more. His research interests comprises of powder metallurgy, nano-structured materials, electrochemistry, corrosion science etc. He is a life member of Powder Metallurgy Association of India (PMAI) and a student member of American Powder Metallurgy Institute (APMI). He was awarded first prize for poster presentation at Indian Institute of Metals NMD ATM-2014, 12-15 November, COEP, Pune. It is one of the biggest metallurgy conferences of India. He is the first recipient of the prestigious "India's grand powder metallurgy student of the year award 2015" by Powder Metallurgy Association of India at an International PM-15 conference held at IIT Bombay. He also represented powder metallurgy student fraternity of India in an International conference on Powder Metallurgy and Particulate Materials, POWDERMET-2015 held at San Diego, USA. He is interested to pursue post-doctoral research in an internationally renowned university in the line of core materials engineering or electrochemistry to unravel the science of interface behind the powder technology and corrosion science.